



University of Salerno

DEPARTMENT OF PHYSICS “E.R.CAIANIELLO”

Doctor of Philosophy in Mathematics, Physics, and Applications –
Curriculum Physics – XXXIV cycle

Doctoral thesis in:

Tailoring the structural and surface properties of TiO₂ thin
films and TiO₂-based nanolayers, with heat treatments,
layer thickness, and oxide mixtures

Dr. Ofelia Durante

PhD Coordinator:

Prof. C. Attanasio

Supervisor:

Prof. F. Bobba

Co-Supervisor:

Dr. C. Di Giorgio

Academic Year 2020/2021

There's plenty of room at the bottom.

Richard Feynman

Contents

Acronyms and Symbols	8
Abstract	10
Chapter 1	12
Introduction	12
1.1 Structural properties of TiO_2	12
1.2 Applications of TiO_2	15
1.2.1 Electronics	18
1.2.2 Photovoltaic cells.....	18
1.2.3 Optical coatings.....	19
1.3 Other oxide materials.....	26
1.3.1 Tantalum Oxide	26
1.3.2 Zirconium Oxide.....	26
1.3.3 Silicon Oxide	27
1.3.4 Aluminum Oxide	27
Chapter 2	34
Materials and Methods	34
2.1 Ion-assisted e-beam deposition (IAD).....	35
2.1.1 Experiment	37
2.2 Ion-beam Sputtering (IBS)	39
2.2.1 Experiment	39
2.3 Scanning Probe Microscopy (SPM)	41
2.3.1 Atomic Force Microscopy (AFM)	42
2.3.2 Kelvin Probe Force Microscopy (KPFM)	44
2.3.3 Experiment	45
2.4 Scanning Electron Microscopy (SEM)	46
2.4.1 Experiment	47
2.5 X-Ray Diffraction (XRD).....	48
2.5.1 Experiment	48
2.6 Raman spectroscopy (RS).....	49
2.6.1 Experiment	51
2.7 Thermal annealing.....	52
2.7.1 Experiment	52
2.8 Substrates	53
Chapter 3	56
Structural and morphological characterization of TiO_2 vs environment	56

3.1 Study of as-grown TiO ₂	57
3.2 Study of TiO ₂ crystallization onset and evolution versus environment	59
3.3 Study of TiO ₂ surface photo voltage versus environment	72
Summary	81
Chapter 4	87
Structural and morphological characterization of TiO₂ vs thickness	87
4.1 Study of as-grown TiO ₂ versus thickness	88
4.2 Study of TiO ₂ crystallization onset versus thickness	92
4.3 Study of TiO ₂ crystallization evolution versus thickness	95
Summary	104
Chapter 5	107
Nanolayers	107
5.1 TiO ₂ /SiO ₂ NLs vs segmentation degree.....	109
5.1.1 Characterization of as-grown TiO ₂ /SiO ₂ NLs	109
5.1.2 Characterization of annealed TiO ₂ /SiO ₂ NLs.....	114
5.3 TiO ₂ -based nanolayers	123
5.3.1 Morphological and structural characterization of TiO ₂ /Ta ₂ O ₅ , TiO ₂ /Al ₂ O ₃ , and TiO ₂ /ZrO ₂ NLs	124
5.4 SiO ₂ -based nanolayers	128
Summary	129
Chapter 6	132
Co-sputtered TiO₂-Ta₂O₅	132
6.1 State of art of co-sputtered materials	133
6.2 Co-sputtered TiO ₂ -Ta ₂ O ₅ deposited on Si.....	134
6.2.1 XRD measurements	134
6.2.2 Raman measurements	137
6.2.3 EDS measurements on as-grown samples	142
6.2.4 EDS measurements on samples annealed at 1000 °C	144
6.2.5 AFM measurements	146
6.2.6 Optical measurements of samples annealed at 1000 °C.....	151
6.3 Co-sputtered TiO ₂ -Ta ₂ O ₅ deposited on SiO ₂	152
6.3.1 XRD measurements	152
6.3.2 Raman measurements	153
6.3.3 AFM measurements	155
Summary	159
Conclusions	163
Acknowledgements	165

Appendix A	166
Appendix B	170
Appendix C	174
Appendix D	177
Appendix E	188
Appendix F	191
List of publications	197

Acronyms and Symbols

AFM	Atomic Force Microscopy
BR	Bragg reflector
CB	Conduction band
DSSC	Dye-sensitized solar cell
EDS	Energy-dispersive X-ray spectroscopy
E _g	Anatase Raman mode
FESEM	Field Emission SEM
FFT	Fast Fourier Transform
FWHM	Full width at half maximum
Γ	Linewidth
γ	Surface free energy
GENS	Gentle Nodal Suspension
GWD	Gravitation-Wave Detector
HI	High refractive index material
IAD	Ion-assisted deposition
IBS	Ion Beam Sputtering
KPFM	Kelvin Probe Force Microscopy
λ _d	Characteristic decay length
LI	Low refractive index material
MIM	Metal-insulator-metal
NL	Nanolayer
PCM	Phase change material
PID	Proportional-integral-derivative
PO ₂	Oxygen pressure

PVD	Physical Vapor Deposition
RS	Raman Spectroscopy
RRAM	Resistive random-access memory
sccm	Standard cubic centimeters per minute
SEM	Scanning Electron Microscopy
SL	Single layer
SPM	Scanning Probe Microscopy
SPV	Surface photovoltage
STEM	Scanning Transmission Electron Microscope
T_a	Annealing temperature
T_c	Crystallization onset temperature
T_{melt}	Melting temperature
VB	Valence band
V_{CPD}	Contact Potential Difference
W	Work function
XRD	X-ray Diffractometry
XRR	X-ray Reflectivity

Abstract

Titanium dioxide (TiO_2), also known as titanium (IV) oxide or titania, is naturally available on the Earth as a bright, fine, and white pigment. Thanks to its unique properties, such as high refractive index, chemical stability, photocatalytic activity, and self-cleaning surface, TiO_2 represents one of the most intensively studied compounds. The properties of TiO_2 , which depend on its three crystalline phases (anatase, brookite, and rutile), have made this material a valuable candidate for applications in many fields, such as optics (Bragg reflectors, meta-surfaces, optical filters), electronic (sensors, phase-change memory and metal insulator-semiconductor devices), and photocatalysis (air purification, water treatments, self-cleaning coatings, dye-sensitized solar cells). Indeed, its band structure, long-term stability, non-toxicity, cost-effectiveness, and strong oxidizing power make TiO_2 highly suitable for wide environmental and energy applications. Moreover, given its impressive optical properties, TiO_2 finds room in the context of amorphous coatings for the development of dielectric mirrors, characterized by low transmittance and thermal noise, to be implemented in the detectors of gravitational waves. Given the impact that both structural and morphological properties have on the optical and electronic performances of TiO_2 , a systematic study on the tailoring of TiO_2 crystal structure and surface properties is of fundamental relevance in many fields.

One of the aims of this work is thus to study the morphological, structural, and photocatalytic properties of amorphous TiO_2 thin films and the impact on these properties of the structural transitions induced by thermal annealing in different environments. Moreover, the tailoring of the morphological and structural properties of TiO_2 as a function of thickness is also investigated. Additionally, the combination of TiO_2 , in its nanolayered form as well as in the state of co-sputtered mixture, with other metal oxides is analyzed to address the extent of their structural and morphological reliability for highly performant high-refractive index candidates in new generation Bragg-like reflectors. In this scenario, Scanning Probe Microscopy based experiments (Atomic Force Microscopy, and Kelvin Probe Force Microscopy), Raman Spectroscopy, and X-Ray Diffractometry have been used to study the morphological, photocatalytic and structural properties of the investigated materials.

An overview of the properties of TiO_2 and its applications, including the one for gravitational wave detectors, i.e., the context where this work arose, is given in Chapter 1. Here the main properties of some other metal oxides (i.e., ZrO_2 , Al_2O_3 , Ta_2O_5 , Al_2O_3) encountered in this thesis are additionally discussed.

Then, Chapter 2 will briefly introduce the fabrication (ion-assisted deposition and ion-beam sputtering) and characterization (Raman Spectroscopy, X-Ray Diffractometry, Scanning Probe and Electron Microscopy) techniques used in this work.

The experimental results will be presented in Chapters 3,4,5, and 6. In particular, in Chapter 3 the effect of thermal treatments in different environments (air, oxygen and vacuum) and at different temperatures on the structural, morphological, and

photocatalytic properties of TiO_2 thin films will be discussed. The influence of the annealing environment on the crystallization onset and evolution of both anatase and rutile phases, as well as on the thin film morphology and photocatalytic properties will be investigated.

Chapter 4 will be focused on the tailoring of the TiO_2 thin film crystallization temperature, in the anatase crystalline phase, by modulating its thickness from hundreds to few nm. Decreasing the layer thickness, an exponential increase of the crystallization onset temperature will be demonstrated. Moreover, the evolution of the crystallization will be studied in an annealing temperature range up to 1000 °C and correlated to the evolution of the phonon lifetime, studied by Raman spectroscopy.

The role of interfacing TiO_2 nanolayers with other nanolayered oxides (SiO_2 , Ta_2O_5 , Al_2O_3 , or ZrO_2), in a similar Bragg-like reflector geometry at the nm scale, on the overall structural and morphological properties of the specimen will be discussed in Chapter 5. The presence of segmentation, as well as of the interfaces with other oxides, will be shown to significantly affect the crystallization onset temperature.

Then, the effect on structural and morphological properties of combining TiO_2 , at different concentrations, with Ta_2O_5 in a co-sputtered mixture will be presented in Chapter 6. The influence of different substrates will be also showed.

Finally, results and conclusions are summarized.

In addition, Appendices are included to i) give an overview on the phonon confinement phenomenon, ii) illustrate theoretical nanolayers modeling and recent technical advances of the apparatus used for the sample fabrication within the Unisa/Unisannio collaboration, iii) describe the results and the knowledge acquired during my periods at the Lancaster University (UK) and at the Gestione Silo company (Florence, Italy).

Chapter 1

Introduction

1.1 Structural properties of TiO_2

Titanium dioxide (TiO_2) can be found in three different crystalline forms [1]:

- 1) Anatase, with a tetragonal crystal cell;
- 2) Brookite, with an orthorhombic crystal cell.
- 3) Rutile, with a tetragonal crystal cell;

The anatase and brookite are considered metastable phases that may convert into the rutile as a consequence of thermal processes [2-4]. The primitive unit cell of the TiO_2 crystal structures is shown in Figure 1, with titanium and oxygen atoms in gray and red, respectively. In particular, in the anatase and rutile phases, two types of Ti–O pairs are observed. In the first, the Ti–O bond lengths are 0.194 and 0.197 nm with O–Ti–O bond angles of 77.7° and 92.6° . In the second, the Ti–O bond lengths are 0.195 and 0.198 nm with O–Ti–O bond angles of 81.2° and 90° . Conversely, brookite phase has a single Ti–O bond length varying between 0.187–0.204 nm and an O–Ti–O bond angle varying from 77° to 105° [5,6]. The other physical properties (space group, lattice parameters, density, and band gap) of the anatase, rutile, and brookite are summarized in Table 1.

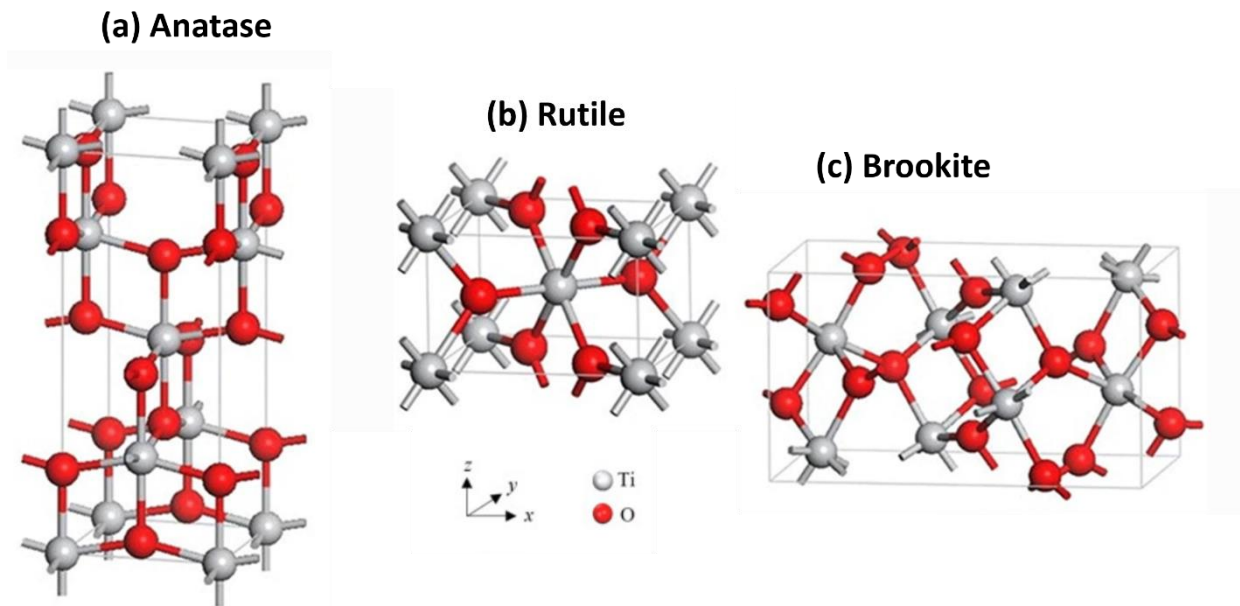


Figure 1: Crystal structures of TiO_2 (a) anatase, (b) rutile, and (c) brookite. Adapted from [7].

TiO ₂	Unit cell	Space group	Lattice parameters	Density	Band gap
Anatase	Tetragonal	I4 ₁ /amd	a = b = 0.3785 nm c = 0.9514 nm	3.9 g/cm ³	3.2 eV
Rutile	Tetragonal	P4 ₂ /mnm	a = b = 0.4594 nm c = 0.2958 nm	4.23 g/cm ³	3.0 eV
Brookite	Orthorhombic	Pbca	a = 0.9184 nm b = 0.5447 nm c = 0.5145 nm	4.13 g/cm ³	3.3 eV

Table 1: Physical properties of the TiO₂ anatase, rutile, and brookite crystalline phase. Adapted from [6,8].

In nature, the anatase occurs in the shape of bipyramidal, pseudo-octahedral crystals and, in the “octahedrite” forms, shows color varying from metallic black to sapphire blue to honey yellow [Figure 2(a)]. Instead, rutile is black, reddish-brown in the largest crystals or it shows various shades of yellow in the finest crystals as a consequence of inclusions. It often appears as an elongated prismatic (often in twins) with very streaked faces [Figure 2(b)]. Finally, the brookite is well-known as a red crystal [Figure 2(c)] or, like rutile, it can occur in brown, reddish-brown, sometimes yellowish, or even black [9].

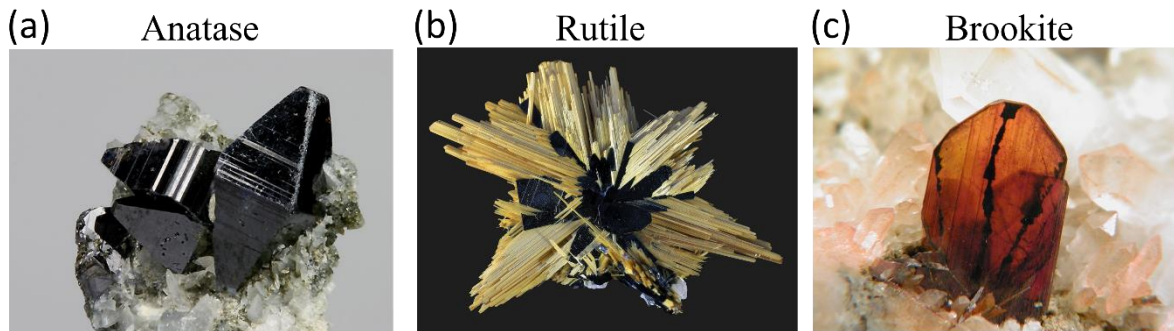


Figure 2: (a) Anatase, (b) rutile, and (c) brookite minerals. Adapted from [9].

In this work, the exact knowledge of the TiO₂ crystalline phases is very useful to study the material structural transition (from amorphous to crystalline and from a crystal phase to another), as well as to take into account the role of the surface free energy (crystal-phase dependent) in the crystallization phenomena observed in nanostructured specimens that will be encountered in Chapter 5.

The surface free energy γ , in particular, is a measure of the excess energy present at the surface of a material, due to the presence of unsaturated bonds from the surface atoms.

This quantity is defined as half of the bond energy ε multiplied by the number of atoms per unit area, n_a , and the number of bonds broken per atom, n_b :

$$\gamma = \frac{1}{2} n_a n_b \varepsilon. \quad (1)$$

The bond energy ε can be evaluated from the sublimation energy of a solid at 0 K, assuming that the cohesive energy of the solid coincide with its sublimation energy at 0 K and that only the nearest neighbor bonds give a contribution to the cohesive energy, see Ref. [10] for more details.

In all applications of TiO_2 , the surface energy, and consequentially the surface reactivity, and the physicochemical properties depend strongly on the exposed crystallographic facet. In particular, surface energies are essential for understanding the phase stability of different TiO_2 polymorphs. The anatase phase is less stable than rutile, but more efficient for several applications (catalysis, photocatalysis). In particular, the (101) surface is the thermodynamically most stable one with a small surface energy of 0.44 J/m^2 , while the (100), (001), and (110) surfaces are the more reactive surfaces with a surface energy of 0.53, 0.9, and 1.09 J/m^2 , respectively. These values differ because of the different density of under coordinated Ti surface atoms on the different surfaces. Then, from the values of the surface energy, the sequence of surface stability is, in turn, $(101) < (100) < (001) < (110)$. From the knowledge of the surface energy, it is possible to determine the equilibrium shape of macroscopic crystals by using the Wulff construction, which minimizes the surface energy of a crystal at fixed volume [11]. Figure 3(a) shows the Wulff shape for the anatase, consisting of truncated tetragonal bipyramid exposing majority (101) and minority (001) facets, so that most stable (101) facets constitute more than 94% of the exposed surface [12,13].

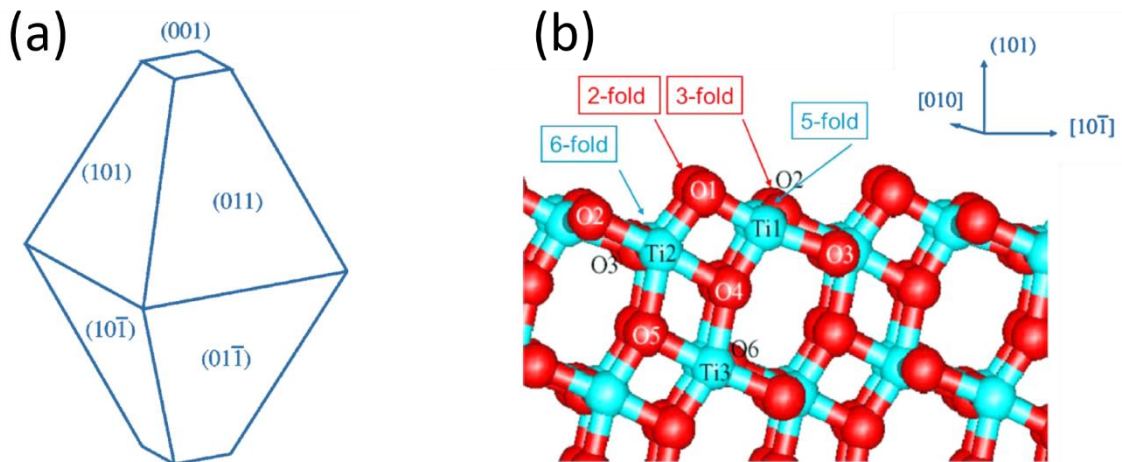


Figure 3: (a) The equilibrium shape of a TiO_2 crystal in the anatase phase. (b) Side view of the anatase (101) surface. Adapter from [13].

The structure of the relaxed stoichiometric (101) surface is shown in Figure 3(b). This surface is characterized by a sawtooth profile perpendicular to the [010] direction, and it exposes both 5-fold- and 6-fold-coordinated Ti atoms and 2-fold and 3-fold oxygens. The atoms on the surface undergo substantial displacements from the ideal bulk-like [13]. This occurs in particular for the 3-fold O and the 5-fold Ti atoms that relax outward and inward. This process induce a small ripple on the sawtooth profile [12]. The bond distances from the relaxed surface and their deviations from the ideal value are reported in Ref. [12].

The surface energy, as well as equilibrium crystal shape, is calculated assuming perfectly clean and defect-free surface, but different kinds of defects can affect the crystalline structure. The most common defects on the TiO₂ surface are oxygen vacancies, Ti interstitial, and steps. For the oxygen vacancies, the formation energy is larger on anatase surface than on rutile one, while this energy decreases as Ti interstitial leaves the surface towards the bulk [12]. Finally, steps on the surface produced by cutting a crystal, strongly influence the reactivity of metal oxide. Indeed, in Ref. [14] steps on the anatase (101) surface are studied, showing that the step reactivity is lower than that of the flat terrace.

The surface energy values given so far are meant for ideally flat surfaces. However, the curvature of the surface affects the surface energy, thus producing effects on various phenomena, such as the melting point, the coarsening of particles (i.e, the Ostwald ripening), and the sintering process. For more details, see Ref. [10].

1.2 Applications of TiO₂

The exciting and rich set of material properties has made TiO₂ a valuable candidate for applications in many fields. The main property is the efficient photoactivity, discovered by Fujishima and Honda in 1972 [15] that plays a highly important role to solve environment problems of pollution and also to provide a renewable and sustainable energy source. The photocatalytic coatings cover a range of products, from the application for urban areas (coating for both indoor and outdoor), to ceramic tiles, and paints and pigments. Recently, TiO₂ nanostructured systems (nanotubes, nanoparticles, nanoporous spheres), characterized by high surface/volume ratio, have been implemented to enhance photocatalytic reactions [16-19].

The photocatalysis process is a chemical reaction that mimics the chlorophyll photosynthesis of trees in absorbing and transforming pollutants into harmless elements. The best catalysts used in photocatalysis to oxidize harmful substances are semiconductors. Among them, TiO₂ is one of the most widely used photocatalyst materials because possesses almost all properties of the ideal photocatalyst. In fact, it is cheap, easily activated by sunlight, stable, chemically inert, available in large quantities, but do not absorb visible light.

In particular, TiO₂ is a n-type semiconductor (electrons as majority charge carriers) with a bandgap (E_g) between 3.3 and 3 eV (corresponding to $\lambda = 375$ and 413 nm). Thanks to

its semiconducting electronic structure, TiO₂ has been widely used as a photocatalyst in the ultraviolet (UV) region ($\lambda < 390$ nm).

The photocatalysis process of TiO₂ is described by the following reaction:

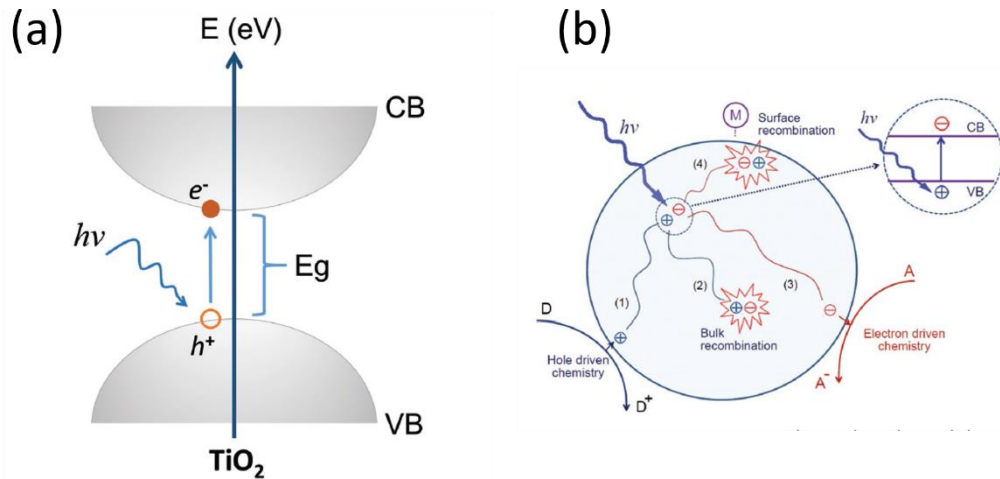
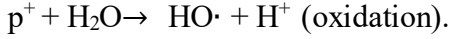
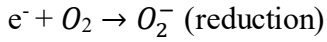
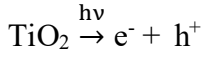


Figure 4: (a) Scheme of a typical excitation of electrons from the filled valence bands to the unoccupied conduction bands. (b) Processes in TiO₂ photocatalysis. Adapted from [20,21].

Figure 4 shows the basic mechanism of photocatalysis. The electronic band structure of semiconductor is given by a valence (VB) and a conduction (CB) bands, completely filled and empty at ground state, respectively. When irradiated with photons ($h\nu$) with an energy higher or equal to E_g , the photons are absorbed, and electrons (e^-) in the occupied VB are excited to the empty CB, creating holes (h^+) in the VB [see Figure 4(a)]. After electron-hole pair separation, only the holes and the electrons that travel towards the surface give rise to two chemical processes: the oxidation and the reduction [process 3 and process 1 in Figure 4(b), respectively]. All the other charge carriers convert their energy into phonons or photons [see processes 2 and 4 in Figure 4(b)] [20].

Ideally, if the semiconductor, such as the TiO₂ film, is infinitely large without defects and impurities, the CB and VB are expected to be flat (spatially at the same level), but, in the real situation, these bands are bent especially near the surfaces or the interfaces. This phenomenon, called *band bending* [21,22], has been observed for the first time by Schottky and Mott in the metal/semiconductor junctions and play a critical role in heterogeneous photocatalysis and the photochemical processes at the surface.

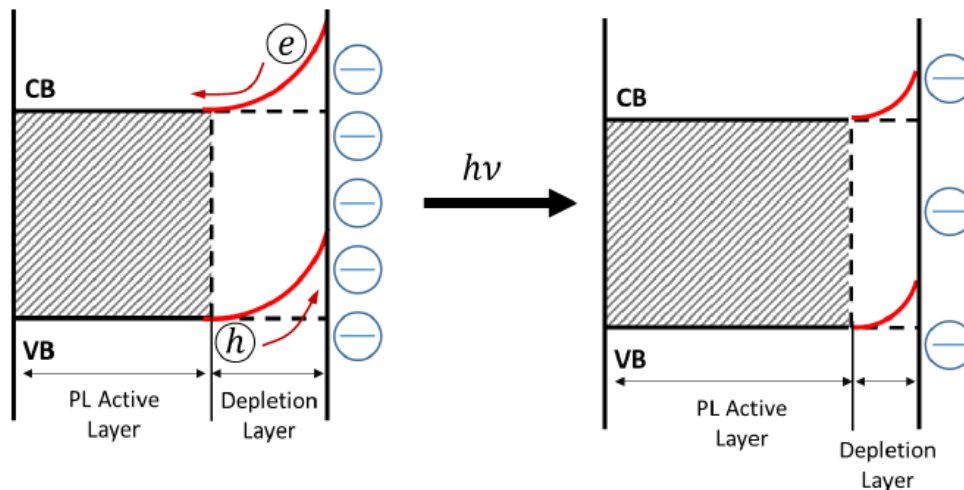


Figure 5: Mechanism of UV induced band flattening. Photoluminescence (PL) active layer represents the region in which the radiative charge recombination occurs. Adapted from [21,22].

The as-grown TiO_2 sample generally shows an upward band-bending. Indeed, given its intrinsic n-type nature (due to the presence of oxygen vacancies and interstitial Ti), the free electrons in excess have the tendency to move toward the surface where they contribute in stabilizing the absorption of molecules from the external environments. Indeed, in general, if the acceptor (donor) molecules adsorb on the surface, the electron will transfer from the semiconductor (molecule) to the molecule (semiconductor) forming a layer on the semiconductor surface, i.e., the Helmholtz layer, and producing the upward (downward) band bending. However, when TiO_2 is UV-irradiated, electrons and holes are excited in the depletion layer, and drifted apart by the potential energy difference associated with the band bending. This process moves electrons into the bulk, while driving holes on the TiO_2 surface. The latter can balance the negative charges present on the surface, producing a lowering of the upward band bending and therefore diminishing the depletion layer. This process is shown in Figure 5, and the effect of UV irradiation on TiO_2 band bending is discussed in Chapter 3.

However TiO_2 finds application in many other fields, such as:

1. water purification processes and self-cleaning,
2. sensors,
3. photovoltaics cells,
4. supercapacitors,
5. electronics,
6. optical coatings (among the others, is also studied as reflective coatings for gravitational wave interferometers).

A review on TiO_2 -based applications was recently given in Ref. [23]. In the following, the excellent TiO_2 electronic, photoelectronic and optical properties will be discussed.

1.2.1 Electronics

TiO₂ has attracted attention in the electronics industry becoming a very promising material for 1) spintronic applications, 2) resistive random-access memories (RRAMs), 3) metal-insulator-metal (MIM) capacitors, and 4) devices based on phase change materials (PCMs). 1) TiO₂ is a material intensely studied for spintronics applications as it exhibits ferromagnetism at room temperature and high Curie temperature [24,25]. 2) The RRAMs represent the new generation of nonvolatile memory (characterized by high endurance, long data retention, high density of data storage, fast switching speed, and low operation voltage) based on resistive switch in metal oxides. Among them, TiO₂ is extensively used as active layer for this kind of memory device [26,27]. 3) The MIM capacitors arise as passive components for microprocessors, high-frequency and integrated circuits. These capacitors are characterized by large capacitance density at radio frequencies with low leakage current. In order to achieve this purpose, many high dielectric materials, in particular TiO₂, have been investigated. Despite its lower dielectric constant and its lower bandgap compared to other dielectric materials, the optical and electrical properties of TiO₂ has been improved by combining it with another electric material, Al₂O₃, to become a good candidates for the MIM applications [28]. 4) The PCMs are materials that can be switched repeatedly between amorphous and one or more crystalline phases. These phases are characterized by diverse physical properties, e.g., electrical conductivity, optical reflectivity, mass density, or thermal conductivity. These features and the repeatability of the switching process make these materials suitable for storing information [29], and the TiO₂ polymorphs can represent a good choice to this aim [23].

1.2.2 Photovoltaic cells

The photovoltaic cells are electric devices that exploit the physical and chemical phenomenon of photoelectricity converting sunlight into electric energy. The most known photovoltaic cells are p-n junction made of semiconductor materials (crystalline or amorphous silicon), but in the recently years a new potential photovoltaics technology has been studied for the simple preparation method, low toxicity and costs. In 1988, Brian O'Regan and Michael Grätzel developed a dye-sensitized solar cell (DSSC), called Grätzel cells, in which an illuminated organic dye can generate electricity [30,31]. In order to deal with the low efficiency, low scalability, and low stability of these cells, the porosity of the electrode is optimized by using a well know TiO₂ in different structures, i.e., nanoparticles, nanocrystalline film, nanotubes, and others. To date, the challenge is to increase the DSSC efficiency, working across the TiO₂-dye-electrolyte interface, reaching and exceeding the 20-30% efficiency of the Si-based solar cells [32-34].

1.2.3 Optical coatings

Optical properties of TiO₂

Recently, research paid much attention to the optical properties of coatings based on TiO₂. This dielectric oxide, transparent in the visible and near-IR range, is characterized by high refractive index that is one of the main features to be used in interference applications. The refractive index (n) and the extinction coefficient (k) of the coating can be estimated from transmission and reflectance data, and are the real and imaginary part of the complex refractive index, i.e. [35],

$$\eta = n + ik. \quad (2)$$

In theoretical simulation, the refractive index (n) and the extinction coefficient (k) are described by the Cauchy and the exponential model, respectively. For transparent materials, the extinction coefficient, i.e., the absorption, can be neglected over the measured wavelength range and consequently $\eta = n$. Then, due to the material dispersion, the wavelength-dependent refractive index can be described by the Cauchy dispersion relationship [36]:

$$n(\lambda) = A + \frac{B}{\lambda^2} + \frac{C}{\lambda^4}, \quad (3)$$

where A is a dimensionless parameter, B (nm^2) and C (nm^4) influence both the curvature and the amplitude of the refractive index for medium wavelengths in the visible and for small wavelengths in the UV, respectively. For wider wavelength ranges, the Cauchy model can be substituted by the Sellmeier Model that accurately describes the optical constants of the transparent materials across a wider spectral range (valid from UV to near-IR region). The formula for the refractive index is [37]:

$$n^2(\lambda) = A + \frac{B\lambda^2}{(\lambda^2 - C)} + \frac{D\lambda^2}{(\lambda^2 - E)}, \quad (4)$$

where A, B, C, D , and E are dimensionless parameters called Sellmeier coefficients specific of each material. The refractive index of TiO₂ depends on many factors, such as its polymorphs. In fact, several works have investigated its dependence on the amorphous, anatase, and rutile phase, observing that the higher is the film density (as in the rutile), the higher is the n values [38,39], as shown in Figure 6(a). The refractive index also depends on the substrate. In Ref. [40], the authors measured the n of TiO₂ thin films deposited on different kinds of substrate (c-sapphire, r-sapphire, and SiO₂) and they observed that n is lower when TiO₂ is deposited on SiO₂ than on sapphire, due to the crystalline phases formed, whereas the dependence on the thickness is negligible. In Figure 6(b), the refractive index curves of TiO₂ films with different thicknesses deposited on c and r-sapphire, and on SiO₂ substrates are reported. The refractive index is also strongly affected by the heat treatments [41-43]. As shown in Figure 6(c), n increases by increasing the annealing temperature due to the increase in packing density and the structural transitions occurring as a result of these processes. Finally, a dependence on the

deposition technique (DC, RF, Magnetron sputtering, electron-beam evaporation) is studied [44,45]. In particular, the ion-assisted deposition (IAD) allows higher packing density and then higher refractive index, due to the higher kinetic energy the atoms possess in the process when hitting the substrate [46,47], see Figure 6(d).

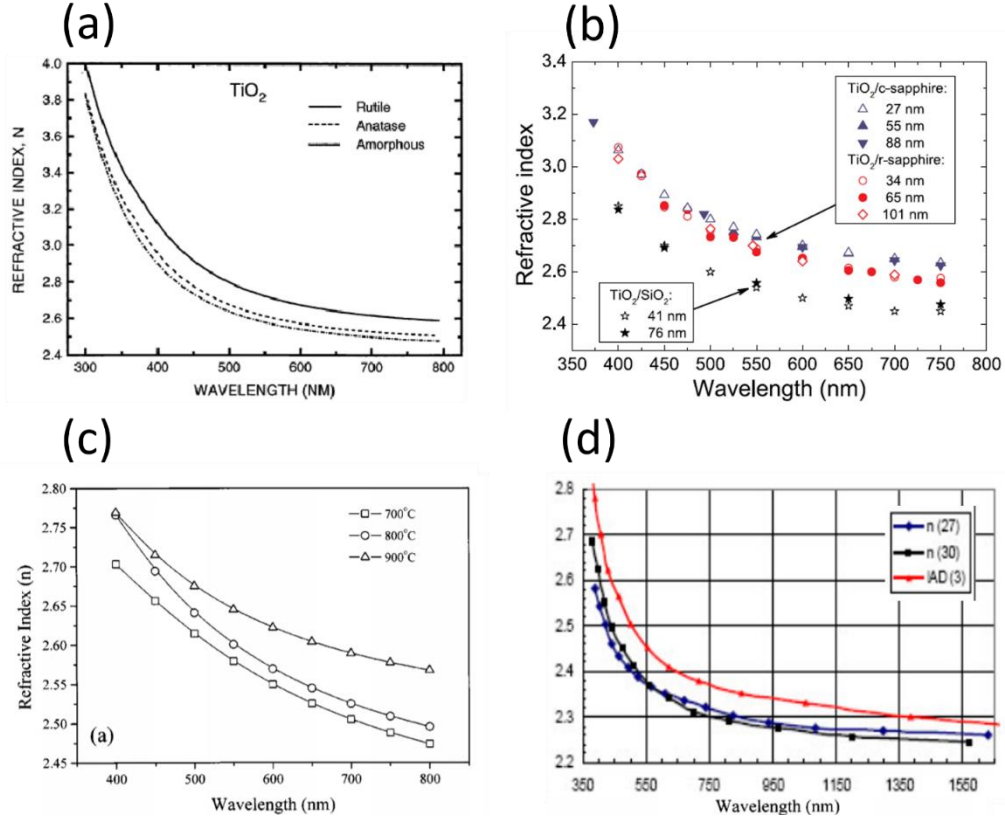


Figure 6: Refractive index of TiO₂ films for different phases (a), substrates (b), and annealing temperatures (c). TiO₂ refractive index after IAD for different annealing temperatures (d). Adapted from [42-47].

Bragg Reflectors

TiO₂ is an excellent material for the realization of dielectric mirrors, also known as Bragg reflectors (BRs), working in the visible range since it has almost no absorption (lossless) and high refractive index.

Indeed, TiO₂ co-sputtered with Ta₂O₅, is used for the high-index layer material in the multilayer mirrors used in the Gravitation-wave Detector (GWD). A BR is a periodic arrangement of alternating high (n_H) and low (n_L) refractive index materials.

In these reflectors, optical thicknesses have to satisfy the following condition [35]:

$$\frac{\lambda_0}{2} = n_H d_H + n_L d_L \quad (5)$$

where d_H, d_L are the geometrical thicknesses of the materials with high and low refractive index, respectively, and λ_0 is the reference wavelength. In the special case of equal high- and low optical thicknesses, Eq.(5) become:

$$\frac{\lambda_0}{4} = n_H d_H = n_L d_L. \quad (6)$$

Unlike the case of metallic mirrors, BRs show small intrinsic absorption and high reflectivity, which are very attractive for the GWD.

A schematic BR is shown in Figure 7(a). An incident light is reflected from every interface of the stack and all reflected components interfere constructively. This multiple-interference effect causes high reflectivity at λ_0 that depends on the refractive index contrast n_H/n_L and the number N of $\lambda_0/4$ pairs [48,49]:

$$R = \left(\frac{1 - \left(\frac{n_S}{n_A}\right) \left(\frac{n_H}{n_L}\right)^{2N}}{1 + \left(\frac{n_S}{n_A}\right) \left(\frac{n_H}{n_L}\right)^{2N}} \right)^2, \quad (7)$$

where n_A and n_S are the refractive indices of the air and the substrate, respectively. Increasing the number of layers and/or the index contrast between them will increase the reflectivity of the BR. In Figure 7(b), an example of the calculated reflectivity spectra of a dielectric mirror with 4 Bragg layer pairs is shown. In this case, the authors set the lower refractive index to $n_L = 1.4$ and the high refractive index to $n_H = 2, 3, 4$.

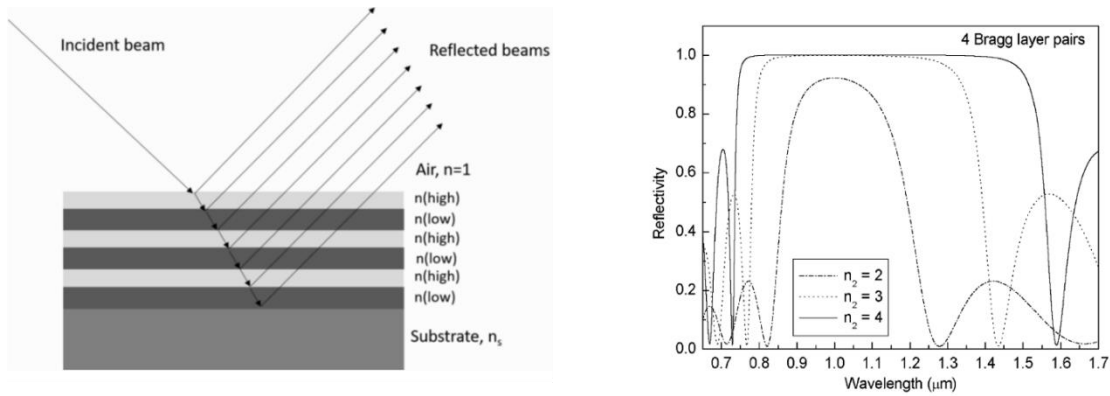


Figure 7: (a) BR and (b) reflectivity of a 4 Bragg layer pairs. Adapted from [48,50].

GWDs and mirror sensitivity

BRs are used in the optical components of the giant Terrestrial Laser Interferometers such as LIGO, Advanced LIGO (aLIGO) [51,52], GEO [53], VIRGO, Advanced Virgo (aVirgo) [54,55], TAMA [56], KAGRA [57], INDIGO [58], and ET [59], to detect the Gravitational Waves (GWs). The GWs, ripples in the space-time predicted by Einstein's General Theory of Relativity, are generated when matter is accelerated in an asymmetrical way (stochastic background, rotating neutron stars, coalescing binary systems, black hole interactions, neutron star coalescences, supernova explosions [60]) producing signals over a wide range of frequencies, from $\sim 10^{-17}$ to $\sim 10^3$ Hz.

Virgo is Michelson interferometer formed by two Fabry-Perot cavities, 3 km long (Nord and West), each composed by two mirrors, called input (IM) and end (EM) mirror, see Figure 8(a-b). Then, a laser source (a CW Nd:YAG laser), with a power of 20 W (200 W in aVirgo) and a wavelength of 1064 nm, is divided in two beams by a beam splitter (BS), characterized by a diameter of 23 cm and a mass of 5 kg and positioned at a 45 degree angle. In order to increase the laser power a posteriori, a power recycling mirror is placed between the laser source and beam splitter. The two beams are propagated in the two cavities and reflected (multiple reflections) by the large mirrors at the end of these arms. In order to achieve high reflectivity, the mirrors are made of SiO_2 , as low index material, and Ta_2O_5 (TiO_2 doped Ta_2O_5 in aVirgo), as the high index material [61], deposited on high quality fused silica substrate, with a diameter of 35 cm and a mass of 21 Kg (42 Kg in aVirgo), see Figure 8(c). Moreover, they are suspended by a complex system of four thin silica fibers attached to a series of attenuators, called Superattenuators. The aim of these high-performance passive isolation systems is to reduce the seismic noise, but also to correctly align different parts of the instrument and to orient the mirrors, exploiting the attenuation properties of simple pendulum. Then, reflected beams are recombined on the beam splitter back-face generating interferences measured by using a photodetector that converts the laser power in an electric signal. The GW causes a variation of the arm lengths, called "Differential Arm" motion, that stretches in one direction and simultaneously compresses in the perpendicular one. In fact, as the lengths of the arms change, the distance traveled by each laser beam modifies, then light beams no longer cause total destructive interference, but a phase shift that is revealed like a flicker on the photodetector. The strain deformation arms measured is $d \sim \Delta L/L$, where L is the effective optical path of the light in each arm, and ΔL is the change in the arm length caused by the GW, that is very small (10^{-19} m). Then, the role of the Fabry-Perot cavities is to increase the optical path length and thus the strain sensitivity. Finally, the residual air molecules can disturb the path of the laser beams, as well as its intensity and phase. In order to limit this disturbance, the whole interferometer is kept under vacuum at $\sim 10^{-7}$ mbar (10^{-9} mbar in aVirgo) [62,63].

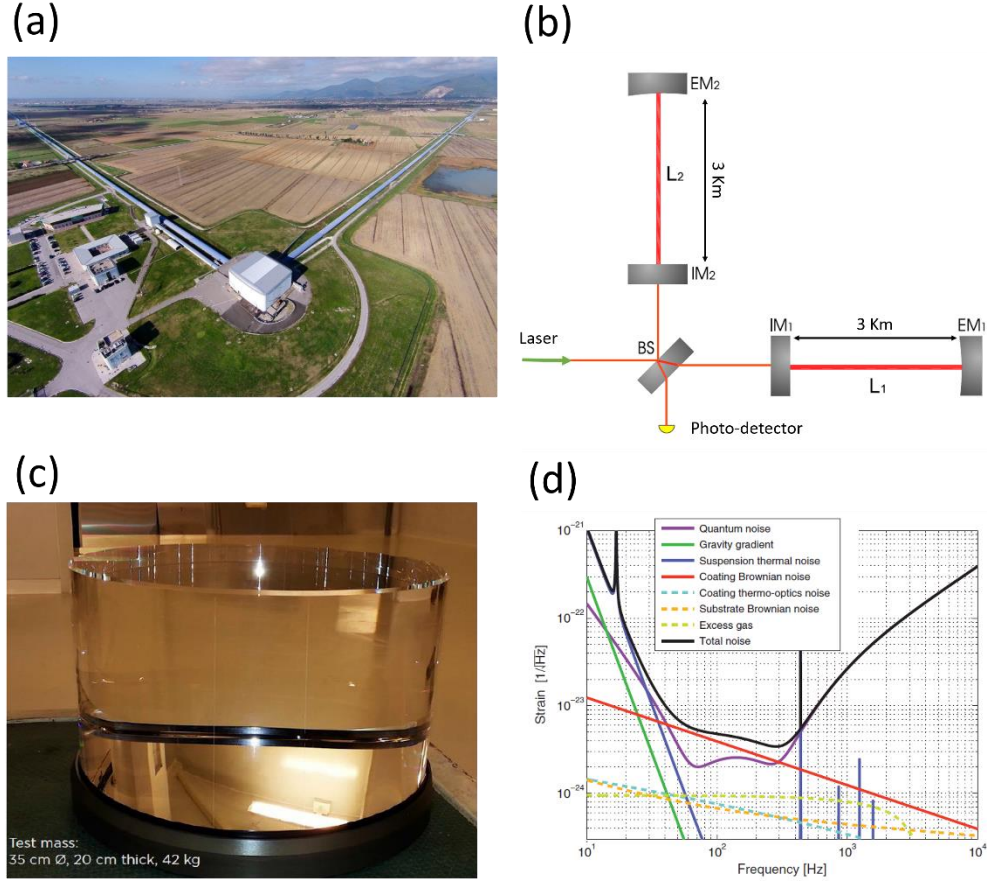


Figure 8: (a) Aerial view of Virgo. (b) Optical configuration of Virgo interferometer. (c) aVirgo test mass. (d) aVirgo sensitivity curve. Adapted from [62-66].

Each interferometer has a sensitivity that varies as a function of frequency. The so-called figure of merit is thus able to provide information about the smallest signal detectable by the instrument. Figure 8(d) shows the expected noise sources, depending on the frequency of interest, of aVirgo once it has reached the design sensitivity [66]. In the low frequency range (10 - 40 Hz) gravity gradient, seismic, and suspensions thermal noises affect the signal. The gravity gradient noise (or Newtonian noise), in the frequency band below 5 Hz, depends on the fluctuation of the local gravitational field due to the seismic waves that alter the mass density distribution. In the frequency band above 10 Hz, the Newtonian noise is covered by seismic noise that is due to the ground vibrations ($1/f^2$) together to the interferometer mirrors. This noise spectrum:

$$S_N(f) = \frac{3 \times 10^{-17}}{f^4}, \quad (8)$$

can be reduced (about 12 orders of magnitude) by using the Superattenuator. The suspensions thermal noise, such as the thermal noise due to the mirrors, cannot reduce because being mechanical oscillators, their position is affected by thermal vibration. For this reason, they represent a fundamental limit to the interferometer sensitivity.

Quantum noise dominates the high frequency range (300 - 10 kHz) of the sensitivity spectrum. This noise source introduces both i) white and ii) $1/f^2$ noise spectrum. i) The white noise depends on the statistical fluctuation of the detected photons number, in particular:

$$S_Q(f) = \frac{1}{L} \sqrt{\frac{\hbar c \lambda}{2\pi P}}, \quad (9)$$

where L and P represent the interferometer arm's length and the input laser power, respectively. ii) The $1/f^2$ noise spectrum depends on the pressure fluctuations on each test mass, M , i.e.:

$$S_M(f) = \frac{1}{2\pi f^2 M L} \sqrt{\frac{8\pi \hbar P}{\lambda c}}. \quad (10)$$

For this reason, in order to reduce the radiation noise, the weight of the test masses is increased from 21 kg (in Virgo) to 42 kg (in aVirgo).

Finally, the thermal noise dominates the mid-frequency range from 40 to 300 Hz. This is due to the Brownian motion, thermo-elastic and thermo-refractive fluctuations of the mirror coating. The power spectral density of the thermal noise, in accordance with the fluctuation–dissipation theorem [67], is:

$$S_T(f) = \frac{2 k_B T (1 - \sigma_s^2)}{\pi^4 f w Y_s} \Phi_c, \quad (11)$$

where k_B is Boltzmann's constant, T is the temperature, σ_s and Y_s are the Poisson ratio and Young's elastic modulus of the substrate, respectively, and w is the half-width of the Gaussian laser beam. Then, Φ_c is the effective coating loss angle, given by [68,69]:

$$\Phi_c = \varphi_L d_L + \varphi_H d_H, \quad (12)$$

where $d_{L,H}$ are the total optical thickness, given by the product of the number of layers and the optical thickness of the individual layers, and $\varphi_{L,H}$ are the specific material loss angles. In particular, $\varphi_{L,H}$ depend on several factors:

$$\varphi_{L,H} = \frac{\lambda_0}{\sqrt{\pi} w} \frac{\Phi_{L,H}}{n_{L,H}} \left(\frac{Y_{L,H}}{Y_s} + \frac{Y_s}{Y_{L,H}} \right), \quad (13)$$

where λ_0 is the operating wavelength, $\Phi_{L,H}$ are the mechanical loss angles of the low and high materials, and $Y_{L,H,S}$ are the Young's modulus of the low, high materials and the substrate, respectively.

The studies performed in this thesis arose from the need of finding a strategy to improve the performance of the coatings, with the aim of producing prototypes of coatings with the highest possible reflectivity and the lowest possible thermal noise. In this sense, a deep a systematic study of the possible materials candidates (dielectric oxides) from the material science point of view, is of fundamental relevance to keep this research on truck. While on one side this thesis is grown in the context of gravitational wave detectors, and, in particular, in the Virgo community, on the other it affords material-related problems

which seem, only apparently, to deviate from the main aim. In practice, the study of the morphology as well as of the structural transition of these materials is at the basis of understanding their performances. Indeed, any peculiar morphological feature can strongly affect the light scattering from the surface and thus the optical performances. Similarly, the light scattering is also affected by the presence of different structural phases, inside the same coating, i.e., crystallites in amorphous matrix, or phase 1-crystallites inside a phase-2 crystal. For this reason, the nowadays used mirrors are produced in their amorphous form. However, it is worth mentioning that, given the well-established need of performing post-deposition thermal treatments to the final mirrors (below the crystallization of their material components), to improve their performances, the study of the behavior of these materials upon annealing, as performed in Chapter 3, is of fundamental relevance.

Besides the investigation of the material, exploring new material combination designs is pivotal for future GWD applications. Some of them are discussed in the following:

I. Nano-layer coating

The aim of the nano-layers strategy already introduced by Ref. [69-71] is to replace the layer with the highest optical losses (TiO_2 -doped Ta_2O_5) with a nanostructured metamaterials, made of alternating nm-thick layers of, again, low and high refractive indexes. While this strategy can barely affect the reflectivity of the final multilayer (as its refractive index is overall slightly lower than that of the high-refractive counterpart), it's extremely useful in increasing the crystallization temperature of the coating, thus allowing for higher temperature annealing with possibly beneficial consequences on the optics and mechanics properties. In this sense, it is very relevant to first study the physics occurring in the single material (TiO_2 in this thesis) as a function of thickness down to the nm regime (Chapter 4), and consequently the coupling with other oxides in a nanolayered structure. Chapter 5 thus focuses on the combination of TiO_2 with SiO_2 , Ta_2O_5 , ZrO_2 , and Al_2O_3 . A smaller amount of this work is dedicated to the study of a possible candidate for the low refractive index material, by following the same strategy and combining SiO_2 with Al_2O_3 , in a nanolayered form.

II. Co-sputtered material

The purpose of making a co-sputtered mixture relies on the discovery that TiO_2 doping can increase the Ta_2O_5 refractive index, and, in the right contact, reduce its losses, and, consequently, the mirror thermal noise [72-75]. In this framework, Chapter 6 will focus on the investigation of several mixtures of TiO_2 and Ta_2O_5 , obtained by varying the TiO_2 content inside the Ta_2O_5 matrix. Importantly, these materials, are fabricated at the Laboratoire des matériaux avancés (LMA) in Lyon, which is the actual developer and provider of the mirrors for Virgo and LIGO GWDs.

III. Multi-Material

Preliminary theoretical results on ternary coatings are shown in Appendix C. The aim of this work is to reduce the thermal noise by using ternary coatings consisting of quarter-wavelength-thick layers, where a third layer is added to the two presently in

use, SiO₂ and Ta₂O₅-TiO₂ [76]. The realistic candidates for the third material are amorphous Silicon (aSi), Silicon Nitrides (SiN_x), and Al₂O₃.

1.3 Other oxide materials

1.3.1 Tantalum Oxide

Tantalum pentoxide, also known as Tantalum oxide or Tantalum (Ta₂O₅), is a metal oxide semiconductor like TiO₂ that is often used as photocatalysis thanks to its wide optical band gap of 4.0 eV [77]. Its properties, such as high transparency in the visible and UV range, good chemical and thermal stability, high dielectric constant, and high refractive index ($n=2.16$ at $\lambda=500$ nm), make this material a good candidate for different applications (proton conductor, high-k gate insulator [78,79]). In the optical field, its amorphous form is widely used in applications where minimal optical and mechanical scattering losses are required (i.e., GWD mirrors). On the other hand, the crystalline phases of Ta₂O₅ have great importance for the microelectronic industry [80]. Ta₂O₅, with a melting temperature of 1872 °C, is characterized by a local structural arrangement of TaO₆ octahedron and TaO₇ pentagonal bipyramid, and TaO₈ hexagonal bipyramid. The crystalline phases can be classified in low temperature (LT) and high temperature (HT) forms, where amorphous-LT and LT-HT phase transitions occur at 650, and 1360 °C, respectively. The most observed LT crystal phases are hexagonal (δ) and orthorhombic (β). The δ -Ta₂O₅ structure is characterized by the lattice parameters $a=b=3.6240$ Å, and $c=3.888$ Å, instead the β -Ta₂O₅ structure has the following lattice parameters: $a=6.198$ Å, $b=40.290$ Å, and $c=3.888$ Å [81,82]. Moreover, despite several deposition techniques have been used to fabricate Ta₂O₅ thin film (electron beam evaporation, sol gel method, pulsed laser deposition), ion beam sputtering is best suited to obtain coatings with low scattering, good stoichiometry, and high packing density [83,84].

1.3.2 Zirconium Oxide

Zirconium dioxide or Zirconia (ZrO₂) is a ceramic material characterized by high melting temperature (2950 K), high dielectric constant, high refractive index ($n=2.16$ at $\lambda=587$ nm), low thermal conductivity, hardness, and high band gap (~ 5 eV). Its physical properties are influenced by its crystal structures. In fact, ZrO₂ exhibits three equilibrium crystal structures: i) monoclinic (lattice parameters $a=5.146$ Å, $b=5.213$ Å, $c=5.311$ Å and $\beta=99.2^\circ$) below 1420 K, ii) tetragonal ($a=b=3.64$ Å and $c=5.27$ Å) from 1440 to 2640 K, and iii) cubic ($a=c=b=5.27$ Å) from 2640 to 2950 K [85]. As for other oxide materials discussed previously, ZrO₂ can be used as photocatalyst [86], for ceramic engineering [87], and for chemical, optical, and mechanical applications [88]. Moreover, thanks also to the low optical loss and scatter in IR region and an excellent radiation tolerance, ZrO₂ is very useful for high-reflectivity mirrors and for nuclear applications, respectively [89,90]. Also

for ZrO_2 material, a large number of fabrication techniques including sol-gel method, chemical vapor deposition (CVD), and RF magnetron sputtering are used, but again a plasma assisted deposition [91] is chosen to produce high-quality films.

1.3.3 Silicon Oxide

Silicon oxide, or silica (SiO_2), is one of the most plentiful chemical elements on Earth and major component of sand. The amorphous SiO_2 has a high melting temperature (1750 °C) and exhibits unique physical-chemical properties, i.e., high resistance to deformation on heating, resistance to thermal shock, chemical durability, spectral transmittance from the near ultraviolet to the near infrared spectrum regions, and high resistance to radioactive radiation [92]. Besides these extraordinary properties, crystalline SiO_2 shows high chemical and thermal stability exhibiting pronounced piezoelectricity, quite important for the micro-electronics industry [93]. In light of this, SiO_2 shows many crystalline phases: low-temperature β -quartz (trigonal), high-temperature α -quartz (hexagonal), low-temperature β -cristobalite (tetragonal), high-temperature α -cristobalite (cubic), medium-temperature β -tridymite (hexagonal), and high-temperature α -tridymite (hexagonal). For its different properties, the SiO_2 has attracted much attention in various application fields, such as lighting, semiconductor, electronic and communication technology, glass and chemical industry, metallurgy, and also for space applications. Finally, in the optical application field, e.g., for GWDs, SiO_2 has been chosen as low-index material in the BRs fabricated by IBS, thanks to its low optical absorption at the typical operation wavelength of the detectors [94].

1.3.4 Aluminum Oxide

Aluminum oxide, or Alumina (Al_2O_3), is an insulating ceramic material characterized by a melting temperature of 2072 °C that can exhibit the amorphous ($a-Al_2O_3$) and several crystal forms (α , γ , δ , θ , κ , ϵ , η , and χ). The crystalline phases are harder (21 GPa) than amorphous one and then preferred for the hard coating applications. The $\alpha-Al_2O_3$, also known as sapphire, is the only stable phase (corundum form) characterized by a hexagonal structure ($a=4.758 \text{ \AA}$, $c=12.91 \text{ \AA}$). The other metastable phases are studied as alumina transitions that occurs at different temperatures [95]: the phase γ and η have cubic structures, δ can be tetragonal or orthorhombic, θ is monoclinic, χ is hexagonal and κ is orthorhombic [96]. Al_2O_3 exhibits high optical transparency, chemical and mechanical stability, corrosion resistance, and high hardness, very useful in a large range of applications, such as corrosion protective coating, sensors, catalysis and thanks to the high bandgap and dielectric constant can replace SiO_2 in dielectric applications [97]. Finally, Chemical (CVD) and physical (PVD) vapor deposition are used to deposit both crystalline and amorphous Al_2O_3 thin films, but the PVD allows to fabricate at lower temperatures (<1000 °C) obtaining hard and dense films [98].

In Table 2, the refractive index at the operation wavelength (@1064) and the thermo-mechanical and optical parameters of these materials are reported.

	Refractive index @1064	Young's Modulus (GPa)	Poisson ratio	Loss angle	Thermal conductivity (W m ⁻¹ K ⁻¹)
SiO ₂	1.4496	60	0.17	5x10 ⁻⁵	0.2-0.5
Al ₂ O ₃	1.7545	210	0.22	2.4 x10 ⁻⁴	0.7-1.1
Ta ₂ O ₅	2.0760	140	0.23	4.72 x10 ⁻⁴	0.3-0.6
ZrO ₂	2.1224	200	0.27	2.3 x10 ⁻⁴	1.09
TiO ₂	2.4789	290	0.28	1.4 x10 ⁻⁴	0.45

Table 2: Thermo-mechanical and optical parameters. Adapted from [99,100].

The research presented in this thesis, being an experimental work that deals with extremely complicated systems, fabrication techniques, and measurements, has been strongly affected by the COVID-19 pandemic since it has slowed down the experimental activities.

References

1. Diebold, U. The surface science of titanium dioxide. *Surface science reports* **2003**, 48(5-8), 53-229.
2. Mikhelashvili, V., Eisenstein, G. Effects of annealing conditions on optical and electrical characteristics of titanium dioxide films deposited by electron beam evaporation. *Journal of Applied Physics* **2001**, 89(6), 3256-3269.
3. Zhang, J., *et al.* UV Raman spectroscopic study on TiO₂. I. Phase transformation at the surface and in the bulk. *The Journal of Physical Chemistry B* **2006**, 110(2), 927-935.
4. Zhang, J., *et al.* UV Raman spectroscopic study on TiO₂. II. Effect of nanoparticle size on the outer/inner phase transformations. *The Journal of Physical Chemistry C* **2009**, 113(5), 1698-1704.
5. Radovic, M. *Low dimensional Ti-Oxide based structures: surface, interfaces, and ultrathin films of SrTiO₃ and TiO₂*. PhD Thesis, University of Naples, **2008**.
6. Prasai, B., *et al.* Properties of amorphous and crystalline titanium dioxide from first principles. *Journal of materials science* **2012**, 47(21), 7515-7521.
7. Samat, M. H., *et al.* Hubbard U calculations on optical properties of 3d transition metal oxide TiO₂. *Results in physics* **2016**, 6, 891-896.
8. Wei, C. H., Chang, C. M. Polycrystalline TiO₂ Thin Films with Different Thicknesses Deposited on Unheated Substrates Using RF Magnetron Sputtering. *Materials Transactions* **2011**, 3(52), 554-559.

9. MinDat. Available online: <https://www.mindat.org/> (accessed on 18 May 2021).
10. Agrawal, D. C. *Introduction to nanoscience and nanomaterials*. World Scientific Publishing Company, Kanpur, India **2013**.
11. Wulff, G. On the question of speed of growth and dissolution of crystal surfaces. *Z. Kristallogr* **1901**, *34(5/6)*, 449.
12. De Angelis, F., *et al.* Theoretical studies on anatase and less common TiO₂ phases: bulk, surfaces, and nanomaterials. *Chemical reviews* **2014**, *114(19)*, 9708-9753.
13. Lazzeri, M., *et al.* Structure and energetics of stoichiometric TiO₂ anatase surfaces. *Physical Review B* **2001**, *63(15)*, 155409.
14. Gong, X. Q., *et al.* Steps on anatase TiO₂ (101). *Nature materials* **2006**, *5(8)*, 665-670.
15. Fujishima, A., Honda, K. Electrochemical photolysis of water at a semiconductor electrode. *Nature* **1972**, *238(5358)*, 37-38.
16. Liang, H. C., *et al.* Photocatalytical properties of TiO₂ nanotubes. *In Solid State Phenomena Trans Tech Publications Ltd* **2010**, *162*, 295-328).
17. Choi, S. K., *et al.* Photocatalytic comparison of TiO₂ nanoparticles and electrospun TiO₂ nanofibers: effects of mesoporosity and interparticle charge transfer. *The Journal of Physical Chemistry C* **2010**, *114(39)*, 16475-16480.
18. Zimbone, M., *et al.* Synthesis and Photochemical Properties of Monolithic TiO₂ Nanowires Diode. *Molecules* **2021**, *26(12)*, 3636.
19. Guo, Q., *et al.* Fundamentals of TiO₂ photocatalysis: concepts, mechanisms, and challenges. *Advanced Materials* **2019**, *31(50)*, 1901997.
20. Linsebigler, A. L., *et al.* Photocatalysis on TiO₂ Surfaces: Principles, Mechanisms, and Selected Results. *Chemical reviews* **1995**, *95*, 735.
21. Zhang, Z., Yates Jr, J. T. Band bending in semiconductors: chemical and physical consequences at surfaces and interfaces. *Chemical reviews* **2012**, *112(10)*, 5520-5551.
22. Ma, Shiliang, *Physically and Chemically Induced Band Bending Changes at the Surfaces of TiO₂ Nanoparticles Studied by Photoluminescence Spectroscopy*, PhD thesis, Zhejiang University (**2013**) and University of Virginia (**2018**).
23. Korotcenkov, G. Titanium Dioxide (TiO₂) and Its Applications. Elsevier. **2020**.
24. Zhao, T., *et al.* Electric field effect in diluted magnetic insulator anatase Co: TiO₂. *Physical review letters* **2005**, *94(12)*, 126601.
25. Ravi, S., Shashikanth, F. W. Magnetic properties of Mo-doped TiO₂ nanoparticles: A candidate for dilute magnetic semiconductors. *Materials Letters* **2020**, *264*, 127331.
26. Shin, J., *et al.* TiO₂-based metal-insulator-metal selection device for bipolar resistive random access memory cross-point application. *Journal of Applied Physics* **2011**, *109(3)*, 033712.
27. Carta, D., *et al.* T. Investigation of the switching mechanism in TiO₂-based RRAM: a two-dimensional EDX approach. *ACS applied materials & interfaces* **2016**, *8(30)*, 19605-19611.
28. Woo, J. C., *et al.* Low leakage current in metal-insulator-metal capacitors of structural Al₂O₃/TiO₂/ Al₂O₃ dielectrics. *Applied Physics Letters* **2012**, *100(8)*, 081101.
29. Raoux, S. Phase change materials. *Annual Review of Materials Research* **2009**, *39*, 25-48.

30. O'regan, B., Grätzel, M. A low-cost, high-efficiency solar cell based on dye-sensitized colloidal TiO₂ films. *Nature* **1991**, 353(6346), 737-740.
31. Grätzel, M. Photoelectrochemical cells. *Materials For Sustainable Energy: A Collection of Peer-Reviewed Research and Review Articles from Nature Publishing Group*. **2011**. 26-32.
32. Hou, X., *et al.* TiO₂ nanotubes for dye-sensitized solar cells—A review. *Energy Science & Engineering* **2020**.
33. Sharma, K., *et al.* Dye-sensitized solar cells: fundamentals and current status. *Nanoscale research letters* **2018**, 13(1), 1-46.
34. Tsvetkov, N., *et al.* Sol-gel processed TiO₂ nanotube photoelectrodes for dye-sensitized solar cells with enhanced photovoltaic performance. *Nanomaterials* **2020**, 10(2), 296.
35. Stenzel, O. *Optical Coatings: material aspects in theory and practice*, Springer-Verlag Berlin Heidelberg, Germany **2014**.
36. Cushman, C., *et al.* An Introduction to Modeling in Spectroscopic Ellipsometry, Focusing on Models for Transparent Materials: The Cauchy and Sellmeier Models. *Vacuum Technology & Coating* **2016**.
37. Ghosh, G. *Handbook of optical constants of solids: Handbook of thermo-optic coefficients of optical materials with applications*. Academic Press **1998**.
38. Bendavid, A., Martin, P. J. Review of thin film materials deposition by the filtered cathodic vacuum arc process at CSIRO. *J. Aust. Ceram. Soc*, **2014**, 50(1), 86-101.
39. Bendavid, A., *et al.* Deposition and modification of titanium dioxide thin films by filtered arc deposition. *Thin solid films* **2000**, 360(1-2), 241-249.
40. Möls, K., *et al.* Influence of phase composition on optical properties of TiO₂: Dependence of refractive index and band gap on formation of TiO₂-II phase in thin films. *Optical Materials* **2019**, 96, 109335.
41. Ting, C. C., *et al.* Structural evolution and optical properties of TiO₂ thin films prepared by thermal oxidation of sputtered Ti films. *Journal of Applied Physics* **2000**, 88(8), 4628-4633.
42. Hasan, M. M., *et al.* Effects of annealing treatment on optical properties of anatase TiO₂ thin films 2008. *International Journal of Chemical and Biological Engineering* **2008**, 1(2), 92-96.
43. Taherniya, A., Raoufi, D. The annealing temperature dependence of anatase TiO₂ thin films prepared by the electron-beam evaporation method. *Semiconductor Science and Technology* **2016**, 31(12), 125012.
44. Brus, V. V., *et al.* Comparison of optical properties of TiO₂ thin films prepared by reactive magnetron sputtering and electron-beam evaporation techniques. *Semiconductor Physics Quantum Electronics & Optoelectronics* **2011**.
45. Chen, H. C., *et al.* Annealing dependence of residual stress and optical properties of TiO₂ thin film deposited by different deposition methods. *Applied optics* **2008**, 47(13), C284-C287.
46. Hwangbo, C. K., Cho, H. J. Ion assisted deposition of TiO₂ thin films by Kaufman and gridless ion sources. *The Review of Laser Engineering* **1996**, 24(1), 103-109.

47. Materion, Available online: <https://materion.com/resource-center/product-data-and-related-literature/inorganic-chemicals/oxides/titanium-oxides-for-optical-coating> (accessed on 29 June 2021).
48. Heiss, W., *et al.* Epitaxial Bragg mirrors for the mid-infrared and their applications. *Progress in Quantum Electronics* **2001**, 25(5-6), 193-228.
49. Muallem, M., *et al.* Room temperature fabrication of dielectric bragg reflectors composed of a CaF_2/ZnS multilayered coating. *ACS applied materials & interfaces* **2015**, 7(1), 474-481.
50. Dynasil, Available online: <https://www.dynasil.com/optical-coatings/dielectric-bragg-mirrors/> (accessed on 5 July 2021).
51. Abbott, B. P., *et al.* LIGO: the laser interferometer gravitational-wave observatory. *Reports on Progress in Physics* **2009**, 72(7), 076901.
52. Aasi, J., *et al.* Advanced ligo. *Classical and quantum gravity* **2015**, 32(7), 074001.
53. Grote, H., *et al.* The status of GEO 600. *Classical and Quantum Gravity* **2008**, 25(11), 114043.
54. Accadia, T., *et al.* Status of the Virgo project. *Classical and Quantum Gravity* **2011**, 28(11), 114002.
55. Acernese, *et al.* Advanced Virgo: a second-generation interferometric gravitational wave detector. *Classical and Quantum Gravity* **2014**, 32(2), 024001.
56. Ando, M., *et al.* Current status of the TAMA300 gravitational-wave detector. *Classical and Quantum Gravity* **2005**, 22(18), S881.
57. Somiya, K. Detector configuration of KAGRA—the Japanese cryogenic gravitational-wave detector. *Classical and Quantum Gravity* 2012, 29(12), 124007.
58. Unnikrishnan, C. S. IndIGO and LIGO-India: scope and plans for gravitational wave research and precision metrology in India. *International Journal of Modern Physics D* **2013**, 22(01), 1341010.
59. Punturo, M., *et al.* The Einstein Telescope: a third-generation gravitational wave observatory. *Classical and Quantum Gravity* **2010**, 27(19), 194002.
60. Fidecaro, F., Ciufolini, I. (Eds.). (1997). *Gravitational Waves: Sources And Detectors- Proceedings Of The International Conference (Vol. 2)*. World Scientific.
61. Granata, *et al.* Progress in the measurement and reduction of thermal noise in optical coatings for gravitational-wave detectors. *Applied optics* **2020**, 59(5), A229-A235.
62. Vajente, G. *Analysis of sensitivity and noise sources for the Virgo gravitational wave interferometer*. PhD Thesis, Scuola Normale Superiore di Pisa, **2008**.
63. Barsotti, L. *The control of the Virgo interferometer for gravitational wave detection*. PhD Thesis, Università degli Studi di Pisa, **2006**.
64. virgo-gw.eu, Available online: <http://public.virgo-gw.eu/virgo-in-a-nutshell/> (accessed on 7 July 2021).
65. Acernese, F., *et al.* Status of advanced virgo. In *EPJ Web of Conferences* **2018**, 182, 02003).
66. Li, T., *et al.* Measurements of mechanical thermal noise and energy dissipation in optical dielectric coatings. *Physical Review D* **2014**, 89(9), 092004.
67. Callen, H. B., Greene, R. F. On a theorem of irreversible thermodynamics. *Physical Review* **1952**, 86(5), 702.

68. Harry, G. M., *et al.* Thermal noise from optical coatings in gravitational wave detectors. *Applied optics* **2006**, *45(7)*, 1569-1574.
69. Principe, M. Reflective coating optimization for interferometric detectors of gravitational waves. *Optics express* **2015**, *23(9)*, 10938-10956.
70. Magnozzi, M., *et al.* Optical properties of amorphous SiO₂-TiO₂ multi-nanolayered coatings for 1064-nm mirror technology. *Optical Materials* **2018**, *75*, 94-101. Pan, H. W., *et al.* Thickness-dependent crystallization on thermal anneal for titania/silica nm-layer composites deposited by ion beam sputter method. *Optics Express* **2014**, *22(24)*, 29847-29854
71. Pan, H. W., *et al.* Thickness-dependent crystallization on thermal anneal for titania/silica nm-layer composites deposited by ion beam sputter method. *Optics Express* **2014**, *22(24)*, 29847-29854.
72. Amato, A., *et al.* Effect of heating treatment and mixture on optical properties of coating materials used in gravitational-wave detectors. *Journal of Vacuum Science & Technology B, Nanotechnology and Microelectronics: Materials, Processing, Measurement, and Phenomena* **2019**, *37(6)*, 062913.
73. Granata, M., *et al.* Mechanical loss in state-of-the-art amorphous optical coatings. *Physical Review D* **2016**, *93(1)*, 012007.
74. Harry, G. M., *et al.* (2006). Titania-doped tantala/silica coatings for gravitational-wave detection. *Classical and Quantum Gravity* **2006**, *24(2)*, 405.
75. Guo, G., Huang, J. Preparation of mesoporous tantalum oxide and its enhanced photocatalytic activity. *Materials letters* **2011**, *65(1)*, 64-66.
76. Pierro, V., *et al.* Ternary quarter wavelength coatings for gravitational wave detector mirrors: Design optimization via exhaustive search. *Physical Review Research* **2021**, *3(2)*, 023172.
77. Ozer, N., Lampert, C. M. Structural and optical properties of sol-gel deposited proton conducting Ta₂O₅ films. *Journal of Sol-Gel Science and Technology* **1997**, *8(1)*, 703-709.
78. Devine, R. A. B., *et al.* Use of carbon-free Ta₂O₅ thin-films as a gate insulator. *Microelectronic engineering* **1997**, *36(1-4)*, 61-64.
79. Chaneliere, C., Four, *et al.* Comparison between the properties of amorphous and crystalline Ta₂O₅ thin films deposited on Si. *Microelectronics Reliability* **1999**, *39(2)*, 261-268.
80. Joseph, C., *et al.* Amorphous to crystalline transformation in Ta₂O₅ studied by Raman spectroscopy. *Journal of Raman Spectroscopy* **2012**, *43(8)*, 1146-1150.
81. Krishnaprasanth, A., Seetha, M. Solvent free synthesis of Ta₂O₅ nanoparticles and their photocatalytic properties. *AIP advances* **2018**, *8(5)*, 055017.
82. Kozlowski, M. R., *et al.* *Thin films for optical systems*. Ed. FR Flory, **1995**.
83. Yoon, S. G., *et al.* Comparison of residual stress and optical properties in Ta₂O₅ thin films deposited by single and dual ion beam sputtering. *Materials Science and Engineering: B* **2005**, *118(1-3)*, 234-237.
84. Song, Y., *et al.* Optical and structural properties of dense SiO₂, Ta₂O₅ and Nb₂O₅ thin-films deposited by indirectly reactive sputtering technique. *Vacuum* **2000**, *59(2-3)*, 755-763.

85. Sickafus, K. E., *et al.* Radiation damage effects in zirconia. *Journal of Nuclear Materials* **1999**, 274(1-2), 66-77.
86. Gionco, C., *et al.* Cerium-doped zirconium dioxide, a visible-light-sensitive photoactive material of third generation. *The journal of physical chemistry letters* **2014**, 5(3), 447-451.
87. Ishikawa, T., *et al.* A general process for in situ formation of functional surface layers on ceramics. *Nature* **2002**, 416(6876), 64-67.
88. Zhang, Q., *et al.* Sol-gel derived ZrO₂-SiO₂ highly reflective coatings. *International Journal of Inorganic Materials* **2000**, 2(4), 319-323.
89. Zhang, Q., *et al.* ZrO₂ thin films and ZrO₂/SiO₂ optical reflection filters deposited by sol-gel method. *Materials letters* **2000**, 45(6), 311-314
90. Clinard Jr, *et al.* Neutron-irradiation damage in stabilized ZrO₂. *Journal of the American Ceramic Society* **1977**, 60(5-6), 287-288.
91. Li, W., *et al.* Structure and properties of zirconia (ZrO₂) films fabricated by plasma-assisted cathodic arc deposition. *Journal of physics d: applied physics* **2007**, 40(8), 2293.
92. Fanderlik, I., *Silica glass and its application*. Elsevier, **2013**.
93. Bechmann, R. Elastic and piezoelectric constants of alpha-quartz. *Physical review* **1958**, 110(5), 1060.
94. Pinard, L., *et al.* Toward a new generation of low-loss mirrors for the advanced gravitational waves interferometers. *Optics letters* **2011**, 36(8), 1407-1409.
95. Levin, I., Brandon, D. Metastable alumina polymorphs: crystal structures and transition sequences. *Journal of the american ceramic society* **1998**, 81(8), 1995-2012.
96. Multone, X. *High vacuum chemical vapor deposition (HV-CVD) of alumina thin films*, PhD Thesis, Ecole polytechnique federale de Lausanne **2009**
97. Boidin, R., *et al.* Pulsed laser deposited alumina thin films. *Ceramics International* **2016**, 42(1), 1177-1182.
98. Edlmayr, V., *et al.* Thermal stability of sputtered Al₂O₃ coatings. *Surface and Coatings Technology* 2010, 204(9-10), 1576-1581.
99. Refractiveindex, Available online: <https://refractiveindex.info/?shelf=main&book=TiO2&page=Siefke> (accessed on 19 July 2021).
100. Flaminio, R., *et al.* A study of coating mechanical and optical losses in view of reducing mirror thermal noise in gravitational wave detectors. *Classical and Quantum Gravity* **2010**, 27(8), 084030.

Chapter 2

Materials and Methods

In this chapter, the experimental methods used to fabricate and study the materials studied in this work will be described. The first section will illustrate the thin films deposition methods, such as ion-assisted e-beam deposition (IAD) and Ion-Beam Sputtering (IBS). The second section will describe the techniques used to study the morphological and photocatalytic properties of the studied materials, i.e., Atomic Force Microscopy (AFM) and Kelvin Force Probe Microscopy (KFPM). Additionally, Scanning Electron Microscopy (SEM) and Energy Dispersive Spectroscopy (EDS) are introduced to gain further information on the morphological properties and chemical composition of the investigated samples, respectively. The third section will illustrate the X-Ray Diffraction (XRD) and Raman Spectroscopy (RS) techniques that are employed to study the structural properties. The third section will describe the equipment set-up with the specific aim of performing thermal treatments in different environments (air, vacuum, or controllable atmosphere). The last section will show the XRD and RS spectra of the substrates adopted in this work namely Silicon (Si) and Silica (SiO_2). Finally, a brief description of the experimental facilities used and measurement parameters will be presented at the end of each section.

2.1 Ion-assisted e-beam deposition (IAD)

The ion assisted e-beam deposition (IAD) is a physical vapor deposition (PVD) technique that combines the electron beam with an ion source (or plasma), directed on the substrate to assist the deposition process. By adding the plasma, it is possible to clean (or etch) the substrate surface, before the deposition, in order to improve the coating adhesion and produce higher molecular packing density during the material evaporation. The deposition process is described in Figure 1. In panel (a) electrons are emitted from a tungsten filament due to the thermionic effect. The generated electron beam is accelerated and permanent magnets bend the trajectory of the beam towards the crucible containing the material to be evaporated (metal oxides, in our case). In panel (b), the target is heated by means of the electron beam so as to reach the melting temperature of the material to be evaporated. In this way, atoms travel toward the substrate thus creating the desired layer (or coating) on the substrate surface. During the deposition, the substrate is continuously bombarded with an ion flow, see panel (c), which volumetric flow rate is measured in "standard cubic centimeters per minute" (sccm). This high-energy beam, i.e., a mixture gas of oxygen (O_2) and argon (Ar), is focused toward the substrate. The assistance with ion bombardment is used to enhance the material uniformity and density [1,2] and to improve the material packing density, as well as the mechanical and optical properties of the films [3]. Additionally, also the evaporated atoms collide with the ions, which transfer them part of their kinetic energy. In this way, the atoms possess enhanced energy when they reach the substrate, which allows for their higher mobility with consequent formation of denser coating.

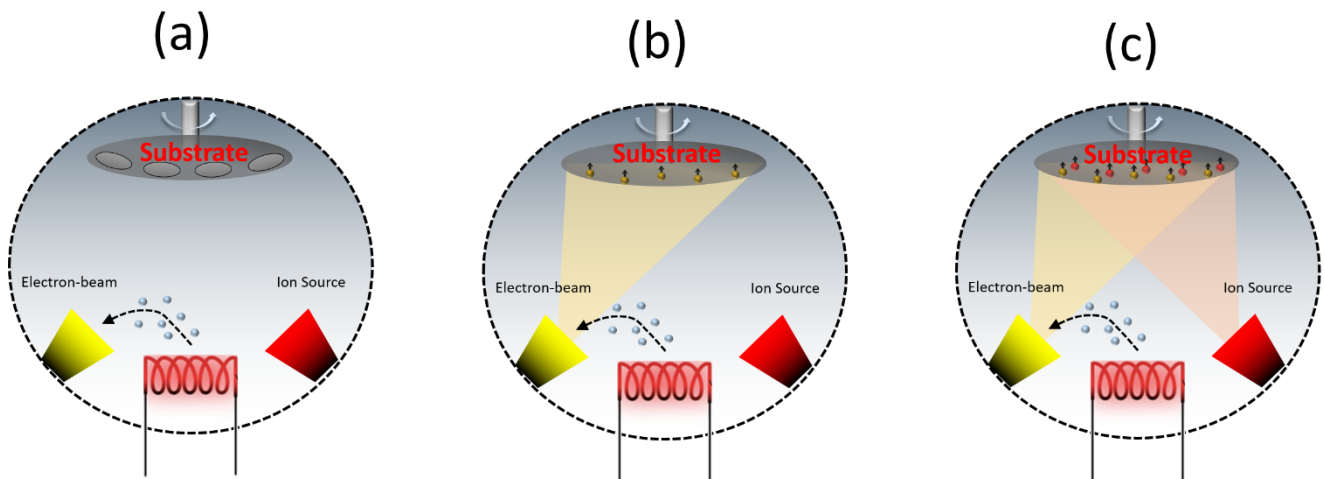


Figure 1: The ion-plasma assisted e-beam deposition (IAD) process. (a) Electrons are emitted from a tungsten filament and directed towards the crucible. (b) The target reaches the melting temperature and emitted atoms travel toward the substrate. (c) The ion beam (plasma) bombards the substrate.

The coater machine used is shown in Figure 2. In particular, Figure 2(a) shows the outside of the coater, and its pumping system. In general, the pre-vacuum is achieved in the system by a two-stage combination of a rotary vane vacuum pump and an upstream roots pump. The turbo-molecular pump evacuates the vacuum chamber to achieve the high vacuum [4]. Figure 2(b) displays the vacuum chamber of the coater. The chamber is made from high-quality stainless steel with the following main components [5]:

1. Substrate carousel
2. Ion gun
3. Material Shutter
4. E-gun
5. Material crucibles
6. Quartz Crystal Monitor
7. Infrared Heater

In particular, the carousel (1) that accommodate the substrates rotates above the plumes of the electron and ion sources, being decentered with respect to it, so that the ion-bombardment (2) works every time the evaporation adds one or few new atomic layers. A shutter (3), between the evaporation source (4) and the substrates, is open when the deposition starts and is closed when the deposited ends. Moreover, the infrared heater (7) can be used to warm up the substrates (up to 1000 °C) and ensures a constant temperature in the vacuum chamber, when required.

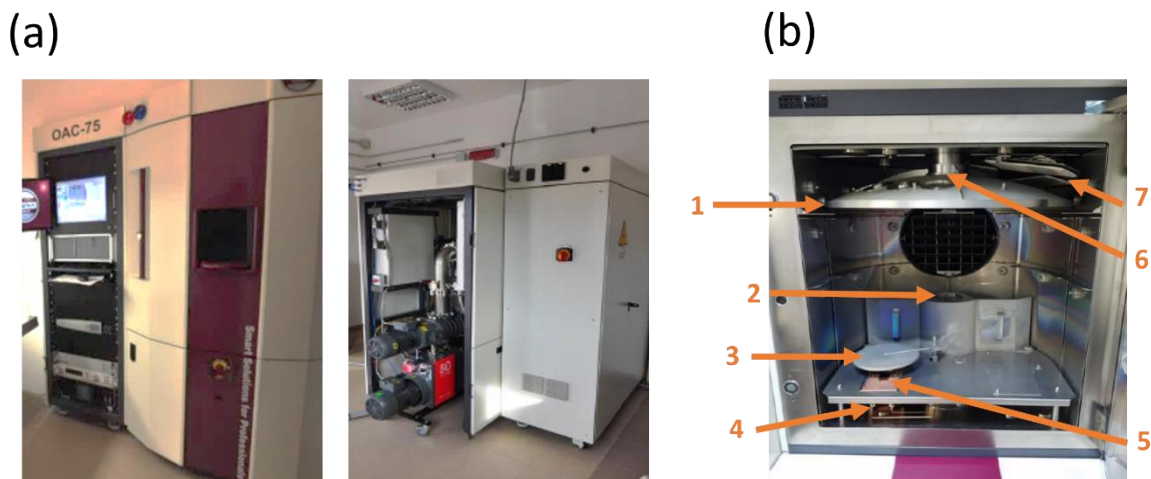


Figure 2: OptoTech OAC-75F coater (a) outside and (b) inside located at University of Benevento. Adapted from [5,6].

Finally, the thickness of the deposited material is measured using a quartz crystal microbalance (QCM) positioned in the center of the chamber (6) close to the substrates position. These resonators measure a mass variation per unit area by measuring the resonant frequency downshifts of the quartz resonator. According to the Sauerbrey equation [4], the added film thickness d is:

$$d = f_0 \frac{\rho_0 \Delta f}{F^2 \rho}, \quad (1)$$

where Δf is the frequency variation coming from the deposition of the material, ρ is the density of the evaporated material, f_0 is the quartz crystal frequency constant (~ 166100 Hz·cm), ρ_0 is the density of the uncoated quartz crystal (2.649 g/cm³), and F is the factory resonant frequency (5.98 MHz). From this equation, the deposition rate, that is the time derivative of the thickness, can be extracted [6]. It is worth mentioning that the measured thicknesses are affected by thermal shock of the quartz monitor crystal in the deposition process discussed in the Appendix E. Indeed, the crystal sensor is affected by the rapid temperature shifts when the hot material starts to evaporate.

2.1.1 Experiment

Most of the samples investigated in this work are fabricated by using the OptoTech OAC-75F coater located at University of Sannio (Benevento). Before the deposition, the vacuum chamber is evacuated down to a base pressure of $\sim 10^{-6}$ - 10^{-7} mbar. During the deposition, the ion flow of O₂ (20 sccm) and Ar (5 sccm) slightly lowers the vacuum up to 10^{-4} mbar. The electron beam is emitted by a Cu filament under DC current, operating at 8 kV, and the plasma assisted is operated with a power of 800 W. The carousel rotates with a speed of 50 rpm and the distance between the carousel and the source is ~ 70 cm. Moreover, the chamber is equipped with six pockets for the oxide materials (TiO₂, Ta₂O₅, ZrO₂, Al₂O₃, HfO₂, SiO₂). All depositions are performed at room temperature. Before the deposition, double-side polished Si (1" or 2" in diameter and 0.5 mm or 1 mm in thickness) and SiO₂ (1" in diameter and 0.5 mm in thickness) substrates, are sonicated in acetone, isopropyl alcohol (30 min each), deionized (DI) water, and blow-dried with ionizing air gun. Table 1 lists the samples under investigation in this work.

Deposition Date	Coating	Deposition Rate (Å/s)	Substrate
20180704	200 nm (1x 2000 Å TiO ₂)	2	1" Si
20190509	128.0 nm (20x 32 Å SiO ₂ , 20x 32 Å TiO ₂)	1	2" Si 1" fused SiO ₂
20190510	128.0 nm (10x 64 Å SiO ₂ , 10x 64 Å TiO ₂)	1	2" Si 1" fused SiO ₂
20190510	128.0 nm (5x 128 Å SiO ₂ , 5x 128 Å TiO ₂)	1	2" Si 1" fused SiO ₂
20190515	128.0 nm (2x 320 Å SiO ₂ , 2x 320 Å TiO ₂)	1	2" Si 1" fused SiO ₂
20190515	128.0 nm (1x 640 Å SiO ₂ , 1x 640 Å TiO ₂)	1	2" Si 1" fused SiO ₂
20190517	127.4 nm (6x 69 Å SiO ₂ , 5x 172 Å TiO ₂)	1	1" Si 1" fused SiO ₂
20190521	127.5 nm (10x 42 Å SiO ₂ , 9x 95 Å TiO ₂)	1	1" Si 1" fused SiO ₂
20190521	127.2 nm (23x 18 Å SiO ₂ , 22x 39 Å TiO ₂)	1	1" Si 1" fused SiO ₂
20190527	126.9 nm (43x 9 Å SiO ₂ , 42x 21 Å TiO ₂)	1	1" Si 1" fused SiO ₂
20200305	124.5 nm (38x 13 Å SiO ₂ , 38x 20 Å TiO ₂)	1	1" Si 1" fused SiO ₂
20190528	64 nm (2x 20 Å SiO ₂ , 1x 640 Å TiO ₂)	1	1/2" Si
20190529	32 nm (2x 20 Å SiO ₂ , 1x 320 Å TiO ₂)	1	1/2" Si
20200206	5.0 nm (1x 50 Å TiO ₂)	1	2" Si
20200827	200.0 nm (1x 2000 Å TiO ₂)	1	1" Si
20200929	100.0 nm (1x 1000 Å TiO ₂)	1	2" Si
20201024	125 nm (1x 20 Å SiO ₂ , 41x 10 Å SiO ₂ , 41x 20 Å TiO ₂)	1	2" Si
20201026	129.4 nm (2x 20 Å SiO ₂ , 38x 13 Å SiO ₂ , 38x 20 Å TiO ₂)	1	2" Si
20201122	244.0 nm (40x 11 Å SiO ₂ , 40x 50 Å Al ₂ O ₃)	1	2" Si
20201124	120.9 nm (2x 20 Å SiO ₂ , 39x 20 Å TiO ₂ , 39x 11 Å Al ₂ O ₃)	1	2" Si
20201125	115.6 nm (2x 20 Å SiO ₂ , 34x 20 Å TiO ₂ , 34x 14 Å Ta ₂ O ₅)	1	2" Si
20201127	114.7 nm (2x 20 Å SiO ₂ , 31x 20 Å TiO ₂ , 31x 17 Å ZrO ₂)	1	2" Si

Table 1: Samples fabricated with the OAC-75F coater at UniSannio [7].

2.2 Ion-beam Sputtering (IBS)

The main types of sputtering are:

- DC sputtering, in which a DC voltage is applied. This kind of sputtering is used to deposit conductive and semi-conductive materials;
- In RF sputtering, a high-frequency alternating field is applied, instead of the DC electric field. In this way insulating materials can be deposited;
- In Magnetron Sputtering, an additional magnetic field is applied to the magnetron sputter behind the cathode. In this process, less material dispersion occurs and this allows to obtain a more dense film. This method is widely used in microelectronics.

The ion-beam sputtering (IBS) is another PVD technique that involves a monoenergetic ion beam (Kaufman gun) to execute the sputtering process. In this case, the target is external to the ion source, in order to reduce the level of contamination in the film and offer the complete and independent control over ion flux. Thus, it is possible to obtain very dense, high quality metals, alloys, oxide thin films, and high performing optical coatings [8]. Moreover, it is used to reduce light absorption and scattering compared to other PVD methods.

The sputtering process uses ions with a low reactivity (usually Ar), that bombard the target surface under high voltage acceleration. In fact, the plasma of Ar is generated by the electric field inside the chamber between the target (cathode) and the substrate holder (anode) [9]. During a low-pressure process, ions collide with the target atoms, and consecutive interactions between the latter can be treated as a series of binary collisions. The incident ion hits the packed atoms that are scattered in all directions (called “collision cascade”). The ejected materials, after a cascade of collisions, are projected towards the substrate forming a thin film [see Figure 3(a)]. Then, process yield:

$$Y = \frac{\text{Atoms extracted}}{\text{incident particle}}. \quad (2)$$

The quantity Y indicates the efficiency of sputtering that depends on both the type and the binding energy of target atoms, the relative mass of ions and atoms, and the incident ion energy and angle. Typically, Y can assume a value in the range 0.01 to 5.

2.2.1 Experiment

Some of the samples studied in this work were fabricated by means of an IBS, called Grand Coater (CG), at Laboratoire des Matériaux Avancés (LMA) in Lyon [see Figure 3(b)] [10]. The system is equipped with an Ar ion source, and TiO₂ and Ta₂O₅ targets. During the deposition process, Argon is injected into the ion-beam sources; the ion beam is characterized by an energy and current of the order of 1 keV and 0.1 A, respectively. Moreover, oxygen is injected into the chamber, achieving total residual pressure inside

the chamber of the order of 10^{-4} mbar. It is worth stressing that the presence of the oxygen in the vacuum chamber allows to increase the oxidation.

In particular, these materials are co-sputtered with different TiO_2 concentrations on different substrates, i.e., single-side polished Si (3" in diameter and 0.5 mm in thickness) and SiO_2 (1" in diameter and 2 mm in thickness). Table 2 lists the samples under investigation in this work.

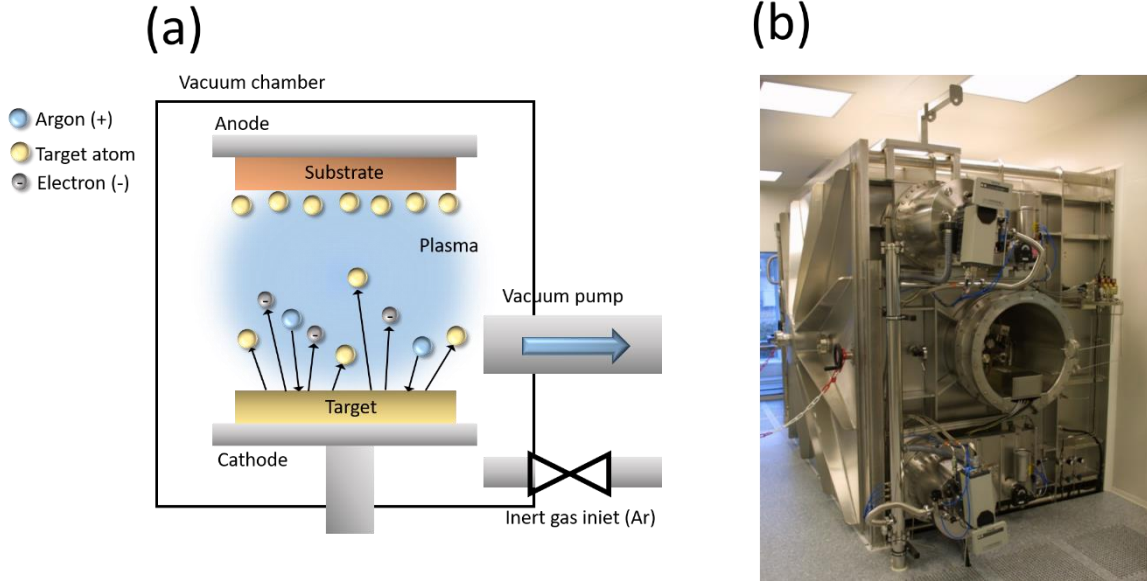


Figure 3: (a) Scheme of the Sputtering process; (b) outside of the IBS in Lyon. Adapted from [9,10].

Deposition Code	Coating	Ti/(Ta+Ti) nominal	Ti/(Ta+Ti) (%)*	Thickness	Substrate
c20014	Ta_2O_5	0	7.1 ± 0.6	430 nm	3" Si/ 1" SiO_2
c19088	$\text{TiO}_2 - \text{Ta}_2\text{O}_5$	25	16.1 ± 0.5	502 nm	3" Si/ 1" SiO_2
c16065	$\text{TiO}_2 - \text{Ta}_2\text{O}_5$	50	38 ± 1	480 nm	3" Si
c20017	$\text{TiO}_2 - \text{Ta}_2\text{O}_5$	75	66	514 nm	1" SiO_2
c20015	$\text{TiO}_2 - \text{Ta}_2\text{O}_5$	80	83 ± 1	848 nm	3" Si/ 1" SiO_2
c19089	$\text{TiO}_2 - \text{Ta}_2\text{O}_5$	90	97	350 nm	1" SiO_2
c20016	TiO_2	100	96 ± 1	542 nm	3" Si/ 1" SiO_2

Table 2: Samples fabricated by using the GC at LMA. The thicknesses have been measured by using a spectrophotometer at LMA and by means spectroscopic ellipsometry at University of Genova. Ti/(Ta+Ti) concentrations are extracted from EDS measurements performed at Unisa and UniPg.

2.3 Scanning Probe Microscopy (SPM)

The Scanning Probe Microscopy (SPM) and other derived techniques have made possible to access and control physics at the nanoscale. This branch of microscopy was invented by G. Binnig, H. Rohrer, and C. Gerber during the '80s. Here, a physical probe scans the surface sample without damaging it.

In the basic SPM setup, a piezoelectric actuator moves the sample (or the probe) with high precision in the x, y, and z directions, a feedback circuit maintains the probe-sample interaction constant by changing their mutual distance, and finally a software interface is used to measure and convert data into images. The schematic experimental setup of an SPM system is shown in Figure 4 [11].

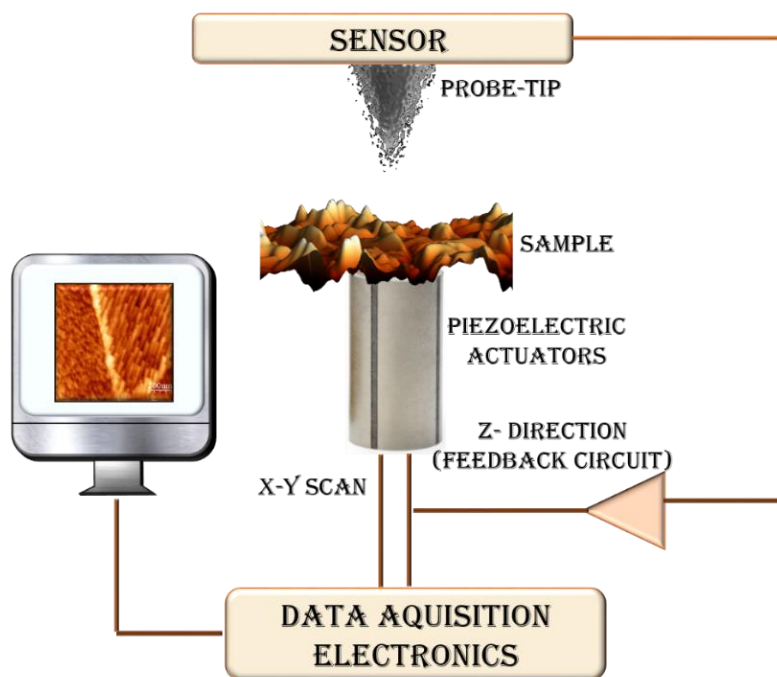


Figure 4: Scanning probe microscopy setup.

Chronologically, the Scanning Tunneling Microscopy (STM) was the first to be invented in 1982, then atomic force microscopy (AFM) in 1986 and after the electric force microscopy (EFM) in 1988 [12-15]. Over time, it has been clearly understood that STM and AFM can provide a high atomic scale resolution and both vertical and lateral scale information [16,17]. In general, there are several SPM types that use different interactions based on several physical principles. All techniques are summarized in Figure 5. In the bottom of this figure, representative SPM images acquired on different materials (MoS₂, FeSe, Py, TiO₂/ZrO₂ multilayers) are shown [18-21].

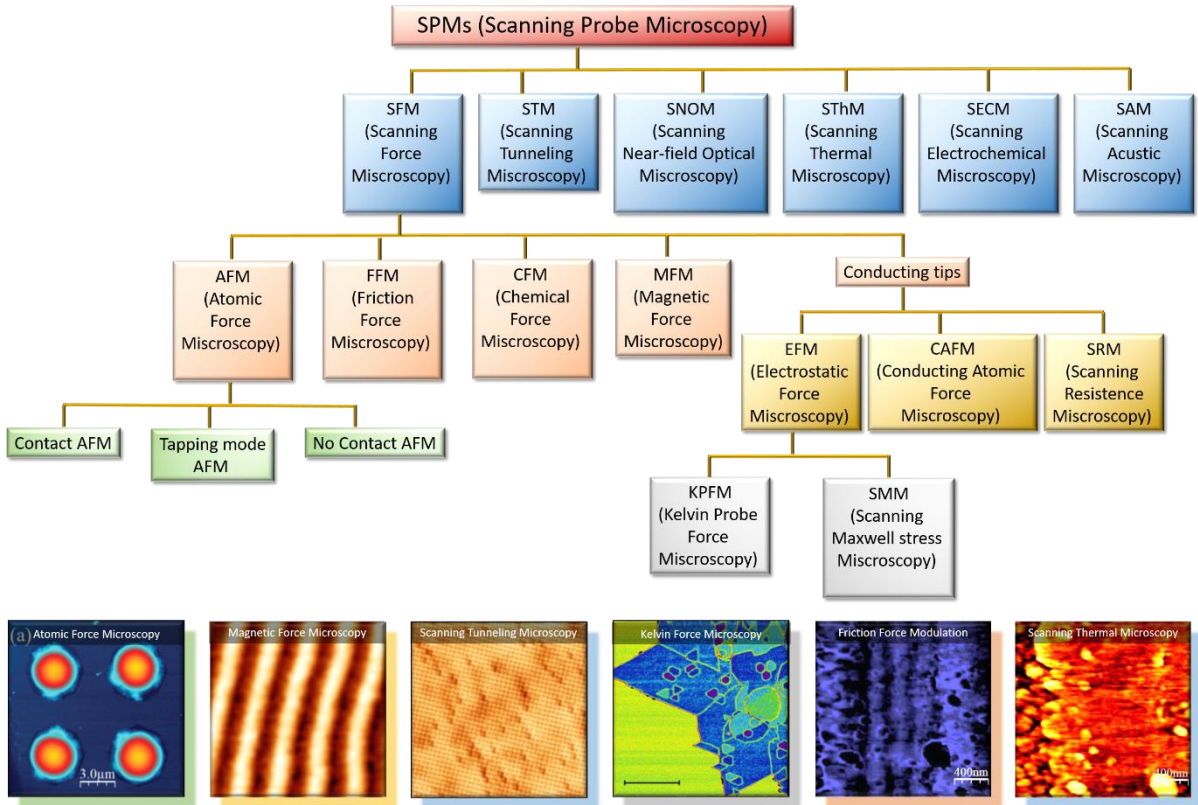


Figure 5: Scanning probe microscopy techniques [16, 17]. In the bottom, representative SPM images adapted from [18-21].

In the following, an explanation of the Atomic force microscopy (AFM) theory and the setup used to investigate the morphological properties of the samples deposited by means of IAD and IBS, is shown.

2.3.1 Atomic Force Microscopy (AFM)

Atomic force microscopy (AFM) is the most well-known SPM technique, where the interaction between probe and sample is described by the Lennard-Jones's potential:

$$U(r) = ar^{-12} - br^{-6}. \quad (3)$$

The interaction force, given by:

$$F(r) = -\frac{dU(r)}{dr} = 12ar^{-13} - 6br^{-7}, \quad (4)$$

is a function of the separation distance (r) between the probe and the sample that can assume both positive (repulsive) and negative (attractive) values.

The plot of interaction force is shown in Figure 6, and it can be separated into three areas:

- attractive regime
- repulsive and attractive regime
- repulsive regime

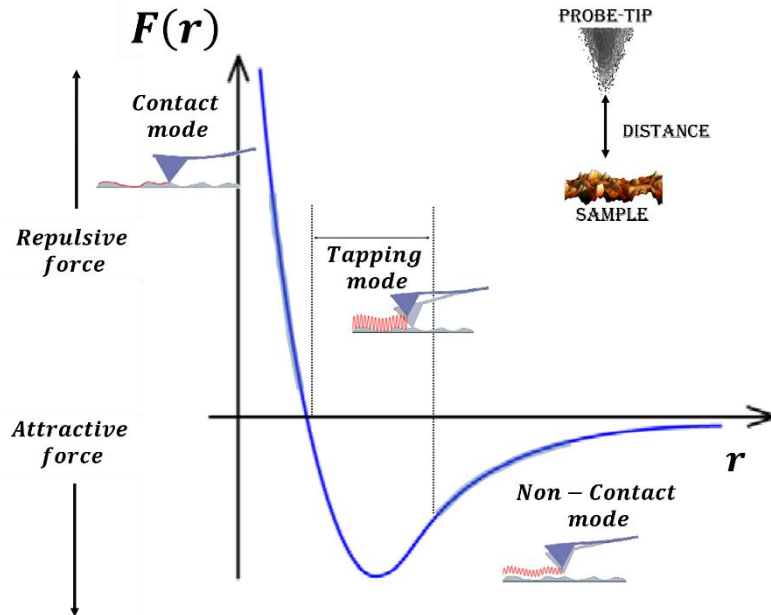


Figure 6: Interaction force as a function of the distance between the probe and the surface sample.

In this way, it is possible to determine three different AFM operation modes: Contact, Tapping, and non-contact. The interaction between probe and sample is measured by using a laser photodiode system through the cantilever deflection (upward or downward), since the AFM probe is formed by a cantilever with a sharp tip.

In the **contact mode**, also known as static mode, the tip is held in stable contact with the sample surface, in the repulsive regime of van der Waals forces [22], see Figure 6. The contact mode allows to extract information about friction, elasticity, and other mechanical properties of the sample at the nanoscale. However, this mode is restricted to flat surface to avoid tip damages.

The **non-contact mode** is a dynamic operation mode. In this case, the cantilever, positioned far from the surface and fixed to a piezo stack, oscillates perpendicularly to the surface at a certain frequency, close to its resonance frequency. When the probe-surface approach occurs, the frequency shifts due to the attractive interaction between probe and sample, so that the AFM works into the first part of the Lennard-Jones's potential (see Figure 6). By using this mode, it is also possible to investigate soft samples.

Also the **tapping mode** is a dynamic operation mode. The probe repeatedly hits the sample switching from repulsive to attractive force regime, see Figure 6. Also in this case, the cantilever oscillates, and the system monitors the amplitude of these oscillations, which reduces or increases, with respect to a reference amplitude, depending on the interaction regimes. By using the tapping mode, biological, hard and soft samples can be investigated.

2.3.2 Kelvin Probe Force Microscopy (KPFM)

The Kelvin Probe Microscopy (KPFM) [23], is a variant of the electrostatic force microscopy (EFM), capable of giving information on both topography and surface potential, by monitoring the electrostatic interaction between a conducting tip and the sample [24]. In the KPFM experiments, a second raster scan of surface (or *Lift mode*) at specific constant height is required after the acquisition of the topographic data. This method allows calculating the work function, W , of the sample that depends on several factors as the surface properties of the material, oxide layer, electrostatic charges, dopant concentration and it may be sensitive to the light exposure.

The work function of the sample can be calculated starting from the contact potential difference (V_{CPD}) between a conducting tip and the sample, defined as:

$$V_{CPD} = \frac{W_{tip} - W_{sample}}{e}, \quad (5)$$

with W_{tip} , W_{sample} , being the tip and sample work functions, respectively, and e is the elementary charge.

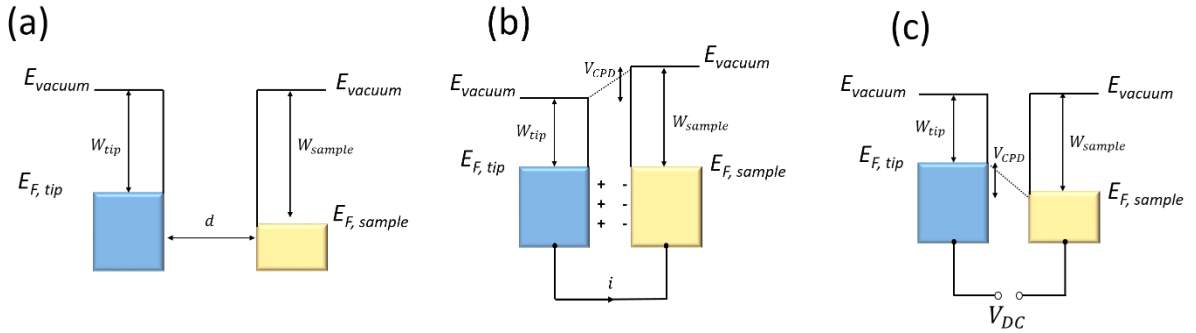


Figure 7: electronic energy levels when (a) tip and sample are separated of a distance d ; (b) tip and sample are in contact with a current i to compensate Fermi levels; (c) between tip and sample is applied an additional external DC potential to align the vacuum levels.

Figure 7 displays the electronic energy levels in the case of (a) the tip is far from the sample surface, (b) the tip is brought close to the sample surface, and (c) an external DC voltage, V_{DC} , is applied. In the case (a), the Fermi levels are misaligned, but not the vacuum levels. In the case (b), the tip and sample are close enough for tunneling current to flow, thus a V_{CPD} is established and an electric force is exerted. To balance this force, V_{DC} is applied for aligning the vacuum levels (c). This means that $V_{DC} = V_{CPD}$, and thus, through Eq. (5) and knowing W_{tip} , one can estimate W_{sample} .

If an additional sinusoidal voltage, $V_{AC} \sin(\omega t)$ is applied to the tip, it oscillates due to the electrostatic force:

$$F = -\frac{1}{2} \frac{dC(z)}{dz} [(V_{DC} \pm V_{CPD}) + V_{AC} \sin(\omega t)]^2, \quad (6)$$

with z being the normal direction to the sample, C is the capacitance of the system, and sign is + (-) if the bias is applied to the sample (tip).

Equation (6) can be recast as the sum of three components $F = F_{DC} + F_{\omega} + F_{2\omega}$ where:

$$F_{DC} = -\frac{\partial C(z)}{\partial z} \left[\frac{1}{2} (V_{DC} \pm V_{CPD}) \right]^2, \quad (7)$$

$$F_{\omega} = -\frac{\partial C(z)}{\partial z} (V_{DC} \pm V_{CPD}) V_{AC} \sin(\omega t), \quad (8)$$

$$F_{2\omega} = \frac{1}{4} \frac{\partial C(z)}{\partial z} V_{AC}^2 [\cos(2\omega t) - 1]. \quad (9)$$

In detail, the F_{DC} contribution produces a static tip deflection, the F_{ω} contribution is used to measure the V_{CPD} , and the $F_{2\omega}$ contribution is employed in the scanning capacitance microscopy [25]. Specifically, for KPFM, Eq. (8) serves to measure V_{CPD} . In fact, when the probe oscillate under F_{ω} at the frequency ω , a lock-in amplifier allows to measure these oscillations; imposing V_{DC} through a feedback system, it is possible to cancel the oscillations, making the electrostatic force zero. In this case, $V_{DC} = V_{CPD}$ and W_{sample} can be inferred.

2.3.3 Experiment

AFM and KPFM measurements, at room temperature and pressure, are performed by using a Nanowizard III, equipped with Vortex electronics from JPK, [Figure 8(a)], and a Bruker Multimode AFM [Figure 8(b)] with Nanoscope V controller, located in the Scanning Probe Microscopy and Nano Matter (SPnM) Lab in Physics Department at University of Salerno.

Most of the AFM measurements have been acquired in tapping mode, by using a Pt coated with a resonance frequency of $f_0 \approx 75$ kHz and elastic constant of $k \approx 3$ N/m (SCM-PIT-V2 by Bruker), and in contact mode by using a L-TESP-V2 probe (resonance frequency of $f_0 \approx 190$ kHz and elastic constant of $k \approx 48$ N/m).

A PtIr probe is also used in the case of the KPFM measurements. The second scan height was fixed at 50 nm, and $V_{AC} = 1500$ mV is established between tip and sample to acquire KPFM maps and improve signal/noise ratio. The KPFM experiments were performed in dark conditions and under UV-lighting.

(a)



(b)

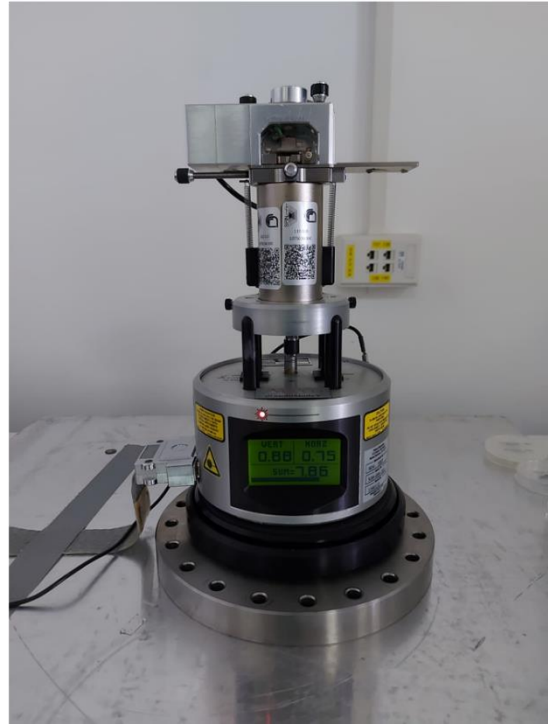


Figure 8: (a) JPK-Nanowizard III and (b) Bruker AFM installed in SPnM lab at the Physics Department.

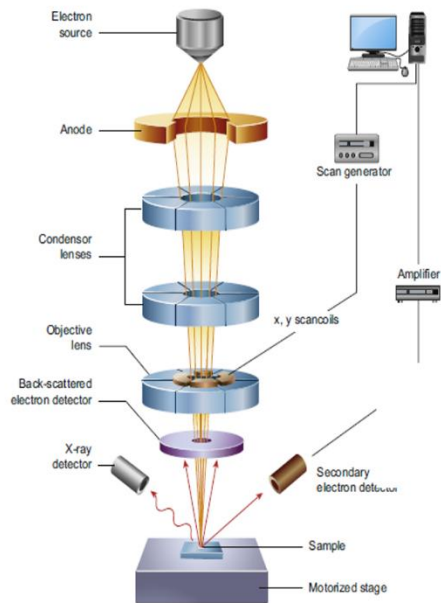
2.4 Scanning Electron Microscopy (SEM)

The Scanning Electron Microscope (SEM) is an electro-optical system invented during the '30s, and constructed in the 1937 by von Ardenne [26]. This microscope uses a beam of electrons as a probe, and it is one of the most functional instruments capable to characterize the conductive and insulating (after metallization of the surface) specimens, with a high resolution, and with a wide range of magnifications, and to perform analysis on chemical composition.

Schematic representation of a SEM equipment is reported in Figure 9(a). All components are collected in a column working in high vacuum conditions, with an extended mean free path of electrons. On the top of the column, the electron beam is thermionically emitted by a tungsten filament (or by field emission effect from a tip shaped wire in the field emission SEM- FESEM). The electrons are accelerated by means of an anode, and are focused on the samples by using a series of lenses (condenser and objective) and slit placed in the column. The electron beam interacts with the sample generating knocked out or backscattered electrons that are collected and the image of the surface is generated by the acquisition system.

Increasing the beam energy, it can be possible to penetrate deeper into the sample, obtaining different emissions detected by secondary electrons (SEs), and backscattered electrons (BSEs) detectors, and X-ray spectrometers [28,29].

(a)



(b)



Figure 9: (a) SEM microscope setup. Adapted from [27]. (b) Electron-matter interaction volume and types of signals; (c) SEM and FE-SEMs equipment installed in the MUSA lab at Physics Department.

The SEs escape from the sample with low energy radiations and determine the topography of the sample. The BSEs, produced a few microns deep in the sample, provides information about the chemical composition of the material. Then, the X-ray radiation allows to obtained accurate chemical information regarding the elements forming the material, detected from the energy dispersive spectrometers (EDS). This detector is formed by a semiconducting Li-doped Si plate situated between two electrodes under an applied voltage of 1 kV. After a photon-semiconductor interaction, hole-electron pairs are generated. The ratio between the number of photo-generated charge carriers and the energy for creating a single pair, gives an estimation of the incident photon energy. Finally, an EDS spectrum is obtained counting the photons as a function of the energy.

2.4.1 Experiment

In our work, FESEM (from SIGMA) is used to provide topographical information with higher resolution and magnification, producing clearer, less electrostatically distorted, high quality images, by using low voltage. The high-resolution SEM micrographs have been acquired using an InLENS detector with an voltage of 10 kV, a working distance of 5 mm and a beam current of 80 μ A. The film composition X-ray microanalysis has been performed by using an Oxford-Inca Energy 300 system, to check chemical composition of the as-grown and annealed films. Both SEMs are located in the MUSA lab, see Figure 9(b).

2.5 X-Ray Diffraction (XRD)

X-Ray Diffraction (XRD), discovered by von Laue in 1912, is a method to determine the crystalline structures of the investigated material. Diffraction phenomenon takes place due to the regular distribution of atoms in the crystal; a three-dimensional picture of the electron density can be obtained from the measure of the angles and intensities of the diffracted beams.

The key elements of a diffractometer are X-ray source, a detector, and a goniometer where the specimen is placed. A focused monochromatic X-ray beam irradiates the sample at different incident angles. During the sample rotation, some reflections disappear and new ones appear. The detector records the intensity of each spot at any orientation of the crystal.

According to the Bragg's model of diffraction, at specific wavelengths (λ) and incident angles (θ), crystals generate intense peak of reflected radiation, see Figure 10. The condition of constructive interference on λ and θ is given by the Bragg's law [30]:

$$2d \sin\theta = n\lambda. \quad (10)$$

with d being the spacing between diffraction planes, and n is a positive integer.

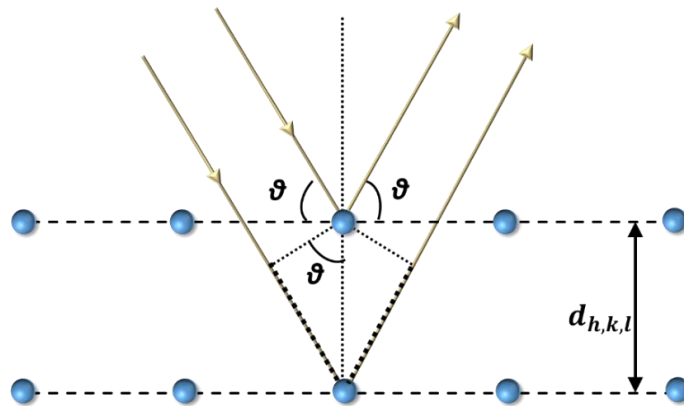


Figure 10: Bragg's law.

2.5.1 Experiment

In order to check the emergence of crystallinity as a function of annealing temperature of the investigated samples, the θ - 2θ scans with a time/step 0.2–0.6 s, a 2θ step of 0.02° , and a 2θ angle ranging from 20 to 75° , by using a D2 phaser diffractometer from Bruker, have been performed. Instead, XRD with a high-resolution and X-ray reflectivity (XRR) have been made by using a Philips X-Pert MRD diffractometer with a monochromatic Cu $K\alpha_1$ radiation with wavelength of 1.54056 \AA . This diffractometer is equipped with a four-crystal Ge220 asymmetric monochromator and a graded parabolic mirror positioned on the primary arm, which reduces the incident beam divergence to 0.12 arc sec. The θ - 2θ scans is done with a time/step of 100 s, 2θ step of 0.02° , and 2θ angle in the range from

20° to 75°. The Philips and Bruker diffractometers are located in the Musa Lab in Physics [Figure 11(a)] and in Chemistry [Figure 11(b)] Departments at University of Salerno, respectively.

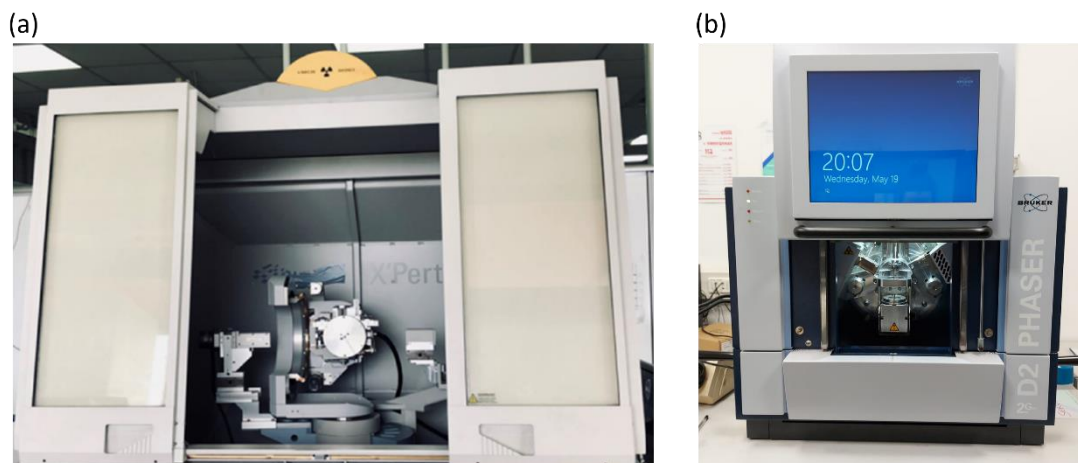


Figure 11: (a) Philips X-Pert and (b) Bruker diffractometers installed in the MUSA lab at Physics Department and in Chemistry Department, respectively.

2.6 Raman spectroscopy (RS)

Raman Spectroscopy (RS) is an analytical technique used to provide both chemical and structural information through the specific spectral patterns (fingerprint). The phenomenon lying at the base of this spectroscopy was first observed in 1928 by the Indian physicist C.V. Raman for which it is named [31-34].

The RS studies the interaction of the matter with light that can be absorbed or scattered. In the scattering process, the light scattered can have the same frequency of the incident light (ν_0), or a different frequency ($\nu_0 \pm \nu_{\text{vib}}$, where ν_{vib} is a vibrational frequency). The first case is referred to the Rayleigh or elastic scattering, instead the other cases are related to the inelastic anti-Stokes and Stokes scattering.

The classical theory of the Raman effect considers the time-dependent electric field of the incident light as:

$$E(t) = E_0 \cos(2\pi\nu_0 t), \quad (11)$$

where E_0 and ν_0 are the amplitude and frequency oscillation of the light, respectively.

This electric field irradiates a diatomic molecule inducing an electric dipole moment P :

$$P(t) = \alpha E(t) = \alpha_0 E_0 \cos(2\pi\nu_0 t) +$$

$$\begin{aligned}
& + \frac{1}{2} \left(\frac{\partial \alpha}{\partial Q} \right)_0 Q_0 E_0 \cos(2\pi (\nu_0 + \nu_{vib})t) + \\
& + \frac{1}{2} \left(\frac{\partial \alpha}{\partial Q} \right)_0 Q_0 E_0 \cos(2\pi (\nu_0 - \nu_{vib})t)
\end{aligned} \tag{12}$$

where α is the polarizability, Q is a variation of the internuclear distance (nuclear distortion), Q_0 is the amplitude of the vibration, and ν_{vib} is the vibration of the molecular nuclei.

From Eq. (12), the oscillating induced dipole moment can emit:

- at the same frequency of the incident light, $\nu_0 = \nu_{vib}$ (the Rayleigh scattering);
- at a frequency $\nu_0 + \nu_{vib}$ (anti-Stokes scattering);
- at a frequency $\nu_0 - \nu_{vib}$ (the Stokes scattering).

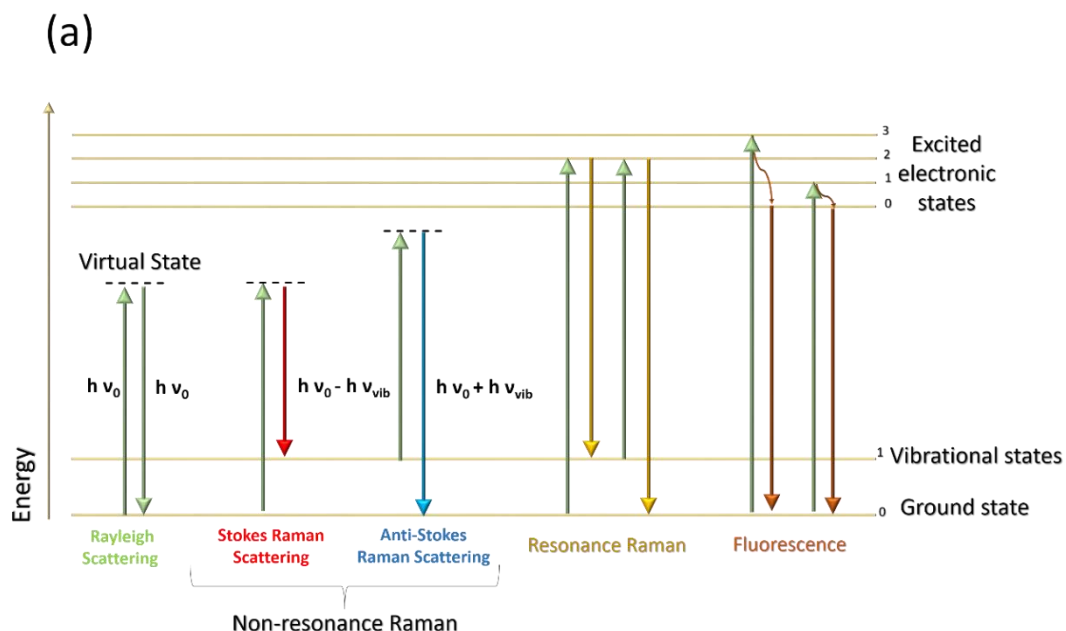
From the quantum point of view, the Raman spectroscopy is described involving the quantized energy levels of the molecule, as shown in Figure 12(a).

Considering the molecule as a quantum harmonic oscillator, its energy can be written as:

$$E_j = \left(n + \frac{1}{2} \right) h\nu, \quad n = 0, 1, 2, 3 \dots, \tag{17}$$

where n is the quantum number, ν is the vibration frequency, and h is the Plank's constant.

The Rayleigh scattering occurs when the molecule in the initial ground state, $n = 0$, can be excited to a virtual energy and quickly returned to the initial state. In this process, the molecule emits the same energy as the one absorbed from the incident light. On the other hand, the Stokes and anti-Stokes Raman scattering, involve virtual energy levels. In the first case, a molecule goes from the ground state to the excited state, $n = 1$, and in the second case, it moves toward the ground state, starting from the excited state, passing through a virtual level. Then, in both cases, the energy after the scattering will be different from initial one.



(b)

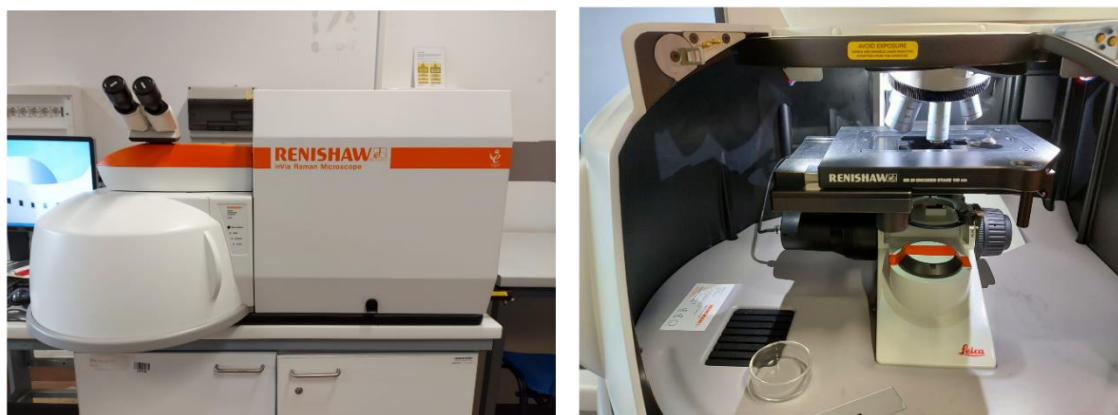


Figure 12: (a) Energy levels diagram for Rayleigh scattering, Raman scattering, Raman resonance and fluorescence. (b) Outside (left) and inside (right) of the Raman instrument.

2.6.1 Experiment

In our experiments, a Raman Spectrometer (RENISHAW InVia) in the backscattering geometry is used to explore the structural and vibrational properties of the investigated samples. A near infrared laser, with a wavelength of 785 nm, was used as the excitation source. Spectra in the range 100–1200 cm^{-1} (by using a 50X magnification, 10 s of exposure time, 5% of laser power, and 5 accumulations) and in the range 100–200 cm^{-1} (with a 50X magnification, 10 s of exposure time, 10% of laser power, and 3 accumulations) have been acquired. Moreover, multiple (≥ 5) Raman measurements have been performed on each sample area. The RENISHAW Raman Spectrometer is located in Pharmacy Department [Figure 12(b)] at University of Salerno.

2.7 Thermal annealing

Thermal annealing is a routine process used in this work to thermally induce structural transitions. In this work, the heat treatments are performed in vacuum conditions (up to $\sim 3 \times 10^{-4}$ mbar), in air, or in controllable atmosphere (O_2 , 1 bar of pressure). All thermal processes take place in three steps, i.e., (i) heating ramp with a fixed rate, (ii) plateau at the desired temperature setpoint, and (iii) cooling ramp with a fixed rate.

2.7.1 Experiment

In this work, all samples have been heated with a rate of $3 \text{ }^\circ\text{C}/\text{min}$, to a temperature setpoint in the range of $100\text{-}1000 \text{ }^\circ\text{C}$, and left at the setpoint for 12 h. Finally, they have been cooled down to room temperature with a rate of $1 \text{ }^\circ\text{C}/\text{min}$. For our purposes, two kinds of heaters for temperatures lower and higher than $800 \text{ }^\circ\text{C}$ are used. The Eurotherm (type 815/818) controller with a proportional-integral-derivative (PID) system with a stability of $0.05 \text{ }^\circ\text{C}$, allows to perform annealing from 100 to $600 \text{ }^\circ\text{C}$ in air, vacuum and controlled atmosphere. The heater is placed in a stainless-steel chamber and it is located in the SPnM lab [Figure 13(a)]. Moreover, a muffle furnace (Carbolite Gero) located in the MUSA lab is used to perform annealing in air from 800 to $1000 \text{ }^\circ\text{C}$ [Figure 13(b)].

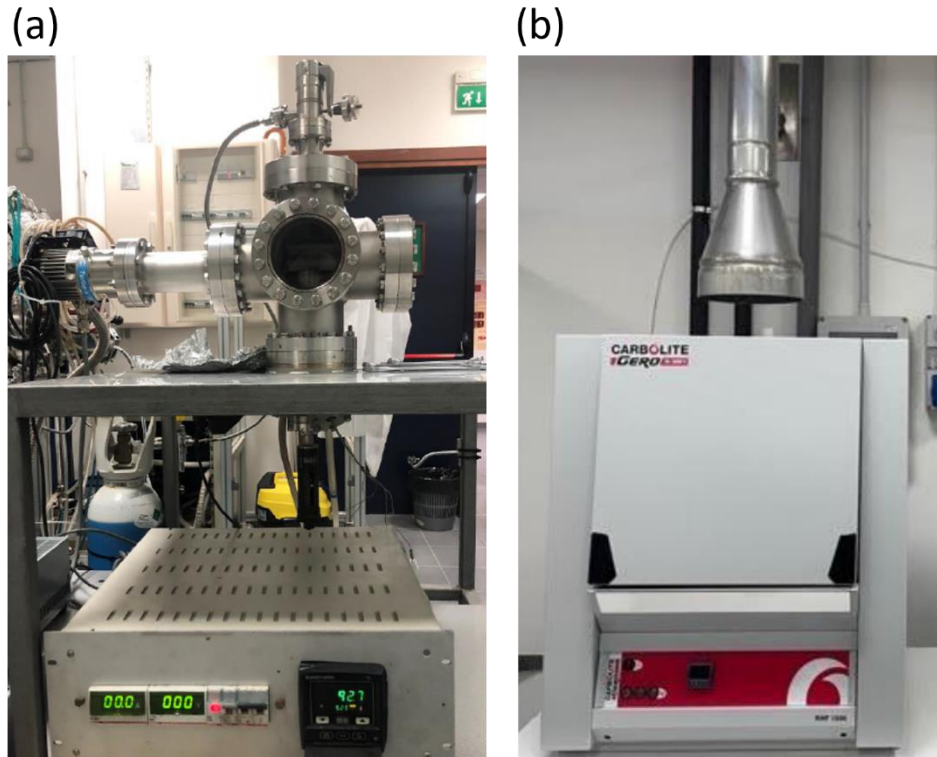


Figure 13: (a) Eurotherm heater and (b) Carbolite Gero muffle furnace installed in the SPnM and MUSA lab at University of Salerno, respectively.

2.8 Substrates

The substrates adopted in the fabrication process namely Si, and SiO₂ are investigated from a structural point of view by using XRD and RS.

In the Figure 14(a), the XRD spectra of Si (black curve), and SiO₂ (red curve) are shown. The intense broad peak observed in the red curve substrate indicates the amorphous nature of SiO₂ [35]. On the other hand, the black curve shows (h,0,0) Si substrate reflections fixed at $2\theta \approx 33, 61,$ and 69° as expected indicating that Si wafer is monocrystalline orienting (h,0,0) crystalline plane toward at the sample surface.

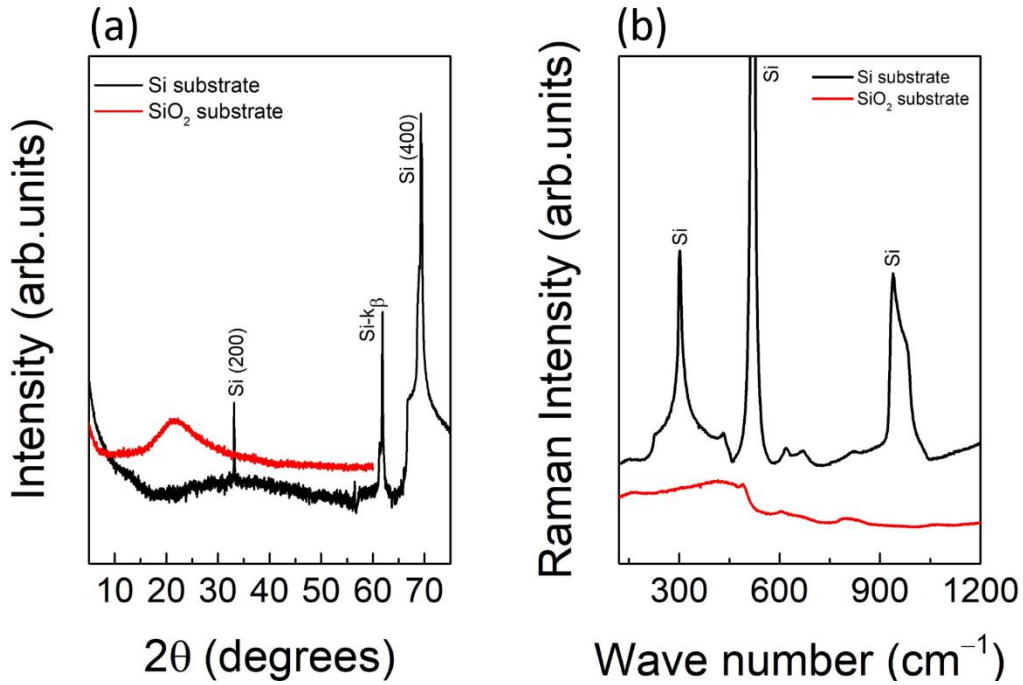


Figure 14: (a) XRD, and (b) Raman spectroscopy of the Si (black curve), and SiO₂ (red curve).

Same situation is observed for the Raman investigation shown in Figure 14(b). The bumps and modes at 492.8 cm^{-1} , 605.5 cm^{-1} , and 795.4 cm^{-1} in the red curve come from the amorphous SiO₂ substrate as shown in the Ref. [36]. Basically, the band in the low frequency region, between 400 to 700 cm^{-1} are all associated with the inter-tetrahedral Si-O-Si bonding, while the bands in the high frequency region near 1050 cm^{-1} and at 1200 cm^{-1} are due to symmetrical stretching of silicon and oxygen in the silicate tetrahedral with non-bridging oxygen atoms [36].

In the case of Si substrate, all the Raman modes observed in the black Raman spectrum of Figure 14(d) are associated to Si indicating its crystalline state (three highest Raman bands at $306, 520, 920 \text{ cm}^{-1}$, and the modes with lower intensity appearing at 460 cm^{-1} and from 618 to 675 cm^{-1}). The first stronger peak at 306 cm^{-1} is related to the second-order spectrum of transverse (T) acoustical (A) phonons at the critical point X of the Brillouin zone for two-phonon combinations - $2TA(X)$. The highest intensity peak at 520 cm^{-1} is due to the optical (O) phonons at the center Γ point of the Brillouin zone (BZ), $O(\Gamma)$. The latter intensity peak at 920 cm^{-1} originates from many two-phonon T,O

combinations at the critical point Σ of the Brillouin zone- $2\text{TO}_2(\Sigma)$. Instead, the weaker intensity peak at 460 cm^{-1} is due to the 2TA phonons at the critical point Σ , while the peaks from 618 to 675 cm^{-1} are associated to the combination of $\text{T}(\text{O})$ and $\text{T}(\text{A})$ at the critical point X and Σ , respectively [37].

References

1. Thielsch, R., *et al.* A comparative study of the UV optical and structural properties of SiO_2 , Al_2O_3 , and HfO_2 single layers deposited by reactive evaporation, ion-assisted deposition and plasma ion-assisted deposition. *Thin Solid Films* **2002**, *410(1-2)*, 86-93.
2. Lee, C. C., *et al.* Effect of thermal annealing on the optical properties and residual stress of TiO_2 films produced by ion-assisted deposition. *Applied optics* **2005**, *44(15)*, 2996.
3. Martin, P. J., *et al.* Ion-beam-assisted deposition of thin films. *Applied Optics* **1983**, *22(1)*, 178-184.
4. Qiao, X., *et al.* Progresses on the theory and application of quartz crystal microbalance. *Applied Physics Reviews* **2016**, *3(3)*, 031106
5. Optotech. Available online: <http://www.optotech.de> (accessed on 20 May 2021).
6. Neisohn, J. *et al.* Pushing the precision of e-beam evaporation for nanolayered coatings, *in preparation*.
7. DCC database, Available online:<https://dcc.ligo.org/T2000692> (accessed on 20 May 2021).
8. Stewart, A. F., *et al.* Ion beam sputtering of optical coatings. In Laser-Induced Damage in Optical Materials. *International Society for Optics and Photonics* **1993**, *2114*, 662.
9. physlab.org, Available online: https://www.physlab.org/wp-content/uploads/2016/04/Murtaza_presentaion.pdf (accessed on 19 June 2021).
10. Laboratoire des Matériaux Avancés (LMA), Available online: <http://lma.in2p3.fr/Moyens/Means.htm> (accessed on 18 June 2021).
11. Voigtländer, B, *Scanning probe microscopy: Atomic force microscopy and scanning tunneling microscopy*, Springer, 2015.
12. Wickramasinghe, H. K., Scanned-probe microscopes. *Scientific American* **1989**, *261(4)*, 98-105.
13. D. Sarid, *Scanning Force Microscopy with Applications to Electric, Magnetic and Atomic Forces*, 2nd ed., Oxford University Press: New York, **1994**.
14. D. Bonnell, *Scanning Probe Microscopy and Spectroscopy: Theory, Techniques, and Applications*, Bonnel Editor, **2001**.
15. B. Bhushan, *et al.* *Applied Scanning Probe Methods (Nanoscience and Technology)*, Springer-Verlag, **2004**.
16. Stevens, G. C., Baird, P. J. Nano-and meso-measurement methods in the study of dielectrics. *IEEE transactions on dielectrics and electrical insulation* **2005**, *12(5)*, 979.
17. Marinello, F. *Atomic force microscopy in nanometrology: modeling and enhancement of the instrument*. PhD Thesis, **2007**.
18. Di Giorgio, C., *et al.* Nanoscale Measurements of Elastic Properties and Hydrostatic Pressure in H_2 -Bulged MoS_2 Membranes. *Advanced Materials Interfaces* **2020**, *7(23)*, 2001024.

19. Mancusi, *et al.* Magnetic pinning in a superconducting film by a ferromagnetic layer with stripe domains. *Superconductor Science and Technology* **2014**, 27(12), 125002.
20. Di Giorgio, C., *et al.* Anisotropic Superconducting Gaps and Boson Mode in FeSe 1– x S x Single Crystals. *Journal of Superconductivity and Novel Magnetism* **2017**, 30(3), 763-768.
21. Precner, M., *et al.* (2018, August). Metastable defects in monolayer and few-layer films of MoS₂. In *AIP Conference Proceedings* **2018**, Vol. 2005, No. 1, p. 020004. AIP Publishing LLC.
22. Margenau, H. Van der Waals forces. *Reviews of Modern Physics* **1939**, 11(1), 1.
23. Kelvin, L. V. Contact electricity of metals. *The London, Edinburgh, and Dublin Philosophical Magazine and Journal of Science* **1898**, 46(278), 82-120.
24. Nonnenmacher, M., *et al.* Kelvin probe force microscopy. *Applied physics letters* **1991**, 58(25), 2921-2923.
25. Hochwitz, T., *et al.* Imaging integrated circuit dopant profiles with the force-based scanning Kelvin probe microscope. *Journal of Vacuum Science & Technology B: Microelectronics and Nanometer Structures Processing, Measurement, and Phenomena* **1996**, 14(1), 440-446.
26. von Ardenne, M. *Improvements in electron microscopes*. British patent, 511204, **1937**.
27. Inkson, B. J. Scanning electron microscopy (SEM) and transmission electron microscopy (TEM) for materials characterization. In *Materials characterization using nondestructive evaluation (NDE) methods* (pp. 17-43). Woodhead Publishing, **2016**.
28. Palaci, I. *Atomic force microscopy studies of nanotribology and nanomechanics* PhD thesis, EPFL, **2007**.
29. Marchetti, M. *Design, synthesis and Chemical-physical characterization of photocatalytic inorganic nanocrystals for technological applications*, PhD thesis, **2013**.
30. Cullity, B.D. *Elements of X-ray Diffraction*, Addison-Wesley Publishing, Boston, MA, USA, 1956.
31. Smith, E., Dent, G. *Modern Raman spectroscopy: a practical approach*. John Wiley & Sons Ltd, **2005**.
32. Raman, C. V. A new radiation. *Indian Journal of physics* **1928**, 2, 387-398.
33. Ferraro, J. R., *et al.* *Introductory Raman spectroscopy* (2nd ed.). San Diego: Academic, **2003**.
34. Auner, G. W., *et al.* Applications of Raman spectroscopy in cancer diagnosis. *Cancer and Metastasis Reviews* **2018**, 37(4), 691-717.
35. Deshmukh, P., *et al.* Determination of silica activity index and XRD, SEM and EDS studies of amorphous SiO₂ extracted from rice Husk Ash. *Transactions of the Indian Institute of Metals* **2012**, 65(1), 63-70.
36. Biswas, R. K., *et al.* Study of short range structure of amorphous Silica from PDF using Ag radiation in laboratory XRD system, RAMAN and NEXAFS. *Journal of Non-Crystalline Solids* **2018**, 488, 1-9.
37. Tanino, H., *et al.* Raman study of free-standing porous silicon. *Physical Review B* **1996**, 53(4), 1937.

Chapter 3

Structural and morphological characterization of TiO₂ vs environment

This chapter discuss the effect of thermal treatments in different environments (air, oxygen and vacuum) and at different temperatures on the structural, morphological and photocatalytic properties of TiO₂ thin films. The study is carried out by means of AFM, SEM, KPFM, XRD, and RS.

The first part will focus on structural and morphological characterization of as-grown samples (amorphous), deposited by electron beam evaporation, by studying the particle size and the roughness. The amorphicity of these samples is confirmed by also XRD and RS measurements.

The second part will show that both the amorphous-to-anatase crystallization onset temperature and the anatase-to-rutile phase transformation depend on the annealing atmosphere. An analysis by using the Spurr equation is made to extract the amount of rutile at any annealing temperature, T_a . The AFM and SEM show morphologies that depend on the annealing environment, especially at the highest temperatures explored in this work. Then, it will describe the crystallization evolution and possible strain, through RS measurements. A monotonic decreases of the E_g Raman mode position as a function of T_a is observed for the air, oxygen, and vacuum samples, moving from wavenumbers that are blue-shifted compared to the expected E_g value at the lowest T_a values, to a very tiny red-shift at the highest temperature. This blue shift of the E_g Raman vibrational mode can be explained by the phonon confinement phenomenon.

Finally, the photocatalytic activity of the TiO₂ thin films, obtained from the surface photovoltage (SPV) that is measured by KPFM, exhibits a strong dependence on both annealing temperatures and environments.

3.1 Study of as-grown TiO_2

TiO_2 amorphous thin films, with a nominal thickness of 200 nm, have been deposited on an unheated (100) Si substrate by electron beam deposition at University of Sannio. All morphological and structural characterizations are performed in Physics (SPnM and MUSA Labs), Pharmacy, and Chemistry Departments at University of Salerno.

The morphological study of an as-grown sample is shown in Figure 1. In panel (a), a representative AFM image is shown on a scan area of $1\ \mu\text{m} \times 1\ \mu\text{m}$ in lateral size acquired in contact mode with a L-TESP tip from Bruker. This panel displays the as-grown surface made by uniformly distributed packed particles that is a typical arrangement for the depositions at room temperature in which an amorphous growth, without any peculiar faceting, occurs [1]. Moreover, surface roughness and features are highlighted by the color scale ranging from a minimum value of 0 nm (dark) to a maximum of 6 nm (bright). These particles and their randomly packed morphology are further confirmed by FESEM measurements shown in panel (b).

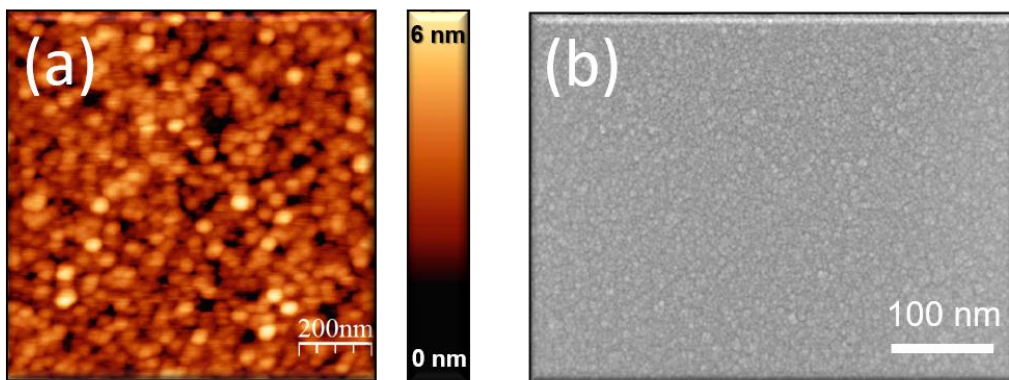


Figure 1: (a) Contact mode AFM topography, $1\ \mu\text{m} \times 1\ \mu\text{m}$ in size, and (b) FESEM image of as-grown TiO_2 . FESEM measurements have been acquired by using an InLENS detector with an acceleration voltage of 10 kV, a working distance of 5 mm and a beam current of $80\ \mu\text{A}$.

Moreover, the size of these particles and root-mean-square (RMS) roughness of the surface were studied through a statistical analysis of AFM images on a scan area of $1\ \mu\text{m} \times 1\ \mu\text{m}$ in size. The RMS roughness, defined as the root mean square of the height distribution of the sampled area, has been chosen to describe the surface morphology. This approach is pursued throughout the thesis. By performing this analysis, an average RMS roughness of $(0.87 \pm 0.06)\ \text{nm}$ is estimated.

Concerning to the particle analysis, a manual sampling of profiles (25 particles per image, one profile per particle) were analyzed by using the WSxM 5.0 software by NanoTec, 2015. Given the strongly packed nature of the morphology, the use of automatic algorithms, such as the so-called watershed or fixed threshold [2], could not be used to this aim. From this statistical analysis, a mean particle size of $(88 \pm 19)\ \text{nm}$ is measured.

However, the measurement of the particle size with AFM, and their approximation as spherical particles, is commonly affected by two factors: i) convolution between particle and tip size (that causes a particle size overestimate), and ii) high packing density (that causes a particle size underestimate). In light of this, taking into account the finite size of the tip with a nominal curvature radius of $r = 30$ nm, the deconvolved particle size can be evaluated as [3]:

$$r = \frac{(R-h)^2}{2h}, \quad (1)$$

where h is the height of the spherical caps as measured with AFM, and R is the particle radius and, thus, $2R$ its size. In doing so, the deconvolved size particle of the as-grown sample is equal to (42 ± 3) nm.

These particles are characteristic of the amorphous phase. The amorphicity of the TiO₂ as-grown films is demonstrated by performing XRD and RS. Figure 2(a,b) show XRD and RS spectra of Si substrate (red curve) and TiO₂ thin film (black curve), respectively. The black XRD spectra of Figure 2(a), shows a broad bump coming from the contribution of the amorphous TiO₂ (in the range 25 - 35°), and Si reflections. Similarly, all the Raman modes observed in the black Raman spectrum of Figure 2(b) are associated to Si substrate (for more details see Chapter 2). The broad Raman spectrum in the range 100 to 200 cm⁻¹ of the as-grown sample (see black curve) is indicative of its amorphous nature [4]. Therefore, both XRD and RS measurements confirm the amorphicity of the as-grown sample.

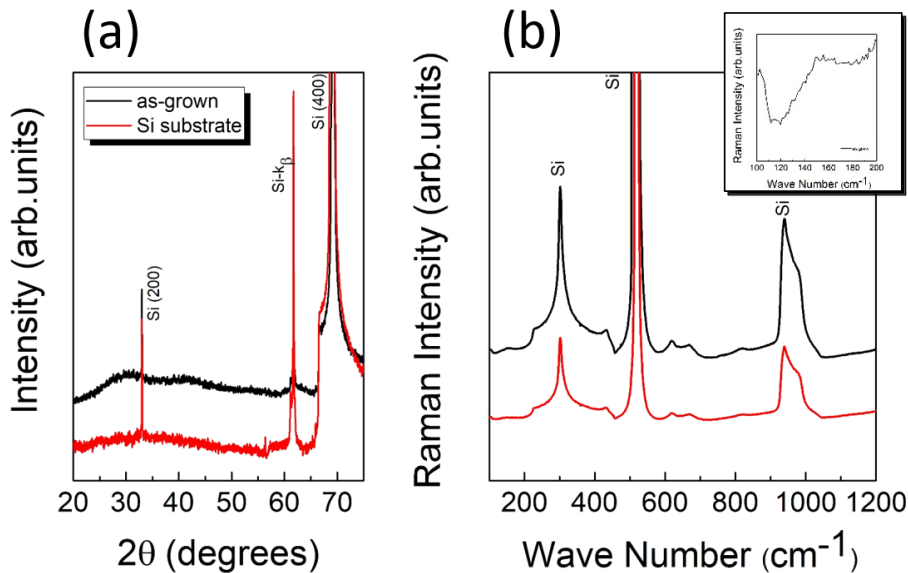


Figure 2: (a) XRD spectra of as-grown TiO₂ in black and Si substrate in red in a 2θ range of 20 to 75°. (b) RS spectra of as-grown TiO₂ in black and Si substrate in red in a wavenumber range of 100 to 1200 cm⁻¹. Black and red spectra have been offset along the y-axis for a better readability. The XRD patterns were acquired with a time/step 0.2 s, a 2θ step of 0.02°, and a 2θ angle ranging from 20 to 75° by using a diffractometer from Bruker. Raman spectra were acquired in the range of 100–1200 cm⁻¹, with a 50X magnification, 10 s exposure time, 5% laser power, and 5 accumulations, by using a Raman Spectrometer from RENISHAW equipped of red laser source (785 nm). Inset in panel (b) highlights the bump in the range 100-200 cm⁻¹.

3.2 Study of TiO_2 crystallization onset and evolution versus environment

The amorphous-crystalline phase transition, and the crystallization evolution in TiO_2 as a function of the annealing environment (air, oxygen – $\text{PO}_2 = 1$ bar, and vacuum – 10^{-4} mbar), is investigated after performing annealing processes for 12 hours in the range 100–800 °C, by using a minimum step of 50 °C, on pristine samples. Here, it is worth to stress that each single treatment has been performed on a pristine as-grown sample, to avoid any memory effect of multiple subsequent heating/cooling cycles.

The XRD and Raman spectroscopies allow determining the crystallization onset temperature, T_c , of the samples annealed in different environments. Figure 3(a) shows the XRD spectra of each sample, just before (light color curves) and after (dark color curves) T_c , by following the strongest A (101) anatase reflection at $2\theta = 25.2^\circ$, of TiO_2 , which appears earlier in temperature than brookite and rutile.

In particular, the transition from amorphous to crystalline occurs between 100 and 150°C in the cases of samples annealed in air (gray and black curves, respectively) and in oxygen (cyan and blue curves, respectively). A different situation is observed when the sample is annealed in vacuum, as the T_c is between 250 and 300°C (pink and red curves, respectively).

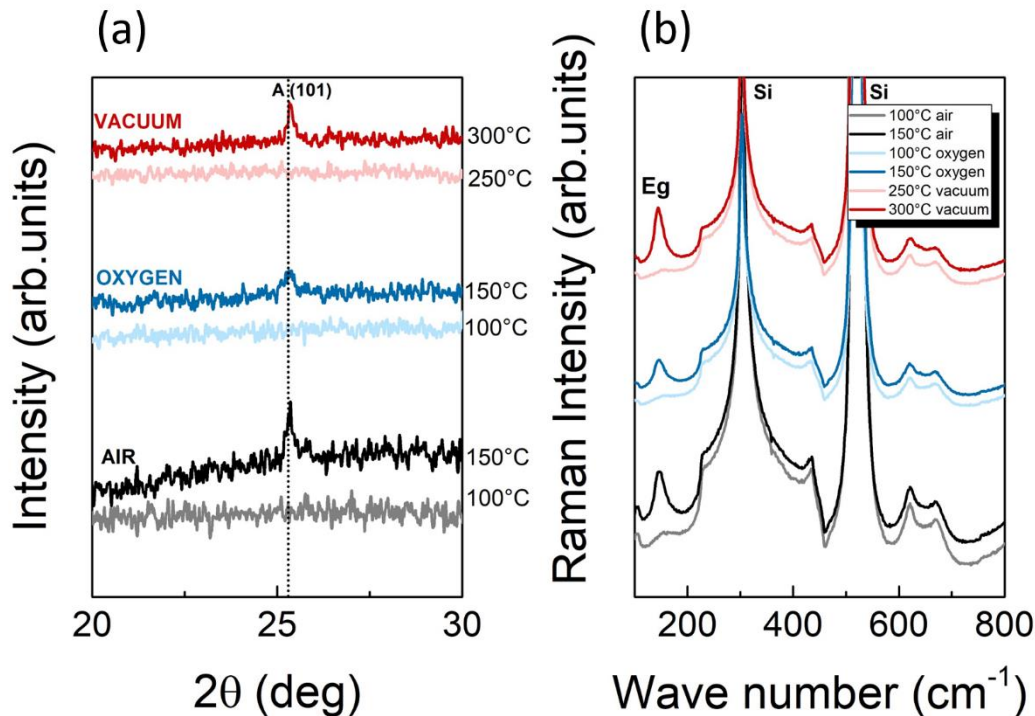


Figure 3: (a) Zoom of XRD spectra and (b) Raman Spectra of TiO_2 annealed in air at 100 (gray) and 150°C (black), in oxygen at 100 (light blue) and 150°C (blue), and in vacuum at 250 (light red) and 300°C (red). The symbols A in (a) and Eg in (b) indicate (101) anatase reflection and anatase Raman mode, respectively.

Similarly, RS measurements were performed to highlight the appearance of the strongest anatase Raman vibrational band, i.e., the Eg mode at $\sim 144 \text{ cm}^{-1}$, arising because of symmetric stretching vibration of O–Ti–O bond in the anatase cell [5], to determine T_c .

This mode appears upon annealing at $150 \text{ }^\circ\text{C}$ for the samples treated in air and in oxygen, and at $300 \text{ }^\circ\text{C}$ for the samples annealed in vacuum [Figure 3(b)], confirming the XRD results. From these measurements, one can state that T_c depends on the annealing environment, i.e., it ranges in between $100\text{-}150 \text{ }^\circ\text{C}$ when the annealing is performed in saturated atmosphere (air and oxygen), and it falls in the range $250 - 300 \text{ }^\circ\text{C}$ when the process is done in vacuum. This can be explained because post-deposition annealing treatments in vacuum cause the breaking of binding bonds between oxygen and titanium, with oxygen release from the material and consequent vacancies formation [6]. On the contrary, the formation of oxygen vacancies is limited in oxygen rich-environment, while in this condition interstitial Ti is expected to form when the material undergoes heat treatments. This process accelerates the amorphous-to-anatase phase transformation [7].

Moreover, on the TiO_2 -sample after annealing process performed in air, the lattice parameters and the size of the crystalline grains by performing a Debye-Scherrer analysis was estimated. In Figure 4(a), the high resolution XRD patterns of TiO_2 -200 nm, annealed in air at different temperatures are shown, where curves of different colors correspond to different T_a , ranging from 150 to $800 \text{ }^\circ\text{C}$.

The occurrence of the anatase phase is monitored through the presence of the (101), (004) and (200) reflections at $\sim 25.2^\circ$, $\sim 37.8^\circ$, and $\sim 50^\circ$, respectively, as indicated in panel (a). According to this figure, the strongest reflection of anatase is the (004), rather than the (101) as expected. This could be related to preferential orientation effects.

Starting from $450 \text{ }^\circ\text{C}$, the emergence of the rutile phase is also observed, with the appearance of its (211) and (002) reflections. All other reflections are associated to the Si substrate. The observed anatase reflections have been fitted by a Lorentzian function; the results, reported in Table 1, have been used to evaluate the lattice parameters at each T_a . Given the tetragonal unit cell of the anatase, the lattice parameters a , b and c have been calculated as $a = b = 2d_{200}$ and $c = 4d_{004}$, respectively at each T_a (the interplanar spacing d_{hkl} for a tetragonal unit cell is given by $\frac{1}{d_{hkl}^2} = \frac{h^2+k^2}{a^2} + \frac{l^2}{c^2}$, where h, k, l are the Miller indexes). The obtained results are shown in Figure 4(b). Within the experimental error, there are no annealing-induced variations in any of the lattice parameter.

T _a (°)	Reflection (101) (deg)	Reflection (004) (deg)	Reflection (200) (deg)	Crystalline size (nm)
150	-	37.767 ± 0.002		-
175	25.22 ± 0.02	37.684 ± 0.006		12 ± 2
200	25.288 ± 0.009	37.774 ± 0.003	47.98 ± 0.01	29 ± 3
250	25.283 ± 0.006	37.783 ± 0.004	47.97 ± 0.02	45 ± 5
300	25.292 ± 0.003	37.784 ± 0.003	47.99 ± 0.01	48 ± 3
600	25.311 ± 0.002	37.852 ± 0.004	48.102 ± 0.009	41 ± 1
800	25.363 ± 0.002	37.843 ± 0.003	48.15 ± 0.01	42 ± 2

Table 1: peak center of the (101), (004), and (200) reflections as obtained by a Lorentz fit of the high resolution XRD spectra for TiO₂ thin film (200 nm) annealed in air at different T_a.

Finally, the Debye-Scherrer analysis of the (101) anatase reflection is performed to evaluate the crystallite size. The Debye-Scherer equation [8] is:

$$D = \frac{k\lambda}{\beta \cos \theta}, \quad (2)$$

where D is the crystallite size in nm, $\lambda = 0.154057 \text{ nm}$ is the wavelength of the incident radiation (Cu- $k\alpha$), $k = 0.9$ is a dimensionless shape factor for a spherical-crystal, θ is the Bragg diffraction angle in radian. β is generally the full width at half maximum height (FWHM) of the considered XRD peak, however, in the Gauss peak approximation, $\beta = 2\sqrt{2\ln 2} \sigma$, with σ being the Gaussian standard deviation. The results of the analysis are listed in Table 1. In Figure 4(c), the behavior of the crystallite size as a function of T_a is reported. The size increases from 12 nm to 48 nm, between 150-300 °C, and it reaches a plateau at ~42 nm.

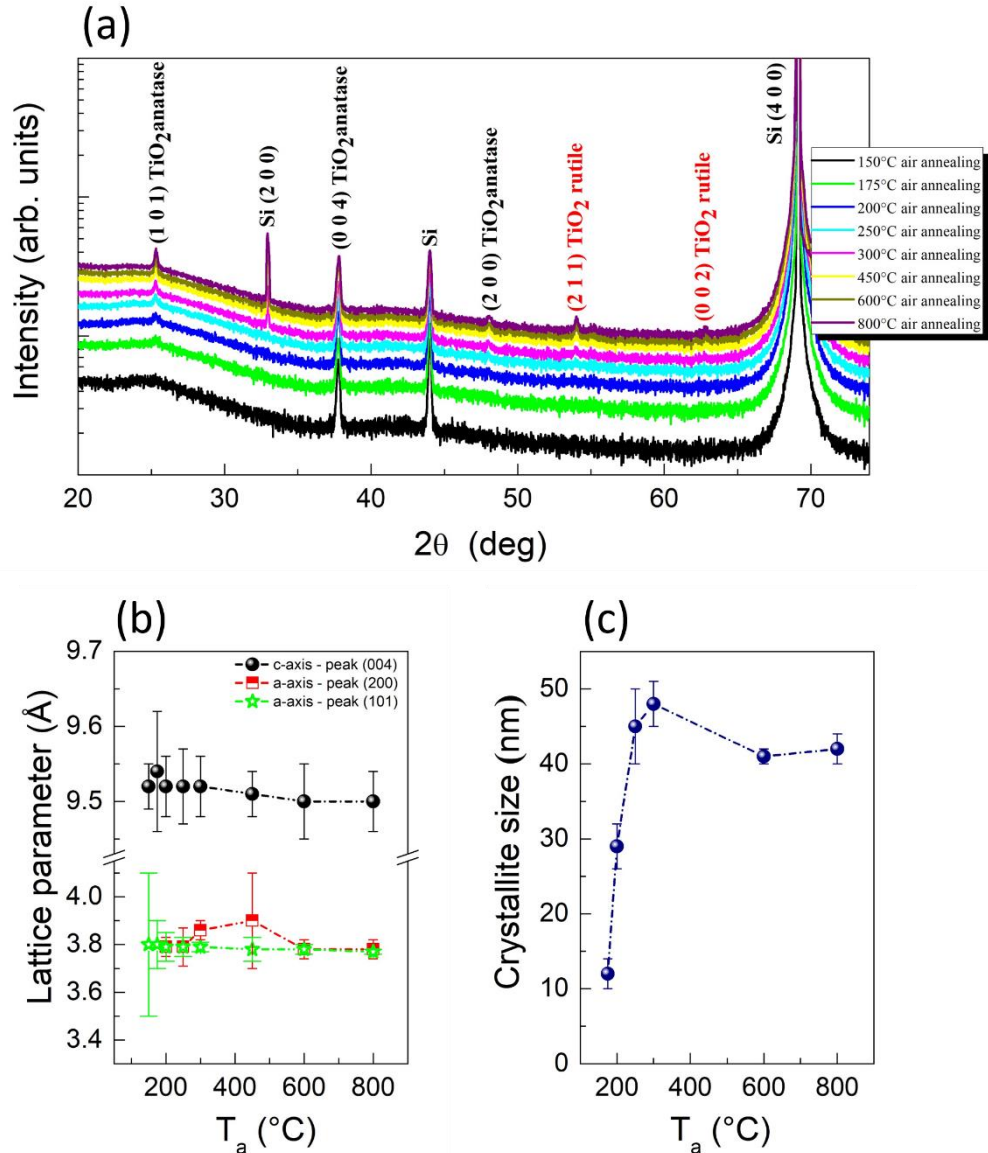


Figure 4: (a) XRD spectra of TiO₂-200 nm annealed in air at different temperatures; (b) *c* and *a=b* lattice parameters as function of T_a; (c) crystal size as a function of T_a, as obtained from a Debye-Scherrer analysis. The XRD measurements were acquired with a Philips X-Pert MRD diffractometer, and θ -2 θ scans are done with time/step of 100 s, 2 θ step of 0.02°, and 2 θ angle in the range from 20° to 75°.

All the others XRD spectra of TiO₂-200 nm, annealed in oxygen and in vacuum at different temperatures were acquired with lower resolution and are shown in Figures 5(a) and (b), respectively. Figure 5(a) displays the XRD spectra of the samples annealed in oxygen at different T_a values in the range 100-800 °C. As previously show, the occurrence of the anatase phase starts at 150 °C, when the (101) reflection shows up. The (004) and (200) reflections appear above 300 °C, together with the rutile (211) reflection, indicated by the red dashed line in the figure. Instead, Figure 5(b) displays XRD spectra acquired in vacuum at different T_a in the range 250-800 °C. In this case, the occurrence of the anatase phase, (101) reflection (~25.2°), is found at 300 °C, as already mentioned.

Starting from 350 °C, both the (004) and (200) anatase reflections and the (211) rutile phase appear, see the red dashed line. At 800 °C, the (111) rutile reflection is also observed. For the sake of completeness, also the XRD spectra of TiO₂ annealed in air [Figure 5(c)] is reported to determine the percentages of anatase and rutile discussed in the following. The spectra in this panel reveal the same information content of Figure 4(a).

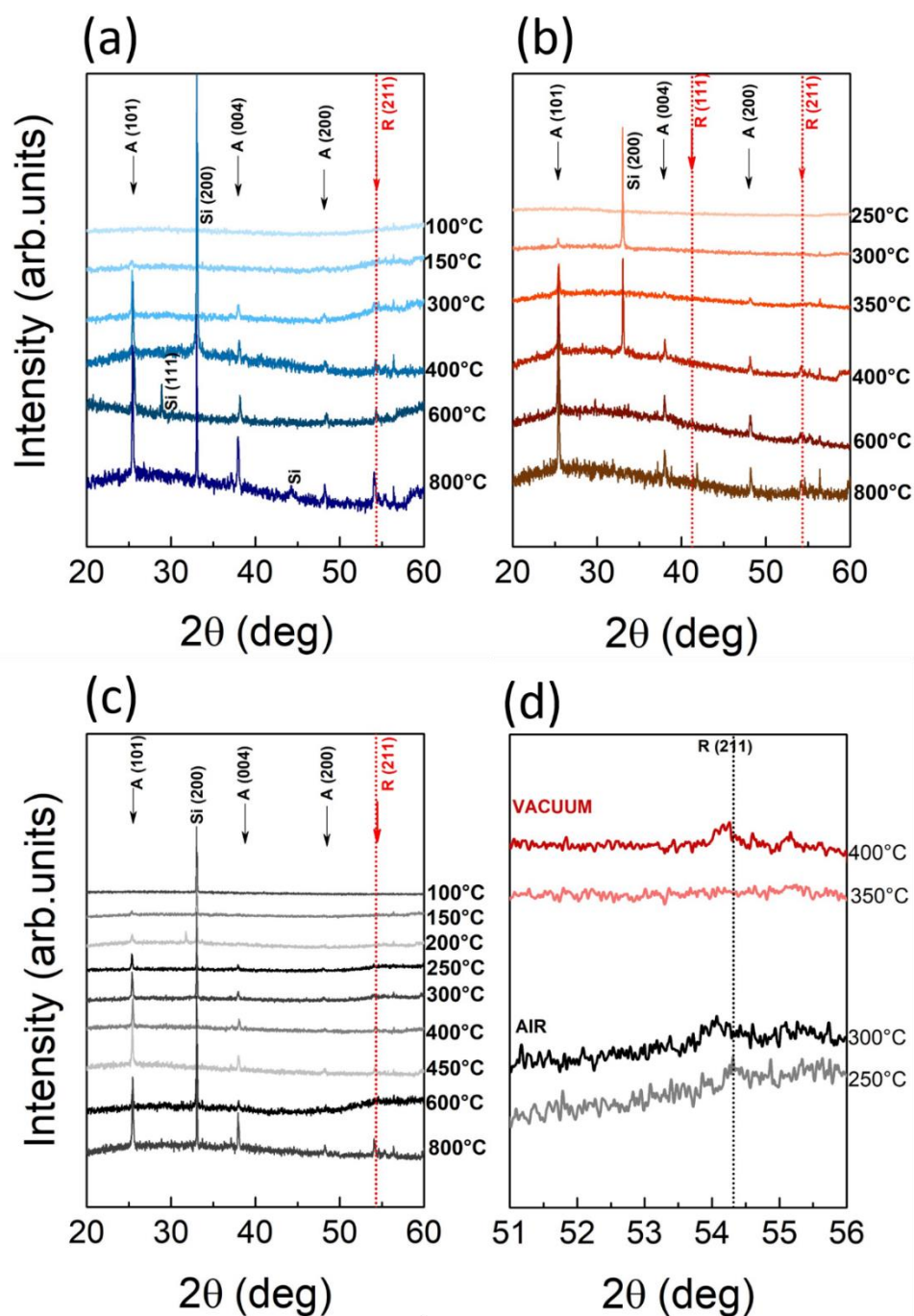


Figure 5: XRD spectra of 200 nm TiO₂ sample annealed in (a) oxygen, (b) vacuum, and (c) air for 12 h at different temperatures. (d) Zoom of XRD spectra annealed in air, at 250 (gray) and 300 °C (black), and in vacuum, at 350 (pink) and 400 °C (red). Symbols A and R refer to the anatase and rutile phases, respectively. All XRD spectra are acquired with a Bruker diffractometer with a time-step of 1 s and a 2θ step of 0.02°, and an offset along the y-axis is applied.

Finally, panel (d) shows that the rutile phase appears between 250 and 300 °C when the annealing is performed in air, with the anatase crystallizing at 150°C, whereas it appears between 350 and 400 °C when the annealing is done in vacuum, with the onset of the anatase at 300 °C.

More generally, it has been demonstrated that both the amorphous-to-anatase crystallization onset temperature as well as the anatase-to-rutile phase transformation depend on the annealing atmosphere, besides other factors such as synthesis method, level of impurities, doping, grain and particle size. Here, indeed, the earlier TiO₂ crystallization in air (150 °C to be compared to 300-350 °C [7]) is attributed to the peculiar particle agglomeration and porosity of the deposited TiO₂ film, which is affected by low material density. In addition to this, the amorphous-to-anatase phase transition of TiO₂ powders has been shown to anticipate by up to 200 °C if the annealing is performed in a pressurized sealed capillary, with respect to the atmospheric air, because of their different activation energies estimated in (10 ± 2) kJ/mol and (38 ± 5) kJ/mol, respectively [7]. Our findings corroborate these results, by exploring, instead, the difference between vacuum and saturated atmosphere (air or oxygen) and confirming the anticorrelation between annealing pressure and crystallization onset temperature: lower is the annealing pressure, greater is the probability of oxygen vacancy formation, higher is the crystallization onset temperature. Then, higher is the annealing pressure, higher is the probability of forming interstitial Ti atoms, which inhibit the structural relaxation of the atomic cell, delaying the phase transition from the anatase to the rutile [9,10]. In this framework, the rutile phase is thus expected to appear at lower temperature when TiO₂ is annealed in vacuum, compared to air and oxygen. Moreover, to extract quantitative information on XRD, the weigh fraction of rutile in thin films annealed in air, oxygen and vacuum, by using the Spurr equation, were estimated [11,12]:

$$W_{rutile} \% = \frac{1}{1+0.8 (I_{anatase}/I_{rutile})} \times 100\%, \quad (3)$$

where $I_{anatase}$ and I_{rutile} are the intensity of the strongest anatase and rutile phases, i.e., (101) and (211) reflections, respectively, extracted from XRD spectra shown in Figure 5(a-c). Fractions of rutile content normalized to the sum of the anatase and rutile for the TiO₂ thin films are report in Table 2.

Air	Phase	Rutile fraction air (%)	Rutile fraction vacuum (%)	Rutile fraction oxygen (%)
300 °C	A+R	13.7	-	20
400 °C	A+R	15.9	9.15	13.8
600 °C	A+R	24.3	6.5	17.6
800 °C	A+R	18.1	6.2	18

Table 2: percentage content of rutile at different temperatures in air, oxygen, and vacuum. A and R refer to the anatase and rutile phases, respectively.

The effects of the heat treatments on the morphology of the TiO₂ samples annealed in air, oxygen, and vacuum are investigated by using AFM technique.

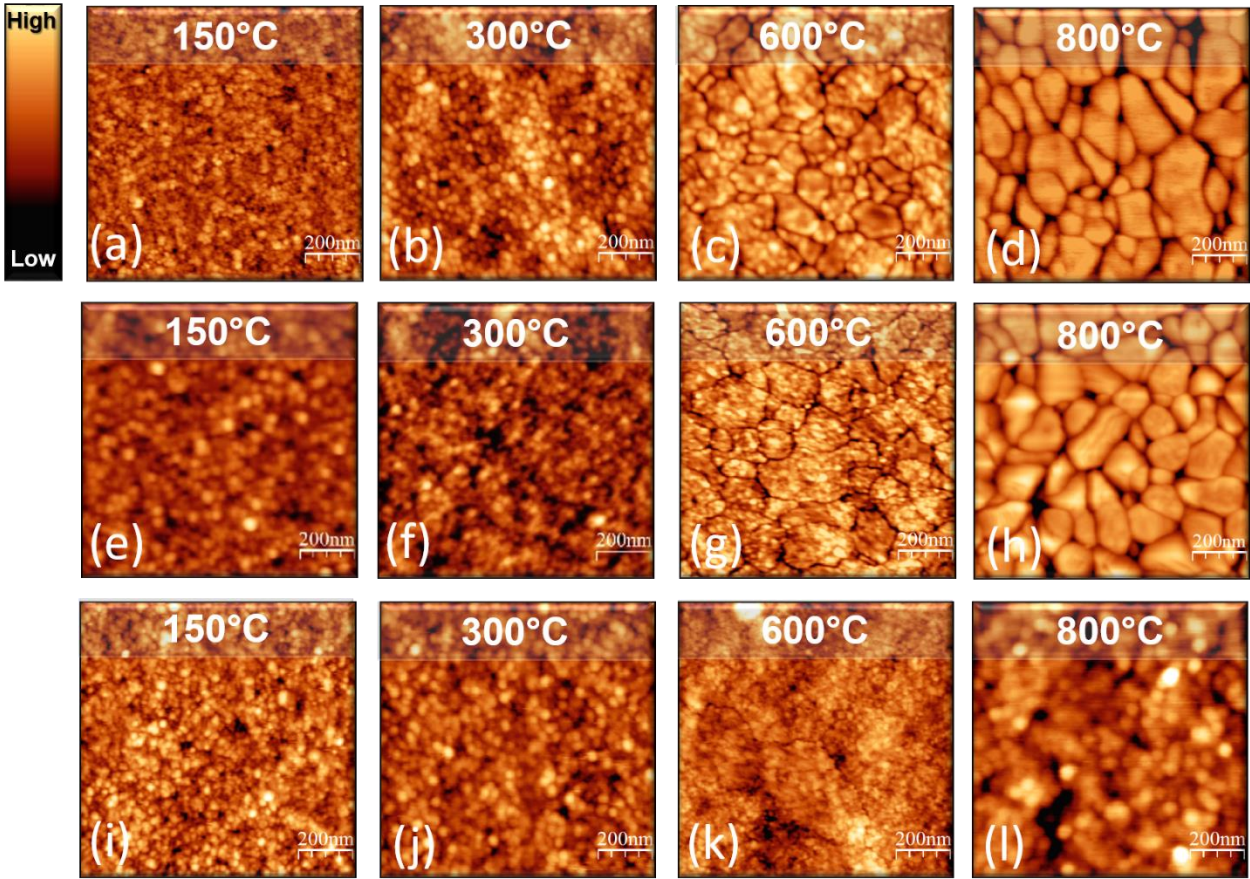


Figure 6: Tapping mode AFM topography, 1 μm x 1 μm in size, of TiO₂ annealed in air at: (a) 150, (b) 300, (c) 600, and (d) 800 $^{\circ}\text{C}$; annealed in oxygen at: (e) 150, (f) 300, (g) 600, and (h) 800 $^{\circ}\text{C}$; annealed in vacuum at: (i) 150, (j) 300, (k) 600, and (l) 800 $^{\circ}\text{C}$; The color scale ranges from 0 to 7 nm in (a), (b), (c), from 0 to 20 nm in (d), from 0 to 7 nm in (e), (f), and (g), from 0 to 45 nm in (h), from 0 to 6 nm in (i), (j), (l), and from 0 to 9 nm in (k).

Figure 6 shows representative AFM topographies acquired on a scan area of 1 μm x 1 μm for TiO₂ samples annealed in air at 150 (a), 300 (b), 600 (c), and 800 $^{\circ}\text{C}$ (d), in oxygen at 150 (e), 300 (f), 600 (g), and 800 $^{\circ}\text{C}$ (h), and in vacuum at 150 (i), 300 (j), 600 (k), and 800 $^{\circ}\text{C}$ (l). No changes of the granular surface texture have ever been measured, in any annealing environment provided that the temperature was kept below 300 $^{\circ}\text{C}$. By increasing the T_a , the material surface starts gradually to manifest a surface reorganization that appear to be strongly dependent on the annealing environment, and clearly visible at 600 $^{\circ}\text{C}$, and even more evident at 800 $^{\circ}\text{C}$. Indeed, while the sample annealed in vacuum preserves its granular morphology at any T_a up to 800 $^{\circ}\text{C}$, the heat-treatments in air and in oxygen cause the formation of large plates, separated by deep cracks, as shown in Figure 6(d) and (h), for air and oxygen, respectively.

These results are corroborated by the measure of RMS roughness extracted from AFM images, plotted in Figure 7 as a function of both annealing temperature and environments

(air, oxygen and vacuum). As shown in the figure, the RMS of all samples is almost constant up to 600 °C, specifically, the values stay below 1.5 nm for samples annealed in air and oxygen, and 1 nm for those annealed in vacuum. The yellow dot indicates the roughness of the as-grown sample. After annealing at 800 °C, the RMS significantly increase up to 4.5 nm, due to the formation of plates and cracks in the oxygen and air environments; instead, it remains lower than 1 nm for the samples annealed in vacuum still due to the perseverance of granular surface.

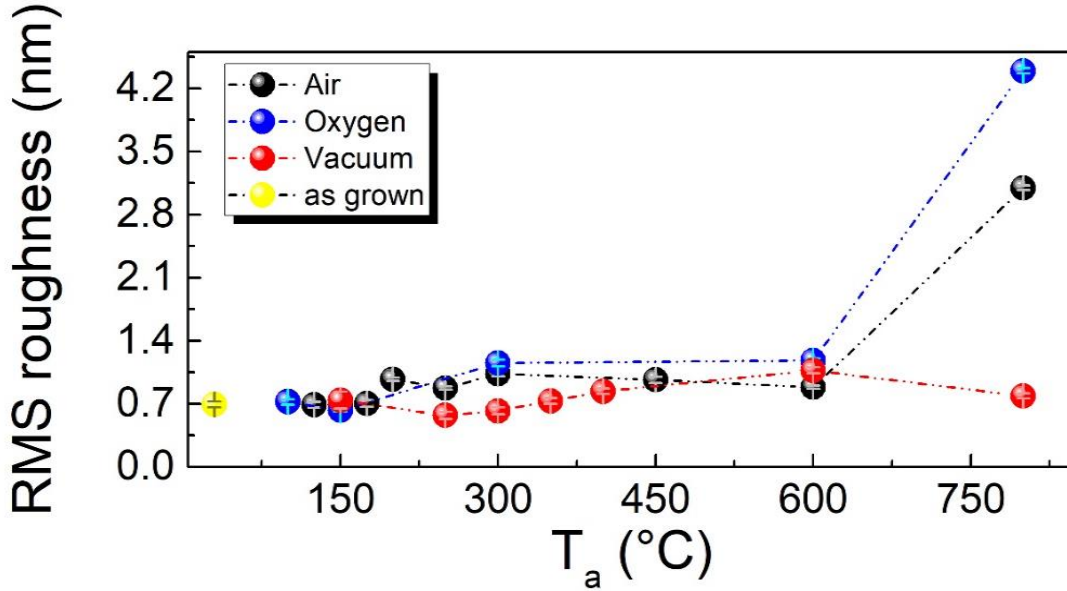


Figure 7: RMS roughness as a function of T_a in three (air, oxygen, and vacuum) annealing environments.

Moreover, the morphological features were also confirmed by FESEM images in Figure 8(a-c). As reported in Ref.[13], the formation of plates, separated by deep cracks, are a just simple manifestation of sintering during the crystallization evolution.

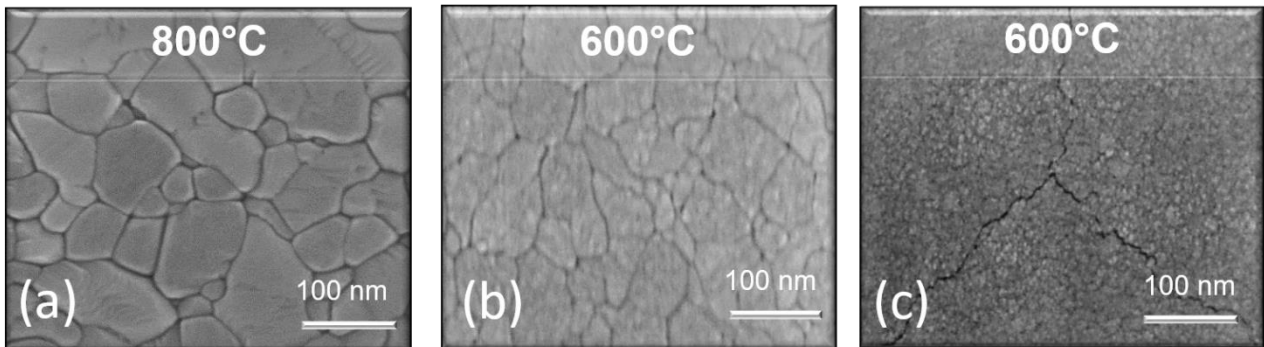


Figure 8: FESEM image of TiO_2 sample annealed in air at (a) 800 °C, in oxygen at (b) 600 °C, and in vacuum at (c) 600 °C. The scan areas are $1.4 \mu\text{m} \times 900 \text{nm}$.

Indeed, TiO_2 is a well-known low-temperature sintering material, and while for the majority of materials the sintering temperature is in the range $0.5 \div 0.9$ of the bulk melting

temperature [14], in the case of TiO_2 , the reported values of the sintering temperature spread of a much wider range of temperature usually lower than the expected one. Also, it has been show that sintering in TiO_2 can be induced by a different methodologies such as UV, infrared focused laser, high pressure, [15-17] in addition to the thermal process [18]. The sintering process is a consequence of the increase of the density of the material, thus producing large crystal grains separated by wide fractures.

The crystallization evolution has been also studied from a structural point of view, measuring the vibrational status that allows to investigate the local strain and chemical compositions of the samples. Indeed, the presence of strain has been studied by following the possible shifts of the E_g anatase Raman mode, as a function of both annealing temperatures and environments. In light of this, Figure 9(a-c) shows RS in a focused range of $100\text{-}200\text{ cm}^{-1}$ (where E_g is supposed to appear) for air, oxygen, and vacuum annealed samples, respectively.

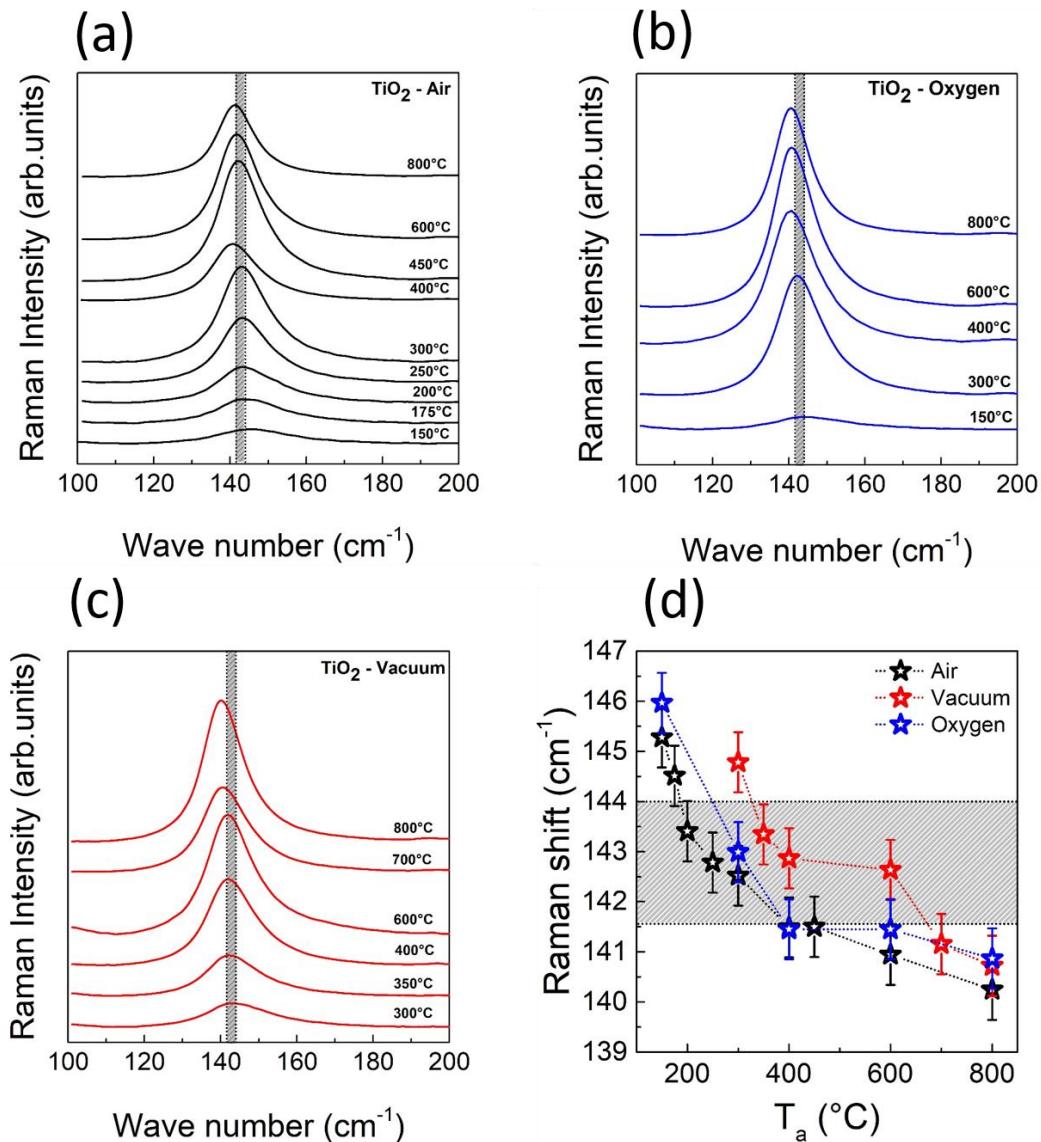


Figure 9: Raman spectra in the range $100\text{-}200\text{ cm}^{-1}$ of TiO_2 annealed in (a) air, (b) oxygen, and (c) vacuum. (d) Plot of the Raman shift as a function of T_a for samples annealed in air, vacuum, and oxygen. The gray region highlights the range where the E_g Raman mode is expected [19,20].

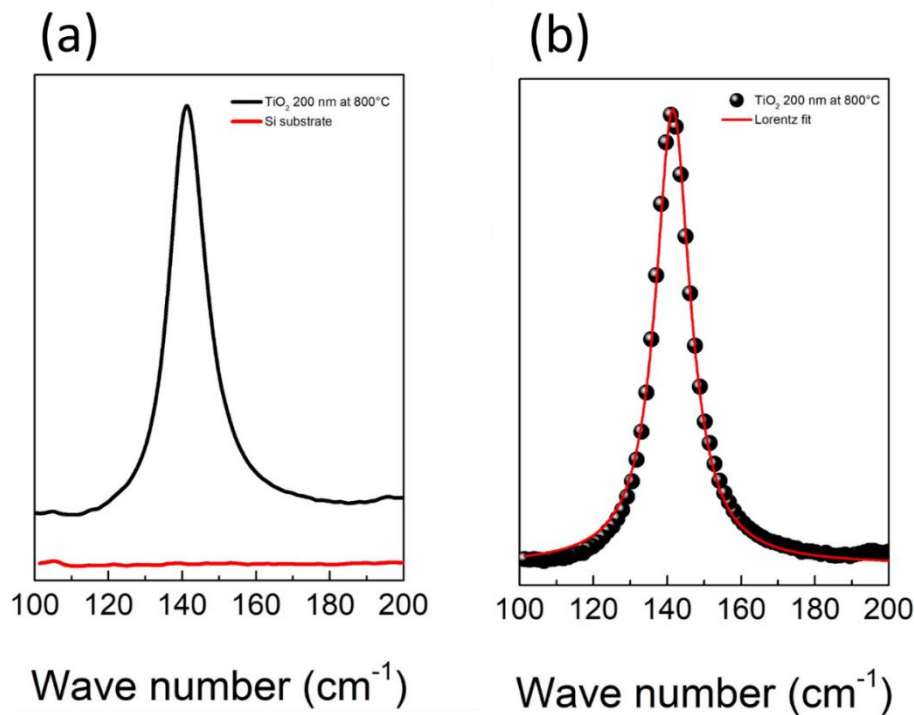


Figure 10: (a) Raw Raman data for TiO₂-200 nm film annealed at 800 °C in air (black curve) and Si substrate (red curve), in the range of interest (100–200 cm⁻¹) (b) Raman data of a TiO₂-200 nm film annealed at 800 °C in air (black scatters) after substrate subtraction and background normalization, and the correspondent Lorentz fit (red curve).

The behavior of the peak position as a function of T_a is shown in Figure 9(d), where black, red, and blue stars indicate the results for samples annealed in air, oxygen, and vacuum, respectively, and the gray shaded area indicates the range of expected wavenumbers for the E_g anatase Raman band [19,20]. In particular, a monotonic decrease of the E_g mode position is observed for all samples moving from wavenumbers that are blue-shifted compared to the expected E_g value at T_c , to a very tiny red-shift at the highest temperature ($T_a = 800$ °C).

Previous published results have pointed toward a relationship between a blue-shift of the E_g Raman vibrational mode and the size of anatase TiO₂ nanoparticles [21,22]. Those results are based on the Heisenberg uncertainty principle, which relates the phenomenon of phonon confinement within the nanoparticle with the appearance of a blue-shift of the characteristic Raman band, compared to the bulk one. It has been theoretically demonstrated that, in the approximation of spherical particles, the phonon is progressively more and more confined within the nanoparticles, as the sphere size decreases from 20 nm to 2 nm, producing a re-shaping of the correspondent vibrational band, whose peak results blue-shifted compared to the bulk value [23]. This effect is expected to be over when the characteristic particle size is ≥ 20 nm. In light of this, the first step was to relate the measured blue shift in TiO₂-200 nm to the size of the crystallites, as derived for the different annealing temperatures by performing a Debye-Scherrer analysis of high resolution XRD spectra reported in Figure 4(c). The results, based on the approximation of spherical crystalline grains, seem to indicate that, in the sample annealed in air, the

crystallites grow from ~12 nm to ~48 nm in size, in a temperature range of 150-300 °C. Herein, they reach a plateau and stays at ~42 nm up to 800 °C. The aforementioned temperature range of 150-300 °C fully agrees with the one showing a blue-shift of the E_g vibrational mode in the RS, even though the crystallites size seems to be compatible with the theory of phonon confinement only at the earliest stage of crystallization (150-200 °C), as shown also in Appendix A. Nevertheless, Zhang *et al.* have reported on the occurrence of blue-shift in TiO_2 nano-sheets with a thickness below 20 nm, but a lateral size well above this value (few μ ms), indicating that one dimension is enough to produce a quantum confinement effect [24]. In this case, a decrease of the blue-shift, very similar to the one reported in Figure 9(d), is measured as the thickness of TiO_2 moves from 3-layers to the bulk. This result is not surprising, since RS is a very well-known tool used to identify the layer number of 2D nanomaterials, such as graphene, MoS_2 and black phosphorus, based on the position in wavenumber of the corresponding Raman bands [25-27]. In addition to this, the comparison between the value of the blue-shift measured in TiO_2 -200 nm and the one measured in few-layers TiO_2 nanosheets [28] may shed light on the average thickness of the crystals, grew by the thermal treatment: when moving from 146 cm^{-1} (150 °C annealing) to 143 cm^{-1} (300 °C annealing) the correspondent thickness is expected to vary from 4 to 7 layers (~3.8 nm to ~6.7 nm, respectively, well inside the size range predicted for the phonon confinement phenomenon to take place).

It's worth mentioning that, in general, a blue-shift of the Raman vibrational mode can be also representative of a compressive stress inside the material. This effect can be neglected in this case, as primary affecting the E_g peak wavenumber. Indeed, since small crystallites grow inside an amorphous, at the beginning of crystallization, there is no reason for them to get compressed from the surrounding material. In any case, to address this point the lattice parameters of the TiO_2 atomic cell were evaluated, as extracted from high-resolution XRD as a function of T_a [see Figure 4(b)], and no sensitive variations representative of any strain were found as a function of the heat treatments. However, in the case of a polycrystalline thin film, compressive or tensile strains, being macroscopic quantities depending on the deposited film, have to be determined not measuring the lattice parameters, but by using different analysis [29].

On the other hand, a tensile strain sets up at the highest annealing temperatures, which causes the vibrational band to be red-shifted with respect to the expected value, as shown in Figure 9(d). As the E_g Raman mode is caused by symmetric stretching vibration of the O-Ti-O bond, in the in-plane directions [30], a progressive phase transition from anatase to rutile, as well as the coexistence of the two phases, as proved by the XRD analysis in Figure 5, can lead to the deformation of the TiO_2 octahedra, thus affecting the position of the Raman bands.

To get further insights into the crystallization dynamic occurring in the 200 nm sample annealed in air, RS as a function of annealing time was performed. Here, multiple heat-treatments were performed on the same sample, by fixing $T_a = 150\text{ °C}$, and gradually increasing the annealing time. The first annealing was performed for 10 minutes, followed by 30-minute step annealing until a maximum total annealing time of 12 h (720 minutes) was reached, as the one performed in the previous experiment (see Figure 11). RS was

performed after each thermal step, and the first sign of crystallization was found after 160-minute annealing total. Figure 11(a) plots representative Raman spectra as a function of annealing time, in the spectral region of interest (100-200 cm^{-1}). Figure 11(b) shows the behavior of the E_g peak center vs time. In this plot, different scatters refer to different sampled areas, explored with RS after each annealing step. A very well-defined blue-shift of the E_g peak, compared to the bulk value, is measured, with a decreasing trend, in time, from $\sim 148.5 \text{ cm}^{-1}$ (160-minute annealing) toward $\sim 146 \text{ cm}^{-1}$ (720-minute annealing). In the inset, the average value of the E_g peak, per each annealing time, is shown and fitted by an exponentially decaying function (black dashed line). The best fit is found by using a decay constant $t' = (87 \pm 11) \text{ min}$ and a saturation value $(145.98 \pm 0.09) \text{ cm}^{-1}$, at $t \gg t'$.

The rapid decrease of the Raman shift in the range 160 - 310 min, highlighted by the gray shaded area, indicates a rapid and progressive growth of the size of the TiO_2 crystallites, while remaining under the quantum size approximation. After 310-minute (~ 5 -hour) annealing, the crystals almost reached a critical size (typical of the annealing conditions), and they seem no longer affected by any longer annealing. The saturation value of the E_g peak coincides with the one found after a single step 12-h annealing [Figure 9(d)]. As done before, one can estimate in four TiO_2 mono-layers, the average thickness of the thermal-induced crystals, by comparing the E_g peak wavenumber with the one reported by Zhang *et al.* [28].

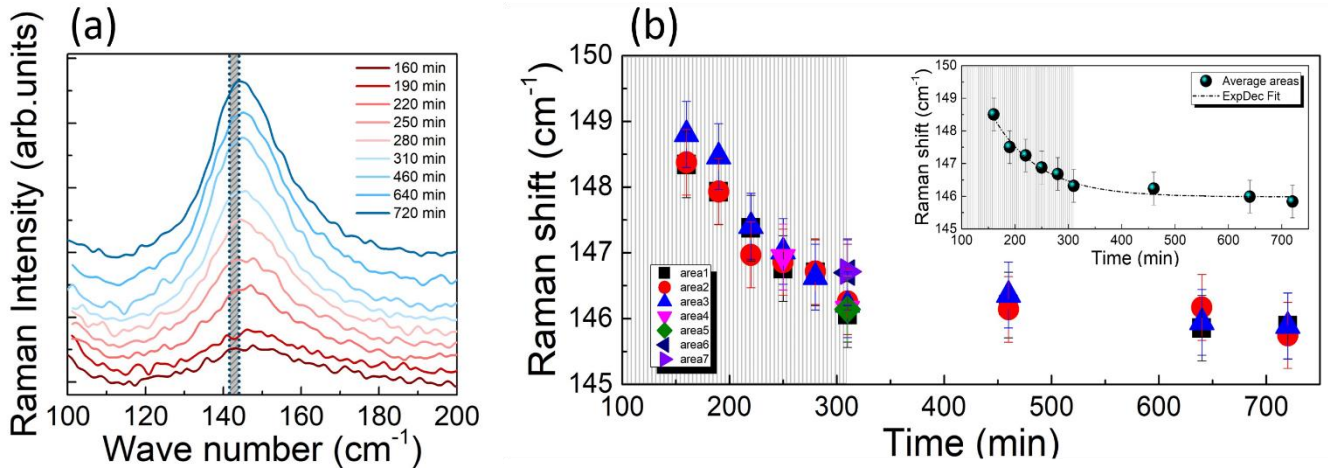


Figure 11: (a) Raman spectroscopy of 200-nm sample at different annealing times, in the range 100-200 cm^{-1} . The gray highlighted region indicates the expected range for the E_g Raman mode. (b) Raman shift as a function of the annealing time for 200-nm sample occurs at 150 $^{\circ}\text{C}$. The colored scatters represent the different areas of the same sample probed with a Raman spectroscopy. Inset: Raman shift as a function of the annealing time for 200-nm sample at 150 $^{\circ}\text{C}$. The black spheres refer to average on the different areas investigated. The dashed line indicates an exponential fit.

Information on the crystallization dynamic can be derived from the plot of FWHM of the E_g anatase mode as function of T_a . Indeed, the trend of FWHM can give general information on the degree of crystallization (the broader the peak, the lower is the crystallization degree), apart from the degree of disorder [31] (FWHM increases as the

disorder increases), non-stoichiometry effects [32], presence of oxygen vacancies [24], and phonon confinement [33].

The linewidth Γ , as well as Eg peak position, is extracted from the Lorentzian fit and corrected by the instrumental broadening, estimated as [35]:

$$\Gamma = FWHM_{TiO_2} - \frac{FWHM_{Si}^2}{FWHM_{TiO_2}}, \quad (4)$$

where $FWHM_{TiO_2}$ is the FWHM of the TiO_2 measured for each spectrum, and $FWHM_{Si} = 3.46 \text{ cm}^{-1}$.

In general, the theory of a spectral line shape of crystal lattice vibrations (or phonons), in a dispersive medium, predicts the line shape to be Lorentzian and its linewidth, a parameter describing the damping effect, to be inversely proportional to the lifetime of the phonons. While in the case of an ideal harmonic crystal, the line shape is expected to be infinitesimally narrow, the experimental evidence shows that the Raman linewidth always has a finite width, indicative of the presence of decay channels, which shorten the phonon lifetimes [30, 36-37].

From the energy-time uncertainty relation [34] one obtains a relation including the phonon lifetime:

$$\frac{1}{\tau} = \frac{\Delta E}{\hbar} = 2\pi c\Gamma, \quad (5)$$

where ΔE is the uncertainty in the energy of the phonon mode, \hbar is the reduced Planck constant, c is the light speed, and Γ is calculated from the Equation (4) in units of cm^{-1} .

The mechanisms of Phonon lifetime shortening are mainly due to two contributions: i) perturbation of the crystal symmetry attributed to impurities and/or defects with a characteristic decay time τ_I ; ii) anharmonic decay of a phonon into other Brillouin zone phonons, with a characteristic decay time τ_A . Then, the total phonon lifetime τ can be written as [34]:

$$\frac{1}{\tau} = \frac{1}{\tau_I} + \frac{1}{\tau_A}. \quad (6)$$

The separation of the two contributions is generally nontrivial, and can be obtained, for example, with a variable-temperature RS.

Figures 12(a-b) show Γ and τ as a function of T_a and environments, respectively. In all the investigated cases, an almost monotonic increase of τ is observed with the annealing temperature that can be related to the evolution of crystallization, which gradually

densifies the material and reduces the number of scattering centers. In particular, the phonon lifetime of samples annealed in air and oxygen is the same at any T_a , inside the experimental error, and longer than the one of the samples annealed in vacuum. This behavior is attributed to the higher density of oxygen vacancies, produced when performing the annealing in vacuum. The latter, indeed, interfere with the translational symmetry of the atomic lattice, and therefore, disturb the characteristic life of the propagating phonon, acting as intrinsic impurities [38].

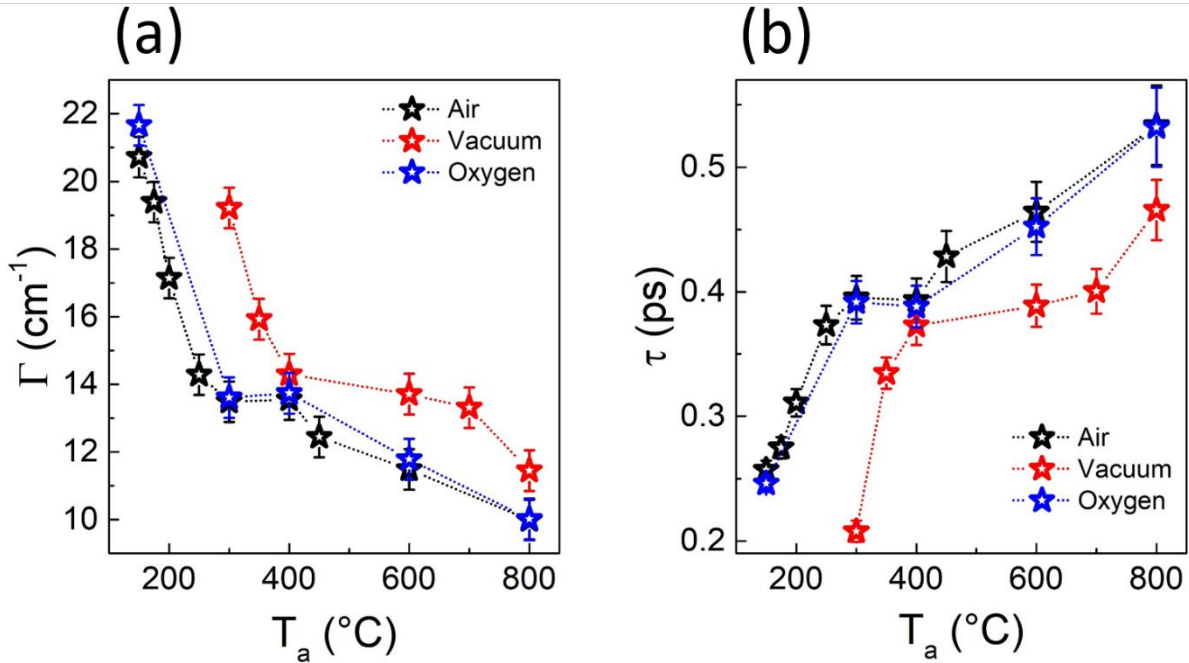


Figure 12: (a) Linewidth Γ values and (b) phonon lifetime τ as a function of T_a for the samples annealed in air, vacuum and oxygen (black, red, and blue stars, respectively).

3.3 Study of TiO_2 surface photo voltage versus environment

The photocatalytic properties of TiO_2 samples annealed in different environments can be measured through the SPV by using KPFM. Photocatalysis depends on both the intrinsic properties of the catalysts (photo absorption, charge generation and separation) and contact properties with the medium (photo charge transportation or reactions). Consequently, the photocatalytic activity results can be directly correlated to the SPV [39].

The SPV monitors the Contact Potential Difference (V_{CPD}) between two materials during dark-light variation [40], i.e., $V_{CPD} = \frac{W_{probe} - W_{sample}}{e}$, where W_{probe} and W_{sample} are the work functions of the probe (PtIr AFM probe) and the sample, respectively, and e is the elementary charge.

The estimate of W_{sample} comes from a good calibration of the AFM probe on a well-known material (usually Au or HOPG), to extract W_{probe} . In these measurements, Gold (Au) was used, because, being a noble metal, is less prone to oxidation, adsorption, and chemical reactions than low-work-function metals.

The contact potential difference V_{CPD} (Au) between the tip and Au is then measured first, and the work function of the probe is found as:

$$W_{probe} = e V_{CPD} (Au) + W_{Au}. \quad (7)$$

Given $W_{Au} = 5,3 \text{ eV}$ from literature, and from the Gaussian fit of the VCPD (Au) distribution shown in Figure 13, and extracted from a KPFM map, one finds $V_{CPD} (Au) = (-0,067 \pm 0,005) \text{ V}$.

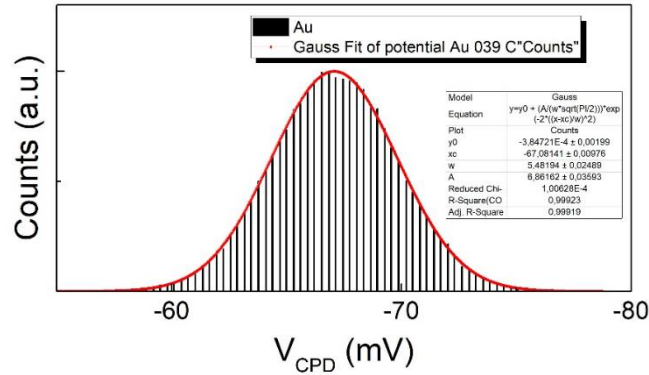


Figure 13: V_{CPD} distributions of the Au sample acquired in dark conditions.

Then, the estimated value for the work function of the tip is $W_{probe} = (5,233 \pm 0,005) \text{ eV}$ that is close to the reference value [41]. This experiment has been carried out in dark but the value of W_{tip} is typically assumed to be unchanged before, during, and after illumination, i.e., $W_{probe}^{Dark} \approx W_{probe}^{UV}$ [42].

Once W_{probe} is known, and sample's V_{CPD} is measured, one can estimate the sample work function as :

$$W_{sample} = W_{probe} - e V_{CPD} (sample). \quad (8)$$

Moreover, by measuring the work function of the sample in dark conditions, W_{dark} , and under UV-lighting, W_{UV} , the SPV can be measured as:

$$SPV = \frac{W_{UV} - W_{dark}}{e} = V_{CPD}(UV) - V_{CPD}(dark), \quad (9)$$

that is not affected by possible inaccuracies in W_{probe} measure.

Figure 14(a) shows V_{CPD} maps, on a scan area of 500 nm x 1 μ m in lateral size, acquired on the as-grown TiO₂; here, top and bottom panels represent the V_{CPD} as acquired in dark conditions and under UV-lighting, respectively. In order to favor the direct comparison between V_{CPD} maps, the same color scale was used with contrast ranging from 200 to 370 mV. The correspondent V_{CPD} distributions are plotted in Figure 14(b) as dark- and light-green histograms, for dark and UV-light conditions, respectively. By performing a Gaussian fit, such distributions are centered at 241 and 353 mV for dark and UV conditions, respectively, with a standard deviation of 6 mV, confirming the spatial uniformity of V_{CPD} in both samples. Then, this gives a surface photovoltage of $SPV = (112 \pm 12)$ mV.

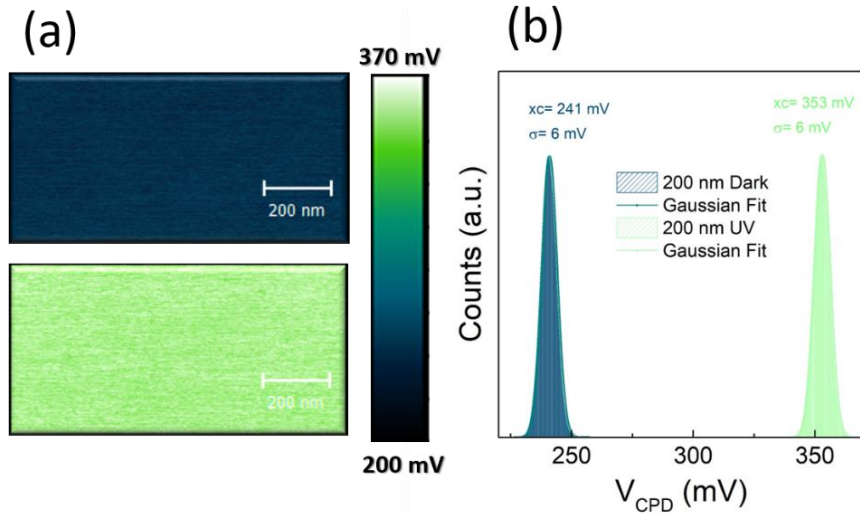


Figure 14: KPFM of as-grown TiO₂: (a) VCPD maps in dark conditions (top) and under UV-lighting (bottom). Scan size is 500 nm x 1 μ m. The color scale ranges from 200 to 370 mV, for both panels. (b) Correspondent VCPD distributions extracted from a statistic of 256 x 256 pixels equally distributed on 1 μ m x 1 μ m scan areas and fitted by a Gaussian function.

A positive SPV corresponds to a reduction of work function when the sample is lighted by UV radiation, compared to the dark case. This behavior can be attributed to the release of adsorbed species from the sample's surface of intrinsically n-doped semiconductors (as TiO₂), due to a local surface discharge [43]. Indeed, when a sample is lighted with radiation having an energy close, or bigger, than its band gap, the formation of electron-hole pairs, with the electrons jumping from the valence band to the conductance band and the holes moving at the opposite, is induced. Near to the surface, the free holes in the valence band move upward along the band bending, which is always present at the semiconductor surface, and discharge the negatively charged species adsorbed. Then, the

W_{UV} is the most accurate measurement of the TiO₂ intrinsic work function, being W_{dark} generally affected by surface pollutants.

Similarly, KPFM experiments have been performed on all the samples annealed in air, oxygen, and vacuum at 300, 600 and 800 °C, in order to identify the effect of thermal annealing in different environments on SPV of TiO₂. The KPFM measurements of these samples are shown in Figure 15, 16, and 17. For all figures, the panels (a) represent the V_{CPD} maps, 500 nm x 1 μm in lateral size acquired in dark (top) and under UV-lighting (bottom) for the samples annealed in air. The panels (c) are the V_{CPD} maps for the samples annealed in oxygen, again, dark and UV-lighting cases are shown in the top and bottom images, respectively. Panels (e) show the V_{CPD} maps acquired in dark (top) and under UV-lighting (bottom) for the samples annealed in vacuum. Each color scale refers to a specific sample. Then, panels (b,d,f) show Gaussian histograms, extracted from V_{CPD} maps of TiO₂ annealed in air, oxygen, and vacuum, respectively.

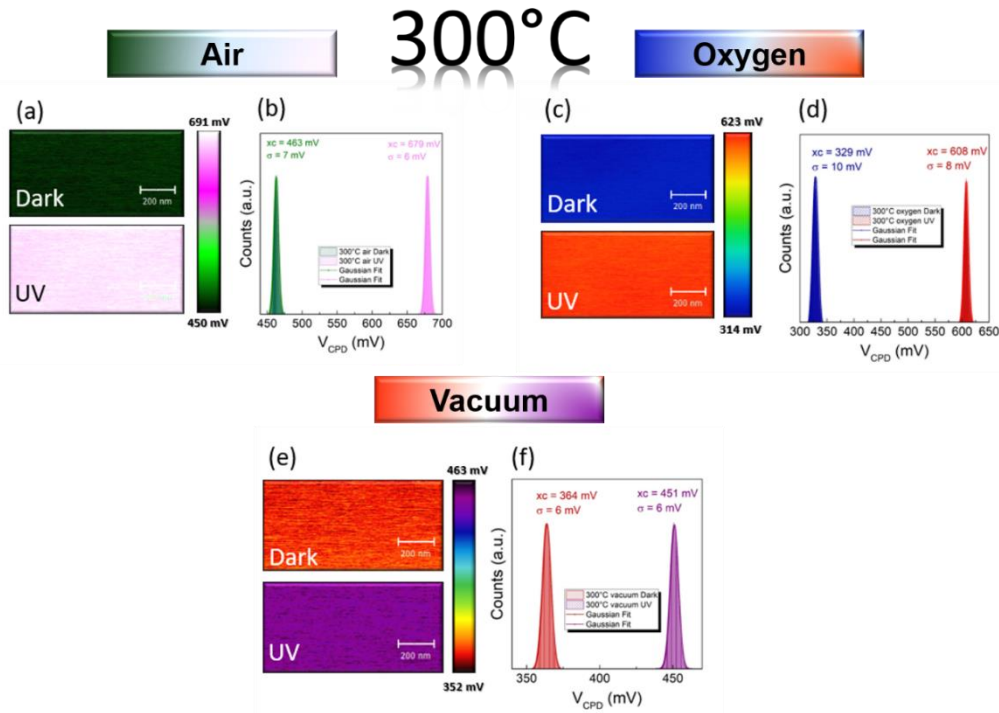


Figure 15: TiO₂ annealed at 300 °C in air (a,b), oxygen (c,d), and vacuum (e,f). Specifically, (a,c,e) KPFM maps, in the dark (top) and under UV-lighting (bottom), and (b,d,f) V_{CPD} distributions, in the dark (left peak) and under UV-lighting (right peak).

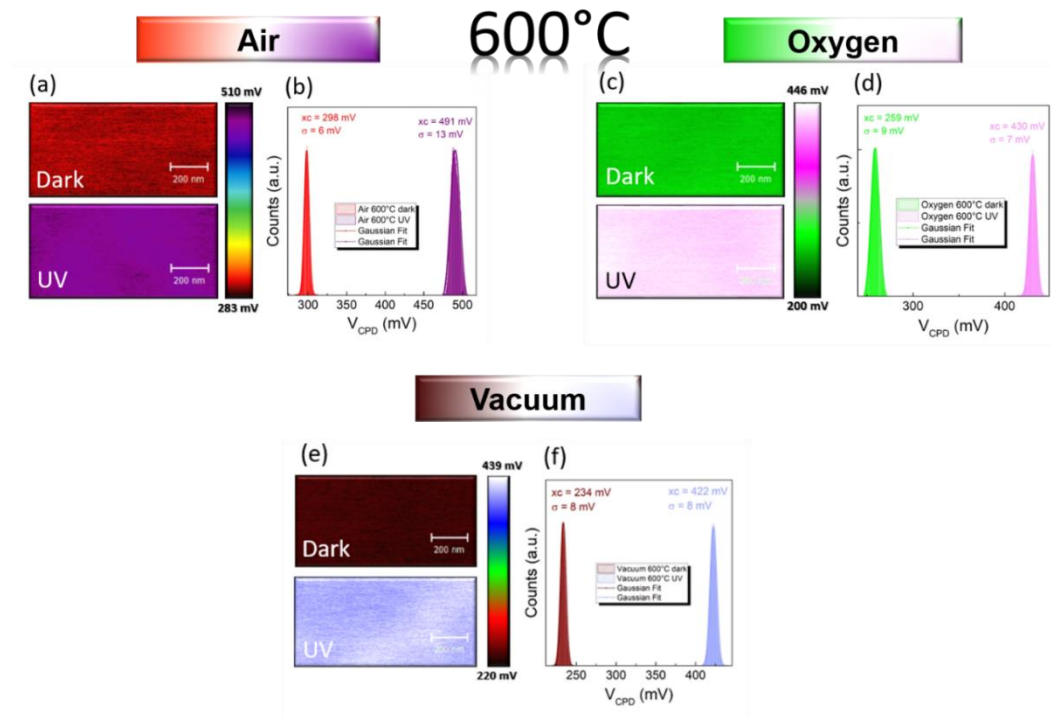


Figure 16: TiO_2 annealed at 600°C in air (a,b), oxygen (c,d), and vacuum (e,f). Specifically, (a,c,e) KPFM maps, in the dark (top) and under UV-lighting (bottom), and (b,d,f) V_{CPD} distributions, in the dark (left peak) and under UV-lighting (right peak).

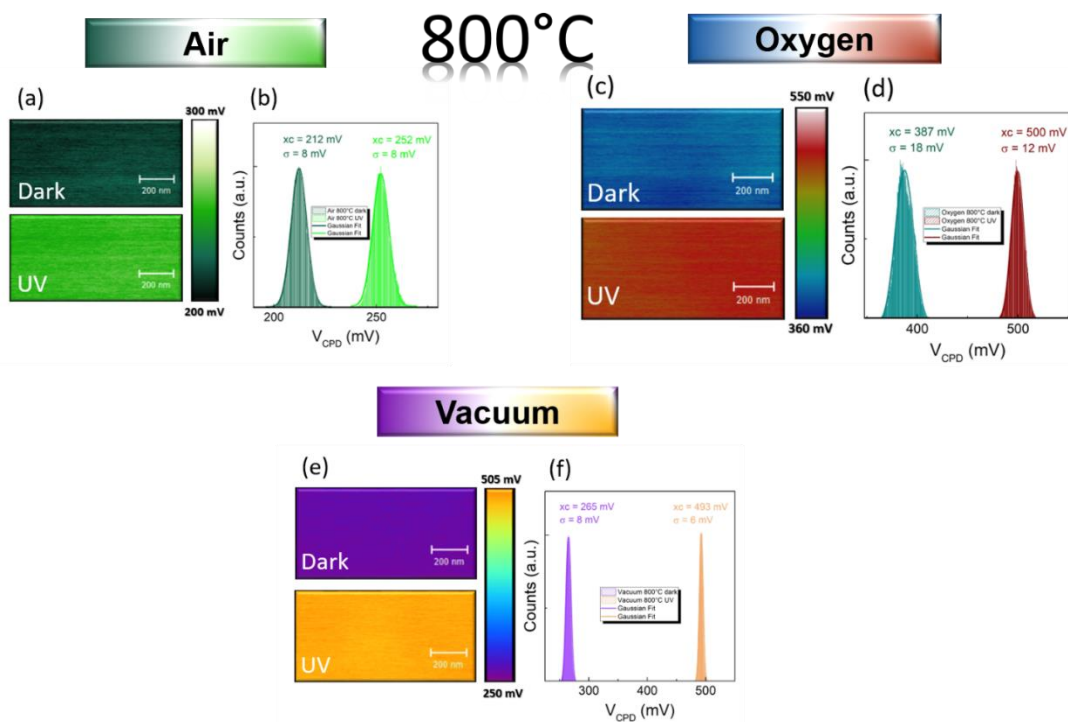


Figure 17: TiO_2 annealed at 800°C in air (a,b), oxygen (c,d), and vacuum (e,f). Specifically, (a,c,e) KPFM maps, in the dark (top) and under UV-lighting (bottom), and (b,d,f) V_{CPD} distributions, in the dark (left peak) and under UV-lighting (right peak).

From these results, the values for W_{dark} , W_{UV} , and SPV of all samples annealed in air, oxygen, and vacuum at different temperatures, are extracted and listed in Table 3.

TiO₂ Sample	W_{sample} - Dark (eV)	W_{sample} - UV (eV)	V_{CPD} - Dark (mV)	V_{CPD} - UV (mV)	SPV (mV)
annealed at 300°C in air	(4.770 ± 0.012)	(4.554 ± 0.011)	(463 ± 7)	(679 ± 6)	(216 ± 13)
annealed at 300°C in oxygen	(4.904 ± 0.015)	(4.625 ± 0.013)	(329 ± 10)	(608 ± 8)	(279 ± 18)
annealed at 300°C in vacuum	(4.869 ± 0.012)	(4.782 ± 0.012)	(364 ± 6)	(451 ± 6)	(87 ± 12)
annealed at 600°C in air	(4.935 ± 0.011)	(4.742 ± 0.018)	(298 ± 6)	(491 ± 13)	(193 ± 19)
annealed at 600°C in vacuum	(4.999 ± 0.013)	(4.811 ± 0.013)	(234 ± 8)	(422 ± 8)	(188 ± 16)
annealed at 600°C in oxygen	(4.974 ± 0.014)	(4.803 ± 0.012)	(259 ± 9)	(430 ± 7)	(171 ± 16)
annealed at 800°C in air	(5.021 ± 0.013)	(4.981 ± 0.013)	(212 ± 8)	(252 ± 8)	(40 ± 16)
annealed at 800°C in oxygen	(4.846 ± 0.023)	(4.733 ± 0.017)	(387 ± 18)	(500 ± 12)	(113 ± 30)
annealed at 800°C in vacuum	(4.968 ± 0.013)	(4.740 ± 0.019)	(265 ± 8)	(493 ± 6)	(228 ± 14)

Table 3: W_{dark} , W_{UV} , and SPV for samples annealed in air, oxygen, and vacuum at 300, 600, and 800 °C.

These results are reported in Figure 18(a, b) and 19(a) where W_{dark} , W_{UV} , and SPV are plotted as a function of the annealing temperature and environment. The black, red, blue, and green stars are used to indicate the as-grown sample, and after annealing in air, oxygen and vacuum, respectively.

As shown in Figure 18(a) and (b), the main effect of thermal annealing is a reduction of the intrinsic (W_{UV}) work function and that masked by the presence of surface adsorbed species (W_{dark}). Indeed, W_{dark} is a function of the total exposed surface area and porosity, besides the density of n-type dopant defects such as oxygen vacancies, and interstitial Ti. Therefore, a proper comparison of the intrinsic material work function is done by investigating the behavior of W_{UV} [Figure 18(b)]. Generally, the discrepancy of work function values measured in different annealing environments can be addressed to: (i) formation of oxygen vacancies, (ii) formation of interstitial Ti atoms, (iii) surface morphology, and iv) crystallization.

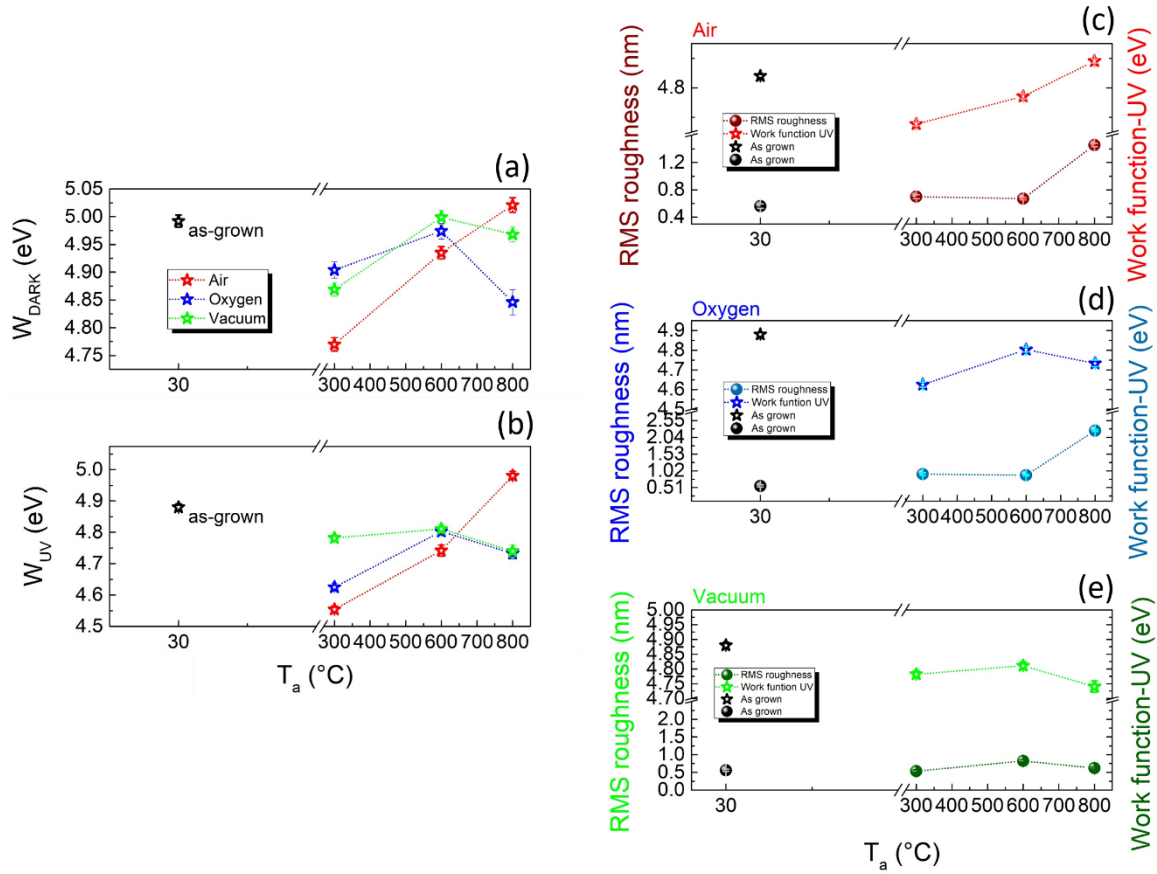


Figure 18: Work function as a function of T_a of the samples annealed in air, oxygen, and vacuum in the dark (a) and under UV-lighting (b). (c) Work function UV and RMS roughness for sample annealed in (c) air, (d) oxygen, and (e) vacuum.

In light of this, after the thermal treatment at 300 °C, the change in work function is expected to be dominated by the presence of oxygen vacancies for vacuum annealed samples, by the amorphous-to-anatase structural transition for samples annealed in air and, finally, by both amorphous-to-anatase transition as well as higher density of interstitial Ti (that seems to be favored in oxygen rich environments [44,45]) for oxygen annealing. According to this, the W_{UV} (300 °C) of the samples annealed in air and in oxygen are quite close to each other. A larger difference is observed when they are compared to that of the sample annealed in vacuum, where the highest density of oxygen vacancies is expected. At 600 °C, the W_{UV} of all the samples seems to reconcile. Indeed, at this temperature, they have all undergone an amorphous-to-crystalline transition and all samples show the coexistence of anatase and rutile phases, even though in different percentage.

The W_{UV} at 800 °C shows a more complicated behavior: while W_{UV} increases for the sample annealed in air, an inverted trend for both TiO₂ annealed in oxygen and vacuum is shown. Compared to the sample annealed in air, a higher density of oxygen vacancies is expected in the vacuum annealed sample, and a higher density of interstitial Ti atoms in the oxygen-annealed TiO₂. Oxygen vacancies and interstitial Ti may give rise to a

similar unsaturated bonding effect with electronic donor nature, with direct consequences on the material work function. The presence of n-type dopants introduces additional states in the bandgap close to the minimum of the conductance band causing the Fermi level to move upward. As the Fermi level increases in energy, the work function decreases, in good agreement with the measured trend. Moreover, the obtained results are comparable with both anatase and rutile work functions, respectively [46,47].

It worth stressing that, as our samples are highly polycrystalline, the measured W_{sample} gives an information that is mediated over all the exposed crystalline faces, without crystallographic distinction.

From literature [48], the work function seems to be correlated to the surface roughness of the materials. Indeed, it is known that the surface roughness has an important effect on the physical, chemical, electronic as well as mechanical properties [49], and many authors have investigated the correlation between surface morphology and work function, showing different results for different materials, in which work function increased/decreased with the increase of surface roughness [48, 50,51].

In light of this, Figures 18 (c-e) show both W_{UV} , and RMS roughness as a function of the annealing temperatures for samples annealed in air, oxygen, and vacuum, respectively. The RMS roughness has been analyzed avoiding the empty spaces (cracks) present in the morphologies, especially in presence of crystalline plates. In panel (a) and (c), the W_{UV} , and RMS roughness correlate, both increasing (decreasing) by increasing the annealing temperature. Different situation is observed for the sample annealed in oxygen environment. In this case, W_{UV} , and RMS roughness counter-correlate, with the RMS behaving as in the other samples. Note that the increase in RMS roughness is due to the formation of crystalline grains. In Ref. [48] the authors correlate the work function with the presence of microstructures (microcracks, holes, grooves, bulges, defects) that produce a rough surface. In this case, the bulgy element brings a weak repulsive force, resulting in an enhanced accumulation of charges at such spots, which is consistent with the Fowler-Nordheim field emission theory [52].

When the surface is smoother, instead, as in the case of vacuum annealing (see Figure 6) the charges are uniformly distributed on the surface, generating evenly-distributed electrostatic field [48].

Moreover, Figure 19(a) displays the behavior of SPV as a function of annealing temperature and environment. It is worth mentioning that all the measured SPVs are positive, thus corresponding to a reduced work function when the sample is lighted by UV radiation, because of surface adsorbates release. The behavior of SPV can be correlated to (i) exposed surface area for projected area, (ii) density of n-type dopants (oxygen vacancies and interstitial Ti), and iii) formation of mixed-crystalline phases of TiO_2 . While the first defines the availability of sites on the material's surface for the environmental species to get physisorbed, the second introduces almost-free charge carriers that stabilize the physisorbed oxygen species at the sample surface, as reported in Ref. [7]. In this framework, the higher the surface area for projected area, the greater

is the surface site availability and larger is the number of n-type dopants, so higher is the probability of stabilizing an oxygen species at the surface.

The SPV of the sample annealed in vacuum increases monotonically with the annealing temperature, while the surface area for projected area remains almost constant [Figure 19(b)]. The measured SPV trend is thus only addressable to the increase in n-dopants, due to the enhancement of oxygen vacancies. On the contrary, the surface area for projected area increases monotonically after the annealing in air and oxygen, anticorrelating with the SPV in both cases. Nevertheless, the SPV of the sample annealed in air stays bigger than the one annealed in vacuum, indicating in the latter a higher concentration of n-type dopants, consistently with the expectation of preferential formation of interstitial Ti atoms in oxygen rich environments.

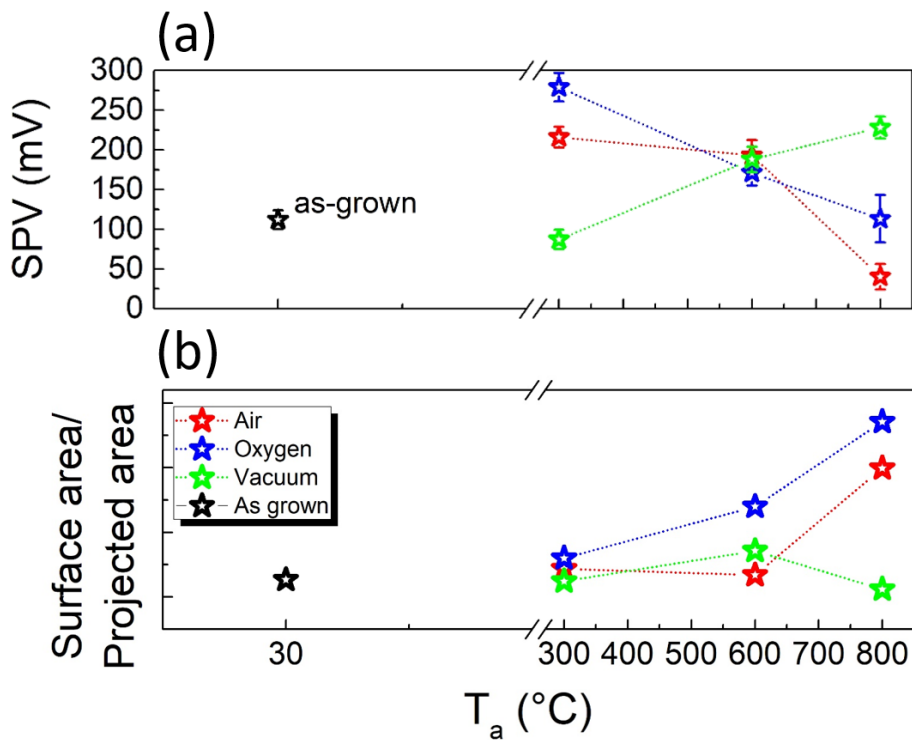


Figure 19: Surface photovoltage, SPV, (a) and ratio of surface area and projected area (b), as a function of T_a of the samples annealed in air, oxygen, and vacuum. The black star indicates the as-grown sample.

Finally, the SPV can be correlated to the formation of mixed anatase-rutile phases in TiO_2 . For samples annealed in air and in oxygen, the highest value of SPV is observed at 300 °C, where both crystalline anatase and rutile phases are measured by XRD (Figure 5). Indeed, as shown in Table 2, the percentage of rutile is 13.7 and 20 wt% for samples annealed in air and oxygen, respectively. Instead, samples annealed in vacuum exhibits a maximum SPV value at 800 °C with 6.2 wt% of rutile crystalline phase. Our results support the Refs. [53,54] in which photocatalytic activity is improved by both high annealing temperature and a certain amount of anatase and rutile phases. Anyway, the

highest value of the SPV and then the photocatalytic activity, is reached from samples annealed at 300 °C in oxygen, whereas the amorphous as-grown samples show a low value of SPV due to the high density of atomic defects and impurities, confirming the results found in literature [55,56].

Summary

This chapter focuses on the investigation of 200-nm TiO₂ thin films deposited on Si substrate, annealed at different annealing temperatures and environments (air, oxygen, and vacuum). The first section, called *Study of as-grown TiO₂*, studied the amorphicity of the as-grown sample, by means of XRD and RS, resumed also by the surface. Indeed, the morphology is made by amorphous particles, typical of room temperature deposition, with a measured size of (88 ± 19) nm, and an average RMS roughness of (0.87 ± 0.06) nm.

In the second section, called *Study of TiO₂ crystallization onset and evolution versus environment*, the amorphous-anatase and anatase-rutile transitions were investigated, by using XRD and RS, in three different environments. In particular, the T_c of the anatase phase is found in the range 100-150 °C for the samples annealed in air and in oxygen, and 250-300 °C for the samples annealed in vacuum. This occurs because the oxygen rich-environment inhibits the oxygen vacancies formation, and, on the contrary, in vacuum this formation is favored by breaking the binding bonds between oxygen and titanium, with oxygen release from the material. Instead, the rutile phase appears between 250 and 300 °C when the annealing is performed in air, whereas it appears between 350 and 400 °C when the samples are annealed in vacuum due different activation energies of the environments that lead a different probability of the oxygen formation. The phase transitions are observed also in the morphology, especially at high annealing temperatures, and can be related to the amount of anatase and rutile. A granular texture in the surface is preserved in any annealing environment at any temperature as high as 300 °C. Instead, at the highest annealing temperature different material reorganizations depending on the environment are observed. In particular, large plates separated by deep cracks, due to sintering phenomenon, are observed for samples annealed in oxygen and air, whereas a granular morphology is preserved in samples annealed in vacuum.

The crystallization evolution has been investigated with RS by looking at the peak position and the linewidth of the E_g mode. For all samples, at the crystallization onset a blue-shift is observed, which is related to the phenomenon of phonon confinement; this result is confirmed also by Raman measurements as a function of time. Then, all samples show a small red-shift at the highest temperature explored in this work (800 °C). Then, the phonon lifetime, which is inversely proportional to the linewidth, increases by increasing the annealing temperature according to the evolution of crystallization, which gradually densifies the material and reduces the number of scattering sites. In particular, the phonon lifetime of samples annealed in air and oxygen is longer than that of samples

annealed in vacuum due to the higher density of oxygen vacancies produced in this environment.

In the last section, called *Study of TiO₂ surface photovoltage versus environment*, the dependence of both annealing temperatures and environments on the TiO₂ photocatalytic activity were studied. First, the work function of the samples in dark, W_{dark} , and under UV-lighting, W_{UV} , conditions, and after SPV are measured. The last is correlated to (i) exposed surface area, (ii) density of n-type dopants (oxygen vacancies and interstitial Ti), and (iii) mixed-crystalline phases of TiO₂.

An increase of SPV as a function of annealing temperatures in vacuum is observed due to the increase in n-dopants for the enhancement of oxygen vacancies, while the surface area remains almost constant. A different behavior is observed for the samples annealed in air and oxygen. Indeed, the SPV decreases by increasing the annealing temperature and the surface area increases. Then, a maximum response of SPV is observed at 300 °C, for air and oxygen annealing, and at 800 °C, for vacuum annealing, due to probably the emergence of the mixed anatase-rutile phases. In conclusion, the photocatalytic performances are considerably affected by thermal treatments, annealing environments, and formation of both anatase and rutile crystalline phases.

References

1. Hadjoub, I., *et al.* Post-deposition annealing effect on RF-sputtered TiO₂ thin-film properties for photonic applications. *Applied Physics A* **2016**, *122*(2), 78.
2. SPIP. Available online: http://www.imagemet.com/WebHelp6/Default.htm#PnP1/Watershed_Packed_Features_detection_method.htm (accessed on 12 November 2021).
3. Colombi, P., *et al.* Self-assembled polystyrene nanospheres for the evaluation of atomic force microscopy tip curvature radius. *Measurement Science and Technology* **2009**, *20*(8), 084015.
4. Smith, K. *et al.* Effects of proton irradiation on structural and electrochemical charge storage properties of TiO₂ nanotube electrodes for lithium-ion batteries. *Journal of Materials Chemistry A* **2017**, *5*(23), 11815-11824.
5. Boda, M. A., Shah, M. A. Fabrication mechanism of compact TiO₂ nanotubes and their photo-electrochemical ability. *Materials Research Express* **2017**, *4*(7), 075908.
6. Iijima, K., *et al.* Influence of oxygen vacancies on optical properties of anatase TiO₂ thin films. *Journal of Luminescence* **2008**, *128*(5-6), 911-913
7. Albetran, H., Low, I. M. Parameters controlling the crystallization kinetics of nanostructured TiO₂—An overview. *Materials Today: Proceedings* **2019**, *16*, 25-35.
8. Cullity, B.D. *Elements of X-ray Diffraction*, Addison-Wesley Publishing, Boston, MA, USA, 1956.

9. Kim, D., *et al.* The origin of oxygen vacancy induced ferromagnetism in undoped TiO₂. *Journal of Physics: Condensed Matter* **2009**, *21(19)*, 195405.
10. Albetran, H., *et al.* Phase transformations and crystallization kinetics in electrospun TiO₂ nanofibers in air and argon atmospheres. *Applied Physics A* **2014**, *116(1)*, 161-169.
11. Spurr, R. A., Myers, H. Quantitative analysis of anatase-rutile mixtures with an X-ray diffractometer. *Analytical chemistry* **1957**, *29(5)*, 760-762.
12. Byrne, C., *et al.* New approach of modifying the anatase to rutile transition temperature in TiO₂ photocatalysts. *RSC advances* **2016**, *6(97)*, 95232-95238
13. Durante O., *et al.* Emergence and evolution of crystallization in TiO₂ thin films: A structural and morphological study, *Nanomaterials* **2021**, *11(6)*, 1409.
14. Chao, S., *et al.* Effects of sintering temperature on the microstructure and dielectric properties of titanium dioxide ceramics. *Journal of materials science* **2010**, *45(24)*, 6685-6693.
15. Schade, L., *et al.* Sintering of thin titanium dioxide nanoparticle films via photothermal processing with ultraviolet continuous-wave lasers. *Applied surface science* **2013**, *278*, 336-340.
16. Ming, L., *et al.* Selective laser sintering of TiO₂ nanoparticle film on plastic conductive substrate for highly efficient flexible dye-sensitized solar cell application. *Journal of Materials Chemistry A* **2014**, *2(13)*, 4566-4573.
17. Liao, S. C., *et al.* Theory of high pressure/low temperature sintering of bulk nanocrystalline TiO₂. *Acta Materialia* **1997**, *45(10)*, 4027-4040.
18. Keddie, J. L., Giannelis, E. P. Effect of heating rate on the sintering of titanium dioxide thin films: competition between densification and crystallization. *Journal of the American Ceramic Society* **1991**, *74(10)*, 2669-2671.
19. RRUFF. Available online: <https://rruff.info/chem=Ti,O/display=default/R070582> (accessed on 18 April 2021).
20. Allen, N.S. *et al.* The effect of crystalline phase (anatase, brookite and rutile) and size on the photocatalytic activity of calcined polymorphic titanium dioxide (TiO₂). *Polymer degradation and stability* **2018**, *150*, 31–36.
21. Rajender, G., Giri, P. K. Strain induced phase formation, microstructural evolution and bandgap narrowing in strained TiO₂ nanocrystals grown by ball milling. *Journal of Alloys and Compounds* **2016**, *676*, 591-600.
22. Golubović, A., *et al.* Raman study of the variation in anatase structure of TiO₂ nanopowders due to the changes of sol–gel synthesis conditions. *Journal of Sol-Gel Science and Technology* **2009**, *49(3)*, 311-319.

23. Arora, A. K., *et al.* Raman spectroscopy of optical phonon confinement in nanostructured materials. *Journal of Raman Spectroscopy* **2007**, *38*(6), 604-617.
24. Zhang, W. F., *et al.* Raman scattering study on anatase TiO₂ nanocrystals. *Journal of Physics D: Applied Physics* **2000**, *33*(8), 912.
25. Ferrari A. C., *et al.* Raman spectrum of graphene and graphene layers. *Physical review letters* **2006**, *97*(18), 187401.
26. Di Giorgio, C., *et al.* Nanoscale Measurements of Elastic Properties and Hydrostatic Pressure in H₂-Bulged MoS₂ Membranes. *Advanced Materials Interfaces* **2020**, *7*(23), 2001024.
27. Castellanos-Gomez, A. *et al.* Isolation and characterization of few-layer black phosphorus. *2D Materials* **2014**, *1*(2), 025001.
28. Zhang, Y., *et al.* Raman study of 2D anatase TiO₂ nanosheets. *Physical Chemistry Chemical Physics* **2016**, *18*(47), 32178-32184.
29. Welzel, U., *et al.* Stress analysis of polycrystalline thin films and surface regions by X-ray diffraction. *Journal of Applied Crystallography* **2005**, *38*(1), 1-29.
30. Tian, F., *et al.* Raman spectroscopy: a new approach to measure the percentage of anatase TiO₂ exposed (001) facets. *The Journal of Physical Chemistry C* **2012**, *116*(13), 7515-7519.
31. Balaji, S. Y. D. J. R., *et al.* Phonon confinement studies in nanocrystalline anatase-TiO₂ thin films by micro Raman spectroscopy. *Journal of Raman Spectroscopy* **2006**, *37*(12), 1416-1422.
32. Richter, H., *et al.* The one phonon Raman spectrum in microcrystalline silicon. *Solid State Communications* **1981**, *39*(5), 625-629.
33. Ager III, J. W., *et al.* Spatially resolved Raman studies of diamond films grown by chemical vapor deposition. *Physical Review B* **1991**, *43*(8), 6491.
34. Cuscó R., *et al.* Temperature dependence of Raman scattering in ZnO, *Physical Review B* **2007**, *75*(16), 165202.
35. Serrano, J., *et al.* Dispersive phonon linewidths: The E₂ phonons of ZnO. *Physical review letters* **2003**, *90*(5), 055510.
36. Klemens, P.G. Anharmonic decay of optical phonons. *Physical Review* **1966**, *148*, 845.35.
37. Maradudin, A.A. Theoretical and Experimental Aspects of the Effects of Point Defects and Disorder on the Vibrations of Crystals. *Solid State Physics* **1966**, *18*, 273–420.
38. Kazan, M., *et al.* Phonon dynamics in AlN lattice contaminated by oxygen. *Diamond and related materials* **2006**, *15*(10), 1525-1534.

39. Wang, B. H., *et al.* Surface photovoltage: an efficient tool of evaluation of photocatalytical activity of materials. *Advanced Materials Research* **2011**, 295, 614-617.
40. Kronik, L., Shapira, Y. Surface photovoltage spectroscopy of semiconductor structures: at the crossroads of physics, chemistry and electrical engineering. *Surface and Interface Analysis: An International Journal devoted to the development and application of techniques for the analysis of surfaces, interfaces and thin films* **2001**, 31(10), 954-965.
41. Lee, N. J., *et al.* The interlayer screening effect of graphene sheets investigated by Kelvin probe force microscopy. *Applied Physics Letters* **2009**, 95(22), 222107.
42. Zhang, F., *et al.* Ultraviolet photoemission spectroscopy and Kelvin probe measurements on metal halide perovskites: Advantages and pitfalls. *Advanced Energy Materials* **2020**, 10(26), 1903252.
43. D'Agostino, D., *et al.* Effects of cobalt substitution on ZnO surface reactivity and electronic structure. *Journal of Materials Chemistry C* **2019**, 7(27), 8364-8373.
44. Fang, D., *et al.* Effect of heat treatment on morphology, crystalline structure and photocatalysis properties of TiO₂ nanotubes on Ti substrate and freestanding membrane. *Applied Surface Science* **2011**, 257(15), 6451-6461.
45. Kim, D., *et al.* The origin of oxygen vacancy induced ferromagnetism in undoped TiO₂. *Journal of Physics: Condensed Matter* **2009**, 21(19), 195405.
46. Chen, J. B., *et al.* Field emission from the structure of well-aligned TiO₂/Ti nanotube arrays. *Thin Solid Films* **2009**, 517(15), 4390-4393.
47. Borodin, A., Reichling, M. Characterizing TiO₂ (110) surface states by their work function. *Physical Chemistry Chemical Physics* **2011**, 13(34), 15442-15447.
48. Xue, M., *et al.* Linear relation between surface roughness and work function of light alloys. *Journal of Alloys and Compounds* **2017**, 692, 903-907.
49. Khan, M. Z. H., *et al.* Effects of chemical treatment of indium tin oxide electrode on its surface roughness and work function. *Surface and Coatings Technology* **2014**, 244, 189-193
50. Li, W., Li, D. Y. On the correlation between surface roughness and work function in copper. *The Journal of chemical physics* **2005**, 122(6), 064708.
51. Song, G. L., Haddad, D. The topography of magnetron sputter-deposited Mg-Ti alloy thin films. *Materials Chemistry and Physics* **2011**, 125(3), 548-552.
52. He, J., Cutler, P. H., Miskovsky, N. M. Generalization of Fowler-Nordheim field emission theory for nonplanar metal emitters. *Applied physics letters* **1991**, 59(13), 1644-1646.

53. Li, H., *et al.* Enhanced photocatalytic activity of electrospun TiO₂ nanofibers with optimal anatase/rutile ratio. *Journal of the American Ceramic Society* **2011**, *94*(10), 3184-3187.
54. Carp, O., *et al.* Photoinduced reactivity of titanium dioxide. *Progress in solid state chemistry* **2004**, *32*(1-2), 33-177.
55. Sun, S., *et al.* Amorphous TiO₂ nanostructures: synthesis, fundamental properties and photocatalytic applications. *Catalysis Science & Technology* **2019**, *9*(16), 4198-4215.
56. Zou, J., *et al.* An amorphous TiO₂ sol sensitized with H₂O₂ with the enhancement of photocatalytic activity. *Journal of Alloys and Compounds* **2010**, *497*(1-2), 420-427.

Chapter 4

Structural and morphological characterization of TiO₂ vs thickness

This chapter will be focused on the tailoring of the TiO₂ thin film crystallization temperature (T_c), in the Anatase crystalline phase, by modulating its thickness from hundreds to few nm. Amorphous TiO₂ thin films have been fabricated by IAD to this aim, subsequently thermally treated in a controlled manner, and investigated by means of AFM, SEM, XRD, and RS. The first part of the chapter will be focused on the morphological and structural characterization of the as-grown amorphous samples, in terms of particle size and roughness, both showing a dependence on the sample thickness. XRD and RS are used to confirm their amorphicity. The second part will be dedicated to the study of the T_c versus thickness, while the third part will investigate the peculiar TiO₂ crystallization evolution as a function of both thickness and heat treatments. Finally, specific aspects of the lattice dynamics, such as the phonon lifetime, will be discussed, as a function of both the thickness and the annealing temperature, T_a .

4.1 Study of as-grown TiO_2 versus thickness

As-grown TiO_2 thin films, with nominal thickness of 5, 32, 64, 100, and 200 nm, deposited on an unheated (100) Si substrate, were first characterized by means of XRD and RS, to check their amorphicity, and by AFM to address the quality of the sample surface, in terms of morphology, particle size, and roughness, as a function of their thickness. Differently from the case discussed in Chapter 3, all samples were fabricated by using an electron-beam evaporator with the assistance of Argon and Oxygen plasma, in order to enhance the material uniformity and density, as well as their mechanical and optical properties (see Chapter 2 for technical discussions).

Preliminarily, the reliability in the thickness estimate of the as-grown samples was checked by both X-ray reflectivity (XRR) and profilometric measurements. For instance, Figure 1 shows an exemplary XRR curve acquired on a 5 nm-sample.

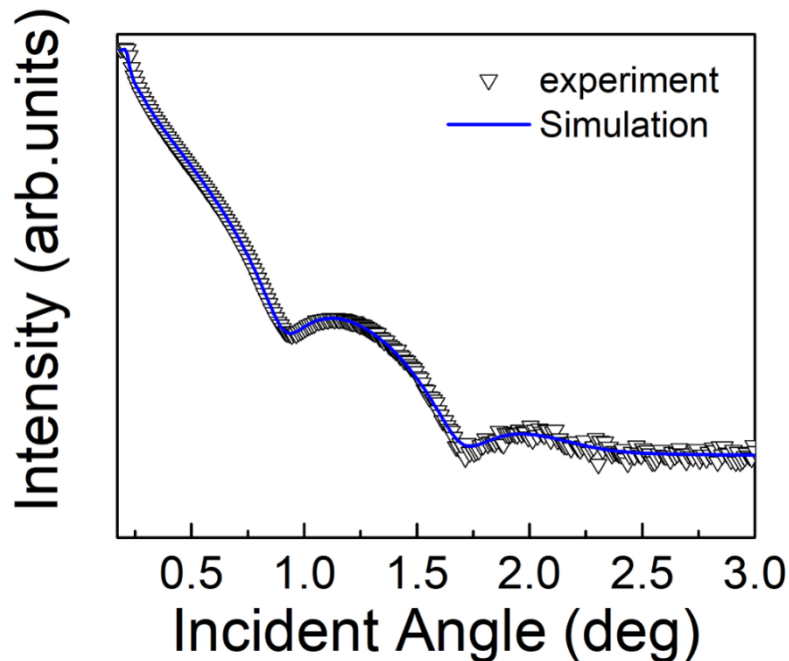


Figure 1: XRR curve of an as-grown TiO_2 -5 nm film (white scatters), fitted by the blue line. The experimental parameters used for the XRR measurement were: time step of 60 s, θ step of 0.01° , and θ range from 0.15 to 3° . Adapted from [1].

White scatters and blue line are the experimental data and the simulated curve, respectively. The latter was obtained by using the X'pert Reflectivity software [2,3]. The fit gives a total film thickness of (5.14 ± 0.02) nm and a density of (3.50 ± 0.03) g/cm^3 . Similarly, in the case of the nominal 100 nm-sample, the film thickness found under profilometric measurements was (98 ± 5) nm, thus confirming the precision and reliability of the fabrication machine used, in two different ranges of film thickness.

Figures 2(a,b) show the RS and XRD measurements, respectively, performed on all the as-grown samples. In both plots, black, red, green, blue, and cyan curves refer to a TiO_2 thickness of 5, 32, 64, 100, and 200 nm, respectively. All the Raman modes visible in Figure 2(a) are associated to the Si [4] substrate (as shown in Chapter 2). Similarly, only the reflections relative to the Si, at $2\theta = 62^\circ$ and 69.16° , are shown in the XRD spectra reported in the main panel of Figure 2(b), together with a broad bump in the 2θ range from 20° to 45° (zoomed in the inset) representative of the amorphous TiO_2 .

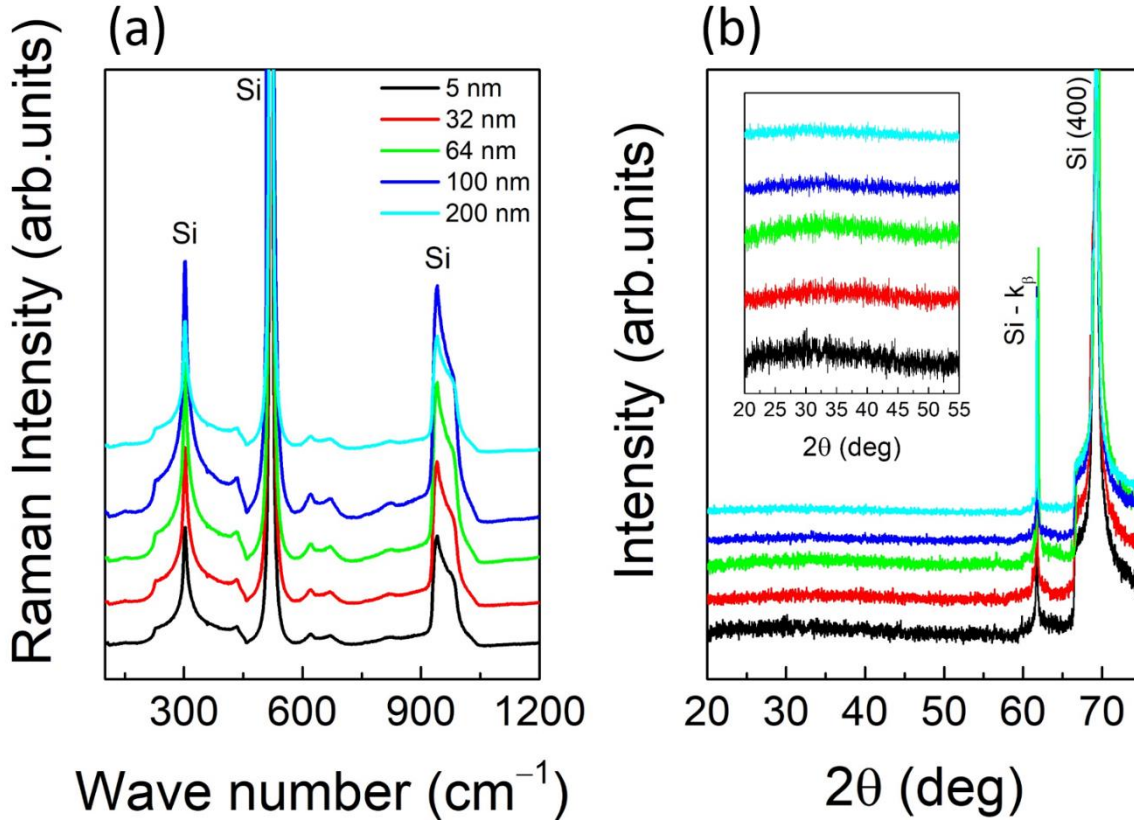


Figure 2: (a) RS spectra with wavenumber range from 100 to 1200 cm^{-1} . (b) XRD spectra with 2θ range from 20 to 75° (main) and from 20 to 55° (inset). Black, red, green, blue, and cyan curves refer to 5, 32, 64, 100, and 200 nm, respectively. The curves have been offset along the y-axis for better readability. The parameters used for the XRD spectra are: θ - 2θ scans with a time/step 0.2–0.6 s, a 2θ step of 0.02° , and a 2θ angle ranging from 20 to 75° by using a diffractometer from Bruker located in Chemistry Department. Instead, for the Raman spectra a 50X magnification, 10 s exposure time, 5% laser power, and 5 accumulations are used by means a Raman Spectrometer from RENISHAW equipped of red laser source (785 nm), located in Pharmacy Department. Adapted from [1].

Figures 3(a-e) show representative AFM morphologies, acquired in tapping mode with a SCM-PIT-V2 tip from Bruker, on a scan area of $1 \mu\text{m} \times 1 \mu\text{m}$ in lateral size, of the as-grown sample surface, as a function of the TiO_2 thickness, from 5 [Figure 3(a)] to 200 nm [Figure 3(e)]. The surface roughness is highlighted by using a black-to-white color scale, from a minimum value of 0 nm to a maximum of 5 nm. As one can see, the surface

is always made of particle agglomerations, more and more evident as the thickness increases.

For the sake of completeness, Figures 3(f-j) also show the AFM images acquired on larger scan areas ($10\ \mu\text{m} \times 10\ \mu\text{m}$), for all the investigated samples. Obviously, enlarging the lateral size causes a leak in the resolution of the tiniest details (as the amorphous particles), with the contrast being dominated by the overall (substrate-imprinted) roughness. As before, all the AFM maps were equalized to the same color contrast, from a minimum value of 0 nm to a maximum of 13 nm.

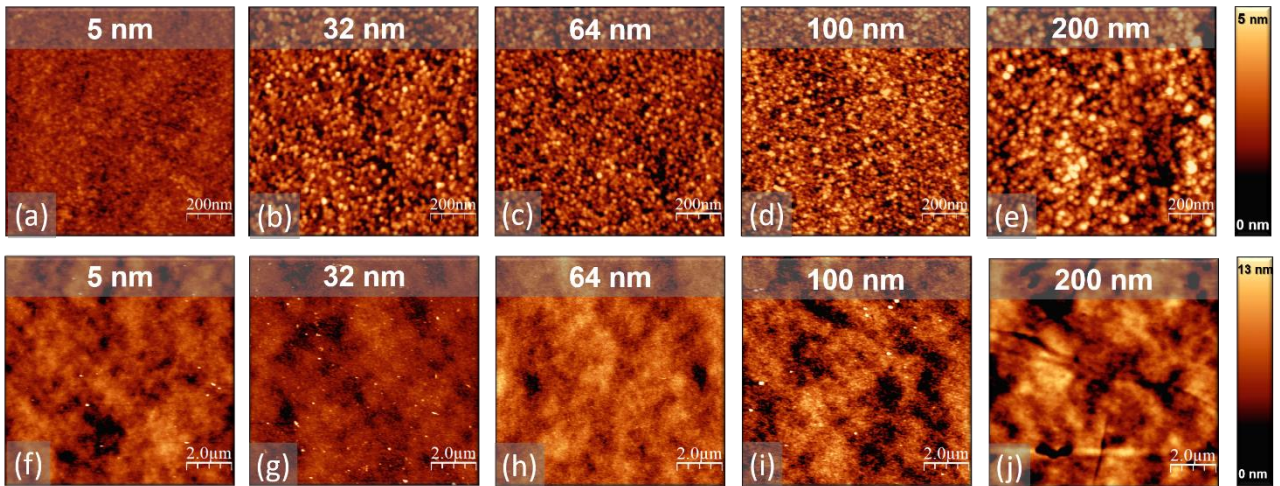


Figure 3: Tapping-mode AFM topography of as-grown TiO_2 sample, (a–e) $1\ \mu\text{m} \times 1\ \mu\text{m}$ and (f–j) $10\ \mu\text{m} \times 10\ \mu\text{m}$ in lateral size. Adapted from [1].

As done in the previous Chapter, a statistical analysis of $1\ \mu\text{m} \times 1\ \mu\text{m}$ AFM images was performed to analyze the dependence of both the particle size and the RMS roughness as a function of the TiO_2 thickness. Concerning to the particle analysis, 25 particle profiles per sample were analyzed, taking into account both the convolution between particle and tip size and the high packing density (as performed also in Chapter 3). The behavior of the measured and deconvolved particle size as a function of the sample thickness is shown in Figure 4(a) by reddish and bluish symbols, respectively. The plot displays a clear monotonic trend: in particular, the measured particle size ranges from (27 ± 5) nm, for the 5 nm sample, to (52 ± 8) nm, for the 200 nm one, while the deconvolved size particle extends from (22 ± 4) nm to (37 ± 3) nm. Thus, both measured and deconvolved particle size disclose an increasing trend as the thickness increases, which is consistent with the expected behavior, based on Ostwald ripening [6-8]. According with this theory, in the initial stage of thin film deposition on top of a substrate surface, ideally made by a uniform distribution of nucleation sites, atoms from the vapor phase condense on the substrate surface, entering the so called “adsorbed state”. In this phase, they can both detach again from the substrate or diffuse over the surface. During the diffusion they combine with

each other, giving rise to clusters of atoms. Each cluster can either grow or decay in size depending on the addition or detachment of adatoms. However, when a critical cluster (or particle) size is reached, the probability of expanding is greater than the one of decreasing. In fact, since the binding energy between surface atoms depends on the particle curvature, inversely proportional to its size, the detachment of an atom is more probable in smaller grains. Because of this, if two particles of different size are situated near each other there will be a gradient in the adatom density, creating a driving force for diffusion from the small particle to the large one. This process, results in a net decrease of smaller particles for a net gain of the larger ones, whose size growth will accelerate. Particle larger than the critical size are referred to as “stable”. From herein, such a stable grain can continue to grow, as the deposition proceeds, i) by keeping capturing adatoms from smaller particles; ii) by capturing additional atoms coming from the vapor phase; iii) by coalescing with each other to form, ultimately, the continuous thin film. Such a continuous growth in size, as well as their ultimate coalescence, is of course favored in longer depositions (thicker films), thus giving rise to bigger grains in thicker samples, justifying the behavior observed in Figure 4(a).

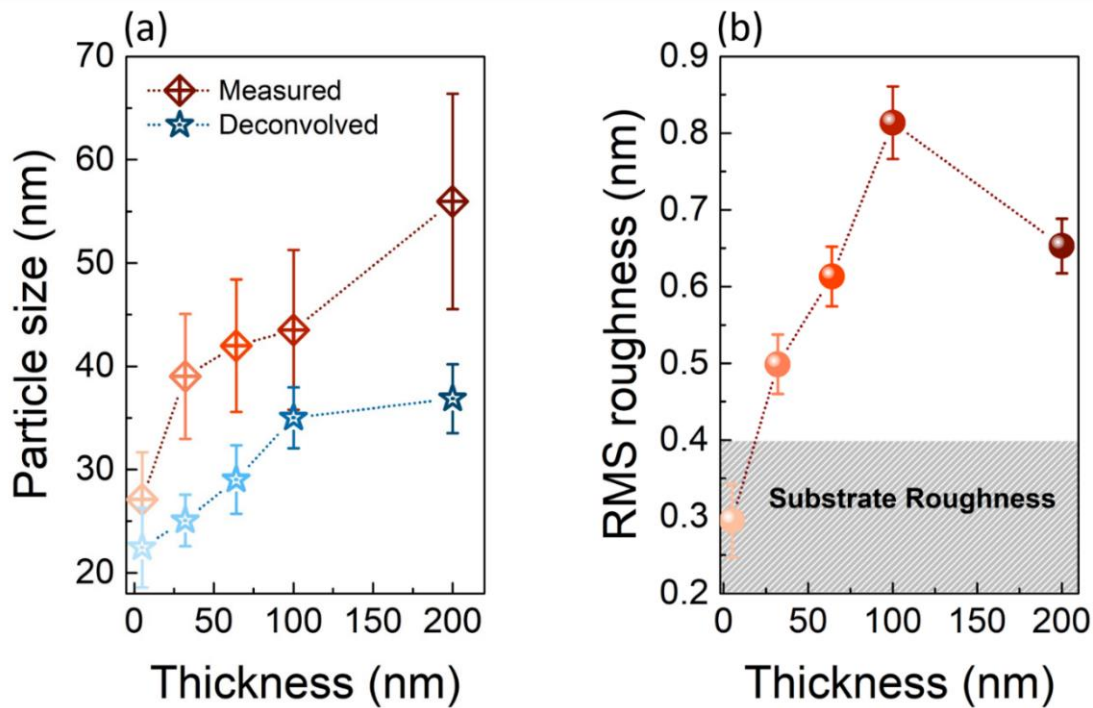


Figure 4: (a) Measured (reddish scatters) and deconvolved (bluish scatters) particle size, (b) average RMS roughness as a function of the TiO₂ thickness in the as-grown samples. Dashed lines are used both in (a,b) as a guide for the eye. In (b), the dashed grey area corresponds to the range of the measured Si substrate roughness. Adapted from [1].

Finally, Figure 4(b) shows the RMS roughness, calculated on several scan areas of 1 $\mu\text{m} \times 1 \mu\text{m}$, as a function of the TiO₂ thickness. As shown by the plot, the average measured RMS roughness increases by increasing the thickness, from (0.29 ± 0.05) nm for the 5 nm-sample, approaching in this case that of the substrate (indicated with the grey region

in figure), to (0.65 ± 0.04) nm for the 200 nm one. A tiny decrease in the RMS roughness is measured between the 100 and 200 nm samples, even if the difference in the correspondent RMSs is extremely small (~ 150 pm).

The use of the IAD technique has thus guaranteed: i) reliability in the sample thickness, as demonstrated by the XRR (see Figure 1); ii) a high coverage uniformity even for an ultra-thin deposition, as shown in the AFM image of the 5 nm sample [see Figure 3(a)] whose RMS roughness approaches the one of the substrate; iii) high surface flatness, because the RMS roughness remains always below 1 nm for all samples.

4.2 Study of TiO_2 crystallization onset versus thickness

This section explores the amorphous-crystalline phase transition, and the TiO_2 Anatase phase, after heat treatments performed in air. The as-grown TiO_2 thin films were heated with a rate of $3^\circ C/min$, up to a set temperature of 250, 300, 400, 450, 500, 600, 800, 1000 $^\circ C$, and left at fixed T for 12 h. Finally, they were cooled down to room temperature with a rate of $1^\circ C/min$. Also in this case, each single treatment has been performed on a pristine as-grown sample.

After the annealing process, XRD and Raman measurements were performed to investigate the early stage of the crystallization and thus the crystallization onset temperature, T_c . Figure 5(a) shows the XRD measurements performed at selected temperature in a 2θ range, enclosing the first anatase reflection, A(101), at $2\theta = 25.3^\circ$. Different colors refer to different TiO_2 thicknesses as clearly indicated in the plot and all curves were offset along the y-axis for a better visualization.

The A(101) peak, and thus the amorphous-anatase transition, appears between 750 and 800 $^\circ C$ (gray and black curves) for the 5 nm sample, between 300 and 350 $^\circ C$ (cyan and blue curves) for the 32 nm sample, and between 250 (light red, light green, and light pink) and 300 $^\circ C$ (red, green, and pink) for the 64, 100, and 200 nm samples.

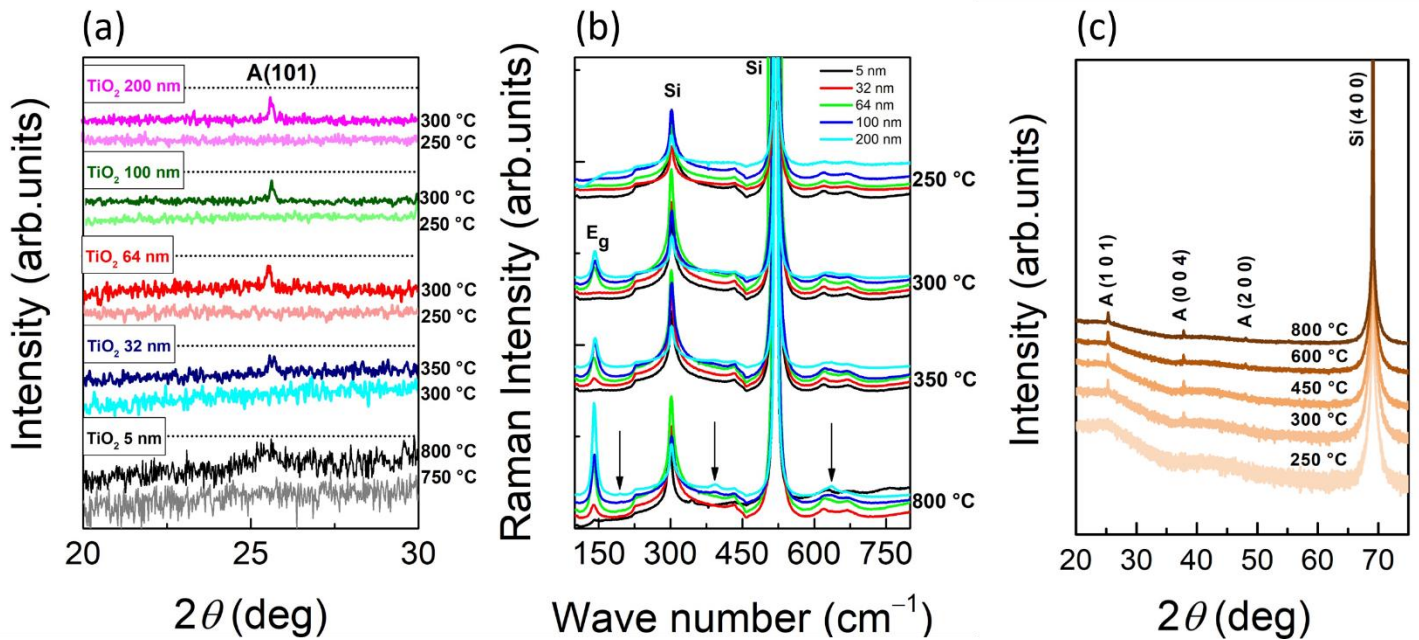


Figure 5: (a) XRD spectra of the 5 nm sample at 750 (grey) and 800 °C (black), the 32 nm sample at 300 (light blue) and 350 °C (blue), the 64 nm sample at 250 (light red) and 300 °C (red), the 100 nm sample at 250 (light green) and 300 °C (green), and the 200 nm sample at 250 (light magenta) and 300 °C (magenta). The symbol A indicates the anatase phase; (b) Raman Spectra of the 5 (black), 32 (red), 64 (green), 100 (cyan), and 200 (blue) samples annealed at different temperatures (250, 300, 350, and 800 °C). (c) high resolution XRD spectra of 200 nm TiO₂ samples annealed in air for 12 h at different temperatures acquired with time/step of 100 s, 2θ step of 0.02°, and 2θ angle in the range from 20° to 75°. The symbol A indicates the anatase phase. Adapted from [1].

Similarly, the amorphous-anatase transition was monitored by RS focusing on the strongest anatase vibrational band, E_g at $\sim 144 \text{ cm}^{-1}$ [9]. Figure 5(b) shows the spectra of 5 (black), 32 (red), 64 (green), 100 (cyan), and 200 (blue) samples annealed at different temperatures (250, 300, 350, and 800 °C). The appearance of this mode is observed at 800 °C for the 5 nm, at 350 °C for the 32 nm sample, and at 300 °C for the 64, 100, and 200 nm samples. Moreover, the Raman spectrum of the 200 nm sample shows additional modes at 800 °C [indicated by the black arrows in Figure 5(b)]. Among these, the mode at 194 cm^{-1} is still attributed to the E_g Raman band, whereas the two modes at 394 and 637 cm^{-1} could be attributed to either anatase or brookite phases. Indeed, these latter are very close to each other (399 and 639 cm^{-1} for the anatase and 396 and 636 cm^{-1} for the brookite [10]) and a non-negligible convolution effect with the Si substrate bands, in this range, can affect a precise determination of the mode centers. However, in order to exclude the presence of the brookite phase, high-resolution XRD spectra of the 200 nm sample were acquired at 800 °C, as well as 250, 300, 400, and 600 °C, and shown in Figure 5(c). Starting from 300 °C, the only visible XRD peaks are related to the (101), (004), and (200) anatase reflections, thus ruling out the presence of any brookite.

Based on these results, one can determine the evolution of the crystallization onset T_c as a function of the sample thickness d . Figure 6(a) shows the T_c vs thickness, colored dots

referring to samples with different thickness. Note that an asymmetric error bar has been used to highlight the uncertainty in the estimate of T_c due to the 50 °C step used in the heat treatments. The behavior of T_c is fitted by using [11]:

$$T_c = T_{ac} + (T_{melt} - T_{ac})e^{-\frac{d}{\lambda_d}}, \quad (2)$$

where T_{melt} is the melting temperature of the bulk crystalline TiO_2 equal to 1843 °C, T_{ac} is the crystallization onset temperature of a thick amorphous film, and λ_d is the characteristic decay length of the crystallization onset temperature. Then, $T_{ac} = (287 \pm 42)$ °C and $\lambda_d = (5.9 \pm 0.3)$ nm have been extracted from the fit of the experimental data. A strong dependence of T_c on the sample thickness was demonstrated, which increases by decreasing the thickness.

Considering that a layer of native SiO_2 is present on Si substrates, these investigated TiO_2/SiO_2 samples can be compared with the Si/SiO_2 , Si/SiO_x , and Ge/SiO_2 superlattices discussed in [11]. In this work, an exponential decrease of the crystallization temperature with increasing the layer thickness is observed, as shown in Figure 6(b).

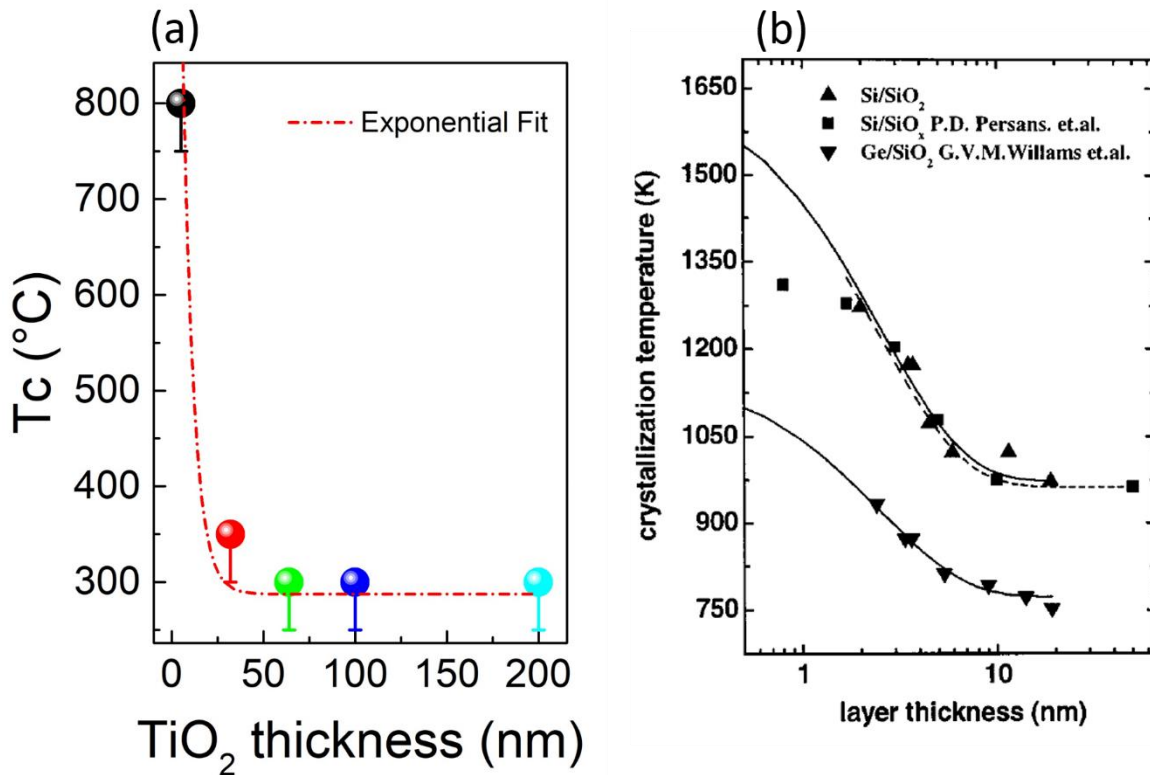


Figure 6: (a) T_c as a function of the TiO_2 thickness. The red dashed line is the exponential fit. (b) Crystallization temperatures of different superlattice structures as a function of the layer thickness. Adapted from [1,11].

4.3 Study of TiO_2 crystallization evolution versus thickness

The structural and morphological changes induced by different thermal annealing treatments were further investigated by AFM, SEM, XRD and RS, as a function of the sample thickness.

Table 1 reports the thermal evolution of the surface morphology in the 5 nm (second row), 32 nm (third row), 64 nm (fourth row), 100 nm (fifth row), and 200 nm (sixth row) samples. All AFM topographies are acquired in tapping mode on a scan area of $10\ \mu\text{m} \times 10\ \mu\text{m}$ in lateral size for samples as-grown, and after annealing performed at 300, 600, 800, and 1000 °C.

The 5 nm-sample (second row) shows an unaltered surface after annealing at 300, and 600 °C. Conversely, randomly distributed holes [depth of (2.9 ± 0.7) nm] and nanorod-like structures appear on the surface at 800 and at 1000 °C, respectively. The depth of these holes indicates a partial de-wetting of TiO_2 , occurring at 800 °C, whereas the “1D-like” material reorganization observed after annealing at 1000 °C, is consistent with the growth of TiO_2 crystalline nanowires, as already observed on a SrTiO_3 perovskite surface after $T_a = 1000$ °C [12]. The surface of 32 nm-sample (third row) shows the tendency to form linear structures first occurring at 300 °C, slightly below its T_c (occurring in between 300 and 350 °C). These structures evolve in temperature and become clearly evident and dense at 800 and 1000 °C. Fourth row reports the thermal evolution of the 64 nm sample. The morphology evolves from disordered particles, in the as-grown, to linear structures at 300 °C. Again, these features become more evident as T_a increases. In fact, they appear very well formed at 600 °C and accompanied by the formation of pronounced boundaries at 800 °C (as indicated by the black dotted arrows). Finally, at 1000 °C the formation of large micrometric slabs characterized by radial ridges, as shown in Ref. [13], and an overall densification of the material is evident. In general, the structures, occurring at or close to the T_c , are interpreted as crystalline plates, forming grains with different crystalline orientations reporting a preferential 2D growth of crystalline TiO_2 [14,15]. The 100 (fifth row) and 200 (sixth row) nm-samples show a very similar evolution, from a topography characterized by particle agglomerations (as-grown, and at 300, 600 °C) to the formation of blocks separated by deep cracks, at 800 and 1000 °C. In conclusion, the evolution of the surface morphology and their peculiar structures are strongly dependent on the TiO_2 thickness. Figure 7 highlights the peculiar occurrence of the crystalline features observed by AFM at 1000 °C, on a completely different length scale, such as the one obtained by optical microscopy. Panels (b,d,f,h) display a 50X magnification of the material organization, after crystallization, for the 5, 32, 64, and 100 nm sample, respectively, showing a flower-like morphology that becomes more and more compact by increasing the sample thickness. Moreover, Figure 7(g) shows a 5X magnification of the 100 nm sample, in which the profound cracks are a consequence of the temperature-driven sintering process. Finally, the optical images of the 200 nm sample [Figures 7(i,l)] confirm the presence of much smaller, separated plates or blocks.

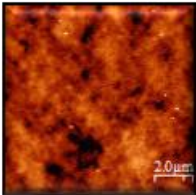
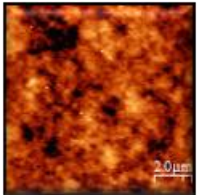
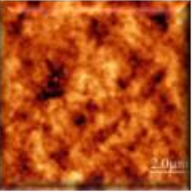
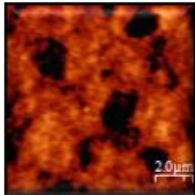
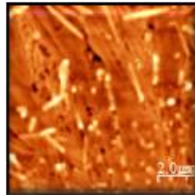
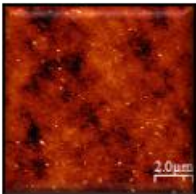
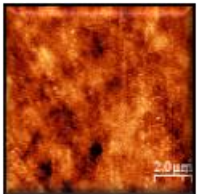
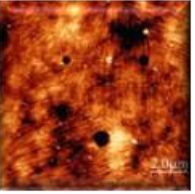
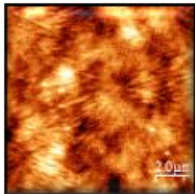
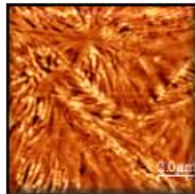
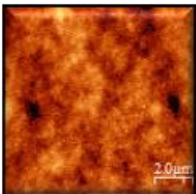
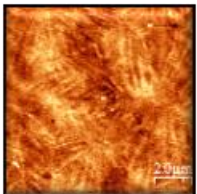
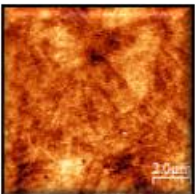
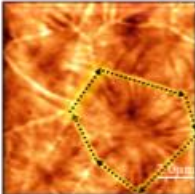
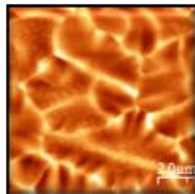
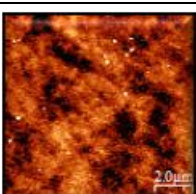

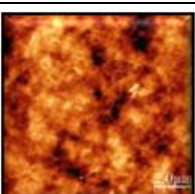
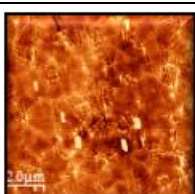
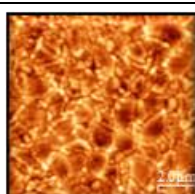
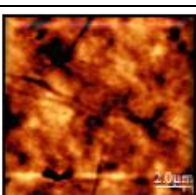
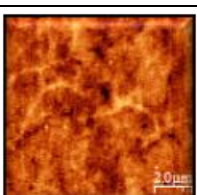
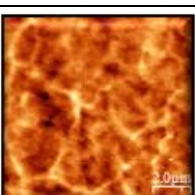
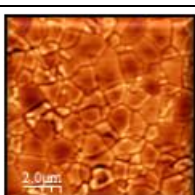
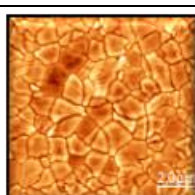
Sample	As-grown	300 °C	600 °C	800 °C	1000 °C
<u>5 nm</u>					
<u>32 nm</u>					
<u>64 nm</u>					
<u>100 nm</u>					
<u>200 nm</u>					



Table 1: Tapping-mode AFM topography, 10 μm x 10 μm in lateral size of: 5 nm sample as-grown, and annealed at 300, 600, 800 and 1000 °C (second row); 32 nm sample as-grown, and annealed at 300, 600, 800 and 1000 °C (third row); 64 nm sample as-grown, and annealed at 300, 600, 800 and 1000 °C (fourth row); 100 nm sample as-grown, and annealed at 300, 600, 800 and 1000 °C (fifth row); 200 nm sample as-grown, and annealed at 300, 600, 800 and 1000 °C (sixth row). The color scale of the samples as-grown, annealed at 300, 600 °C ranges from 0-6 nm. The color scale of the samples annealed at 800 °C ranges from: 0 to 5 nm for 5, 64 and 100 nm; 0 to 2 nm for 32 nm; 0 to 15 nm for 200 nm. The color scale of the samples annealed at 1000 °C ranges from: 0 to 90 nm for 5 nm; 0 to 60 nm for 32, 64 and 100 nm; 0 to 80 nm for 200 nm. Adapted from [1].

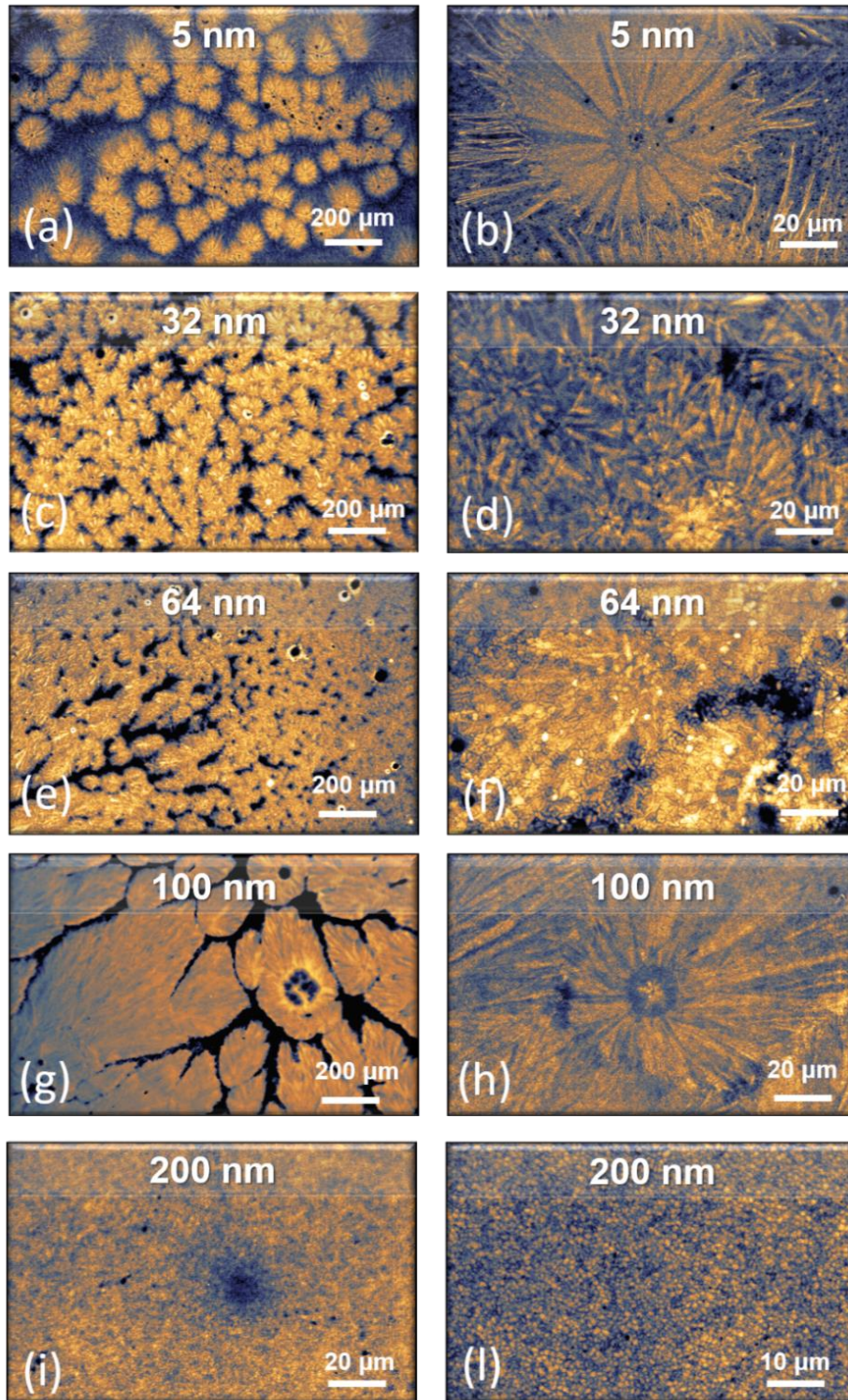


Figure 7: Optical microscope images of TiO_2 samples annealed at $1000\text{ }^\circ\text{C}$ with different magnification: (a,b) 5; (c,d) 32; (e,f) 64; (g,h) 100 and (i,l) 200 nm. Adapted from [1].

While Table 1 shows the thermal evolution of the sample morphology per each thickness, Figure 8 compares the morphology evolution as a function of the thickness at the fixed temperature of 800 °C. Both AFM and SEM images are shown for the 32 [Figure 8 (a,e)], 64 [Figure 8(b,f)], 100 [Figure 8(c,g)], and 200 nm [Figure 8(d,h)] samples. All AFM images are acquired on a scan area of 1 $\mu\text{m} \times 1 \mu\text{m}$ in lateral size in tapping mode. As shown in Figure 8(a,b), at 800 °C, 32 and 64 nm samples still exhibit a surface made of particles. However, these appear aligned in preferential directions, disclosing a tendency toward a higher order in material organization. The morphology of the 100 nm sample, instead, [Figure 8(c)] shows crystalline blocks separated by deep cracks, resembling the formation of a polycrystal. Indeed, each block seems to exhibit different crystalline orientation (as indicated by the white dashed lines). This suggests that TiO₂ tends to crystallize into plates with the same orientation within each block. Similarly, 200 nm sample [Figure 8(d)] shows crystalline blocks larger than those formed in the 100 nm samples. Moreover, these blocks show a much flatter topmost average RMS of 0.72 nm, demonstrating a higher degree of order by increasing the thickness. Same information are extracted from the SEM images: 32 and 64 nm samples [Figures 8(e,f)] show a morphology made by particles, and a similar trend towards grain boundaries formation. Instead, 100 and 200 nm samples [Figures 8(g,h)] display well-defined blocks, with evident “plate like” crystal morphology.

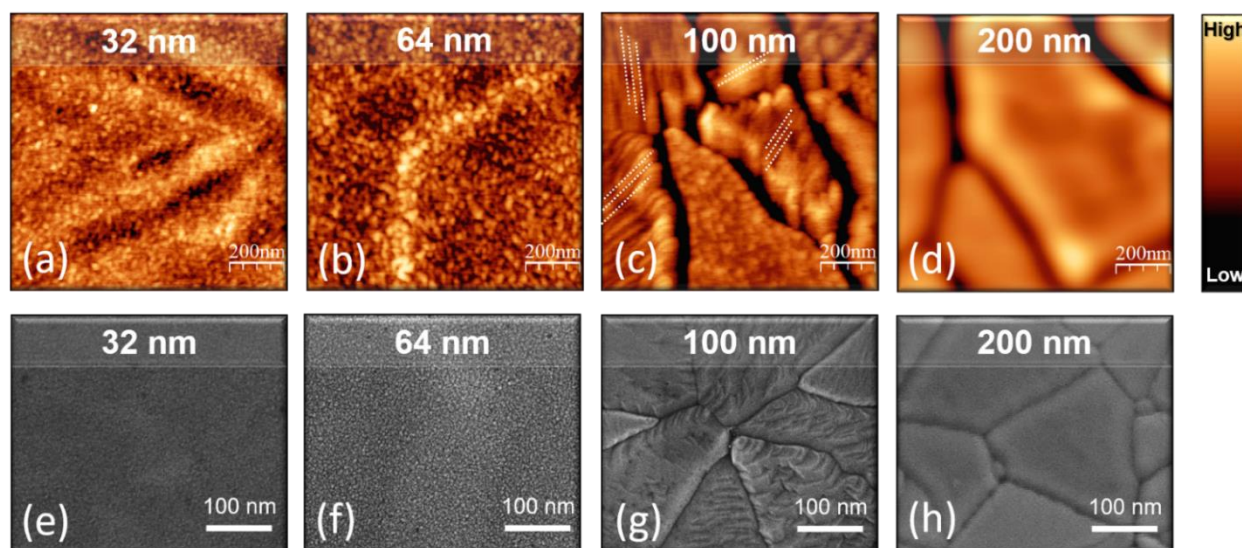


Figure 8: AFM topography on a scan area of 1 $\mu\text{m} \times 1 \mu\text{m}$ in lateral size, of (a) 32, (b) 64, (c) 100, and (d) 200 nm samples annealed at 800 °C. The color scale ranges from: 0 to 5 nm for the 32 and 64 nm samples; 0 to 20 nm for the 100 nm, and the 200 nm samples. SEM images of (e) 32, (f) 64, (g) 100, and (h) 200 nm samples, annealed at 800 °C. Adapted from [1].

In order to exclude any possible influence of Si substrate on thin films after thermal annealing, its morphological and structural behavior upon heat treatments was additionally investigated. Figures 9(a,b) show the AFM images, on a scan area of 10 $\mu\text{m} \times 10 \mu\text{m}$, of pristine Si substrate and after annealing at 1000 °C, respectively. The RMS roughness is 0.53 and 0.4 nm for (a) and (b), respectively and in both cases a very flat surface appears, confirming that the Si surface is morphologically unchanged after

thermal annealing. On the other hand, Figure 9(c) shows the Raman spectra of the used substrate in its pristine form as well as at different T_a (300, 600, 800, and 1000 °C). The figure focused on the range 250–350 cm^{-1} , where the Si Raman band occurs (301.65 cm^{-1}) [4]. No shift is measured in the vibrational mode position, as a function of T_a , thus confirming that no structural changes are produced because of the annealing and no stress is induced or released in the substrate in the considered heating range.

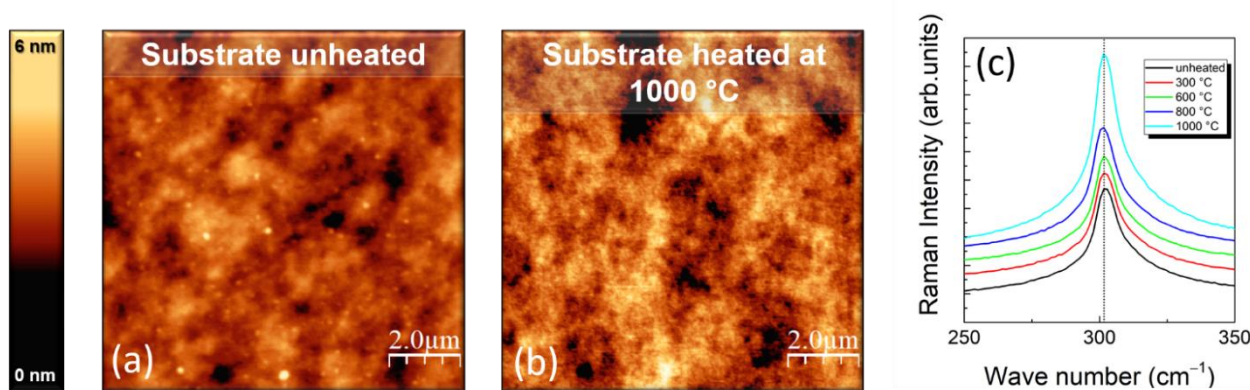


Figure 9: AFM topography, $10\ \mu\text{m} \times 10\ \mu\text{m}$ in size, of Si substrate (a) pristine and (b) annealed at 1000 °C. All images have been equalized to the same color scale, from a minimum value of 0 (black) to a maximum of 6 nm (white), to favor their comparison (c) Raman spectroscopy of the Si substrate unheated (black) and annealed at different temperatures, in the range 250–350 cm^{-1} . Adapted from [1].

To investigate the crystalline structural phases of TiO_2 , after thermal annealing, additional XRD measurements were acquired, and reported in Figures 10(a–e), at different annealing temperatures. While thicker samples (64, 100, 200 nm) are only disclosing the XRD reflections of the anatase phase, indexed as $A(h,k,l)$ in Figure 10, the thinnest ones (5 and 32 nm) show the coexistence of both the anatase and rutile phases, the latter indexed as $R(h,k,l)$, upon annealing at the highest T (1000 °C). Generally, the anatase-rutile phase transition and its related temperature depends on film growth technique, annealing environment, impurities, grain and particle size [16-27]. Fixed the fabrication method, our samples are certainly affected by changes in grain and/or particle size as a function of thickness [see Figure 4(a)]. On the other hand, one should notice that the annealing process breaks the bonds between Ti and O, causing the release of oxygen from the material and forming both oxygen vacancies and interstitial Ti atoms. These so-formed impurities of the crystal lattice influence as well the anatase-rutile transition, and might be more relevant as the TiO_2 material volume is reduced (for instance in the thinnest 5 and 32 nm samples).

Then, Figure 10(f) shows the result of the Debye–Scherrer analysis [28], performed on the strongest anatase peak (101), for the XRD spectra acquired at 800 °C, showing an increase of the crystallite size, from 10 nm (32 nm-sample) to 63 nm (200 nm-sample), upon increasing the film thickness.

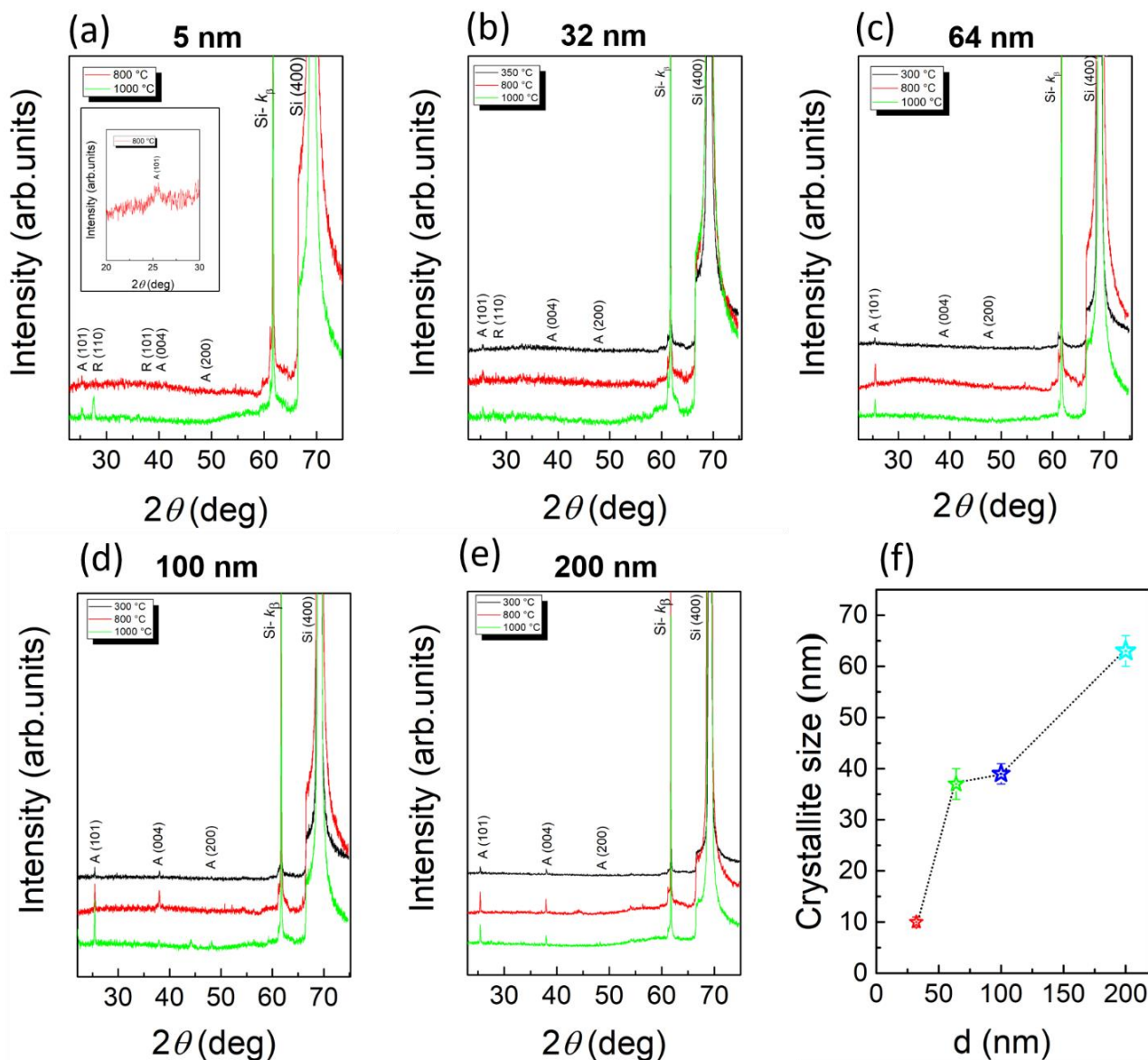


Figure 10: XRD spectra of (a) 5, (b) 32, (c) 64, (d) 100, and (e) 200 nm TiO₂ samples, annealed at different temperatures. Symbols A and R refer to the anatase and rutile phase, respectively.

Inset of Figure 11(a): zoom on the A(101) peak – annealing at 800 °C. The θ - 2θ scans were acquired with a time-step of 0.6 s and a 2θ step of 0.02° and all curves have been offset along the y-axis. (f) Crystallite size of TiO₂ 32 (red star), 64 (green star), 100 (blue star) and 200 (cyan star) nm films after $T_a = 800$ °C. The dashed line is used as a visual guide. Adapted from [1].

Finally, the evolution of the vibrational properties of TiO₂ as a consequence of crystallization process and crystallization evolution was explored by RS and by focusing on possible shifts and changes in the linewidth of the strongest E_g Raman anatase mode as a function of both thickness and T_a .

Figures 11 (a-e) show Raman spectra in the range 100–200 cm⁻¹ as acquired for the 200, 100, 64, 32, and 5 nm samples, respectively. The raw data spectra are treated as discussed in Chapter 3.

While all samples exhibited a spatially uniform Raman response at any annealing temperature, the 5 nm one [Figure 11 (e)] disclosed a more complex Raman behavior at its T_c of 800 °C. As shown by Figure 11(e), different behaviors were found, thus showing that the Raman response is strongly inhomogeneous and dependent on the position over the sample surface. It is worth noticing that, even though the 5 nm sample exhibited a uniform crystallization behavior to the XRD, the RS has much higher spatial resolution compared to XRD ($\sim 1\text{--}100\ \mu\text{m}^2$ in RS versus mm^2 in XRD) and is thus able to reveal any crystallization inhomogeneity. The non-uniformity can be explained by taking into account the partial de-wetting of the film observed with AFM (second row of Table 1), after $T_a = 800\ \text{°C}$, and thus it can be a consequence of a non-uniform coverage across the sample surface. On the contrary, upon complete crystallization at 1000 °C, the sample discloses a uniform Raman behavior.

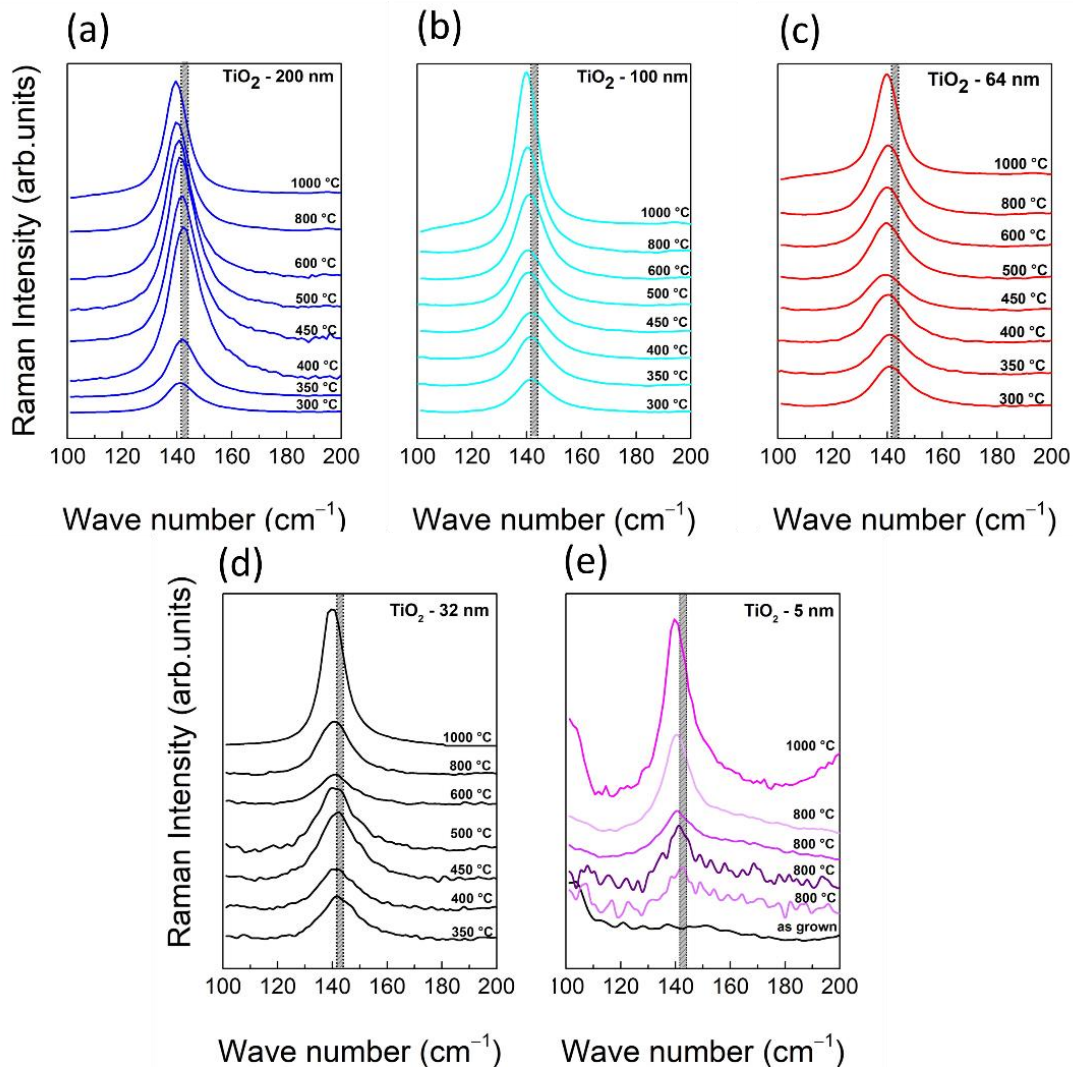


Figure 11: Raman spectra of (a) 200; (b) 100; (c) 64; (d) 32 nm, and (e) 5 nm samples at different T_a in the range 100–200 cm^{-1} . The gray dashed area indicates the E_g Raman band position range as reported in literature [10,30]. For the 5 nm sample Raman spectra of as-grown, annealed at 800 °C in different locations, and annealed at 1000 °C are shown. The Raman spectra were acquired with a power laser of 10%, an exposure time of 10 s, and 3 accumulations. Adapted from [1].

Finally, Figure 12(a) shows the behavior of E_g peak as a function of T_a and for different TiO_2 thicknesses. Blue, cyan, red, black, and violet stars refer to the Raman shift of 200, 100, 64, 32, and 5 nm samples, respectively, while the gray dashed area indicates the E_g Raman band position range as reported in literature [10,30]. As a red laser source, with a wavelength of 785 nm, is used in the presented experiments, the position of TiO_2 - E_g is expected at 141.5 cm^{-1} . In a temperature range between 300-500 °C, all samples show a E_g Raman mode position that fluctuates around the expected value. At temperatures equal or higher than 600 °C, a red shift is observed indicating the setting up of a tensile strain, as shown in Refs. [31,32]. In these latter, the development of tensile stress, with a rapid increase for a reduced film thickness, has been observed upon crystallization, together with the formation of grain boundaries and cracks, as those imaged with AFM and SEM, to the aim of releasing the strain. As expected, a different and inhomogeneous behavior is observed for the 5 nm sample, at its crystallization temperature, i.e., 800 °C. In fact, the E_g Raman mode assumes values from 140.5 to 142.5 cm^{-1} further demonstrating that the peculiarities of the crystallization are location-dependent.

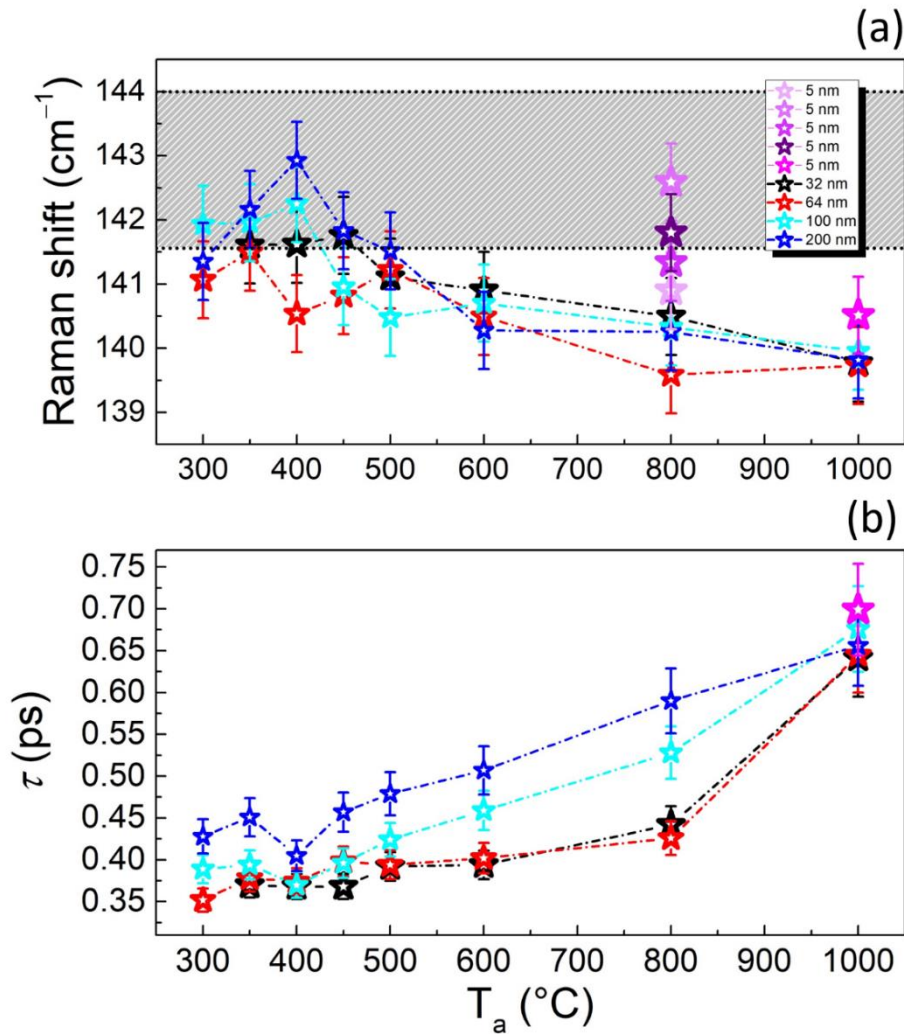


Figure 12: (a) Raman shift as a function of the T_a . The grey region highlights the range where the E_g Raman mode is expected [10,30]. (b) phonon lifetime τ as a function of the T_a . The blue, cyan, red, and black stars indicate the 200, 100, 64, and 32 nm samples, respectively. Adapted from [1].

Figure 12(b) shows the behavior of phonon lifetime (τ) as a function of TiO_2 thickness and T_a . In Chapter 3, the mechanism of the phonon lifetime and the procedure to estimate τ were deeply discussed.

For all samples, τ increases for increasing the annealing temperature. The monotonic increase of τ can be exclusively related to the evolution of crystallization, which gradually densifies the material and reduces the number of scattering centers. Indeed, Energy-dispersive X-ray spectroscopy (EDX) measurements were performed to exclude the presence of external contaminations. For instance, Figure 13 shows a representative EDX spectra of as-grown TiO_2 -200 nm in which only O = (15.10 ± 0.15) %, Ti = (6.35 ± 0.06) %, and Si = (78.5 ± 0.1) % (from substrate) were measured. In light of this, the only source of scattering can be associated to the boundaries between amorphous and crystalline areas, as well as between crystalline areas with different orientation and/or phase.

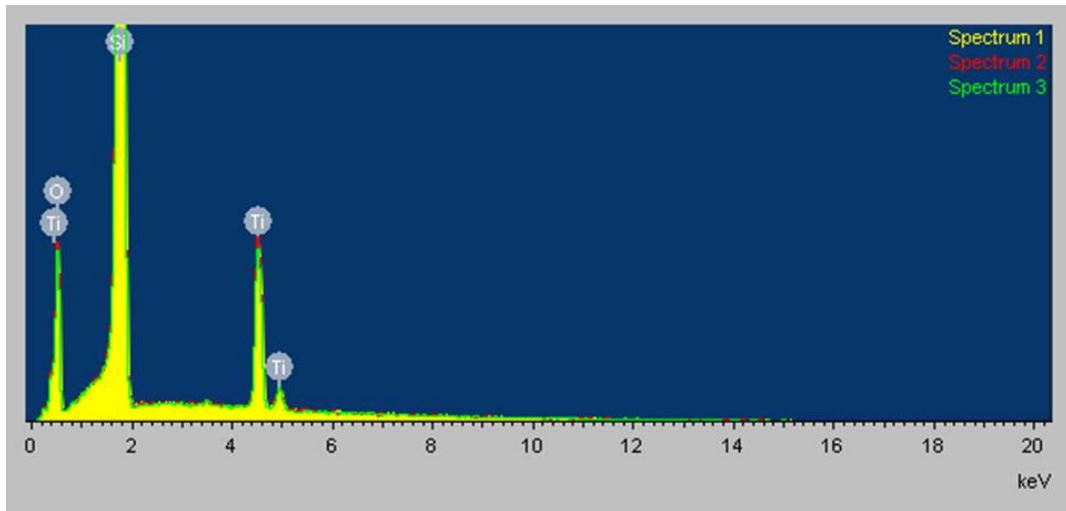


Figure 13: EDS analysis of an as-grown TiO_2 -200 nm film. Adapted from [1].

In fact, at any T_a up to 800 °C, the phonon lifetime of the thicker samples (200 and 100 nm) is longer than the thinner ones. Indeed, the latter are still made by individual particles, even at 800 °C, and their boundaries act as scattering centers. Only upon annealing at 1000 °C, the phonon lifetimes measured for all the TiO_2 thickness values studied become equal within the error bars. Interestingly, the phonon lifetime of the 200 nm sample keeps increasing smoothly within the whole T_a , while stiffer jumps are measured above 800 °C as the thickness is reduced. In particular, the phonon lifetimes of the 32 and 64 nm samples evolve almost identically, with both samples being characterized by a transition from a morphology still made by particles, at 800 °C, to a much higher densification degree at 1000 °C.

Summary

This chapter focused on the investigation of the crystallization onset and evolution of TiO₂ films, with thickness varying between 5 and 200 nm. The first section, called *Study of as-grown TiO₂ versus thickness*, shows that as-grown thin films, deposited by IAD, are uniform in thickness, for both thin (5 nm) and thick (100 nm) films as shown by XRR and profilometric measurements, respectively. The as-grown samples are amorphous as shown by RS and XRD measurements. Indeed, no anatase Raman mode and X-ray reflection are observed in the RS and XRD spectra. Then, the surface of all the as-grown samples is made of amorphous particles. This analysis, performed on a scan area of 1 μm × 1 μm in lateral size, demonstrates that those particles are more evident as the thickness increases. The particle size varies from (22 ± 4) nm for the 5 nm sample to (37 ± 3) nm for the 200 nm one, if the tip deconvolution and the high packing density are considered. Moreover, also the average measured RMS roughness increases by increasing the thickness, from (0.29 ± 0.05) nm for the 5 nm-sample to (0.65 ± 0.04) nm for the 200 nm one.

The second section, called *Study of as-grown TiO₂ crystallization onset versus thickness*, showed that the amorphous-to-crystalline transition occurs between 300 and 350 °C for the 32 nm sample, between 250 and 300 °C for the thickest samples (64, 100, and 200 nm), whereas only a tiny feature of crystallization is found in the thinnest one (5 nm) at 800 °C. This has been observed following the first anatase reflection, (101), at 2θ = 25.2° and the anatase Raman vibrational band, E_g, at ~144 cm⁻¹ in the XRD and Raman spectra, respectively. Then, an exponential increase of the crystallization temperature with decreasing the layer thickness is observed, deriving a crystallization temperature of a thick bulk amorphous material of 287 °C.

The third and final section, called *Study of TiO₂ crystallization evolution versus thickness*, displayed that at temperatures higher than T_c, remarkable differences emerge upon varying the sample thickness. Indeed, while all as-grown samples have a surface characterized by amorphous particles, the evolution of these topographical features, in temperature, is very peculiar of each thickness. In particular, for the 5 nm sample a partial de-wetting together with a non-uniform crystallization at 800 °C is observed, followed by a whisker-like material reorganization at 1000 °C. The 64 and 32 nm samples show micrometer size domains with structures characterized by radial ridges. Then, both 100 and 200 nm samples disclose the progressive formation of crystalline grains, separated by deep cracks, of a few hundreds of nm in lateral size. Finally, the behavior of the Raman E_g vibrational mode and the phonon lifetime by varying T_a and thickness, was used to describe the lattice dynamics. In the temperature range between 300-500 °C, the samples with a thickness of 32, 64, 100, and 200 nm show an E_g Raman mode position that scattered around the expected value of 141.5 cm⁻¹. At temperatures equal or higher than 600 °C, a red shift is observed, toward lower value than expected one, indicating a tensile strain. For the 5 nm sample annealed at 800 °C, the E_g Raman mode assumes values from 140.5 to 142.5 cm⁻¹ demonstrating that the crystallization depends on the location and at 1000 °C a red shift is observed. Then, all samples exhibit almost the same behavior of Raman shift versus temperature, with only a small red-shift at the highest T_a. On the contrary, the phonon lifetime is peculiar for each thickness, up to 800 °C. In particular, the trend of τ, and its higher value in the thickest films, can be correlated with the

densification of the material due to the annealing, and a consequent reduction of phonon scattering sites. Moreover, all samples revealed the same phonon lifetime upon annealing at $T_a = 1000$ °C.

Finally, this deep, systematic, and extensive study, devoted to both T_c and evolution as a function of both material thickness and post-deposition treatments, has established clear bases for a detailed TiO_2 phase diagram that describes the amorphous-to-crystalline phase transition. The strong cross-talking among the complementary techniques used (AFM and SEM for surface imaging and XRD and RS for structural spectroscopies) suggests that also surface imaging can provide distinctive information on material crystallization.

References

1. Durante, O., *et al.* Emergence and Evolution of Crystallization in TiO_2 Thin Films: A Structural and Morphological Study. *Nanomaterials* **2021**, *11*(6), 1409.
2. Sintonen, S., *et al.* X-ray reflectivity characterization of atomic layer deposition Al_2O_3/TiO_2 nanolaminates with ultrathin bilayers. *Journal of Vacuum Science & Technology A: Vacuum, Surfaces, and Films* **2014**, *32*(1), 01A111.
3. Stoev, K. N., Sakurai, K. Review on grazing incidence X-ray spectrometry and reflectometry. *Spectrochimica Acta Part B: Atomic Spectroscopy* **1999**, *54*(1), 41-82.
4. Tanino, H., *et al.* Raman study of free-standing porous silicon. *Physical Review B* **1996**, *53*(4), 1937.
5. Colombi, P., *et al.* Self-assembled polystyrene nanospheres for the evaluation of atomic force microscopy tip curvature radius. *Measurement Science and Technology* **2009**, *20*(8), 084015.
6. Ostwald, W.Z. Blocking of Ostwald ripening allowing long-term stabilization. *Physical Chemistry* **1901**, *37*, 385.
7. Voorhees, P. W., The theory of Ostwald ripening, *Journal of Statistical Physics* **1985**, *38*(1), 231-252.
8. Ratsch, C., Venables, J. A., Nucleation theory and the early stages of thin film growth, *Journal of Vacuum Science & Technology A: Vacuum, Surfaces, and Films* **2003**, *21*(5), S96-S109.
9. Boda, M. A., Shah, M. A. Fabrication mechanism of compact TiO_2 nanotubes and their photo-electrochemical ability. *Materials Research Express* **2017**, *4*(7), 075908.
10. Allen, N. S., *et al.* The effect of crystalline phase (anatase, brookite and rutile) and size on the photocatalytic activity of calcined polymorphic titanium dioxide (TiO_2). *Polymer degradation and stability* **2018**, *150*, 31-36.
11. Zacharias, M., Streitenberger, P. Crystallization of amorphous superlattices in the limit of ultrathin films with oxide interfaces. *Physical Review B* **2000**, *62*(12), 8391.
12. Wrana, D., *et al.* A bottom-up process of self-formation of highly conductive titanium oxide (TiO) nanowires on reduced $SrTiO_3$. *Nanoscale* **2019**, *11*(1), 89-97.
13. Reklaitis, I *et al.* A comparative study on atomic layer deposited oxide film morphology and their electrical breakdown. *Surface and Coatings Technology* **2020**, *399*, 126123.

14. Kim, Y.H. *et al.* High-temperature dielectric responses of molecularly-thin titania nanosheet. *Journal of the Ceramic Society of Japan* **2015**, *123*, 335–339.
15. Zhang, Y. *et al.* Raman study of 2D anatase TiO₂ nanosheets, *Physical Chemistry Chemical Physics* **2016**, *18*, 32178–32184.
16. Albetran, H. Low, I. Parameters controlling the crystallization kinetics of nanostructured TiO₂ – An overview. *Materials Today: Proceedings* **2019**, *16*, 25–35.
17. Shannon, R.D. Pask, J.A. Kinetics of the Anatase-Rutile Transformation. *Journal of the American Ceramic Society* **1965**, *48*, 391–398.
18. Eppler, R.A. Effect of Antimony Oxide on the Anatase-Rutile Transformation in Titanium Dioxide. *Journal of the American Ceramic Society* **1987**, *70*, C-64–C-66.
19. Akhtar, M.K. *et al.* Dopants in Vapor-Phase Synthesis of Titania Powders. *Journal of the American Ceramic Society* **1992**, *75*, 3408–341.
20. Ding, X.Z. *et al.* Grain size dependence of anatase-to-rutile structural transformation in gel-derived nanocrystalline titania powders. *Journal of materials science letters* **1996**, *15*, 1789–1791.
21. Gennari, F.C. Pasquevich, D.M. Kinetics of the anatase–rutile transformation in TiO₂ in the presence of Fe₂O₃. *Journal of Materials Science* **1998**, *33*, 1571–1578.
22. Zhang, H. Banfield, J.F. Understanding polymorphic phase transformation behavior during growth of nanocrystalline aggregates: insights from TiO₂. *The Journal of Physical Chemistry B* **2000**, *104*, 3481–3487.
23. Okada, K. *et al.* Effect of Silica Additive on the Anatase-to-Rutile Phase Transition. *Journal of the American Ceramic Society* **2004**, *84*, 1591–1596.
24. Barakat, M.A. *et al.* Effect of Cobalt Doping on the Phase Transformation of TiO₂ Nanoparticles. *Journal of nanoscience and nanotechnology* **2005**, *5*, 759–765.
25. Zhang, H. Banfield, J.F. Size Dependence of the Kinetic Rate Constant for Phase Transformation in TiO₂ Nanoparticles. *Chemistry of materials* **2005**, *17*, 3421–3425.
26. Fang, D *et al.* Effect of heat treatment on morphology, crystalline structure and photocatalysis properties of TiO₂ nanotubes on Ti substrate and freestanding membrane. *Applied Surface Science* **2011**, *257*, 6451–6461.
27. Liu, R *et al.* The effect of calcination conditions on the morphology, the architecture and the photo-electrical properties of TiO₂ nanotube arrays. *Materials Research Bulletin* **2013**, *48*, 1458–1467.
28. Cullity, B.D. *Elements of X-ray Diffraction*, Addison-Wesley Publishing, Boston, MA, USA, **1956**.
29. Boda, M. *et al.* Fabrication mechanism of compact TiO₂ nanotubes and their photo-electrochemical ability. *Materials Research Express* **2017**, *4(7)*, 075908.
30. RRUFF. Available online: <https://rruff.info/chem=Ti,O/display=default/R070582> (accessed on 9 August 2021).
31. Matěj, Z. *et al.*, L. X-Ray diffraction analysis of residual stress in thin polycrystalline anatase films and elastic anisotropy of anatase. *Metallurgical and Materials Transactions A* **2011**, *42*, 3323–3332.
32. Kužel, R. *et al.* In-situ X-ray diffraction studies of time and thickness dependence of crystallization of amorphous TiO₂ thin films and stress evolution. *Thin Solid Films* **2010**, *519*, 1649–1654.

Chapter 5

Nanolayers

Both the high and low refractive index materials, herein called HI and LI, used for the Bragg reflectors adopted in GWDs, present issues that need to be solved. In particular, the HI one, especially in its as-grown form, is affected by high mechanical and optical losses as a consequence of an insufficient material densification. To reduce these losses, and thus improving the optical/mechanical performances, a thermal annealing process is routinely performed (to date up to 500 °C). The maximum annealing temperature is limited by the threshold of material crystallization, which is strongly detrimental to the material's optical/mechanical properties.

This Chapter introduces a new strategy for “creating” ad-hoc a material with both HI and high crystallization temperature (thus enabling higher temperature annealing). The latter is made by a nanometric segmentation of the HI layer into nanolayers (NLs) made of two different materials (again with HI and LI).

With this in mind, nanostructures formed by TiO₂ nanolayers (HI) alternating with SiO₂, Ta₂O₅, Al₂O₃, or ZrO₂ nanolayers (LI) have been fabricated by IAD, and studied by AFM, XRD, and RS.

Same strategy can be applied to the LI. Indeed, even though SiO₂ is considered one of the best LI choices for high precision applications, such as the mirrors of GWDs, given its high optical performances, low mechanical losses, and high crystallization temperature, it suffers of an increase of mechanical losses when cooled down at low temperature. The latter is not compatible with the future interferometers design, expected to operate at cryogenic temperatures. Nano-structured metamaterials thus deserve to be taken into consideration also for possible cryogenic operations. In the following, SiO₂ and Al₂O₃ will be studied as the binary pair for new LI nanolayered metamaterials.

Figure 1(a) shows the actual design of the Bragg-reflectors used in Virgo, and made of $\text{SiO}_2/\text{Ta}_2\text{O}_5$ (or TiO_2 -doped Ta_2O_5 in a Virgo) doublets capped by a protective topmost SiO_2 layer and ending with a bottom SiO_2 layer, to decouple the mirror from the ultrapure fused SiO_2 substrate [1].

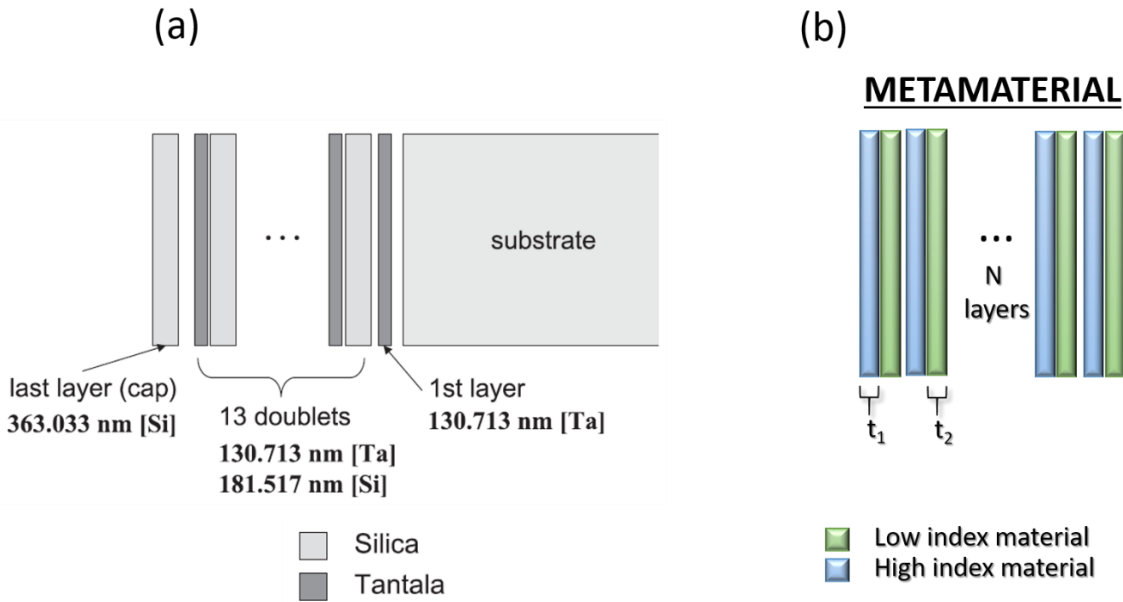


Figure 1: A sketch of (a) mirror used in the Virgo interferometer (Adapted from [1]), and (b) the nanolayering design. t_1 and t_2 (with $t_1, t_2 \ll \lambda$) are the thickness of the high and low refractive index material, respectively, N is the number layers.

Figure 1(b) sketches the proposed change to be made to the HI layer, which goes from an homogeneous mixture of TiO_2 and Ta_2O_5 to a discrete segmentation in NLs, alternating LI and HI, for the same total thickness as the mixture. The advantage of NLs over the mixture, relies on the higher optical density, and the inhibition of crystallization (as demonstrated in Chapter 4). By doing so, higher thermal processes are allowed, which further improve optical coating properties like absorption and densification, induce a relaxation of the internal stress [2], reduce optical and mechanical losses [3], and therefore the thermal noise [4].

The present chapter will mainly discuss the effect of:

- 1) Interfacing the TiO_2 with the SiO_2 in NLs with different degree of segmentation (from 11 to 85);
 - 2) Interfacing the TiO_2 with other LI oxides (Ta_2O_5 , Al_2O_3 , or ZrO_2) in NLs with extreme segmentation degree;
- for the HI counterpart, and:
- 3) Interfacing the SiO_2 with the Al_2O_3 for the LI one.

5.1 TiO_2/SiO_2 NLs vs segmentation degree

TiO_2/SiO_2 NLs have been deposited on Si substrate by using IAD, and characterized by means of AFM, EDS, XRR, RS, and XRD, both in their as-grown and annealed form.

The number of layers, the average thickness of TiO_2 and SiO_2 , the total thickness of the structure, and the effective refractive index are shown in Table 1. It is important to stress that the control of thickness is crucial to reach the desired optical properties of the prototype. In fact, small variations of thickness may cause remarkable differences in the refractive index of the NL.

These prototypes are designed following different strategies:

- 1) setting the effective index at the nominal value of 2.09 that is the one of TiO_2 doped Ta_2O_5 currently in use as a HI constituent of LIGO-Virgo coatings;
- 2) setting the reflectivity equal to that of the actual LIGO coating, to obtain the maximum reduction of thermal noise.

Sample	Average Thickness (nm)		Total Thickness (nm)	Refractive index
	TiO_2	SiO_2		
11-layers	18.0 ± 0.2 (x5)	7.3 ± 0.1 (x6)	133.8 ± 1.6	2.087
19-layers	10.1 ± 0.1 (x9)	4.6 ± 0.1 (x10)	139.9 ± 1.9	2.084
45-layers	4.5 ± 0.1 (x22)	2.2 ± 0.1 (x23)	150 ± 5	2.082
76-layers	3.05 ± 0.06 (x38)	0.75 ± 0.11 (x38)	144 ± 7	2.135
82-layers	2.01 ± 0.3 (x41)	0.9 ± 0.2 (x41)	119 ± 21	2.189
85-layers	3.2 ± 0.1 (x42)	1.3 ± 0.1 (x43)	190 ± 9	2.100

Table 1: Sample list of TiO_2/SiO_2 NLs.¹

5.1.1 Characterization of as-grown TiO_2/SiO_2 NLs

Morphological and roughness investigations have been performed by tapping AFM on scan areas of $1 \mu m \times 1 \mu m$, and $20 \mu m \times 20 \mu m$ in lateral size, see Figure 2. All the AFM images have been analyzed by using the WSxM 5.0 software by NanoTec, 2015. Similarly to the single layer characterization previously showed in Chapters 3 and 4, the surface of the as-grown samples, i.e., deposited at room temperature, appears always

¹ The measured thicknesses are affected by thermal shock of the quartz monitor crystal in the deposition process discussed in the Appendix E. The refractive index are calculated by using the Drude model.

made of a packing of rounded amorphous particles [5], with sizes that become time by time smaller as the thickness of the layers is reduced, because of the increases segmentation. Just looking at Figure 2, one can note that these particles are evident on the 11- and 19-layer [panel (a)-(b)] and become smaller and less pronounced as the layer number becomes higher, from 45-[panel (c)] to 85 [panel (f)]-layer. On large scan area, Figure 2(g-n), the details of amorphous particles are lost due to the poor resolution of data points, and no differences in the surface morphology are appreciated as a function of the layer number.

The roughness of the surface plays an important role along all this research, because of its impact on the different physical properties of the fabricated nanostructures, such as their mechanical and optical performance.

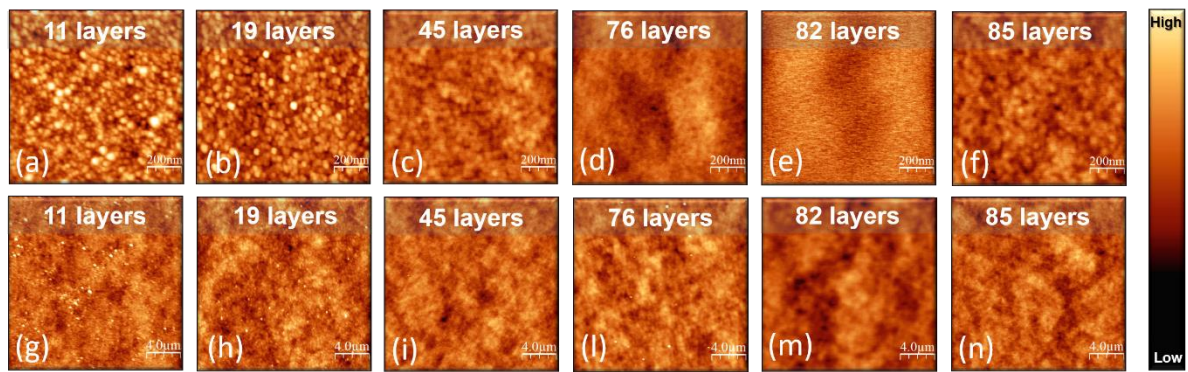


Figure 2: Tapping-mode AFM topography on a scan area of $1 \mu\text{m} \times 1 \mu\text{m}$ in size, of as-grown $\text{SiO}_2/\text{TiO}_2$ samples with (a) 11, (b) 19, (c) 45, (d) 76, (e) 82, and (f) 85 layers. The color scale in these AFM images ranges from 0 to 8 nm for the 11-layer sample, from 0 to 7 nm for 19-layer sample, from 0 to 3 nm for 45-, 76-, 82- and 85-layer samples. Tapping-mode AFM topography, $20 \mu\text{m} \times 20 \mu\text{m}$ in size, of as-grown samples with (g) 11, (h) 19, (i) 45, (l) 76, (m) 82 and (l) 85 layers. A color scale ranges from 0 to 7 nm for all samples.

Figure 3(a) shows the RMS roughness dependence on the number of layers. It is interesting to note that by increasing the number of layers, the RMS roughness decreases from (1.09 ± 0.08) nm for the 11-layer sample to (0.2 ± 0.07) nm for the 82-layer one. The shaded grey band in both panels of Figure 3 indicates the RMS roughness of the Si substrate surface measured before the deposition. It can be observed that the roughness of the NLs stays within the grey band for those samples having a number of layers higher than 45, indicating that for these highly segmented NLs the surface roughness is only dictated by the substrate one. On a large scan area, the roughness is almost constant among the different NLs, varying between (0.74 ± 0.04) nm for the 11- layers, and (0.64 ± 0.04) nm for 82-layers, see Figure 3(b).

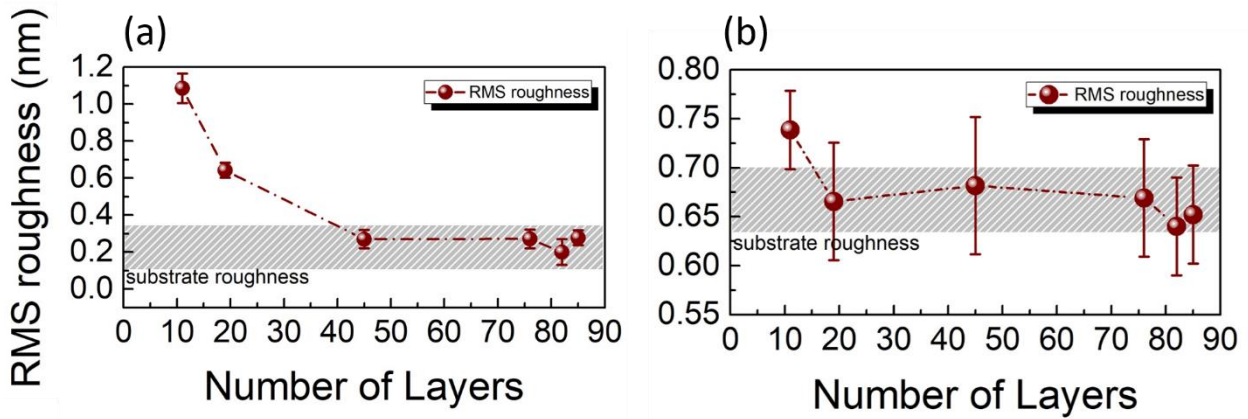


Figure 3: RMS roughness as a function of the number of layers in the as-grown samples on a scan area of (a) $1\ \mu\text{m} \times 1\ \mu\text{m}$, and (b) $20\ \mu\text{m} \times 20\ \mu\text{m}$ and. In both panels, the shaded grey area corresponds to the range of the measured Si substrate roughness. Dot-dashed lines are used as a guide for the eye.

Raman spectra for the as-grown $\text{TiO}_2/\text{SiO}_2$ NLs are shown in Figure 4. Here, red, green, blue, cyan, and magenta colors refer to 11, 19, 45, 76, 82, and 85 layers, respectively.

Within the range $100\text{-}200\ \text{cm}^{-1}$, the absence of any peak for the E_g mode of TiO_2 indicates that as-grown samples are all amorphous [6]. Moreover, all peaks in the range $300\text{-}950\ \text{cm}^{-1}$ are related to the modes of the crystalline Si (see Chapter 2). No any other significant peak is present in the spectra, confirming the absence of other materials.

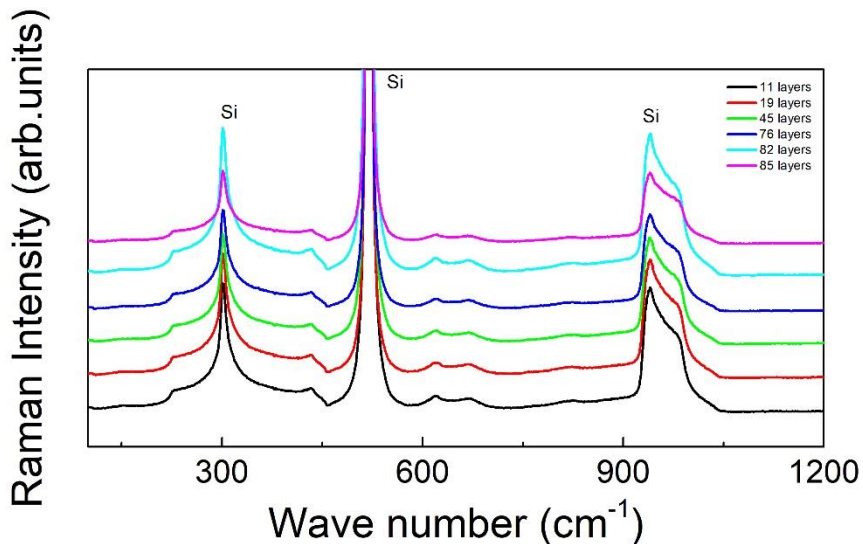


Figure 4: (a) Raman spectra with wavenumber ranging from 100 to $1200\ \text{cm}^{-1}$ of $\text{TiO}_2/\text{SiO}_2$ nanostructures with different layer numbers. The parameter used are: 5% of laser power, 5 accumulations, 50X magnification, and 10 s of exposure time in the range $100\text{-}1200\ \text{cm}^{-1}$. For clarity of representation, all Raman curves have been shifted along the y-axis.

In order to check that the deposition process had been able to correctly form a nanolayered structure, with the expected periodicity and layer thicknesses, XRR technique has been used, and the acquired data for the (a) 76- and (b) 82-layer samples are plotted in Figure 5. In this figure, the experimental data and the simulated curves are showed, respectively, in black and red, for 76-layer, and in green and blue, for 82-layers.

In the 76-layer sample, three interference resonances occur at the angles of $\theta \approx 1.2, 2.4, 3.5^\circ$ indicating that a nano-stratification satisfying the Bragg condition has been formed. From the data analysis, a period of (3.6 ± 0.6) nm, average thicknesses of (2.2 ± 0.4) nm for TiO_2 , and (1.4 ± 0.2) nm for SiO_2 , are deduced (X'pert Reflectivity software [7,8]). Consequently, the total thickness of the NL is 136.8 nm, very close to the expected value of 144 nm. Moreover, XRR allows to extract the interfacial roughness of each layer, from which an average interfacial roughness of (0.4 ± 0.1) nm can be recovered.

Similarly, the 82-layer sample discloses a period of (2.87 ± 0.14) nm, average thicknesses of (1.94 ± 0.06) nm for the TiO_2 and of (0.93 ± 0.08) nm for the SiO_2 layers, giving a total thickness of 117.67 nm, and an average interface roughness of (0.7 ± 0.1) nm. Note that individual as well as total layer thicknesses deduced by XRR, are very close to the values expected and reported in Table 1.

Moreover, from the analysis of XRR data, also the substrate roughness can be obtained, resulting in (0.24 ± 0.07) nm for the 76-layer sample and in (0.5 ± 0.2) nm for the 82-layer, consistently with the AFM measurements.

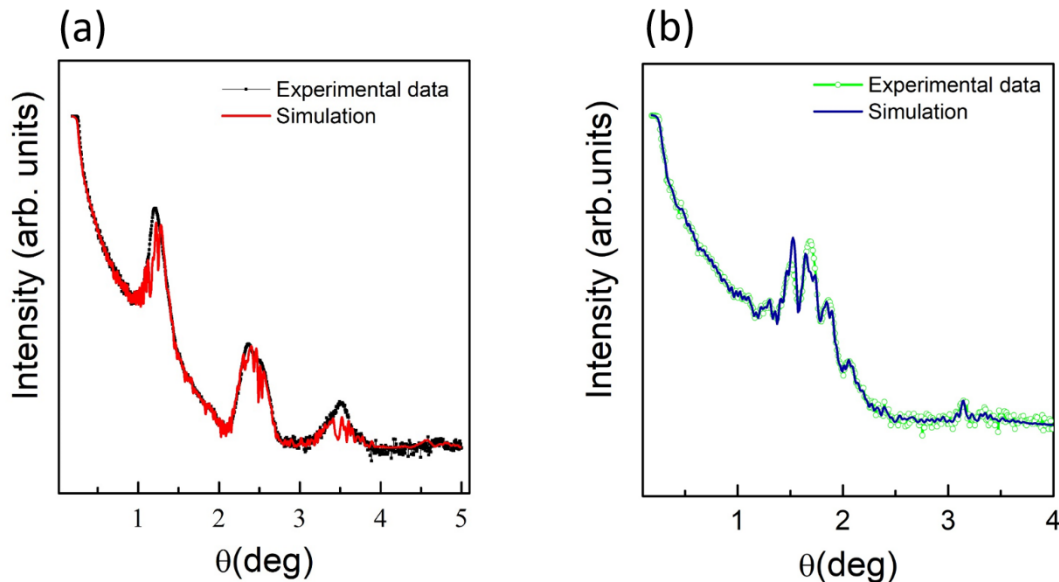


Figure 5: X-ray reflectivity (XRR) curves of (a) 76 and (b) 82 layer samples. All measurements have been performed at incident grazing angles in the range $(0.15 - 5)^\circ$, with a step angle of 0.005° , and a step time of 60 s.

To complete the investigation on both samples periodicity and thicknesses, cross sectional analyses have been performed by means of a scanning transmission electron microscope (STEM). The STEM image acquired on the 76 layers, along a scan area of 396 nm x 396 nm, is showed in Figure 6(a) both in dark and bright field, see left and right panel,

respectively. The bright field image shows a better contrast at the substrate interface whereas the dark field image allows a better visualization at the free interface (surface). On the right, for appreciating the detail of the single layers a zoom is shown. Clearly, all the 76 layers are correctly formed, as they can be counted and numbered. Moreover, the analysis of the STEM image can be used to evaluate the periodicity, the thicknesses of each single layer, as well as the total one, to be compared with the one measured by XRR. One can also note that at the interface with the Si substrate, a brighter contrast thin region is present, due to the formation of the 2 nm thick silicon oxide native layer, that should not be counted as one of the deposited nanolayers.

Figure 6(b) shows the depth profile measured along the dashed line traced in panel (a). After the first region corresponding to the air, in the range 0-48 nm, the fabricated nanostructures become visible counting a number of 38 $\text{TiO}_2/\text{SiO}_2$ doublets with a total thickness of 143.16 nm. The average estimate of the periodicity can be extracted by means of Fourier analysis showed in Figure 6(c,d). The position of the two sharp peaks in the Fast Fourier Transform (FFT) map indicates a periodicity of (3.7 ± 0.1) nm. Moreover, a roughness of 0.49 nm from FWHM of the peak has been estimated, in agreement with the XRR measurements. These results helped to validate the calibration of the thickness monitor apparatus used at University of Sannio during the NLs deposition.

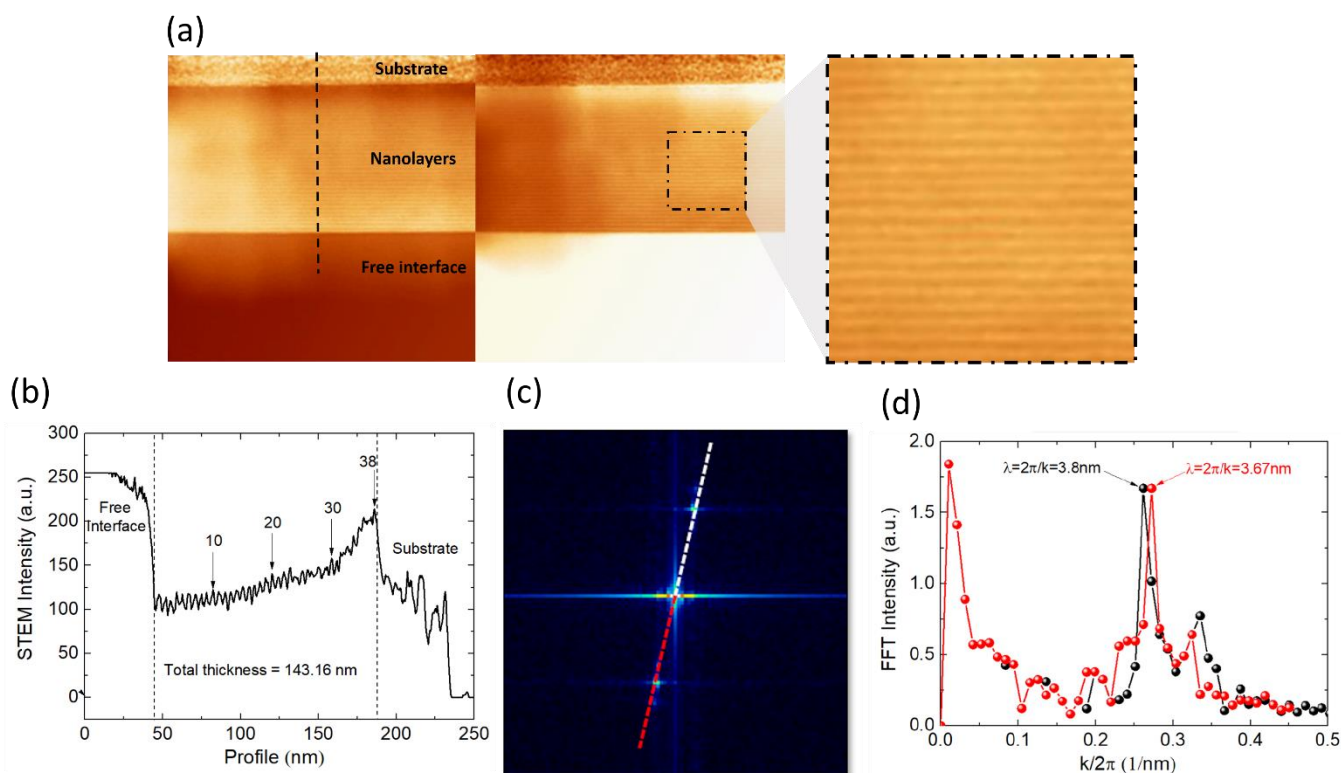


Figure 6: (a) STEM image (courtesy of CNR of Florence) on a scan area of 396 nm x 396 nm and a zoom, by using a voltage of 30 kV, a work distance of 5 mm, and a magnification of 531X. (b) Profile line (c) FFT image, and (d) FFT vs frequency of the 76-layer sample.

5.1.2 Characterization of annealed TiO₂/SiO₂ NLs

In order to explore how the amorphous-to-crystalline phase transition is modified by the nanolayer segmentation, the complete set of samples from the 11 to 85-layers was annealed at different annealing temperatures for 12 hours in air. As already done for single layer samples (see Chapters 2,3), each thermal annealing is done starting from a pristine fragment of the as-grown sample. As a first step, the crystallization onset temperature, T_c , variation as a consequence of the nano-layering is investigated. To do this, Raman spectra for the 11- to 85-layer samples have been measured after annealing in the range 250-1000 °C, as showed in Figure 7.

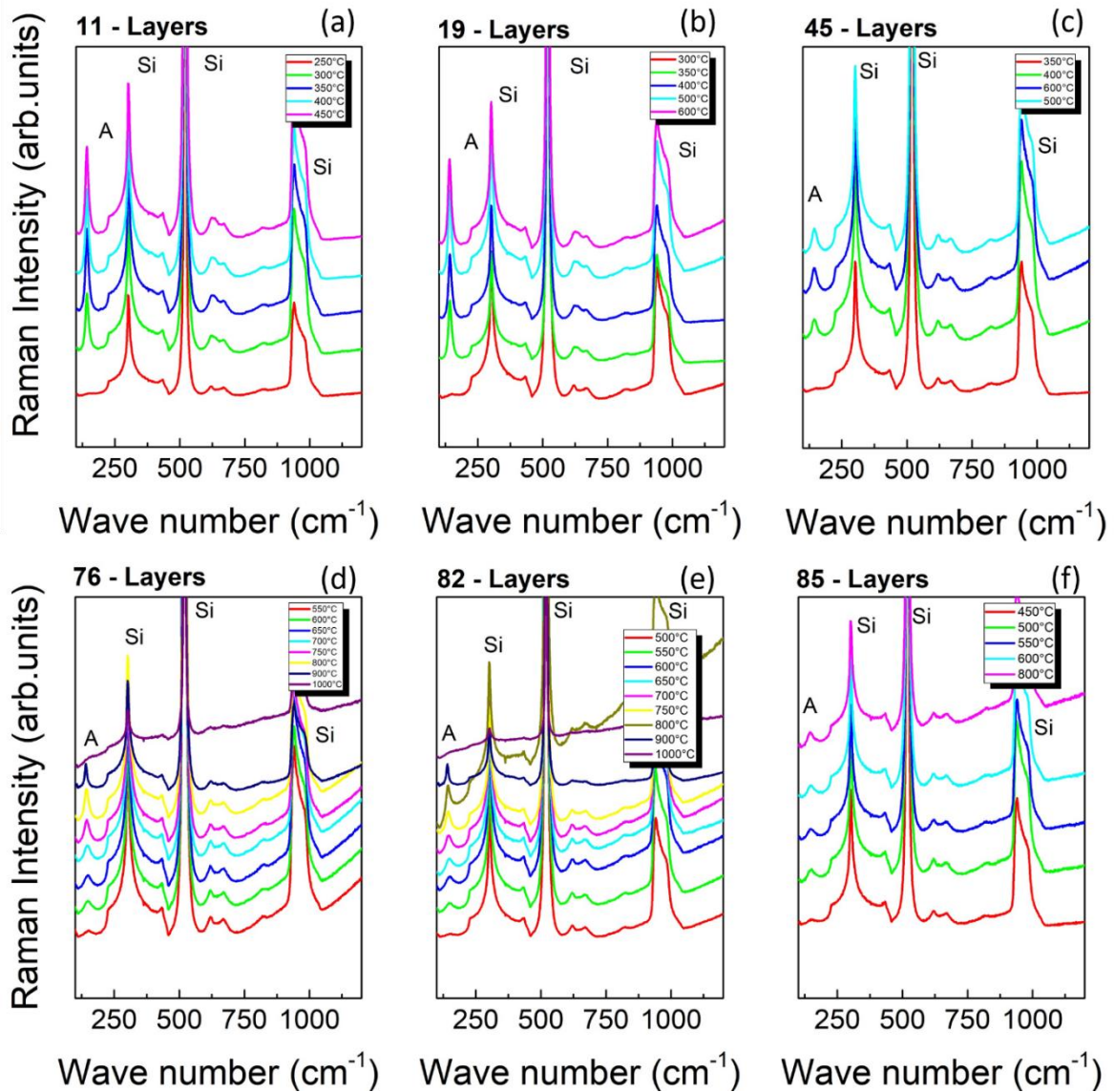


Figure 7: RS spectra for (a) 11-, (b) 19-, (c) 45-, (d) 76-, (e) 82-, and (f) 85-layer samples at different T_a . The symbols A and Si indicate the TiO₂ anatase and Si Raman modes, respectively.

As usual, the E_g Anatase mode at $\sim 144 \text{ cm}^{-1}$ represents a fingerprint for the amorphous to crystalline transition. RS analysis indicates that the T_c is driven towards higher temperatures by segmentation and the results are summarized in Table 2, just like the two plots of Figure 8 illustrating how the T_c varies as a function of the number (a) and thickness (b) of layers.

Sample	T_c (°C)
11-layers	250 - 300
19-layers	300 - 350
45-layers	350 - 400
76-layers	550 - 600
82-layers	500 - 550
85-layers	450 - 500

Table 2: Crystallization onset temperature for $\text{TiO}_2/\text{SiO}_2$ NLs.

As a general trend, the T_c increases together with the segmentation, starting from a T_c of $300 \text{ }^\circ\text{C}$ for the 11-layers and reaching a maximum of $600 \text{ }^\circ\text{C}$ for the 76-layers. Only the 82 layers seems to be slightly out-of-trend as demonstrated by Figure 8 (b). The results obtained on the NLs are thus consistent with the crystallization trend showed by the crystallization of TiO_2 single layer vs thickness. In both cases, T_c moves towards higher temperatures when reducing the volume. Figure 8(c) shows the comparison between the single layer (SL) and the NLs. Both nano- and single-layers exhibit an increasing trend of the crystallization temperature when reducing the thickness. However, the increasing rate is much stiffer when the TiO_2 is interfaced with the SiO_2 , rather than with the air. For instance, the thickest TiO_2 (18 nm), occurring in the least segmented NL (11 layers), exhibit a $T_c = 300 \text{ }^\circ\text{C}$, comparable to the one measured in the single layer case for thickness higher than 64 nm. On the other hand, the T_c extrapolated for a single layer TiO_2 , 18 nm thick, is about $360 \text{ }^\circ\text{C}$, thus higher than the NL case. Similarly, while the 5-nm thick single layer TiO_2 exhibit a T_c as high as $800 \text{ }^\circ\text{C}$, the thinnest TiO_2 occurring in the NLs (2-3 nm) stabilize at lower temperature, around $500\text{-}600^\circ\text{C}$. To justify this discrepancy, one needs to correlate the reduced dimensionality of the TiO_2 inside the NLs with the presence of the $\text{SiO}_2/\text{TiO}_2$ interfaces, whose role might be different from the pristine case of TiO_2/air interface considered in Chapter 4.

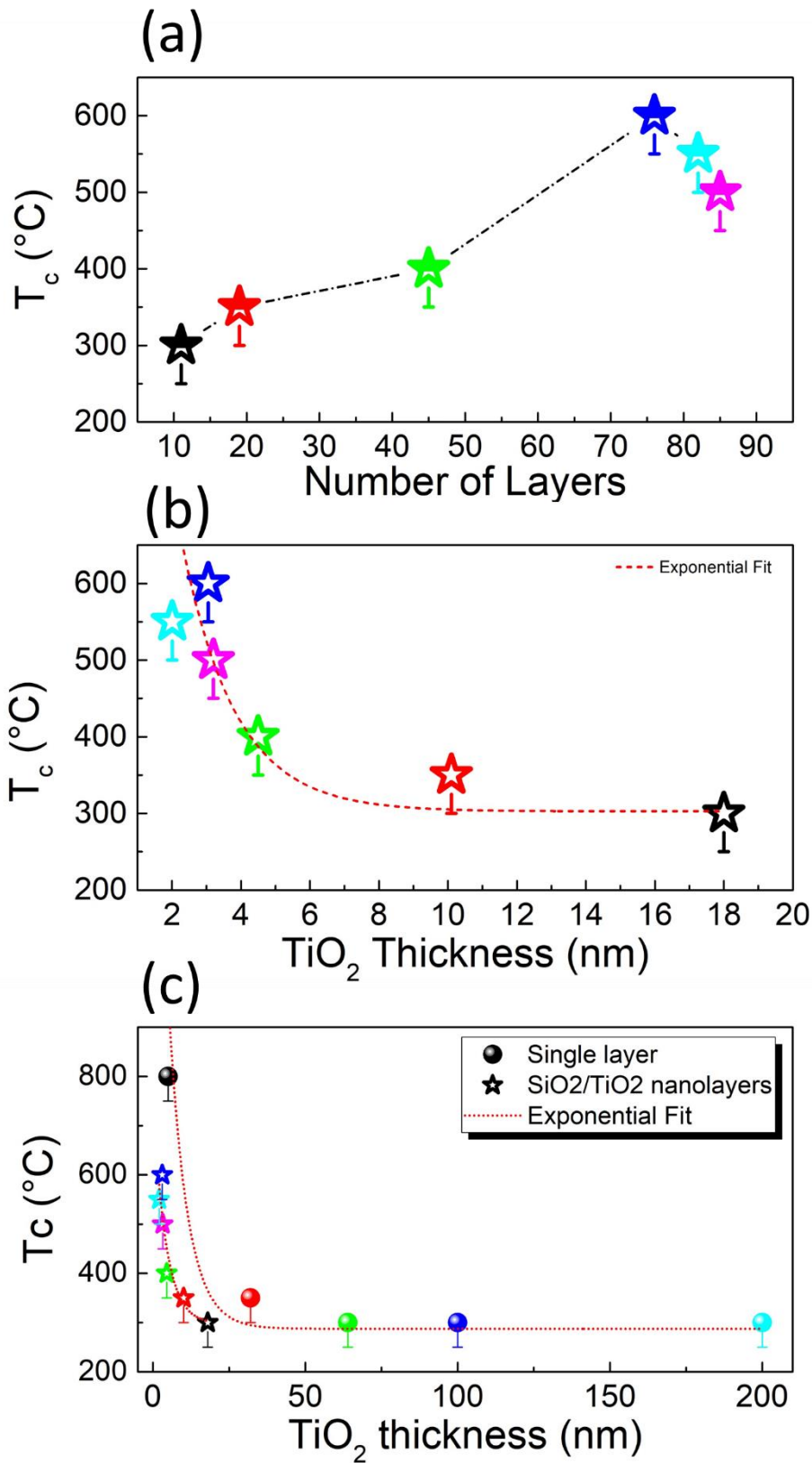


Figure 8: T_c as a function of (a) the layer number, and (b) TiO_2 thickness, in the $\text{TiO}_2/\text{SiO}_2$ nanolayers. (c) Comparison of T_c for the single layers (colored dots), and nanolayers (colored stars). Dashed black line in (a) is used as a guide for the eye, instead dashed red lines in (b,c) represent exponential fit.

Ref.[9] addresses the predominant role of the surface energy in the crystallization process of materials with reduced dimensionality. Here, one can assume that the nucleation of a crystallite occurs within the TiO₂ layer, enclosed by two adjacent amorphous SiO₂ layers, thus forming two SiO₂/TiO₂ interfaces. A sketch of this model is shown in Figure 9, where a TiO₂ crystalline cluster of typical size “*h*” nucleates in the middle of an amorphous TiO₂ layer of thickness “*d*”. The crystal is separated by a distance “*l*” from the two TiO₂/SiO₂ interfaces. For very thin films, i.e., few lattice constant thick, *l* can be set to 0, resulting in *h* = *d*.

In general, in an amorphous film the nucleation of crystalline clusters occurs in correspondence of “discontinuities” such as defects, impurities, and also interfaces.

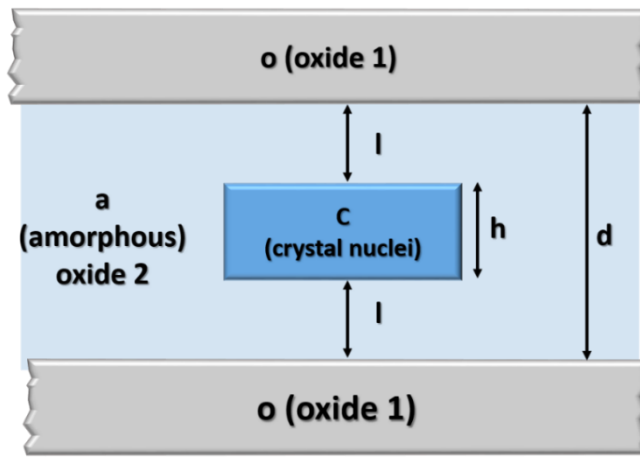


Figure 9: Model of nanocrystals embedded in an amorphous film with oxide interfaces. Adapted from [9].

To describe the problem, three interface energies per unit area can be defined as:

- 1) $\gamma_{aT/cT}$ is the interface energy between the amorphous TiO₂ and the embedded TiO₂ crystalline nucleus,
- 2) $\gamma_{aS/aT}$ is the interface energy between amorphous SiO₂ and the amorphous TiO₂,
- 3) $\gamma_{aS/cT}$ is the interface energy that occurs when the TiO₂ crystal is big enough to be interfaced to the amorphous SiO₂.

A value of $\gamma_{aT/cT} = 0.44 \text{ J/m}^2$ is here assumed for the amorphous/crystalline TiO₂ interface energy, as in Ref. [10].

In general, the crystallization onset temperature T_c , depends on interface energies as follow:

$$T_c = T_{ac} \left(1 + \frac{\gamma_{aS/cT} - \gamma_{aT/cT} - \gamma_{aS/aT}}{\gamma_{aT/cT}} e^{-\frac{d}{\lambda_d}} \right), \quad (1)$$

where λ_d is a characteristic length, and T_{ac} is the amorphous to crystalline transition temperature for bulk films [9].

On the other side, the melting temperature T_{melt} is proportional to the surface energy of pure metals [11]. Indeed, as discussed in details in Ref. [9], it follows that:

$$T_{melt_NL} = T_{ac} \frac{\gamma_{aS/cT} - \gamma_{aS/aT}}{\gamma_{aT/cT}} = T_{ac} \frac{\Gamma_{NL}(\gamma_{aS/cT}, \gamma_{aS/aT})}{\gamma_{aT/cT}}. \quad (2)$$

By combining eq. (1) and (2), one finds:

$$T_c = T_{ac} + (T_{melt} - T_{ac})e^{-\frac{d}{\lambda_d}}. \quad (3)$$

This translates into $T_{ac} = T_c$ for thick films, and $T_{ac} = T_{melt}$ for extremely thin ones. When $d = \lambda_d$, the discrepancy between the crystallization temperature of the thin film and that of the bulk must be about 37% of the discrepancy between the melting temperature and crystallization temperature in the bulk.

In the case of the single TiO_2 film, the interfaces are not symmetric, being Si/native SiO_2 on the substrate side and air on the topmost surface. The description of the problem is thus more controversial and requires introducing additional surface energies:

- 1) $\gamma_{aT/cT}$ is the interface energy between the amorphous TiO_2 and the embedded TiO_2 crystalline nucleus,
- 2) $\gamma_{aS/aT}$ is the interface energy between amorphous SiO_2 (substrate side) and the amorphous TiO_2 ,
- 3) $\gamma_{air/aT}$ is the interface energy between the air (surface side) and the amorphous TiO_2 ,
- 4) $\gamma_{aS/cT}$ is the interface energy that occurs when the TiO_2 crystal is big enough to be interfaced to the amorphous SiO_2 (on the substrate side),
- 5) $\gamma_{air/cT}$ is the interface energy that occurs when the TiO_2 crystal is big enough to be interfaced with the air (on the surface side).

While the relation intercurring among the so defined surface energies might be quite complex, the experimental result presented in Chapter 4 on the SL TiO_2 , demonstrate that it follows the trend of Eq. (3), with T_{melt} and T_{ac} satisfying the expected melting temperature and crystallization temperature for the bulk material.

In light of this, one could include in the definition of T_{melt} for the single TiO_2 layer, a more complex function of the surface energies as:

$$T_{melt_SL} = T_{ac} \frac{\Gamma_{SL}(\gamma_{aS/cT}, \gamma_{air/cT}, \gamma_{aS/aT}, \gamma_{air/aT})}{\gamma_{aT/cT}} \quad (4)$$

The fitting parameters and results for the behavior of the crystallization temperature vs layer thickness [red dashed lines in Figure 8(b)], both in the case of SLs and NLs are reported in the following table:

	SLs	NLs
T_{ac} (°C)	287	297
T_{melt} (°C)	1843	756
$\Gamma = \frac{T_{melt}}{T_{ac}} \gamma_{aT/cT}$ (J/m ²)	2.83	1.12

Table 3: T_{ac} , T_{melt} , Γ for SLs and NLs.

Accordingly with the expectation, the T_{ac} found for SL and NLs are very close to each other, and consistent with the ones found for thin films with thickness equal or higher to 64 nm. Importantly, the values found for Γ_{SL} is higher than the one found for Γ_{NL} .

Since these quantities are related to the discrepancy between i) the surface energies at the interfaces between TiO₂ crystallites and amorphous SiO₂ (or air) and ii) the surface energy at the interface between amorphous TiO₂ and amorphous SiO₂ (or air), one can conclude that the surface energies at the interfaces between TiO₂ crystallites and amorphous SiO₂ (or air) is much higher (and thus less favorable) in the single layers compared to the NLs, thus justifying the earlier occurrence of crystallization in NLs.

Besides identifying the T_c , the Raman spectra of Figure 7 show the evolution of crystallization as a function of annealing temperature up to 1000 °C. Interestingly, the 76- and 82-layer result affected by a fluorescence background that starts appearing at 900 °C, and further increases at 1000 °C (possibly given by the presence of contaminants, specifically Na, as measured by EDS in the next chapter [12]). In this case, the E_g intensity at the highest temperature drops down by reducing by 58%, probably due to the unwanted and spurious fluorescence, that could partially hinder the mode. Nevertheless, one cannot exclude the beginning of the anatase-rutile transition [13], as well as a possible effect due to the coexistence of these two phases. Indeed, as shown in the Chapter 4 for the SL TiO₂, the rutile phase is also expected at the highest annealing temperatures in very thin films, with thickness similar to the 76- to and 85-layers.

In order to investigate the presence of strains, Figure 10(a) shows the E_g peak position as a function of T_a ; the grey shaded region includes the wave number positions for the E_g mode, as reported in Refs. [14,15].

After annealing, samples with few layers, i.e., 11 and 19 layers (corresponding to a TiO₂ thickness of 18 nm and SiO₂ of 7.3 nm for the former, and TiO₂ thickness of 10.1 nm and SiO₂ of 4.6 nm for the latter) show that the E_g mode maximum position stays inside, or very close to, the shaded gray region and it slightly moves towards smaller wave numbers as T_a increases, with a slope of about $-0.003 \text{ cm}^{-1}/^\circ\text{C}$. The 45-layer sample, corresponding to a TiO₂ thickness of 4.5 nm and SiO₂ of 2.2 nm, stays almost constant in temperature just above the grey region, being slightly with respect to the 11- and 19-layer ones. For all the other highly segmented samples, 76-, 82-, and 85-layers, the blue shift of the E_g mode is much more intense. Indeed, at the beginning of the crystallization, the peak is around $148\text{-}149 \text{ cm}^{-1}$. By increasing the annealing temperature, the peak position moves toward the grey region with a similar rate of about $-0.021 \text{ cm}^{-1}/^\circ\text{C}$, for the 76- and 82-layer samples, and eventually cross it by reaching 140.6 cm^{-1} after annealing at $T_a = 900$

°C. This small red shift indicates that tensile strain is affecting the nanolayers after high temperature annealing.

The blue shift, as already discussed in previous chapters, is expected when a confinement effect takes place as a consequence of the quantum size of the very first crystallites that are nucleated at beginning of crystallization. One can analyze the early stage of crystallization by comparing the blue shift measured for single thin films (Chapter 4) with that for the nanolayers, see Figure 10(b). It appears that the phonon confinement effect is stronger and more efficient in nano-layers than in single layers of equivalent thickness.

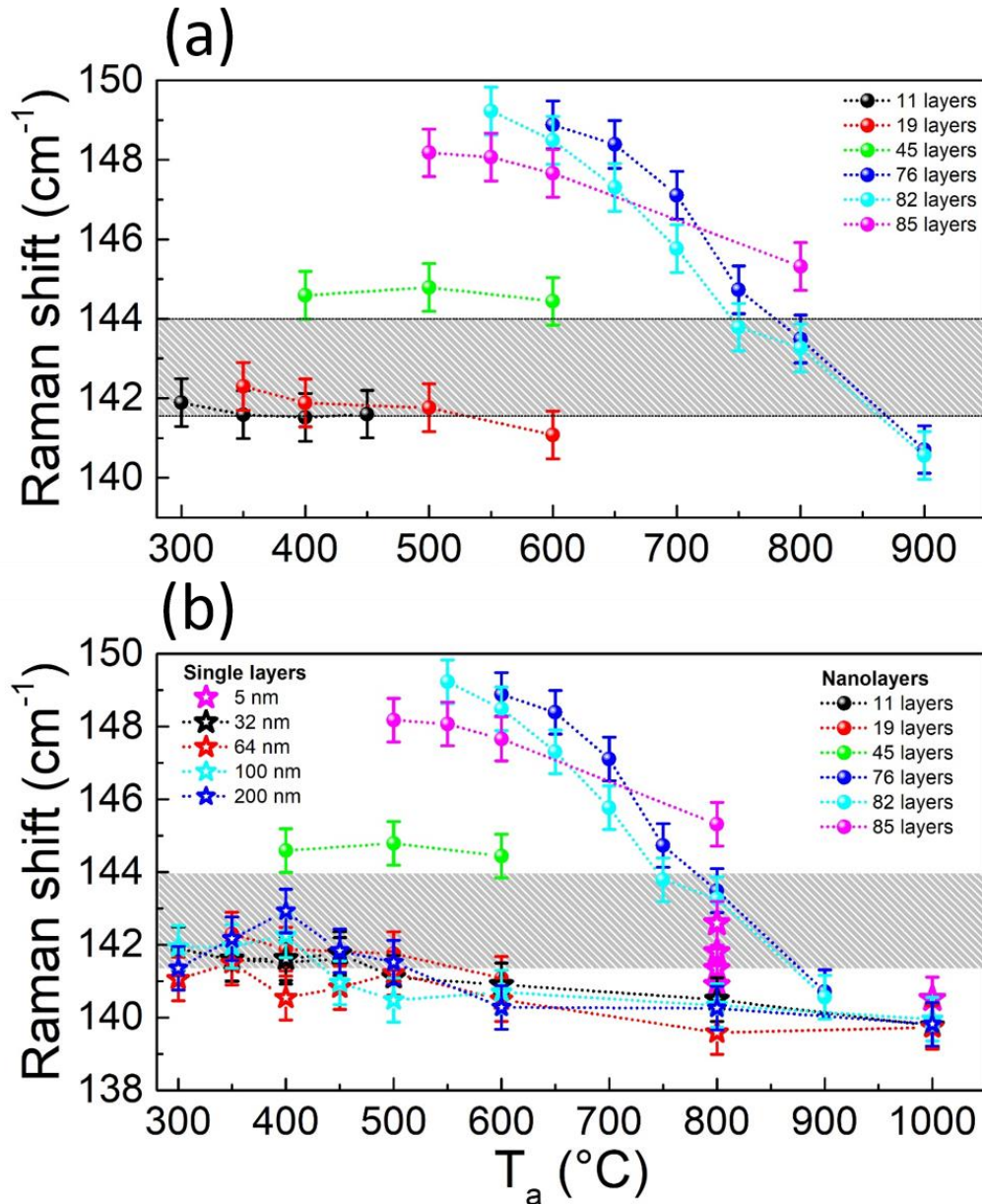


Figure 10: (a) Raman shift of NL, and (b) Comparison of Raman shift for NL and single layers. The grey region in (a) highlights the range where the E_g Raman mode is expected [14,15].

Legend in panel (a) refers to all panels.

Moreover, information on the crystal quality can be quantified by the FWHM of the Eg peak, which has to be smaller as the crystalline structure is closer to the ideal one. As already pointed out in previous chapters, lower is the concentration of scattering centers, longer is the phonon lifetime, τ , smaller is the width of the Eg peak. Figure 11(a) shows the temperature dependence of the Eg linewidth Γ (FWHM corrected by the instrumental broadening as done in Chapters 3).

Among all the samples, three different Γ values can be roughly identified at the earliest stage of crystallization, allowing to discretize them in three groups of different crystalline quality. The less segmented samples, that are those with a thicker TiO₂ layer (11 and 19) belongs to the “first group”, i.e., the one with lower Γ . The 45-layer stands by itself in the “second group”, with intermediate value of Γ , while the samples with the highest segmentation (76, 82, and 85 layers) lie together in the “third group”, with the highest Γ . These results bring to the conclusions that, at the beginning of crystallization, 1) thicker is the TiO₂ layer, better is the crystalline quality, 2) NL segmentation enhance the scattering, as proved by the lower value of phonon lifetime shown in figure 11(b), by the NLs with the highest segmentation. Moreover, Figure 11 shows that at higher T_a the crystal quality increases. Indeed, a maximum crystalline quality is reached after annealing at $T_a = 900$ °C, with a Γ of 9.33 cm⁻¹, and a correspondent phonon lifetime of about 0.6 ps (increased by a factor of 3 compared to $T_a = 550$ °C).

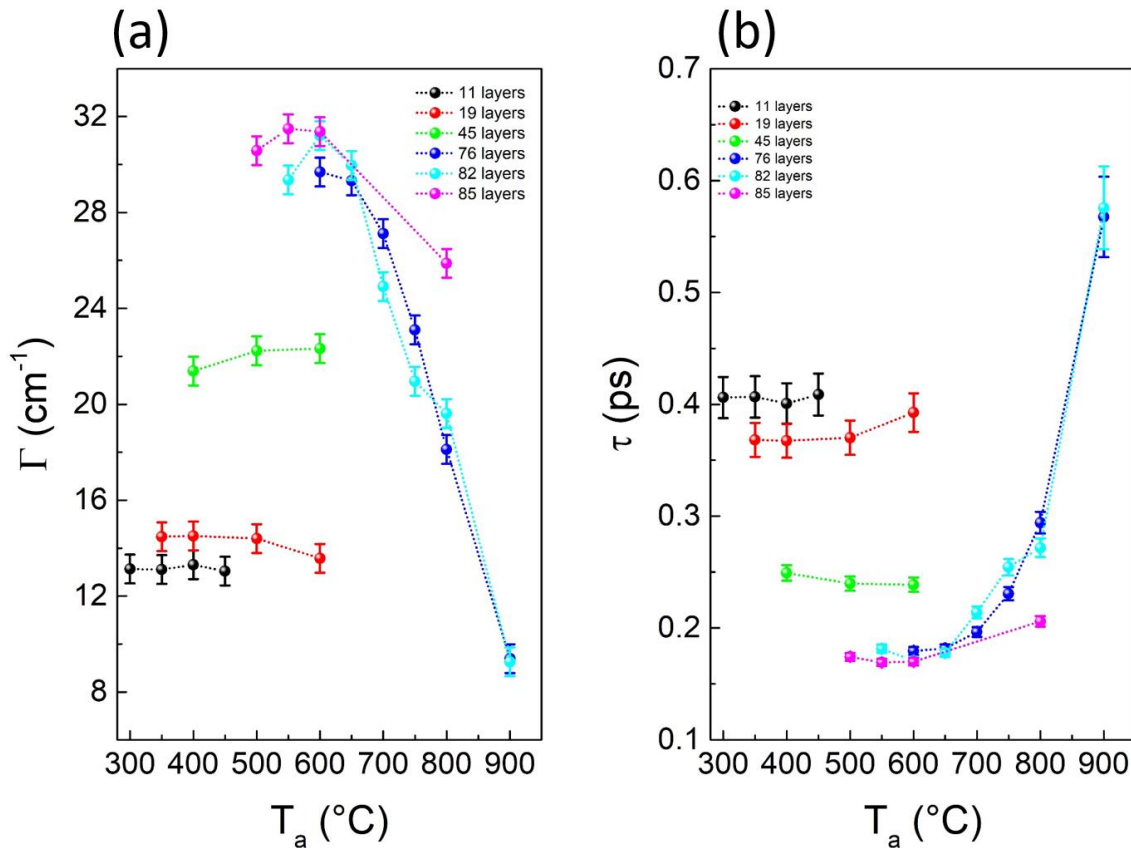


Figure 11: (a) FWHM corrected (Γ), and (b) Phonon lifetime (τ) for all samples as a function of the T_a .

Finally, the morphological changes of the surface after the annealing process have been further investigated by means of AFM. For instance, Figure 12 (a-i) shows, the results obtained on the 76- and 82-layers as acquired on a $10\ \mu\text{m} \times 10\ \mu\text{m}$ scan area for the as-grown (a,f) and annealed at $300\ \text{°C}$ (b,g), $700\ \text{°C}$ (c,h), and $1000\ \text{°C}$ (d, i). By increasing T_a up to $700\ \text{°C}$ the surface preserves its flatness (with an RMS lower than $1\ \text{nm}$), whereas it becomes corrugated, as formed by small faceted grains, upon annealing at $1000\ \text{°C}$. Thus, the RMS roughness jumps from $1\ \text{nm}$ to 4 and $5\ \text{nm}$, for the 76- and 82-layers, respectively.

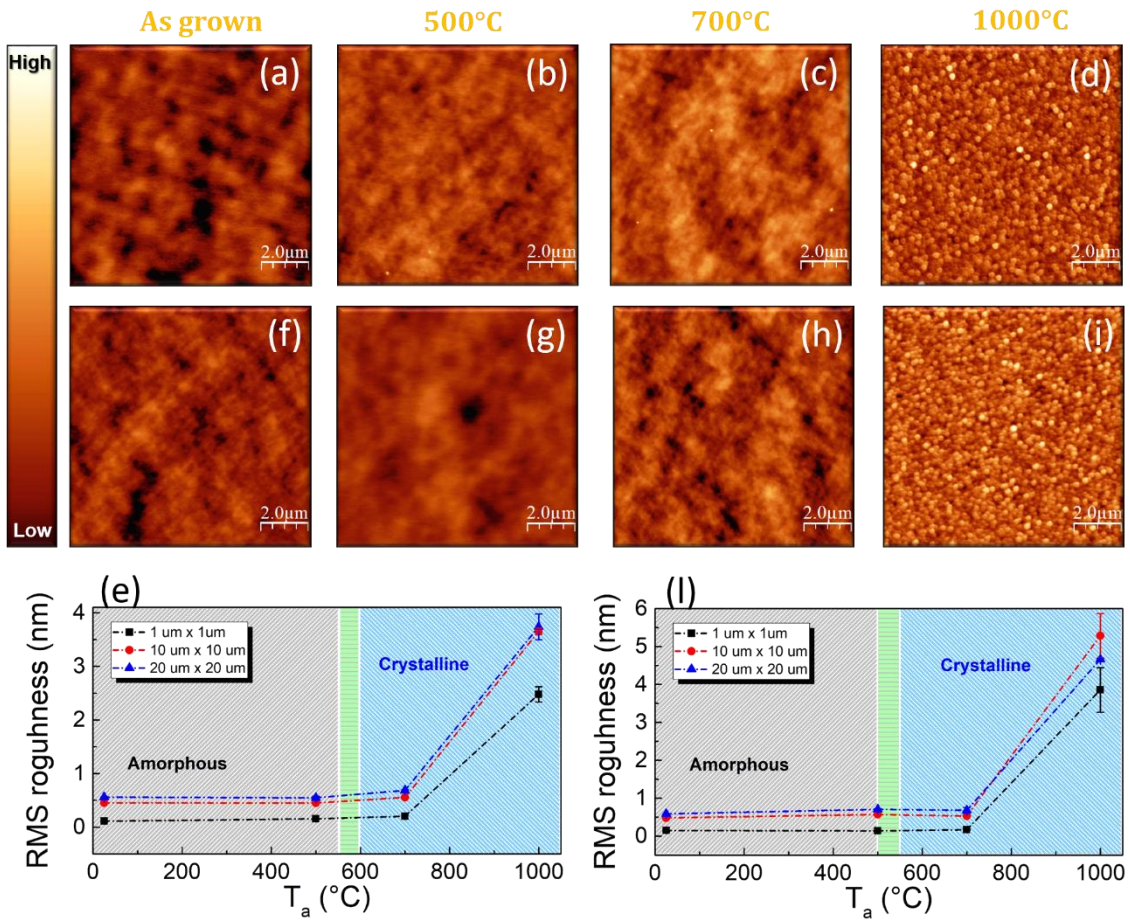


Figure 12: Tapping mode AFM topography, $10\ \mu\text{m} \times 10\ \mu\text{m}$ in size, of 76- and 82-layer sample (a,f) as-grown and annealed at (b,g) $500\ \text{°C}$, (c,h) $700\ \text{°C}$, and (d,i) $1000\ \text{°C}$. The color scale ranges from 0 to $10\ \text{nm}$ in (a–c,f–h) and from 0 to $100\ \text{nm}$ in (d,i). RMS roughness on $1\ \mu\text{m} \times 1\ \mu\text{m}$ (black squares), $10\ \mu\text{m} \times 10\ \mu\text{m}$ (red circles), and $20\ \mu\text{m} \times 20\ \mu\text{m}$ (blue triangles) scan areas, as a function of the T for (e) 76- and (l) 82-layer samples.

5.3 TiO₂-based nanolayers

In this section, NLs formed by alternating TiO₂ with Ta₂O₅, Al₂O₃, and ZrO₂ are considered. These oxides are characterized by a higher refractive index compared to SiO₂. For example, at the wavelength of 1064 nm, which is the one of the laser used in the gravitational wave antennas, the refractive index are: 2.48, 2.12, 2.07, 1.75, and 1.45 for TiO₂, ZrO₂, Ta₂O₅, Al₂O₃, and SiO₂, respectively.

As before, the NLs have been fabricated by IAD technique, and characterized by means of RS, XRD, and AFM thereafter. This time, the design adopted for the NLs keeps constant the TiO₂ thickness at 2 nm, and modulate the number (and thickness) of the other oxide to reach a desired refractive index of 2.25-2.3. Moreover, two additional thin SiO₂ layers, with a thickness of 2 nm each, have been added to the NLs design, the first at the very bottom as buffer layer with the substrate and the second at the very top of the NLs as a surface protective coating. In Table 4, the thickness of the individual layer, the total thickness, and the refractive indexes of the NLs are reported.

Sample	Average Thickness (nm)		Total Thickness (nm)	Refractive index
	TiO ₂	Ta ₂ O ₅		
TiO₂/Ta₂O₅- 68 layers	TiO₂ 1.99 ± 0.20 (x34)	Ta₂O₅ 1.39 ± 0.17(x34)	115 ± 13	2.320
TiO₂/Al₂O₃- 78 layers	TiO₂ 1.98 ± 0.21(x39)	Al₂O₃ 1.08 ± 0.18(x39)	119 ± 15	2.249
TiO₂/ZrO₂- 62 layers	TiO₂ 1.98 ± 0.26 (x31)	ZrO₂ 1.66 ± 0.35(x31)	113 ± 19	2.320

Table 4: Sample list of TiO₂/Ta₂O₅, TiO₂/Al₂O₃, and TiO₂/ZrO₂ NL.²

² The measured thicknesses are affected by thermal shock of the quartz monitor crystal in the deposition process discussed in the Appendix E. The refractive index are calculated by using the Drude model.

5.3.1 Morphological and structural characterization of $\text{TiO}_2/\text{Ta}_2\text{O}_5$, $\text{TiO}_2/\text{Al}_2\text{O}_3$, and $\text{TiO}_2/\text{ZrO}_2$ NLs

By adopting the same strategy as before, RS and XRD have been used to determine the structural phase of the NLs, and the results are showed in Figure 13 and 14, respectively. As usual, RS and XRD analyses have been performed in the as-grown state as well as after annealing at different temperatures. For all the amorphous samples, the Raman peaks present in the spectra can be associated only to the Si substrate, see Chapter 2. The crystalline Eg anatase Raman mode starts developing after annealing at 550 °C for $\text{TiO}_2/\text{Ta}_2\text{O}_5$, and at 650 °C for $\text{TiO}_2/\text{Al}_2\text{O}_3$.

In panel (c-d), the Raman shift of Eg anatase mode as a function of the annealing temperature, T_a , for $\text{TiO}_2/\text{Ta}_2\text{O}_5$, and $\text{TiO}_2/\text{Al}_2\text{O}_3$ samples, is shown. While $\text{TiO}_2/\text{Al}_2\text{O}_3$, is affected by a monotonic decreasing trend toward a slight red shift, $\text{TiO}_2/\text{Ta}_2\text{O}_5$ discloses a significative red-shift down to 138 cm^{-1} . This latter is even bigger than the one observed in $\text{SiO}_2/\text{TiO}_2$ NLs, and specifically in the 76- and 82-layer samples, having a similar TiO_2 thickness of about 2 nm.

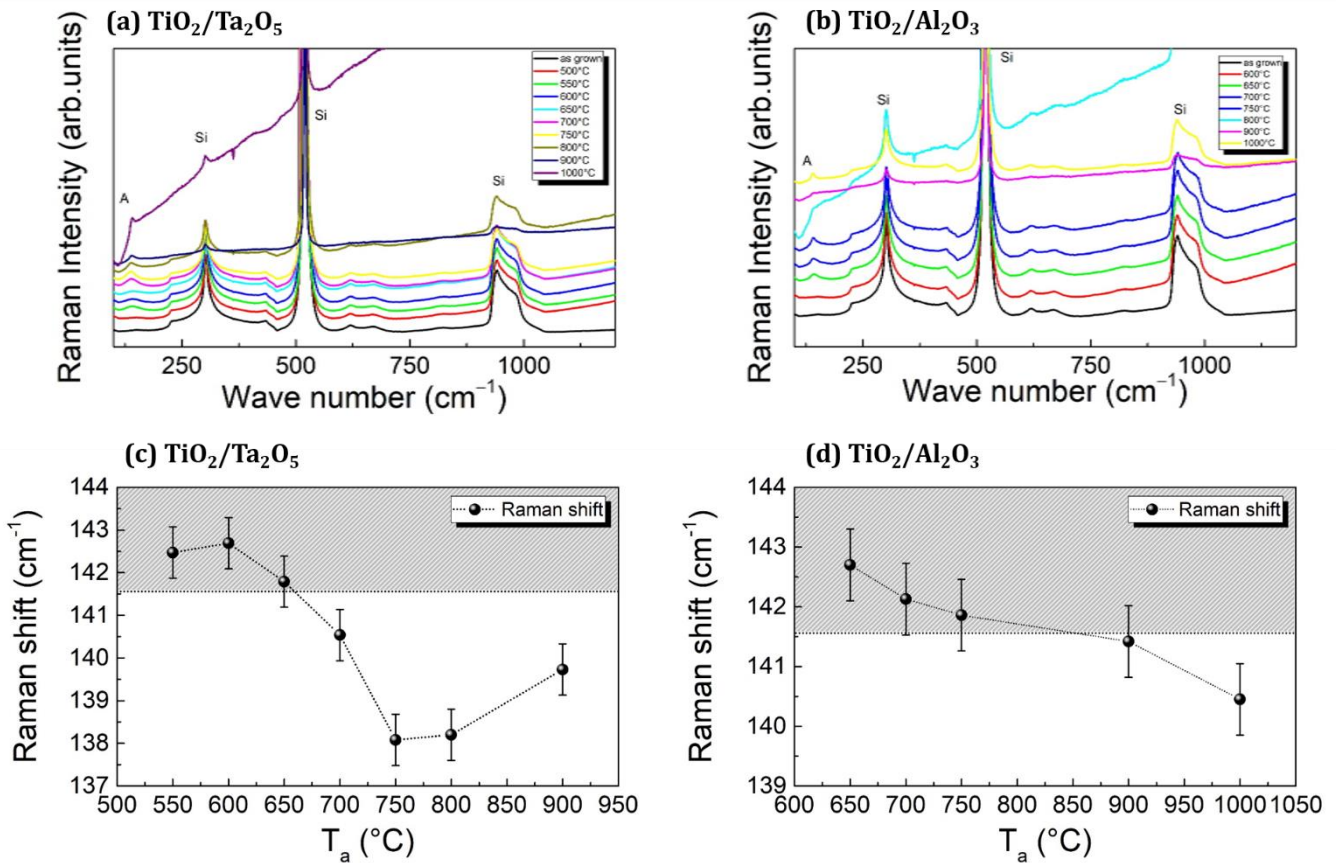


Figure 13: RS spectra for (a) $\text{TiO}_2/\text{Ta}_2\text{O}_5$, (b) $\text{TiO}_2/\text{Al}_2\text{O}_3$. For clarity of representation, all RS curves have been offset along the y-axis. Raman shift of (c) $\text{TiO}_2/\text{Ta}_2\text{O}_5$, (d) $\text{TiO}_2/\text{Al}_2\text{O}_3$ as-grown and at different T_a . The symbol A and Si indicate the TiO_2 anatase phase and Si substrate, respectively. The grey region highlights the range where the Eg Raman mode is expected [14,15].

This indicates that the crystallization in $\text{TiO}_2/\text{Ta}_2\text{O}_5$ NLs is more prone to be affected by a tensile strain of the crystal lattice. The contrary happens with respect to the phonon confinement in $\text{TiO}_2/\text{Ta}_2\text{O}_5$, where the blue shift is quite negligible at the early stage of crystallization, indicating for the case of $\text{TiO}_2/\text{Ta}_2\text{O}_5$ a crystalline growth rate vs temperature higher than what was observed in $\text{SiO}_2/\text{TiO}_2$.

The case of $\text{TiO}_2/\text{ZrO}_2$ is more controversial and require a combined analysis of XRD and RS. The former is shown in Figure 14 where one can observe that: i) the as-grown sample (black curve) is clearly amorphous (indeed, only Si reflections are visible), after annealing at 650 °C ii) an evanescent peak is observed around $2\theta = 25^\circ$ (see the inset) as possibly due to the TiO_2 crystallization incipit, iii) two small peaks at $2\theta = 29.8^\circ$, and 30.7° appear, very close to the reference value of $2\theta = 30.07^\circ$ expected for the (111) reflection of cubic ZrO_2 [16]. The presence of two peaks as well as the angle mismatch from the expected value be justified by the presence of a mixture of ZrO_2 crystallites of different phases if inside the volume irradiated by the X-ray [16].

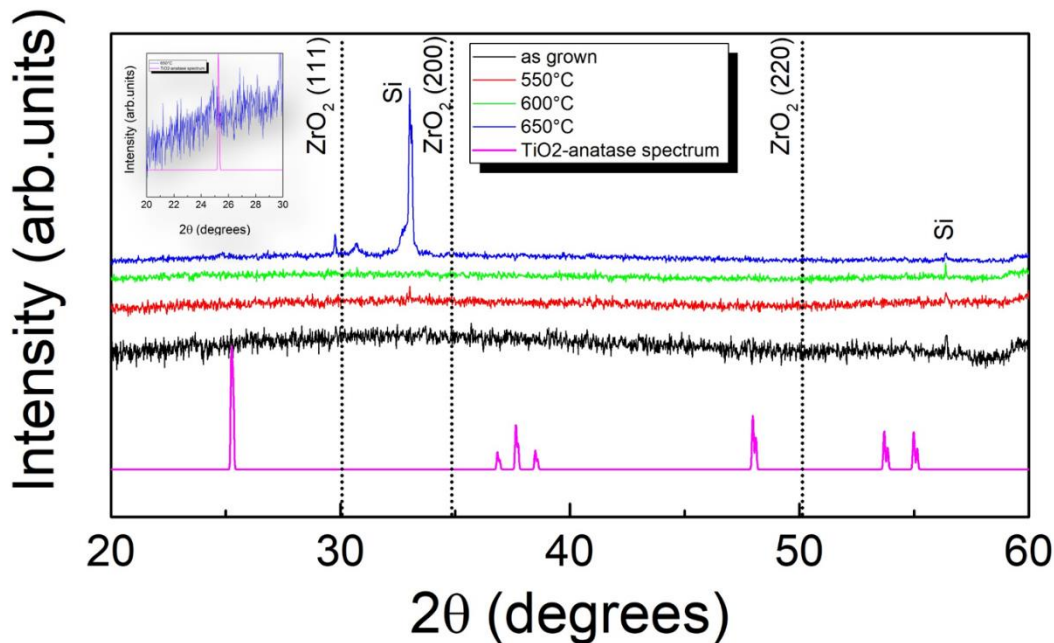


Figure 14: XRD of $\text{TiO}_2/\text{ZrO}_2$ as-grown and at different T_a . XRD spectra- 2θ range from 20 to 60° (main) and from 20 to 30° (inset). The symbol Si indicates Si reflections, and black dashed lines the ZrO_2 reflections [17].

The crystallization incipit of both ZrO_2 and TiO_2 at $T_a = 650^\circ\text{C}$ is further confirmed by RS. The E_g modes for ZrO_2 and TiO_2 are indeed expected to be centered at $\sim 177\text{ cm}^{-1}$ and $\sim 144\text{ cm}^{-1}$ respectively, however the acquired RS spectra show just the emergence of a very broad peak from 120 cm^{-1} to 190 cm^{-1} , especially visible after annealing at 700 and 800 °C. Figure 15 presents a simple comparison between the measured spectrum and the algebraic sum of the two reference Raman spectra for ZrO_2 and TiO_2 [15,18], this

simple comparison shows that the wave numbers span in the same range of values, supporting the idea that crystallization of both TiO_2 and ZrO_2 is ongoing.

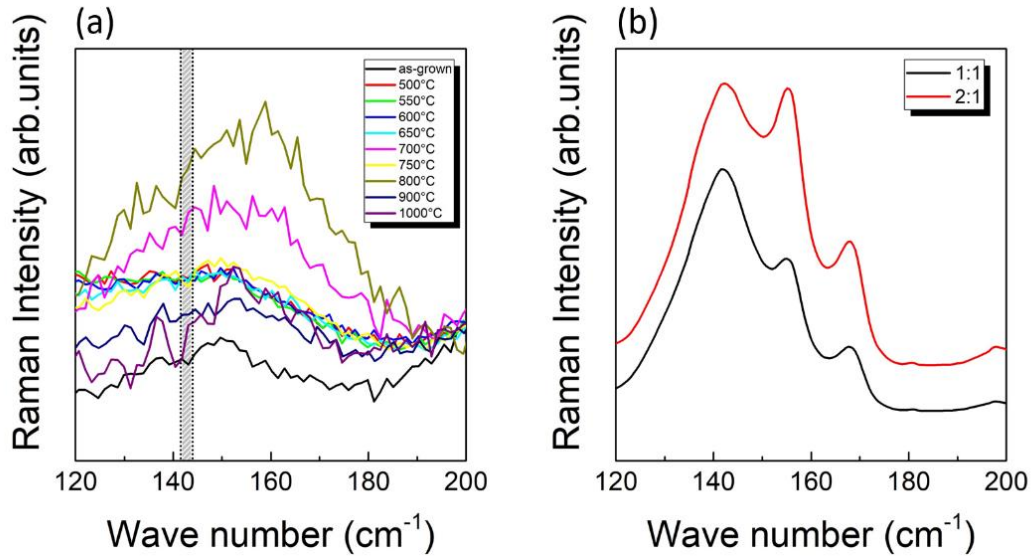


Figure 15: (a) Raman spectra in the range 120-200 cm^{-1} for the $\text{TiO}_2/\text{ZrO}_2$ for different T_a (b) Sum of TiO_2 and ZrO_2 modes with a ratio of 1:1 (black), and 2:1 (red). [15,18]

The morphology evolution of $\text{TiO}_2/\text{Ta}_2\text{O}_5$, $\text{TiO}_2/\text{Al}_2\text{O}_3$, and $\text{TiO}_2/\text{ZrO}_2$ surfaces after annealing at different temperatures is shown in Table 5. The surfaces look flat and stay unchanged up to 500 °C. At this temperature, the samples are still amorphous as suggested by XRD and RS. Signatures of crystallization start being visible at 700 °C with the formation of several morphological features such ripples and holes on the surface of $\text{TiO}_2/\text{Ta}_2\text{O}_5$. On the contrary, the $\text{TiO}_2/\text{Al}_2\text{O}_3$ and $\text{TiO}_2/\text{ZrO}_2$ surface remains more flat, due to the higher crystallization temperature. Only after annealing at $T_a = 1000$ °C, the $\text{TiO}_2/\text{Al}_2\text{O}_3$ and $\text{TiO}_2/\text{ZrO}_2$ NLs disclose clear signs of crystallization, with the AFM imaging showing profound changes. While ripples are observed in the topography of $\text{TiO}_2/\text{ZrO}_2$, a crystallite dense packing is visible in the $\text{TiO}_2/\text{Ta}_2\text{O}_5$ and $\text{TiO}_2/\text{Al}_2\text{O}_3$ morphologies.

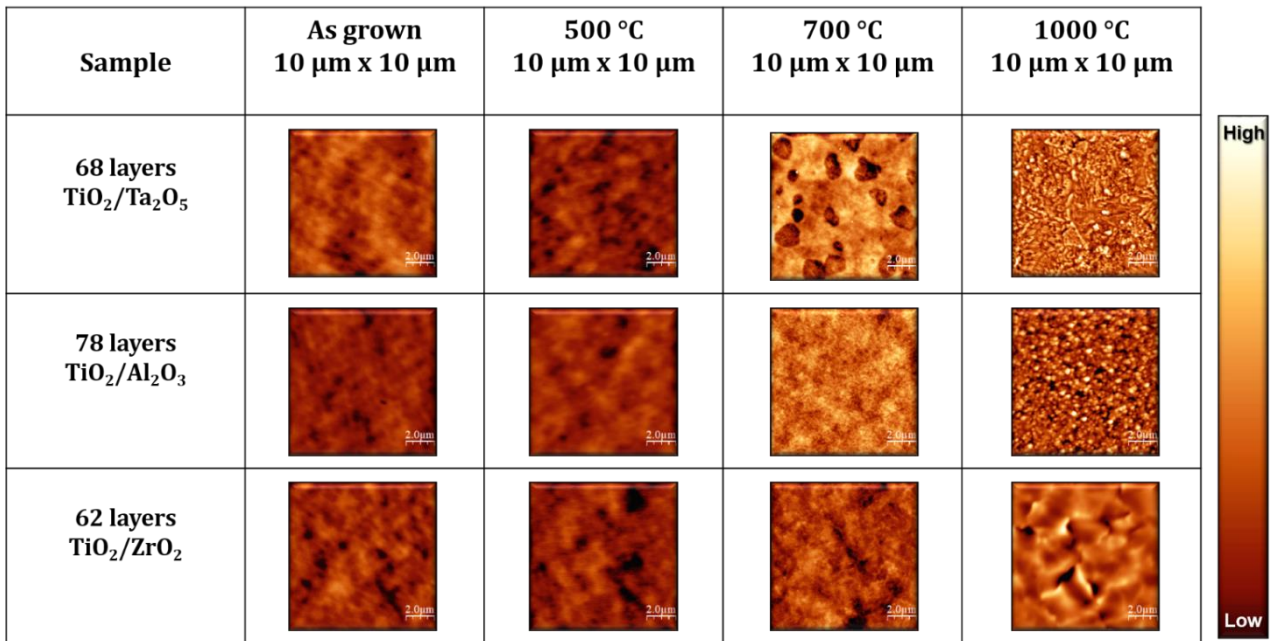


Table 5: Tapping mode AFM topography, 10 μm \times 10 μm in lateral size, of $\text{TiO}_2/\text{Ta}_2\text{O}_5$ (second row), $\text{TiO}_2/\text{Al}_2\text{O}_3$ (third row), $\text{TiO}_2/\text{ZrO}_2$ (fourth row) as-grown and annealed at different temperatures (500, 800, 1000 $^{\circ}\text{C}$). The color scale ranges from 0 to 10 nm in second, third, and fourth column, and from 0 to 100 nm in fifth column.

Finally, the study of the RMS roughness of $\text{TiO}_2/\text{Ta}_2\text{O}_5$, $\text{TiO}_2/\text{Al}_2\text{O}_3$, and $\text{TiO}_2/\text{ZrO}_2$ NLs as a function of T_a is showed in Figure 16(a-c). The evolution of roughness is very similar among all the NLs, staying below 1 nm up to $T_a = 500$ $^{\circ}\text{C}$, and increasing soon after, with the $\text{TiO}_2/\text{ZrO}_2$ that for $T_a=1000$ $^{\circ}\text{C}$ shows the smallest RMS roughness value.

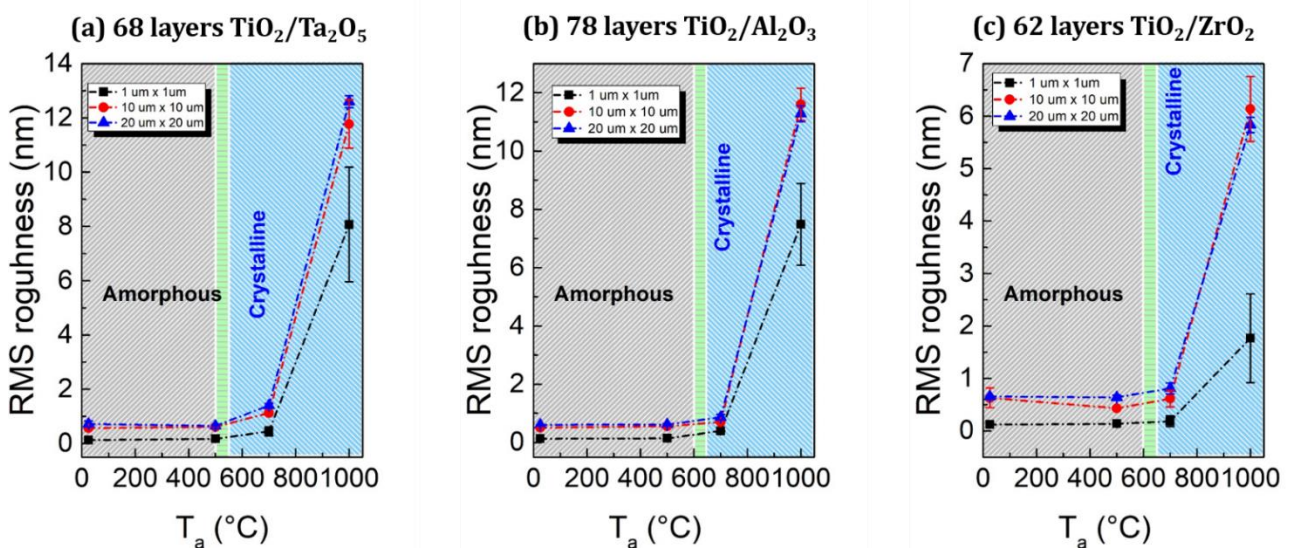


Figure 16: RMS roughness, on 1 μm x 1 μm (black squares), 10 μm x 10 μm (red circles), and 20 μm x 20 μm (blue triangles) scan areas, as a function of the T_a for (a) $\text{TiO}_2/\text{Ta}_2\text{O}_5$, (b) $\text{TiO}_2/\text{Al}_2\text{O}_3$, and (c) $\text{TiO}_2/\text{ZrO}_2$ samples.

5.4 SiO₂-based nanolayers

In this section, the preliminary results obtained on a LI prototype made of SiO₂-Al₂O₃ doublets, is discussed. The latter have been deposited by using IAD, and have been characterized by means XRD, and AFM. This time, the NLs are segmented in 40 doublets made of 40 layers of SiO₂, with 1.1 nm thick, and 40 layers of Al₂O₃, 5 nm thick, and with a total thickness of 244 nm. The effective refractive index is expected to be 1.704 at 1064 nm.

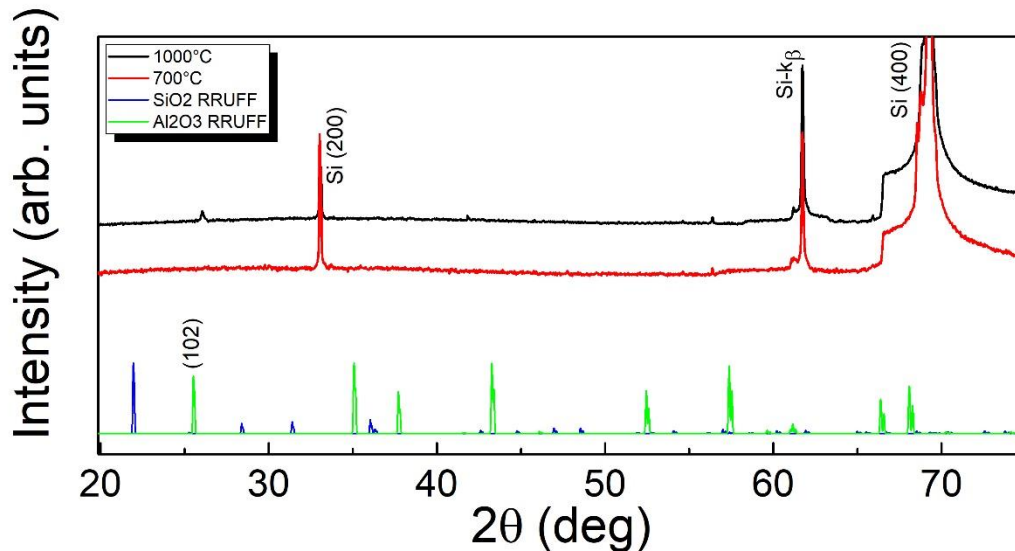


Figure 17: XRD spectra of SiO₂/Al₂O₃ NL annealed at 700 (red curve) and 1000 °C (black curve). The green and blue curves represent the reference spectra of Al₂O₃ and SiO₂ [19,20], respectively.

The XRD analysis shown in Figure 17 indicates the amorphicity of the NL up to 700 °C (the red curve only discloses the Si reflections). At 1000 °C (black curve) Al₂O₃ crystallization occurs through (102) reflection, setting the T_c for this sample between 700 and 1000 °C.

From a morphological point of view, Figures 18 (a-d) display the temperature evolution of the topography showing a surface that stays unchanged up to 700 °C, while is profoundly modified by the annealing at 1000 °C. This result is further confirmed by the RMS roughness, see Figure 18 (e), which stays lower than 2 nm up to 700 °C, and then increases above 10 nm at 1000 °C.

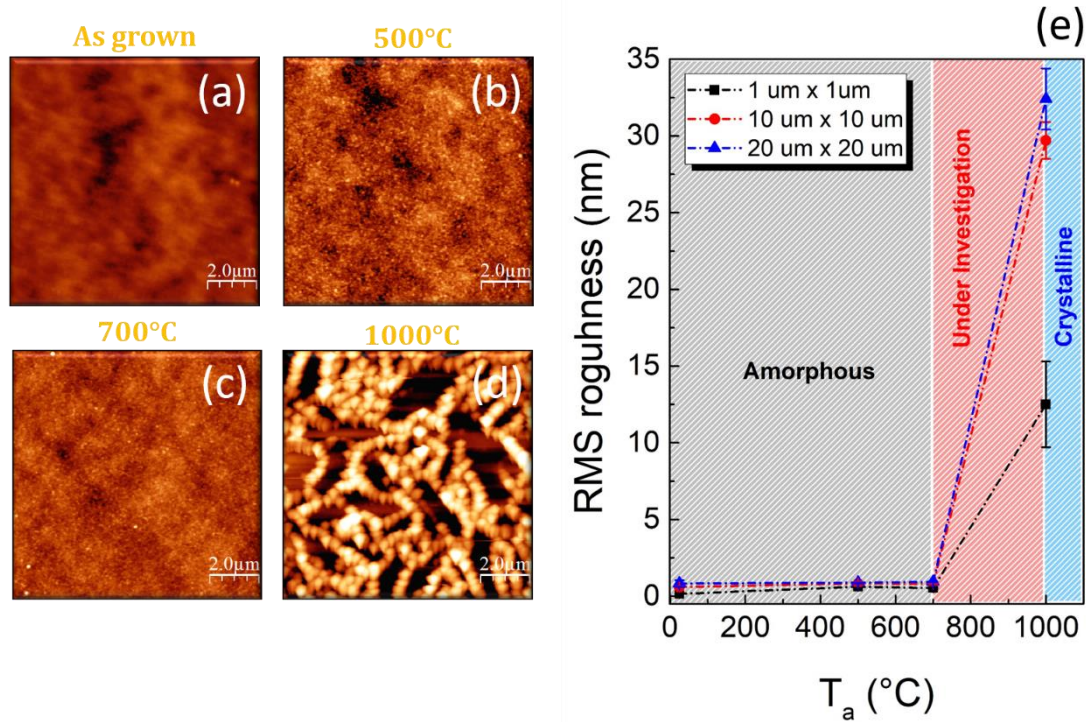


Figure 18: Tapping mode AFM topography, $10\ \mu\text{m} \times 10\ \mu\text{m}$ in size, of $\text{SiO}_2/\text{Al}_2\text{O}_3$ sample (a) as-grown and annealed at (b) 500, (c) 700, and (d) 1000 °C. The color scale ranges from 0 to 10 nm in (a–c) and from 0 to 100 nm in (d). (e) RMS roughness as a function of the T_a for $1\ \mu\text{m} \times 1\ \mu\text{m}$ (black squares), $10\ \mu\text{m} \times 10\ \mu\text{m}$ (red circles), and $20\ \mu\text{m} \times 20\ \mu\text{m}$ (blue triangles) scan areas.

Summary

This chapter focused on the study of the morphological and structural properties of i) NL of $\text{SiO}_2/\text{TiO}_2$, ii) NL formed by alternating TiO_2 with different materials (Ta_2O_5 , Al_2O_3 , ZrO_2), and iii) $\text{SiO}_2/\text{Al}_2\text{O}_3$ nanostructures, deposited on Si substrate by using IAD.

The motivations of the chosen design are given in the introduction and related to the context of thermal noise reduction for applications as reflectors in the GWDs. The strategy relies on a design able to provide high reflectivity and high crystallization temperature, as the annealing has been shown to further improve the materials' optical and mechanical losses.

The first section, called *SiO₂/TiO₂ nanolayers vs segmentation degree*, illustrated the properties of $\text{SiO}_2/\text{TiO}_2$ samples, characterized by different layer thickness and therefore different number of layers (total thickness is kept constant to preserve the Bragg condition). The high resolution morphology of these samples, in the as-grown phase, shows particles that become less pronounced as the layer number increase (layer thickness is reduced). This behavior is reflected by the RMS roughness, which decreases by increasing the number of layers. Moreover, Raman measurements confirm that all the as-

grown samples are amorphous. Importantly, the estimate of the inner layer thickness has pursued by using both XRR and STEM, and confirmed the expected, nominal values.

A dependence of the crystallization temperature on the number of layers, i.e., on the layer thickness, is also observed. While the qualitative trend is similar to the one observed in single layer TiO₂, the behavior of T_c in the NLs is much stiffer. Consideration on the variation in surface energies, between SLs and NLs, are given to explain the observed discrepancy. Insights on the presence of crystallization-induced strain are given by studying the evaluation of Raman spectra vs annealing temperature. Consistently with the expectation, the AFM morphology of the studied samples preserves their flatness up to 700 °C, to undergo a deep change upon high temperature annealing.

The second section, called *TiO₂-based nanolayers*, focused on the morphological and structural properties of the NL of TiO₂ alternated with Ta₂O₅, Al₂O₃, and ZrO₂. In this case, the crystallization temperatures are found to be in between 500-550 °C for the TiO₂/Ta₂O₅ sample, and between 600-650 °C for both the TiO₂/Al₂O₃ and the TiO₂/ZrO₂. The latter exhibits a more controversial behavior, probably related to the simultaneous crystallization of both TiO₂ and ZrO₂. Further investigations are needed to address the validity of this conclusion. As before, a thermal evolution of the morphology is observed by AFM, showing peculiar structures appearing after annealing at T_a = 1000 °C.

The final section, called *SiO₂-based nanolayers*, introduced a single example of nanolayering strategy applied to the LI. This time the crystallization temperature reaches even higher temperature, being somewhere in between 700 and 1000 °C. The morphology evolves accordingly.

References

1. Villar, A. E., *et al.* Measurement of thermal noise in multilayer coatings with optimized layer thickness. *Physical Review D* **2010**, *81(12)*, 122001.
2. W. H. Wang S. Chao. Annealing effect on ion-beam-sputtered titanium dioxide film. *Optics letters* **1998**, *23(18)*, 1417-1419.
3. Magnozzi, M., *et al.* Optical properties of amorphous SiO₂-TiO₂ multi-nanolayered coatings for 1064-nm mirror technology. *Optical Materials* **2018**, *75*, 94-101.
4. Harry, G. M., *et al.* Thermal noise in interferometric gravitational wave detectors due to dielectric optical coatings. *Classical and Quantum Gravity* **2002**, *19(5)*, 897.
5. Hadjoub, I., *et al.* Post-deposition annealing effect on RF-sputtered TiO₂ thin-film properties for photonic applications. *Applied Physics A* **2016**, *122(2)*, 78.
6. Smith, K. *et al.* Effects of proton irradiation on structural and electrochemical charge storage properties of TiO₂ nanotube electrodes for lithium-ion batteries. *Journal of Materials Chemistry A* **2017**, *5(23)*, 11815-11824.
7. Sintonen, S., *et al.* X-ray reflectivity characterization of atomic layer deposition Al₂O₃/TiO₂ nanolaminates with ultrathin bilayers. *Journal of Vacuum Science & Technology A: Vacuum, Surfaces, and Films* **2014**, *32(1)*, 01A111.
8. Stoev, K. N., Sakurai, K. Review on grazing incidence X-ray spectrometry and reflectometry. *Spectrochimica Acta Part B: Atomic Spectroscopy* **1999**, *54(1)*, 41-82

9. Zacharias, M., Streitenberger, P. Crystallization of amorphous superlattices in the limit of ultrathin films with oxide interfaces. *Physical Review B* **2000**, *62*(12), 8391.
10. Mansoorianfar, M., *et al.* Amorphous/crystalline phase control of nanotubular TiO₂ membranes via pressure-engineered anodizing. *Materials & Design* **2021**, *198*, 109314.
11. Qi, W. H., *et al.* Surface-Area-Difference model for melting temperature of metallic nanocrystals embedded in a matrix. *In Solid State Phenomena* **2007**, *121*, 1181-1188.
12. Wei, D., *et al.* Review of fluorescence suppression techniques in Raman spectroscopy. *Applied Spectroscopy Reviews* **2015**, *50*(5), 387-406.
13. Sankur, H., Gunning, W. Crystallization and diffusion in composite TiO₂-SiO₂ thin films. *Journal of applied physics* **1989**, *66*(10), 4747-4751.
14. Allen, N.S *et al.* The effect of crystalline phase (anatase, brookite and rutile) and size on the photocatalytic activity of calcined polymorphic titanium dioxide (TiO₂). *Polymer degradation and stability* **2018**, *150*, 31-36.
15. RRUFF. Available online: <https://rruff.info/chem=Ti,O/display=default/R070582> (accessed on 20 September 2021).
16. Lu, F., *et al.* Phase transformation of nanosized ZrO₂ upon thermal annealing and intense radiation. *The Journal of Physical Chemistry C* **2011**, *115*(15), 7193-7201.
17. Zhao, C., *et al.* In situ crystallisation in ZrO₂ thin films during high temperature X-ray diffraction. *Microelectronics Reliability* **2001**, *41*(7), 995-998.
18. RRUFF. Available online: <https://rruff.info/chem=Zr,O/R100171> (accessed on 29 October 2021)
19. RRUFF. Available online: <https://rruff.info/chem=O,Si/display=default/R061107> (accessed on 24 September 2021).
20. RRUFF. Available online: <https://rruff.info/chem=O,Al/display=default/R040096> (accessed on 24 September 2021).

Chapter 6

Co-sputtered TiO₂-Ta₂O₅

This chapter will address the extent of combining the TiO₂ with another high-refractive index dielectric oxide, such as the Ta₂O₅, in a co-sputtered mixture, to unveil the effect of Ta₂O₅ on the crystallization and crystallization evolution of TiO₂, whose crystallization-related properties have been systematically studied in previous chapters. This study, conducted by using AFM, XRD, RS, and EDS, will focus on a range of mixture, TiO₂ (0, 25, 75, 80, 90, 100 %), where the percentage indicates the nominal amount of TiO₂ in the final TiO₂-Ta₂O₅ mixture. In the percentage of 20, co-sputtered TiO₂-Ta₂O₅ has direct applications in the nowadays gravitational wave detectors, as the high-index mirror's counterpart. Noteworthy, the samples investigated here are produced at LMA in Lyon that develops and delivers all the optical components for the gravitational antennas. In this field, further structural, morphological, optical, and mechanical studies are very much needed to determine if different percentages can exploit similar/better performances compared to the one currently in use. For this reason, the mixture studied in this chapter were explored on both Si substrate – more convenient, for technical reasons, for some of the employed characterization techniques - and on fused SiO₂ – necessary to implement the final application.

The first paragraph of this chapter will thus focus on the state of art of the co-sputtered TiO₂-Ta₂O₅ materials used for the mirrors for gravitational wave detectors, and fabricated at LMA by using an IBS. The second part will be dedicated to the structural and morphological study of the as-grown and annealed TiO₂-Ta₂O₅ thin films, deposited on Si substrate, XRD, RS, and AFM analyses allowed determining the crystallization onset temperature, T_c, of the compound and the counterpart of TiO₂, and Ta₂O₅, the strain/stress inside the materials, and the peculiar morphological structures occurring at the surface, respectively. Note that the role of the surface is fundamental in the light scattering for optical applications. Additionally, EDS measurements are carried out to determine any contamination apart from the expected materials. Finally, the third part of the chapter will describe the structural and morphological properties of the as-grown and annealed co-sputtered TiO₂-Ta₂O₅ deposited on SiO₂. Differently from the samples deposited on Si, and given the crucial importance of making reliable characterizations of the properly treated materials, on their proper substrate for optical applications, this study is not carried out in a full range of thermal annealing but just restricted to the 500 °C one. This restriction is based on the procedure of optimal post-deposition annealing, developed at LMA. Thus, the annealed sample analyzed here were heat-treated at LMA to perform the procedure in the most similar way compared to the final mirrors.

6.1 State of art of co-sputtered materials

The study, development and delivery of co-sputtered $\text{TiO}_2\text{-Ta}_2\text{O}_5$ materials was done by LMA with the aim of reducing the contribution of mirror's thermal noise, and increase the observational sensitivity of the gravitational wave detectors [1-5]. As discussed in the introduction, thermal noise comes from the thermal fluctuations of the massive suspended mirrors (Bragg reflectors) [6,7] due to the random motion of particles (atoms and molecules) in both coatings and substrates [8,9]. Several works [10-14] demonstrated that both post-deposition annealing at 500 °C and TiO_2 doping increase the Ta_2O_5 refractive index and reduce absorption and mechanical losses, preserving the amorphous phase.

Figure 1 shows the coating loss angle of $\text{TiO}_2\text{-Ta}_2\text{O}_5$ samples, deposited by IBS, performed by using an innovative method to study and measure the mechanical performances of the coated mirror, without damaging the film, based on a point suspension, and thus called gentle nodal suspension (GENS) [15,16]. GENS measurements of $\text{TiO}_2\text{-Ta}_2\text{O}_5$ as a function of TiO_2 doping are shown in Figure 1 (a), while a comparison with the coating loss angle of Ta_2O_5 is shown in (b). Panel (a) shows that the lowest loss angle is reached at 18% of TiO_2 . Instead, panel (b) shows the comparison of Ta_2O_5 with $\text{TiO}_2\text{-Ta}_2\text{O}_5$ (18%), after annealing at 500 °C for 10 h. It is evident that the loss angle of $\text{TiO}_2\text{-Ta}_2\text{O}_5$, is even lower than the one of pure Ta_2O_5 .

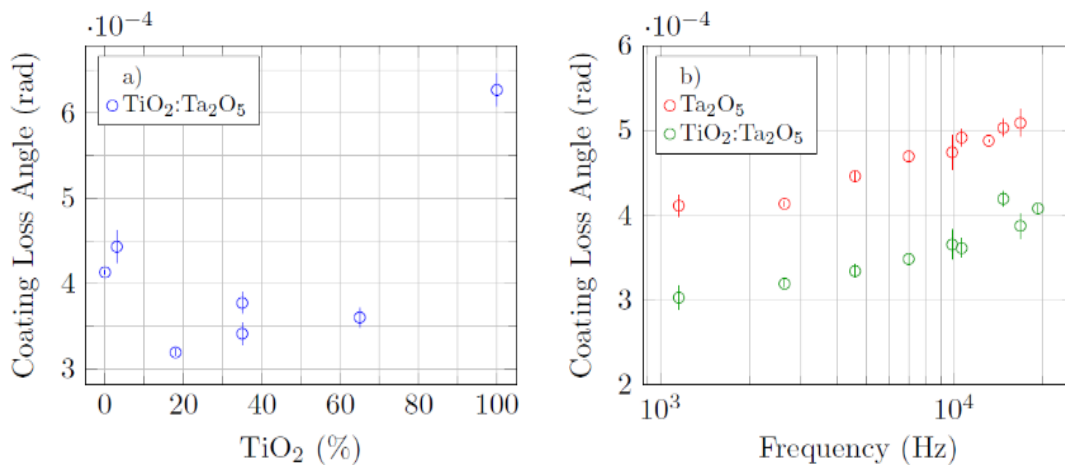


Figure 1: (a) Coating loss of $\text{TiO}_2\text{:Ta}_2\text{O}_5$ as function of TiO_2 doping. (b) Comparison of Ta_2O_5 and 18%-doped $\text{TiO}_2\text{:Ta}_2\text{O}_5$ coating loss. Adapted from [12].

Moreover, the TiO_2 doping potentially increase the crystallization temperature. In fact, it has been shown that the T_c of Ta_2O_5 and $\text{TiO}_2\text{-Ta}_2\text{O}_5$ (with a cation ratio = 0.27) films is 650 and 700 °C, respectively [17].

6.2 Co-sputtered $TiO_2-Ta_2O_5$ deposited on Si

The $TiO_2-Ta_2O_5$ thin films on Si substrate were deposited by using IBS at LMA, and studied at University of Salerno by means of AFM, EDS, XRD and RS. All samples have been routinely characterized in the as-grown state as well as after in-air thermal annealing, in the temperature range of 300 – 1000 °C. Thermal processes have been performed at the University of Salerno by employing the following procedure: (1) heating ramp with a fixed raising temperature rate (3 °C/min), (2) plateau at the desired temperature setpoint, for 12 h, and (3) cooling ramp with a fixed decreasing temperature rate (1 °C/min). A minimum temperature step of 50 °C is used among the different thermal treatments. Also in this case, each treatment is performed on a pristine fragment of the as-grown sample, to avoid any memory effect of multiple subsequent heating/cooling cycles. Table 1 shows the codes and the properties (nominal and measured concentration, and thickness) of the investigated samples.

Code	Sample	Ti/(Ta+Ti) (%) nominal	Ti/(Ta+Ti) From EDS @UniSa (%)*	Thickness (nm) ³
c20014	Ta ₂ O ₅	0	7.1±0.6	430
c19088	TiO ₂ - Ta ₂ O ₅ (25%)	25	16.1±0.5	502
c16065	TiO ₂ - Ta ₂ O ₅ (50%)	50	38±1	480
c20015	TiO ₂ - Ta ₂ O ₅ (80%)	80	83±1	848
c20016	TiO ₂	100	96±1	542

Table 1: Sample list (* values extracted by EDS measurements are discussed in the next sections).

6.2.1 XRD measurements

In order to study the T_c of the provided coatings, all samples have been routinely analyzed by XRD measurements. The notation used in the following refer to the nominal concentration values for the measured samples. For the effective values, refer to Table 1.

³The thicknesses have been measured by using a spectrophotometer at LMA and by means spectroscopic ellipsometry at University of Genova.

Figure 2(a-d) shows the XRD spectra of Ta₂O₅ and TiO₂-Ta₂O₅ (25%, 50%, 80%). In all panels the black dashed lines indicate the Ta₂O₅ hexagonal reflections [18], instead in Figure 2(b-d), the magenta and blue curves represent the reference spectrum of the TiO₂ anatase and rutile phase, respectively [19,20].

In agreement with the literature [21], the T_c of pure Ta₂O₅ [Figure 2(a)] occurs at a temperature higher than 600°C. Indeed, the XRD spectrum of the as-grown sample (black) and that of the one annealed at T_a = 600 °C (red) are still identical, indicating the persistence of amorphicity up to that temperature. On the contrary, the Ta₂O₅ hexagonal reflections appear after annealing at T_a = 700 °C (green), and further develop at 800 °C (blue).

On the other hand, the interpretation of the XRD spectra of TiO₂-Ta₂O₅ is more complicated since it may require discriminating the T_c of the two TiO₂ and Ta₂O₅ counterparts. At the lowest doping content (25%) [Figure 2(b)], the first features of Ta₂O₅ crystallization appear in a temperature range between 650-700 °C (red and green curves), similar to the pristine one, while a tiny peak representative of the TiO₂ anatase crystallization appears at 2θ~25° only upon T_a = 800 °C (yellow).

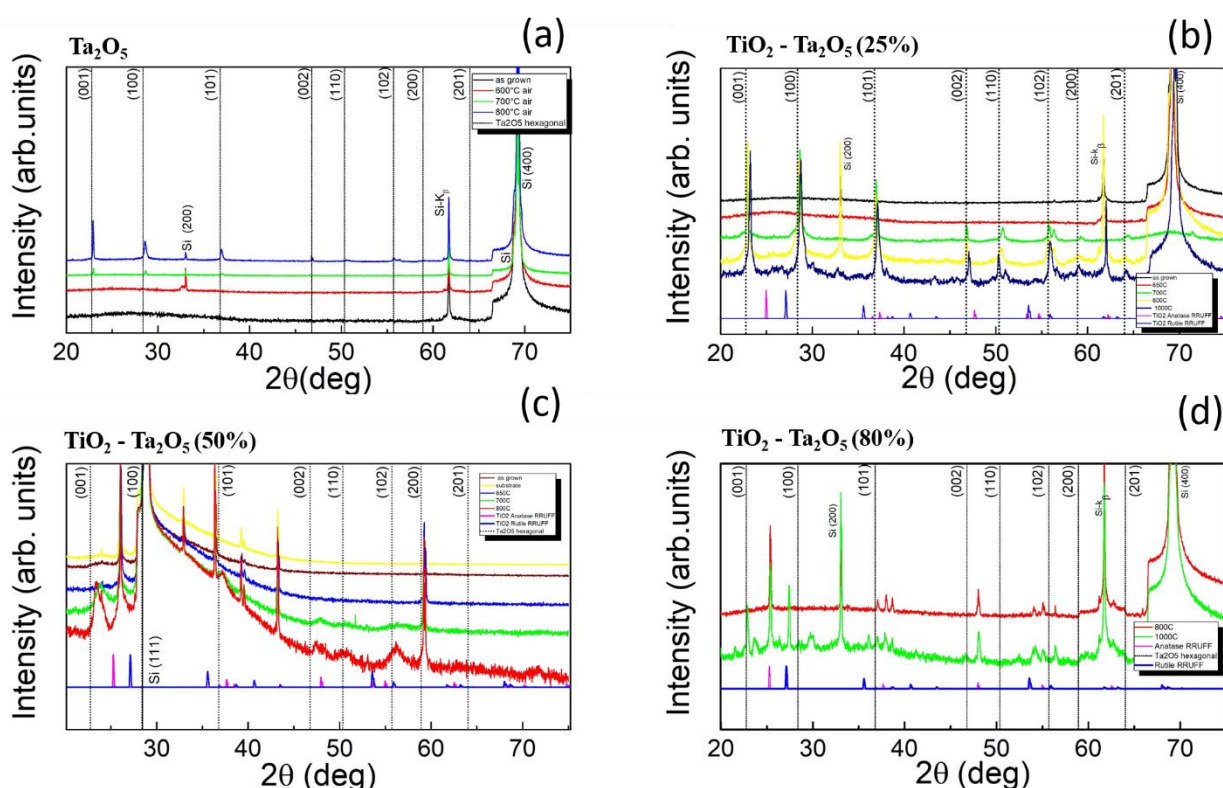


Figure 2: XRD spectra of: (a) Ta₂O₅; (b) TiO₂ - Ta₂O₅ (25%); (c) TiO₂ - Ta₂O₅ (50%); (d) TiO₂ - Ta₂O₅ (80%). The XRD spectra were acquired with time/step of 0.6 s, and 2θ step of 0.02°. The magenta and blue spectra in (b), (c), (d) is the reference for TiO₂ anatase and rutile phases, as extracted from the RRUFF database [19,20]. The dashed black lines indicate the reflections of the Ta₂O₅ hexagonal phase [18].

At the highest doping content (80%) [Figure 2(d)], the Ta₂O₅ counterpart appears still amorphous upon annealing at T_a = 800 °C (red curve), while it develops crystalline reflections (green curve) at 1000 °C, thus proving that the T_c of Ta₂O₅ is in a temperature range of 800-1000 °C. One can notice that other peaks besides the expected Ta₂O₅ reflections appear, which deserve further investigations. On the other hand, the anatase peaks of the TiO₂ counterpart are well defined already at 800°C (red curves), as the T_c of this sample is in between 450-500 °C (not reported in the XRD here, but shown by the Raman measurements in the next section). Moreover, for both samples at 1000 °C, it is possible to evince the presence of the TiO₂ rutile phase that is more pronounced in the TiO₂-Ta₂O₅ (80%) than TiO₂-Ta₂O₅ (25%).

The crystallization of TiO₂-Ta₂O₅ (50%) is, instead, more controversial. First, it should be noticed that the used Si substrate (yellow curve) has a different crystalline orientation, i.e., (111), compared to that of the other samples, which is instead (h00) (see Chapter 2) [22]. Most importantly, a tiny peak from the substrate appears in between the expected position of Ta₂O₅ (001) and anatase (101) reflection, making the analysis even more complicated. However, three additional broad bumps emerge in the XRD spectrum upon annealing at T_a = 700 °C (green curve) at 2θ ≈ 23.81, 37.25, and 47.78°, possibly resembling the crystallization of the TiO₂ anatase phase in a stressed configuration (due to the presence of the Ta₂O₅ counterpart). Many other peaks develop upon annealing at T_a = 800 °C (red curve): in particular, the peak at 2θ ≈ 23.41° becomes more pronounced but still very broad, as it possibly includes both the Ta₂O₅ (001) and anatase (101) reflection (indeed, it moved toward lower angles). As an additional proof of Ta₂O₅ crystallization, the emergence of a broad peak at 2θ ≈ 56.14°, close to the (102) Ta₂O₅ reflection is also measured only at 800 °C. In this sense, one could infer that, in TiO₂ - Ta₂O₅ (50%), TiO₂ crystallizes in between 650-700 °C and Ta₂O₅ in between 700-800 °C, with the peak position in XRD affected by a reciprocal strain. Further analyses are needed to confirm these results. In particular, RS will be used to try discriminating between the two T_c and to verify the validity of these conclusions.

Based on the discussed findings, Figure 3 shows the T_c of both the TiO₂ and Ta₂O₅ counterparts of the TiO₂-Ta₂O₅ coatings, as a function of the TiO₂ concentration, including the results from both the XRD and RS analyses (discussed below). Red and black scatters are used to refer to Ta₂O₅ and TiO₂, respectively. In addition to this, an asymmetric error bar has been used to highlight the uncertainty in the determination of the exact T_c, due to the discrete steps used in the annealing process. As shown in the figure, lower is the Ta₂O₅ concentration, earlier is the emergence of the TiO₂ crystallization proving the strong influence of the two materials, and of their content, on the crystallization properties of the whole coatings.

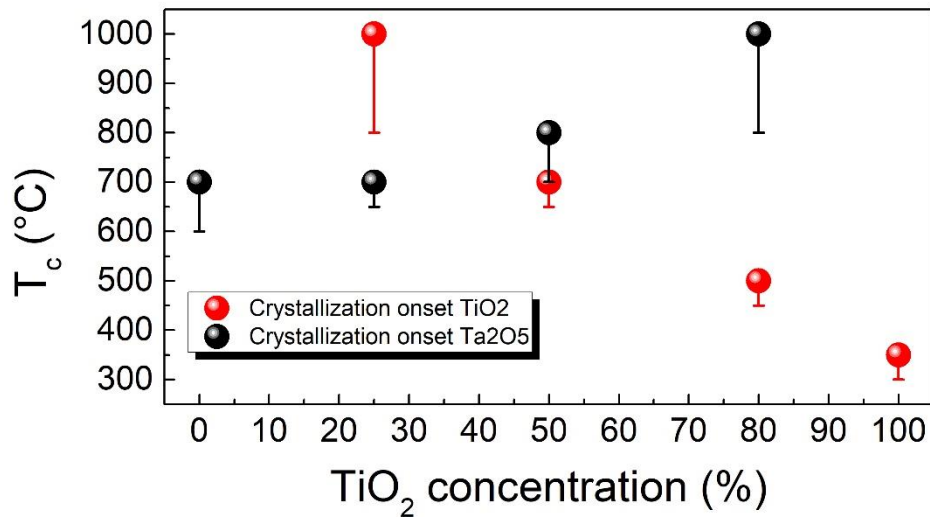


Figure 3: T_c of the $\text{TiO}_2\text{-Ta}_2\text{O}_5$ compounds, as a function of the TiO_2 concentration.

6.2.2 Raman measurements

RS measurements were performed in order to study the T_c , vibrational properties, and possible strain/stress of the investigated coatings.

The Raman spectra of Ta_2O_5 , $\text{TiO}_2\text{-Ta}_2\text{O}_5$ (25, 50, 80%), and TiO_2 annealed at different temperatures, in the range $100\text{-}1200\text{ cm}^{-1}$, are shown in Figure 4. All the as-grown samples (black curves) disclosed observed Raman only associated to Si substrate, as indicated by the labels, confirming their amorphicity.

Unfortunately, no change in the RS is found at any annealing temperature, when measuring pure Ta_2O_5 , possibly addressable to a non-appropriate laser wavelength used. Indeed, as reported in [23], a laser wavelength of 535 nm would be more suited to investigate the Ta_2O_5 crystalline structure, and generally all the inorganic oxides with very low Raman signal. Then, the 785nm used may not be effective to probe the crystallization of Ta_2O_5 and, only XRD measurements can be used to get consistent results on the crystallization of Ta_2O_5 and its counterpart in $\text{TiO}_2\text{-Ta}_2\text{O}_5$ mixture.

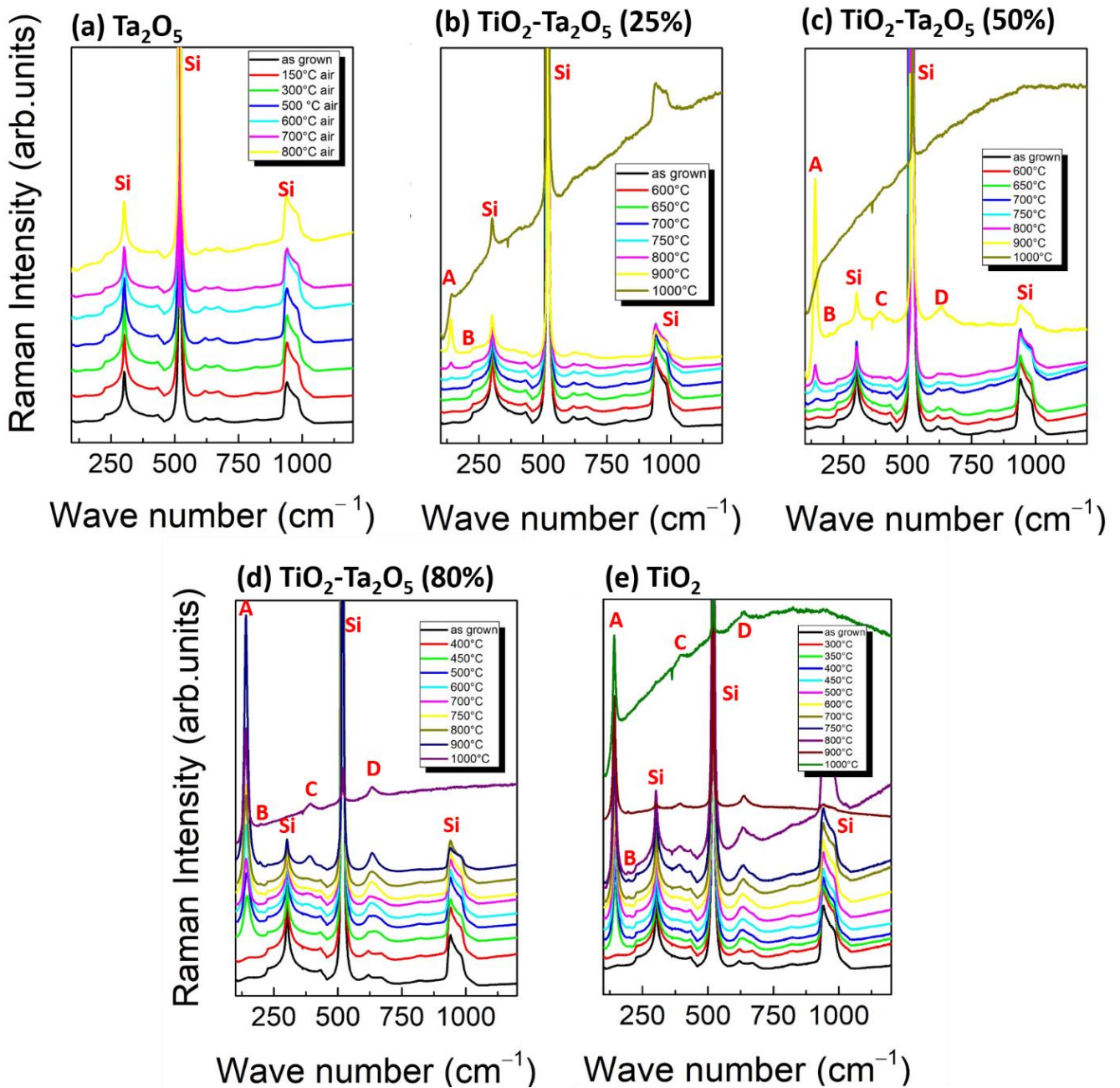


Figure 4: Raman spectra in the range 100-1200 cm^{-1} of (a) Ta_2O_5 , (b) $\text{TiO}_2\text{-Ta}_2\text{O}_5$ (25%), (c) $\text{TiO}_2\text{-Ta}_2\text{O}_5$ (50%), (d) $\text{TiO}_2\text{-Ta}_2\text{O}_5$ (80%), and (e) TiO_2 at different T_a . The Raman spectra were acquired with 50 \times of magnification, 10 s of exposure time, 5% of laser power, and 5 accumulations. The symbol A, B, C and D refer to the observed Raman modes. The labels Si refer to the Si substrate.

From herein, RS will be only used to address and study the crystallization of the TiO_2 counterpart, by observing the emergence of the strongest TiO_2 anatase mode at $\sim 144 \text{ cm}^{-1}$. Figures 4(b) and (c) display the Raman spectra of the $\text{TiO}_2\text{-Ta}_2\text{O}_5$ (25%) and $\text{TiO}_2\text{-Ta}_2\text{O}_5$ (50%) at several T_a , respectively. The first evidence of crystallization thus occurs at 750 and at 700 $^\circ\text{C}$ for $\text{TiO}_2\text{-Ta}_2\text{O}_5$ (25%) and $\text{TiO}_2\text{-Ta}_2\text{O}_5$ (50%), respectively.

The RS study of $\text{TiO}_2\text{-Ta}_2\text{O}_5$ (80%) and TiO_2 are shown in Figure 4(d) and (e), respectively. Starting from 450 °C [green curve in Figure 4(d)] and 350 °C [green curve in Figure 4(e)] a peak develops in the $\text{TiO}_2\text{-Ta}_2\text{O}_5$ (80%) and pristine TiO_2 pristine, respectively, at $\sim 144\text{ cm}^{-1}$, representative of the E_g anatase Raman band, thus proving the occurrence of crystallization.

By further increasing T_a above T_c , all samples show the enhancement of the E_g peak at $\sim 144\text{ cm}^{-1}$ (A) and the appearance of different TiO_2 anatase modes (B, C, and D) due to the evolution of the crystallization. The B and D refer to E_g mode arising from symmetric stretching vibrations of O–Ti–O bond, while C is the B_{1g} mode that describes the symmetric bending vibration of O–Ti–O bond [24].

Moreover, all the samples annealed at 1000 °C, $\text{TiO}_2\text{-Ta}_2\text{O}_5$ show a raising of the Raman background. This could be due to an increased fluorescence, possibly attributable to the formation of impurities or metal nanoparticles [25]. Indeed, EDS measurements acquired on the sample annealed at 1000 °C, and reported in the next section, show the presence of Na contaminations after annealing, probably coming from the simultaneous annealing of the crucible, nominally made by Al_2O_3 but often retaining some Na.

However, in order to exclude possible contributions of both the laser power and the Si substrate on the enhanced background signal for the samples annealed at 1000 °C, further investigations were performed. Figure 5(a) shows the RS of the pristine TiO_2 sample at the same T_a s of Figure 4(e), but changing the laser power, from 5% to 0.0001%.

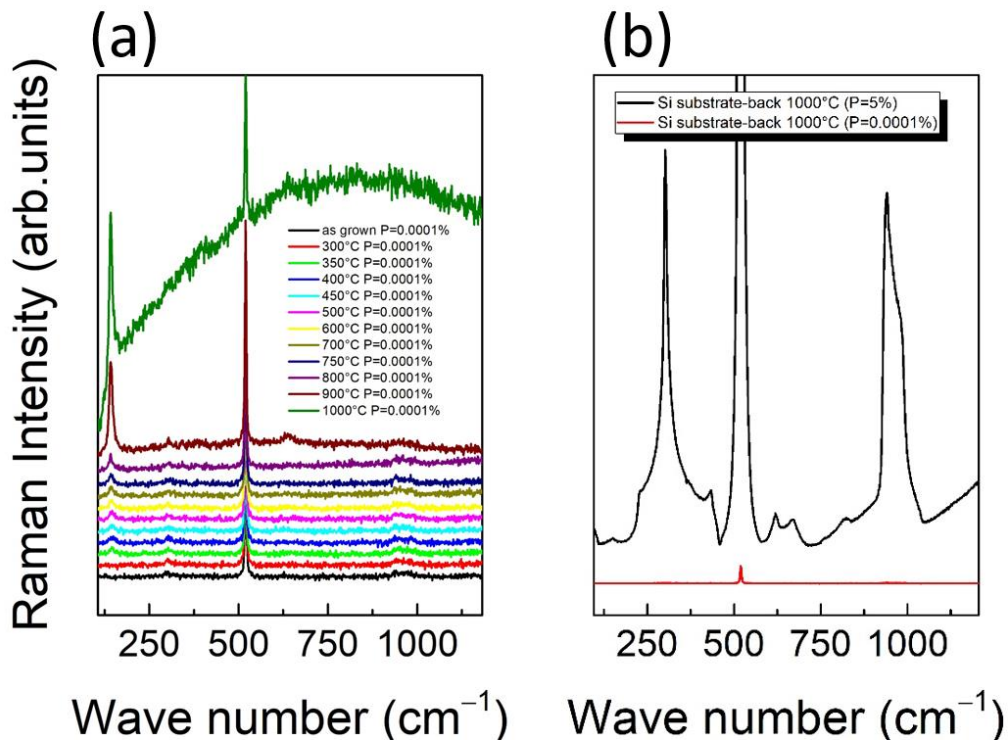


Figure 5: Raman spectra in the range 100-1200 cm^{-1} of TiO_2 sample at T_a for power laser of 0.0001%. (b) Raman spectra of Si substrate after $T_a = 1000\text{ °C}$ at different laser powers.

As expected, the Raman intensity of each mode decreases, but the raising of the background is preserved. Figure 5(b) investigates the contribution from the substrate (if any), by measuring the back face of the same pristine TiO₂ sample, by using two different laser powers of 5 and 0.0001% (black and red curves, respectively). No fluorescence is measured what so ever, thus ruling out the influence of the substrate, as well as the one of the laser power, in the measured results.

The temperature evolution of the Eg Raman mode, and its linewidth Γ (FWHM, corrected by the instrumental broadening, as discussed in Chapter 3), are shown in Figure 6(a) and (b), respectively. The exact peak position and the FWHM are extracted by removing the Si contribution and performed a Lorentzian fit on the as-treated data.

The gray patterned area of Figure 6(a) indicates the range of wavenumbers expected for the Eg anatase Raman band [19, 26]. Compared to these values, TiO₂ and TiO₂-Ta₂O₅ (80% and 50%) (black, blue and green dots respectively), show a blue-shift in their initial stage of crystallization. This phenomenon can be attributed to a crystallite size under the quantum-confinement condition, which is usually true only at the very beginning of the crystallization. A monotonic decrease of the Eg peak center as a function of the T_a is then observed, moving toward a tiny red-shift. The latter is associated to the tensile strain, occurring as a consequence of crystallization or of a partial anatase-rutile transformation at 1000 °C [27]. Differently, the Raman shift of TiO₂-Ta₂O₅ (25%) sample (red dots) exhibit a red-shift in the entire investigated range.

Figure 6(b) shows the behavior of Γ as a function of T_a, of the TiO₂, TiO₂-Ta₂O₅ (25%), TiO₂-Ta₂O₅ (50%), and TiO₂-Ta₂O₅ (80%) samples. The FWHM gives information about the degree of crystallization, non-stoichiometry effects, and the presence of oxygen vacancies [20, 26]. A monotonically decrease of Γ is observed in TiO₂, TiO₂-Ta₂O₅ (50%), and TiO₂-Ta₂O₅ (80%) samples, consistently with the evolution of crystallization. On the contrary, the TiO₂-Ta₂O₅ (25%) sample shows an increasing trend of Γ that can be associated to an increase of disorder and then, a decrease of crystallization degree.

Finally, the phonon lifetime τ as a function of both TiO₂ concentration and T_a is shown in Figure 6(c). The expression of τ has already been shown in the Eq. (5) of Chapter 3. For TiO₂, TiO₂-Ta₂O₅ (50%), and TiO₂-Ta₂O₅ (80%) samples, the almost monotonic increase of the phonon lifetime with increasing the T_a can be related to the evolution of crystallization and the reduction of the number of scattering sites. As the temperature rises and the crystal size enlarges, also the phonon density increases, and the temperature-dependent anharmonic phonon coupling grows [28,29]. On the contrary, TiO₂-Ta₂O₅ (25%) sample shows a decrease of phonon lifetime as function of T_a due to an increase of defects, like oxygen ones.

In particular, at 750 °C, the phonon lifetime TiO₂, TiO₂-Ta₂O₅ (50%), and TiO₂-Ta₂O₅ (80%) samples is shorter than the one of the TiO₂-Ta₂O₅ (25%), indicating high density

of defects in the former samples. Moreover, the phonon lifetime can decrease as the sample transforms from anatase to rutile [29].

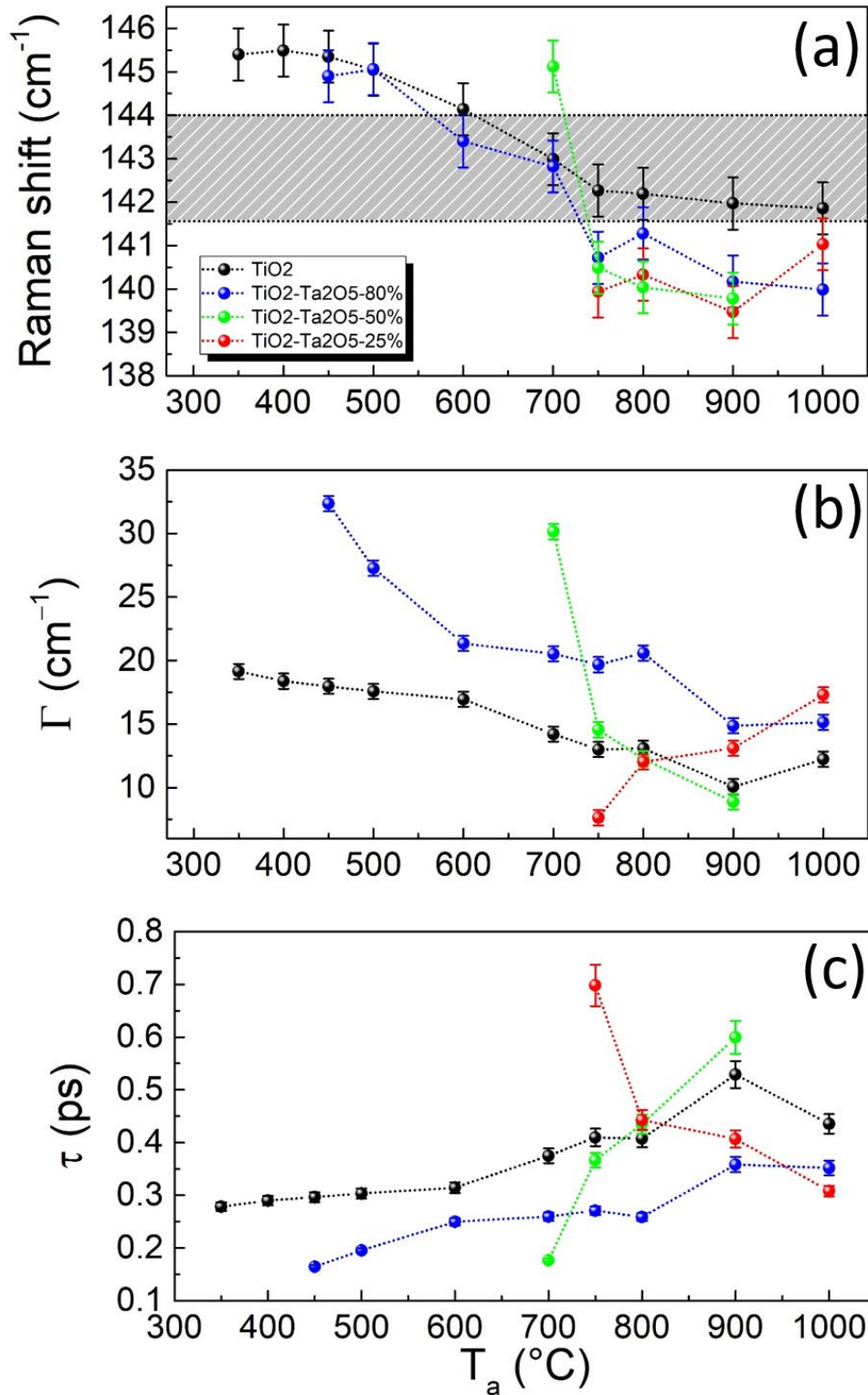


Figure 6: (a) Raman shift, (b) Γ , and (c) τ as a function of the T_a for TiO₂, TiO₂-Ta₂O₅ (25%), TiO₂-Ta₂O₅ (50%), and TiO₂-Ta₂O₅ (80%) samples. The gray region in (a) highlights the range where the E_g Raman mode is expected.

6.2.3 EDS measurements on as-grown samples

The energy-dispersive x-ray spectroscopy (EDS) measurements for all as-grown films, listed in Table 1 are shown in Figure 7(a-e). This analysis is carried out to determine the material concentration and the presence of contaminants. An Oxford INCA Energy 300 energy- EDS system attached to a Leo EVO 50 scanning electron microscope (SEM) was used to this aim.

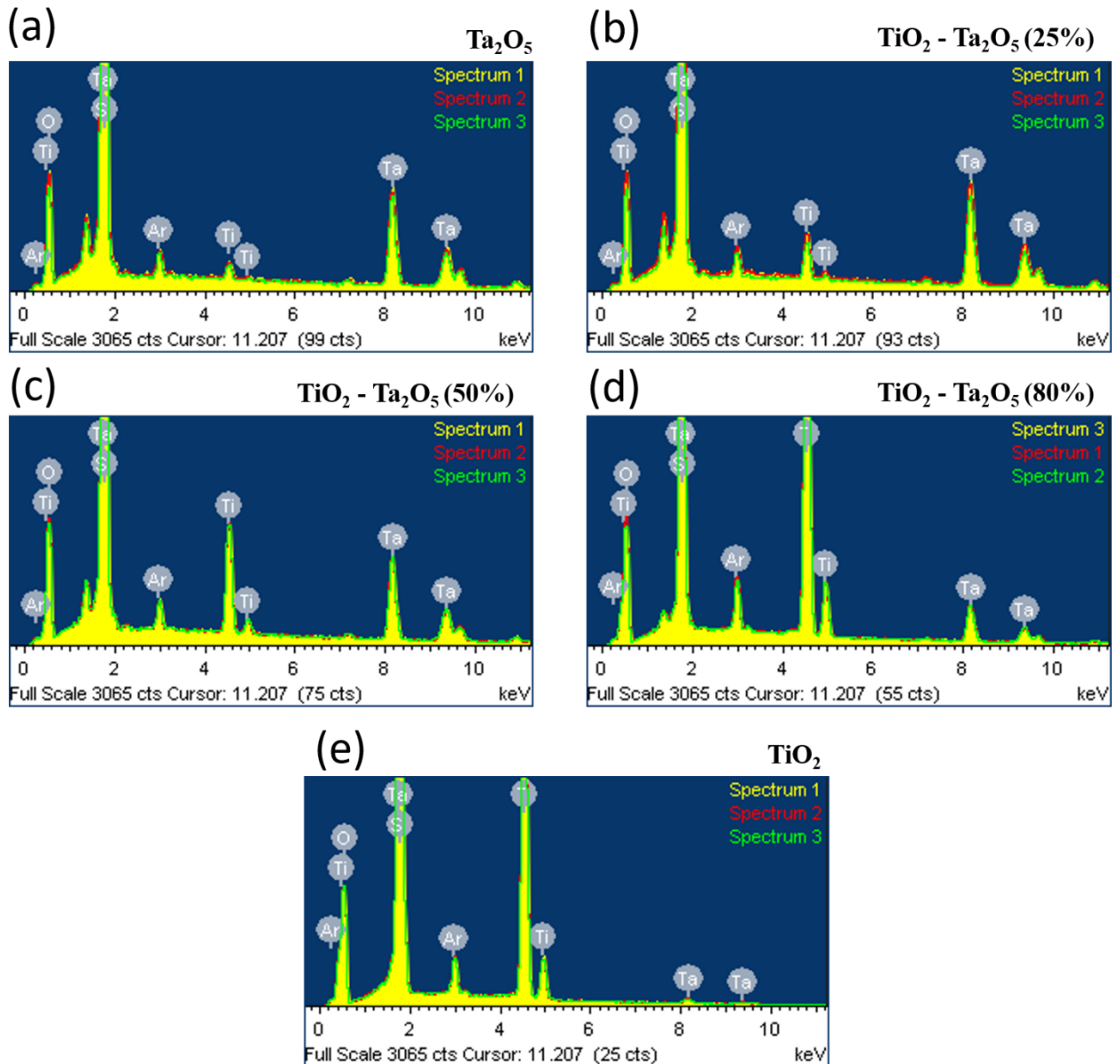


Figure 7: EDX analysis of the (a) Ta_2O_5 , (b) $TiO_2-Ta_2O_5$ (25%), (c) $TiO_2-Ta_2O_5$ (50%), (d) $TiO_2-Ta_2O_5$ (80%), and (e) TiO_2 film, listed in Table 1. The parameter values set for the EDS analysis are: 20 kV voltage, 8.5 mm of working distance using an aperture size of 50 μm and a probe current of 200 pA.

Three different regions were investigated per each sample and three EDS spectra were acquired per each area. The measured atomic% are shown in Table 2. Finally, the last row reports the TiO₂ concentrations with respect to the percentage of the compound. Apart from the expected atoms, i.e., Ti, Ta and O, the EDS spectra certify the presence of Si (coming from the substrate) and Argon (being the gas used for the ion bombardment in the deposition process).

	Ta₂O₅	TiO₂ - Ta₂O₅ (25%)	TiO₂ - Ta₂O₅ (50%)	TiO₂ - Ta₂O₅ (80%)	TiO₂
Ta	12.4±0.1	13.84±0.08	9.3±0.1	3.9±0.1	0.47±0.05
Ti	0.95±0.07	2.65±0.06	5.8±0.1	18.5±0.1	12.12±0.06
O	39.3±0.3	43.2±0.3	40.9±0.3	49.1±0.4	38.3±0.4
Ar	1.65±0.09	1.88±0.07	1.56±0.07	2.16±0.07	1.23±0.04
Ti/(Ti+Ta) (%)	7.1±0.6	16.1±0.5	38±1	83±1	96±1

Table 2: Atomic% extracted from EDS measurement of Ta₂O₅ (second column), TiO₂-Ta₂O₅ (25%) (third column), TiO₂-Ta₂O₅ (50%) (fourth column), TiO₂-Ta₂O₅ (80%) sample (fifth column), and TiO₂ (sixth column) samples.

6.2.4 EDS measurements on samples annealed at 1000 °C

Moreover, the EDS measurements for all films annealed at 1000 °C, listed in Table 1 are performed and shown in Figure 8(a-e). The instrument and the experimental parameters are the same used in the previous section. Also in this case, three different regions were investigated per each sample and three EDS spectra were acquired per each area.

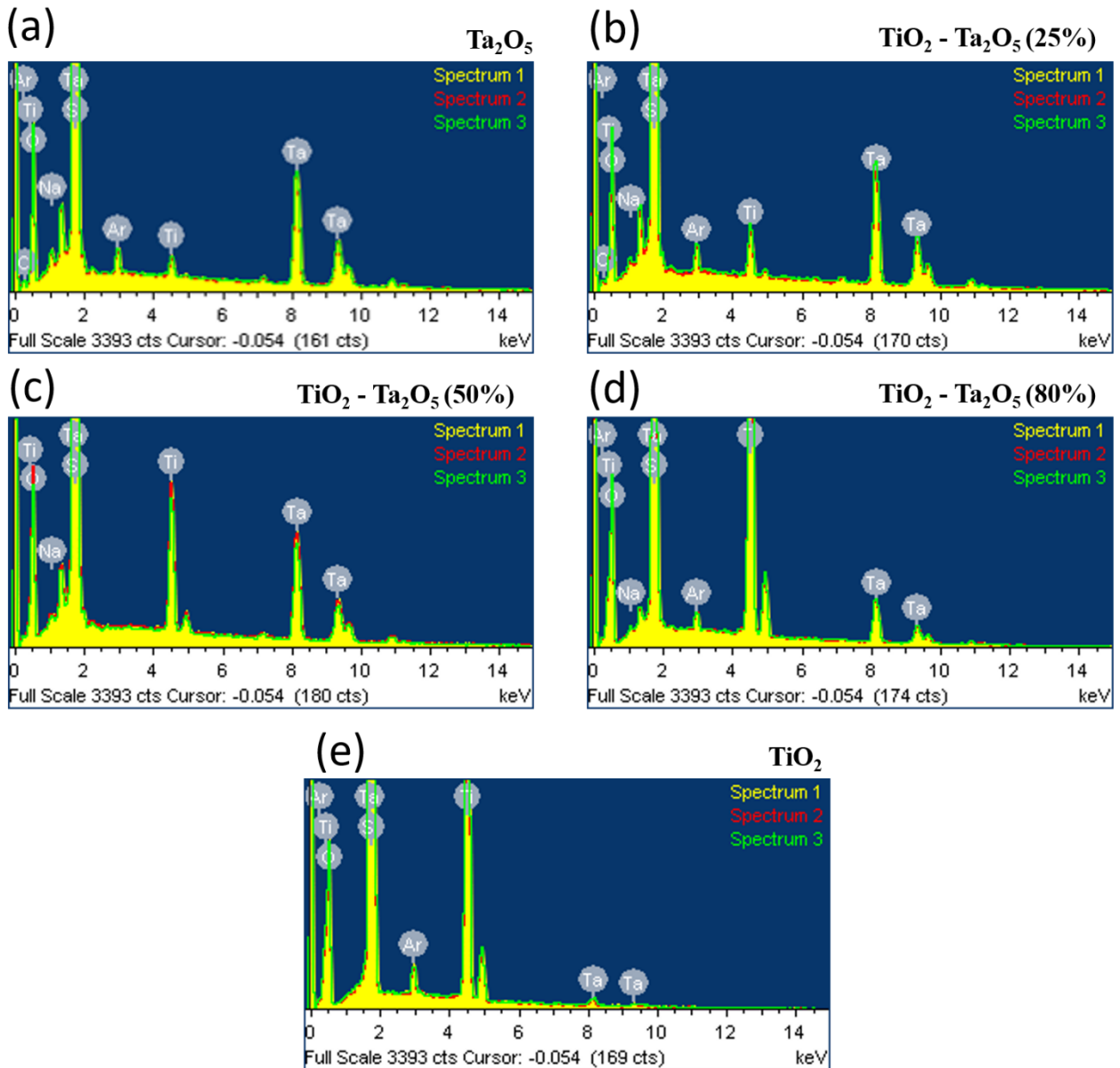


Figure 8: EDX analysis of the (a) Ta₂O₅, (b) TiO₂-Ta₂O₅ (25%), (c) TiO₂-Ta₂O₅ (50%), (d) TiO₂-Ta₂O₅ (80%), and (e) TiO₂ films annealed at 1000 °C, listed in Table 1.

The measured atomic% are shown in Table 3. As before, EDS the presence of the expected atoms, such as Ti, Ta, O, Si and Ar, with an additional contamination of Na. The latter is possibly coming from the Al₂O₃ crucible, used for the annealing. Indeed, as reported in Ref.[30], similar crucibles incorporate a small percentage of Na that evaporates at temperatures higher than 800 °C.

	Ta₂O₅	TiO₂- Ta₂O₅ (25%)	TiO₂-Ta₂O₅ (50%)	TiO₂-Ta₂O₅ (80%)	TiO₂
Ta	11.4±0.1	13.5±0.2	9.43±0.08	3.65±0.06	0.50±0.02
Ti	0.89±0.04	2.59±0.07	6.03±0.04	17.6±0.2	12.57±0.06
O	42.5±0.4	46.4±0.3	44.5±0.3	52.6±0.2	42.9±0.3
Ar	1.25±0.08	1.49±0.04	-	0.42±0.02	0.76±0.02
Na	0.70±0.05	0.30±0.05	0.46±0.05	0.46±0.05	0.07±0.01
Ti/(Ti+Ta) (%)	7.2±0.4	16.1±0.7	39±0.6	82±2	96±1

Table 3: Atomic% extracted from EDS measurement of Ta₂O₅ (second column), TiO₂-Ta₂O₅ (25%) (third column), TiO₂-Ta₂O₅ (50%) (fourth column), TiO₂-Ta₂O₅ (80%) sample (fifth column), and TiO₂ (sixth column) samples annealed at 1000 °C.

6.2.5 AFM measurements

In order to investigate the effects of the heat treatments on the samples surface a routinely study based on AFM measurements was performed to compare the as-grown and annealed coating surfaces. AFM images have been acquired with a JPK Nanowizard III, equipped with Vortex electronics, in the standard tapping mode technique, using a Bruker SCM-PIT-V2 tip.

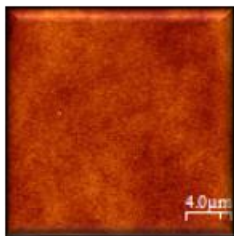
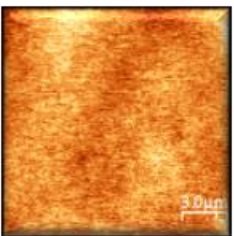
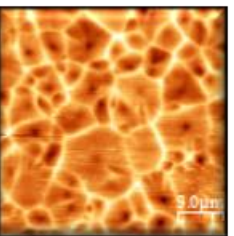
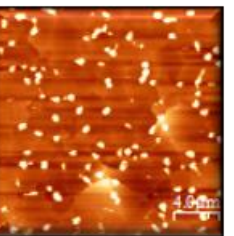
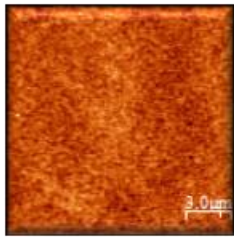
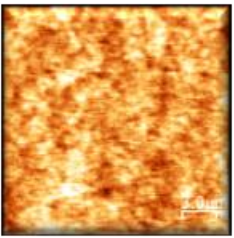
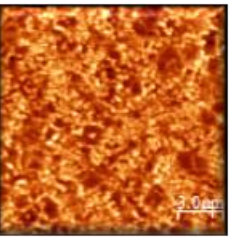
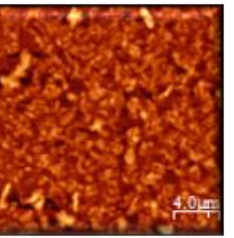
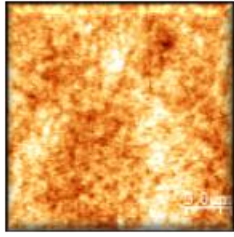
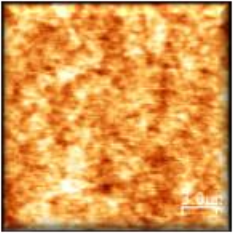
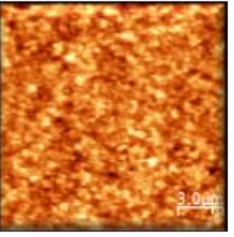
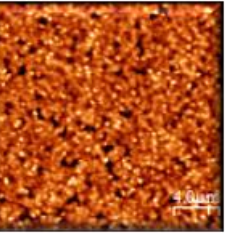
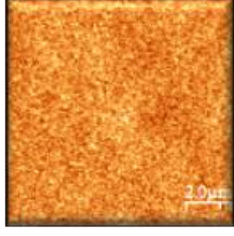
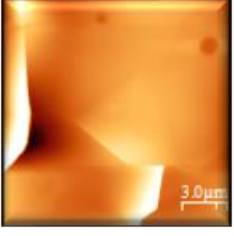
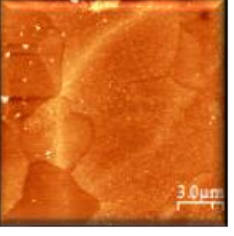
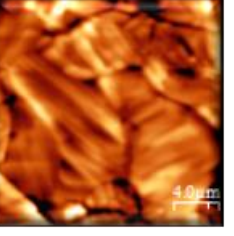
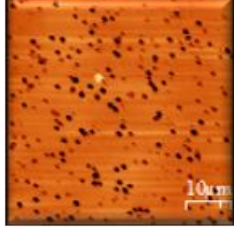
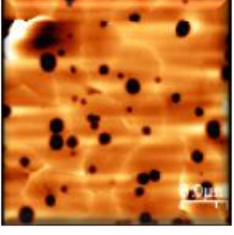
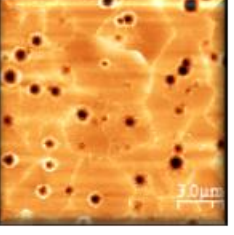
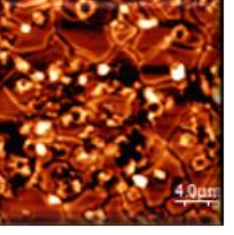
Sample	As-grown	500 °C	800 °C	1000 °C
Ta₂O₅				
TiO₂-Ta₂O₅ (25%)				
TiO₂-Ta₂O₅ (50%)				
TiO₂-Ta₂O₅ (80%)				
TiO₂				

Table 4: Tapping-mode AFM topography on a large scan area (from a minimum of 10 μm x 10 μm to a maximum of 50 μm x 50 μm in lateral size) of all samples as-grown (second column) and annealed at 500 °C (third column), 800 °C (fourth column), and 1000 °C (fifth column), listed in Table 1.

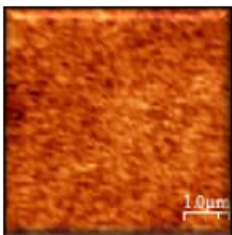
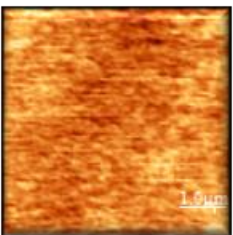
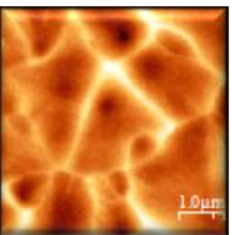
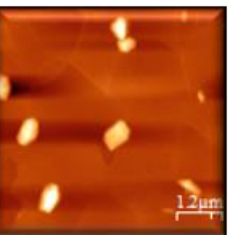
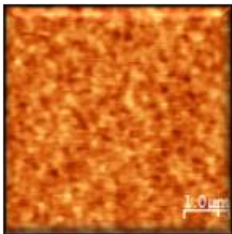
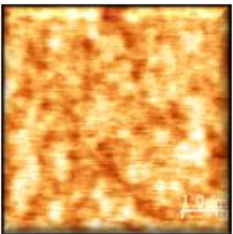
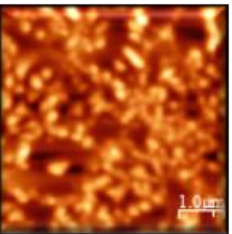
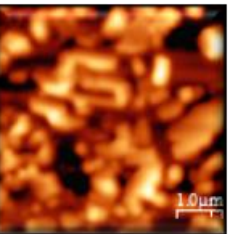
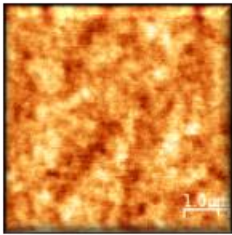
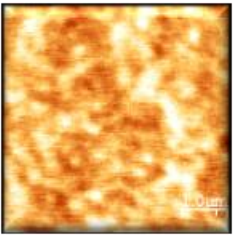
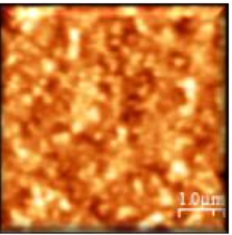
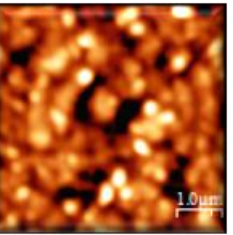
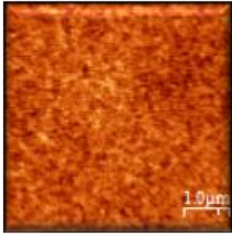
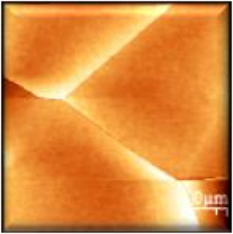
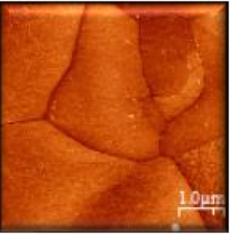
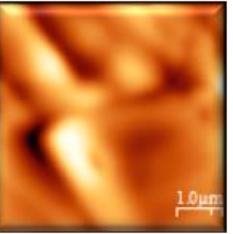
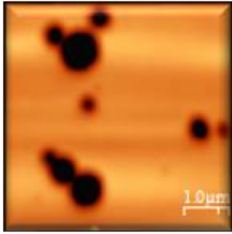
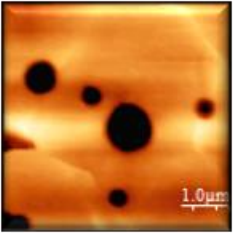
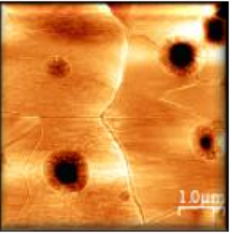
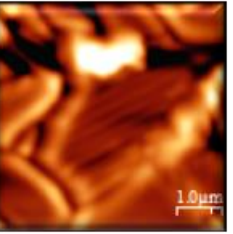
Sample	As-grown	500 °C	800 °C	1000 °C
Ta₂O₅				
TiO₂- Ta₂O₅ (25%)				
TiO₂- Ta₂O₅ (50%)				
TiO₂- Ta₂O₅ (80%)				
TiO₂				

Table 5: Tapping-mode AFM topography on a medium scan area, 5 μm x 5 μm in lateral size, of all samples as-grown (second column) and annealed at 500 °C (third column), 800 °C (fourth column), and 1000 °C (fifth column), listed in Table 1.

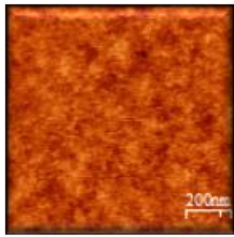
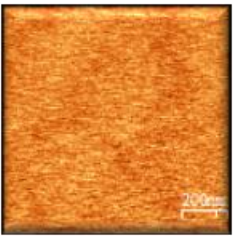
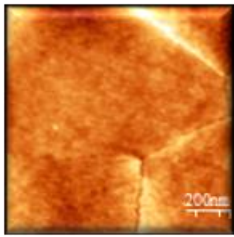
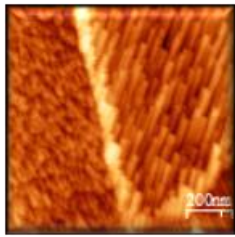
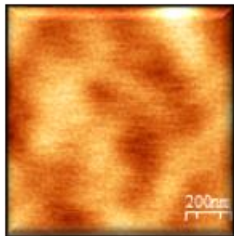
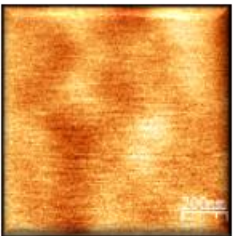
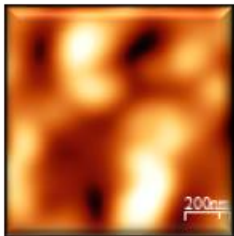
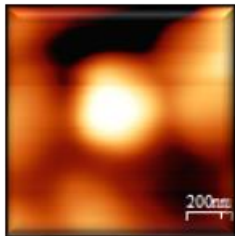
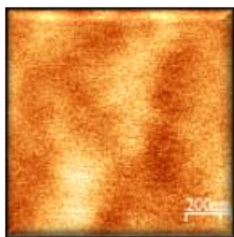
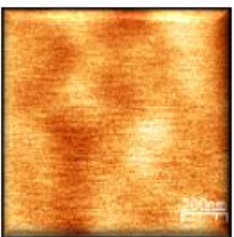
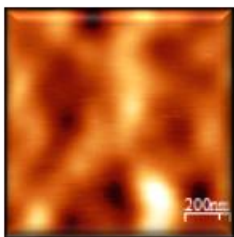
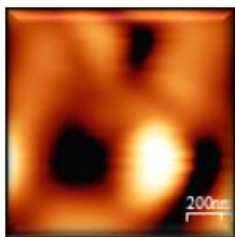
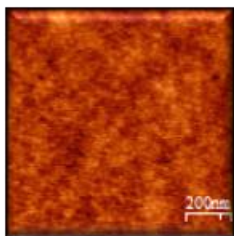

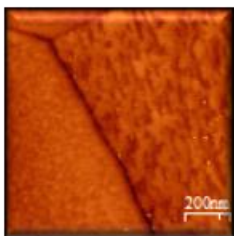
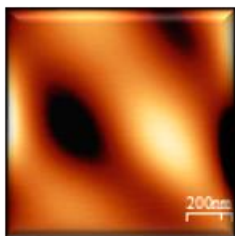
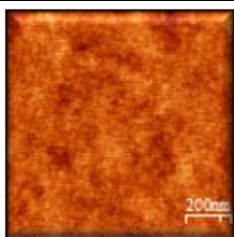

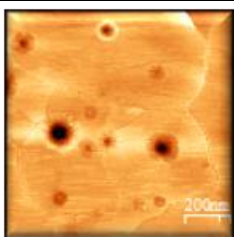
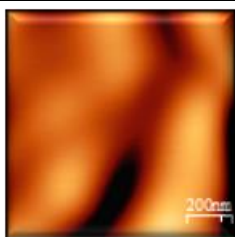
Sample	As-grown	500 °C	800 °C	1000 °C
Ta₂O₅				
TiO₂- Ta₂O₅ (25%)				
TiO₂- Ta₂O₅ (50%)				
TiO₂- Ta₂O₅ (80%)				
TiO₂				



Table 6: Tapping-mode AFM topography on a small scan area, 1 μm x 1 μm in lateral size, of all samples as-grown (second column) and annealed at 500 °C (third column), 800 °C (fourth column), and 1000 °C (fifth column), listed in Table 1.

Table 4 shows the thermal evolution of the surface morphology of the provided samples, as a function of temperature. In particular, the AFM topographies, on large scans area (from a minimum of 10 μm x 10 μm to a maximum of 50 μm x 50 μm in lateral size), are shown for each sample, as-grown and after annealing treatments at 500, 800, and 1000

°C. For all samples, a black-to-white color scale has been used to highlight the surface features.

The temperature evolution of the pure Ta_2O_5 sample is shown in the second row. Its surface looks flat and almost unchanged up to 500 °C, whereas at 800 °C, the formation of plates bounded by taller ridges occurs, consistently with the amorphous-to-crystalline transition measured by XRD. Moreover, even taller structures are formed and observed upon annealing at $T_a=1000$ °C.

Similarly, TiO_2 - Ta_2O_5 (25%) and (50%), third and fourth rows, respectively, show flat surfaces up to 500 °C, while a material rearrangement is observed at 800 and 1000 °C, consistently with the occurrence of crystallization.

Differently, when the TiO_2 concentration is 80% or 100%, (fifth and sixth rows, respectively), the surface shows the formation of plates and ripples already at 500 °C, demonstrating the TiO_2 crystallization. As a result of the amorphous-to-crystalline transition, ripples are observed in morphology as a consequence of the contact between the as-formed crystalline plates: either both the edges of the touching plates rise (see the light-to-light edges in the morphology) or one of the two goes below the other (see the light-to-dark edges in the morphology). Similar situation is observed at 800 °C, while at 1000 °C the surfaces evolve toward more complicated organization. It is worth stressing the presence of holes in the as-grown pure TiO_2 case (sixth row), with a mean depth of (21.9 ± 6.3) nm, that are still evident up to 800 °C.

Tables 5 and 6 show the temperature evolution of the sample surface on medium and small scan areas, respectively, confirming the scenario discussed so far in the case of large scan areas (Table 4).

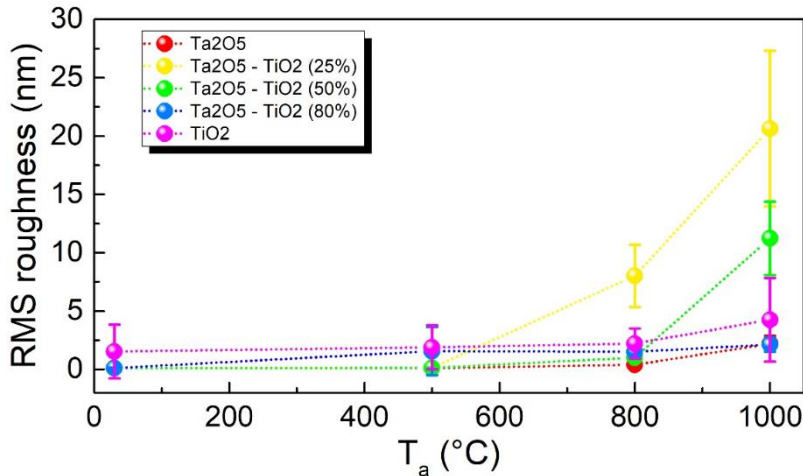


Figure 9: Average RMS roughness calculated on a small scan area, $1 \mu m \times 1 \mu m$, as a function of the T_a . Different color scatters represent different samples: Ta_2O_5 sample (red); TiO_2 - Ta_2O_5 (25%) sample (yellow); TiO_2 - Ta_2O_5 (50%) sample (green); TiO_2 - Ta_2O_5 (80%) sample (blue); TiO_2 sample (magenta).

Finally, a statistical analysis of the AFM images, on a scan area of $1\ \mu\text{m} \times 1\ \mu\text{m}$, was performed to study the RMS surface roughness as a function of the T_a for different TiO_2 concentrations, see Figure 9.

The RMS roughness of the samples as-grown and annealed at $500\ ^\circ\text{C}$ is almost the same for all the investigated coatings. At the highest temperatures (800 and $1000\ ^\circ\text{C}$), the roughness value strongly depends on the manifestation of crystallization. A general increasing trend in the RMS as a function of the T_a , is observed which is especially enhanced for $\text{TiO}_2\text{-Ta}_2\text{O}_5$ (25% and 50%), whose RMS approach ~ 21 and ~ 11 nm, respectively. This result could be affected by i) different orientation of the Si substrate used for the $\text{TiO}_2\text{-Ta}_2\text{O}_5$ (25%), ii) aging effect on both $\text{TiO}_2\text{-Ta}_2\text{O}_5$ (25%) and (50%), produced in 2019 and 2016, respectively.

6.2.6 Optical measurements of samples annealed at 1000 °C

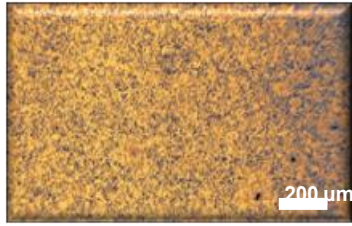
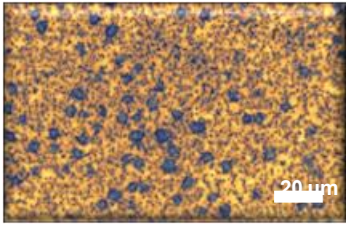
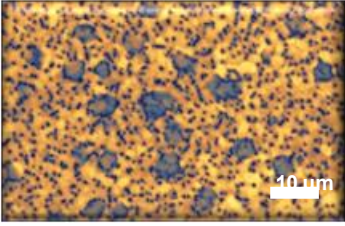
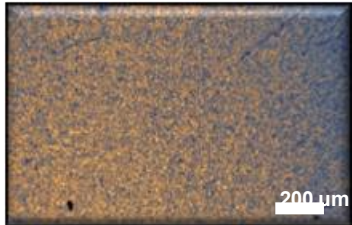
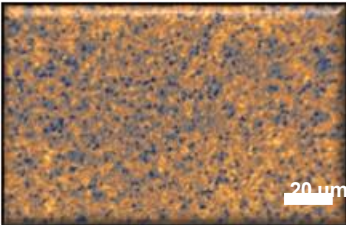
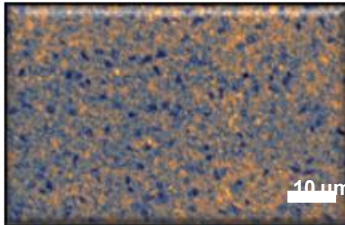

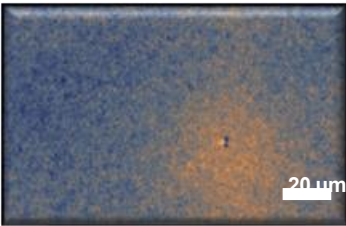
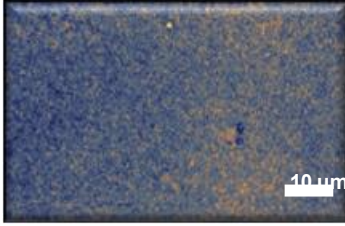
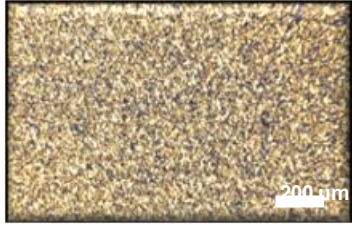
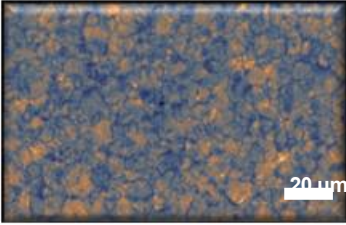
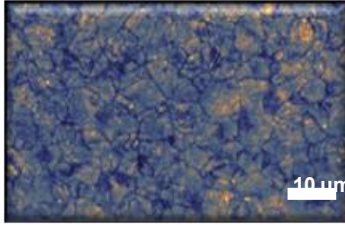
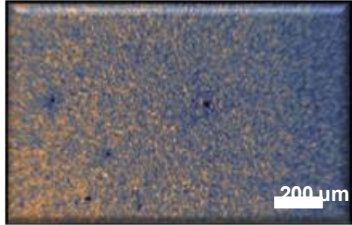
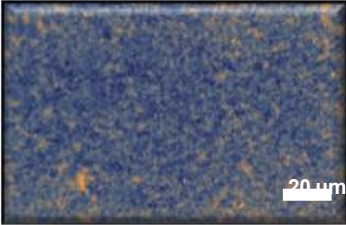
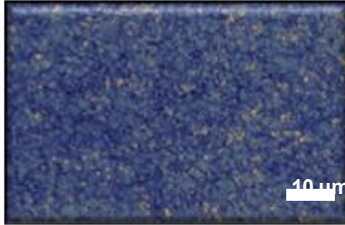
Sample	5X	50X	100X
Ta₂O₅			
TiO₂-Ta₂O₅ (25%)			
TiO₂-Ta₂O₅ (50%)			
TiO₂-Ta₂O₅ (80%)			
TiO₂			

Table 7: Optical microscope images of Ta₂O₅ sample (first row), TiO₂-Ta₂O₅ (25%) sample (second row), TiO₂-Ta₂O₅ (50%) sample (third row), TiO₂-Ta₂O₅ (80%) sample (fourth row), and TiO₂ sample (fifth row).

Table 7 shows the optical images of all samples annealed at 1000 °C. The Ta₂O₅, and TiO₂-Ta₂O₅ (25%) and (50%) samples (second, third and fourth row), show similar morphologies at the lowest magnification (5X), with a de-wetting tendency, which is more evident in Ta₂O₅ than in the TiO₂-doped compounds [see the highest magnification

(100X)]. Instead, TiO₂-Ta₂O₅ (80%) (fifth row) and TiO₂ (sixth row) clearly show the formation of cracks.

6.3 Co-sputtered TiO₂-Ta₂O₅ deposited on SiO₂

Table 8 lists the codes and the thickness of the TiO₂-Ta₂O₅ coatings, produced and investigated on SiO₂ substrate. As mentioned before, these samples were studied in their as-grown and annealed form, with the latter being only restricted to a 500 °C thermal annealing process for 10h.

Code	Sample	Ti/(Ta+Ti) (%) [*]	Thickness ⁴
c20014	Ta ₂ O ₅	7.1±0.6	430 nm
c19088	TiO ₂ -Ta ₂ O ₅ (25%)	16.1±0.5	502 nm
c20017	TiO ₂ -Ta ₂ O ₅ (75%)	66	514 nm
c20015	TiO ₂ -Ta ₂ O ₅ (80%)	83±1	848 nm
c19089	TiO ₂ -Ta ₂ O ₅ (90%)	97	350 nm
c20016	TiO ₂	96±1	542 nm

Table 8: Sample list. (*Ti/(Ta+Ti) concentrations are extracted from EDS measurements performed at Unisa and UniPg).

6.3.1 XRD measurements

In order to study the crystallization status of the provided coatings, XRD measurements are performed. The notation used in the following refer to the nominal concentration values for the measured samples. For the effective values, refer to Table 8.

As shown in Figure 10(a-f), all the as-grown samples (black spectra) are amorphous, with a big bump coming from the amorphous SiO₂ substrate. The gray curves in Figures 10(b-f) represents the reference spectrum of the TiO₂ anatase phase [19].

⁴ The thicknesses have been measured by using a spectrophotometer at LMA and by means spectroscopic ellipsometry at University of Genova.

Moreover, no change is measured in the XRD spectra of the samples Ta_2O_5 , $\text{TiO}_2 - \text{Ta}_2\text{O}_5$ (25%), and $\text{TiO}_2 - \text{Ta}_2\text{O}_5$ (75%) annealed at 500 °C [red curves in Figure 10(a-c)], confirming that these coatings have a T_c higher than 500 °C.

On the contrary, the XRD spectra of the samples $\text{TiO}_2 - \text{Ta}_2\text{O}_5$ (80%), $\text{TiO}_2 - \text{Ta}_2\text{O}_5$ (90%), and TiO_2 , annealed at 500 °C [red curves in Figure 10(d-f)], show the TiO_2 anatase reflections (101), (004), and (200), thus suggesting that they crystallize at a temperature lower than 500°C.

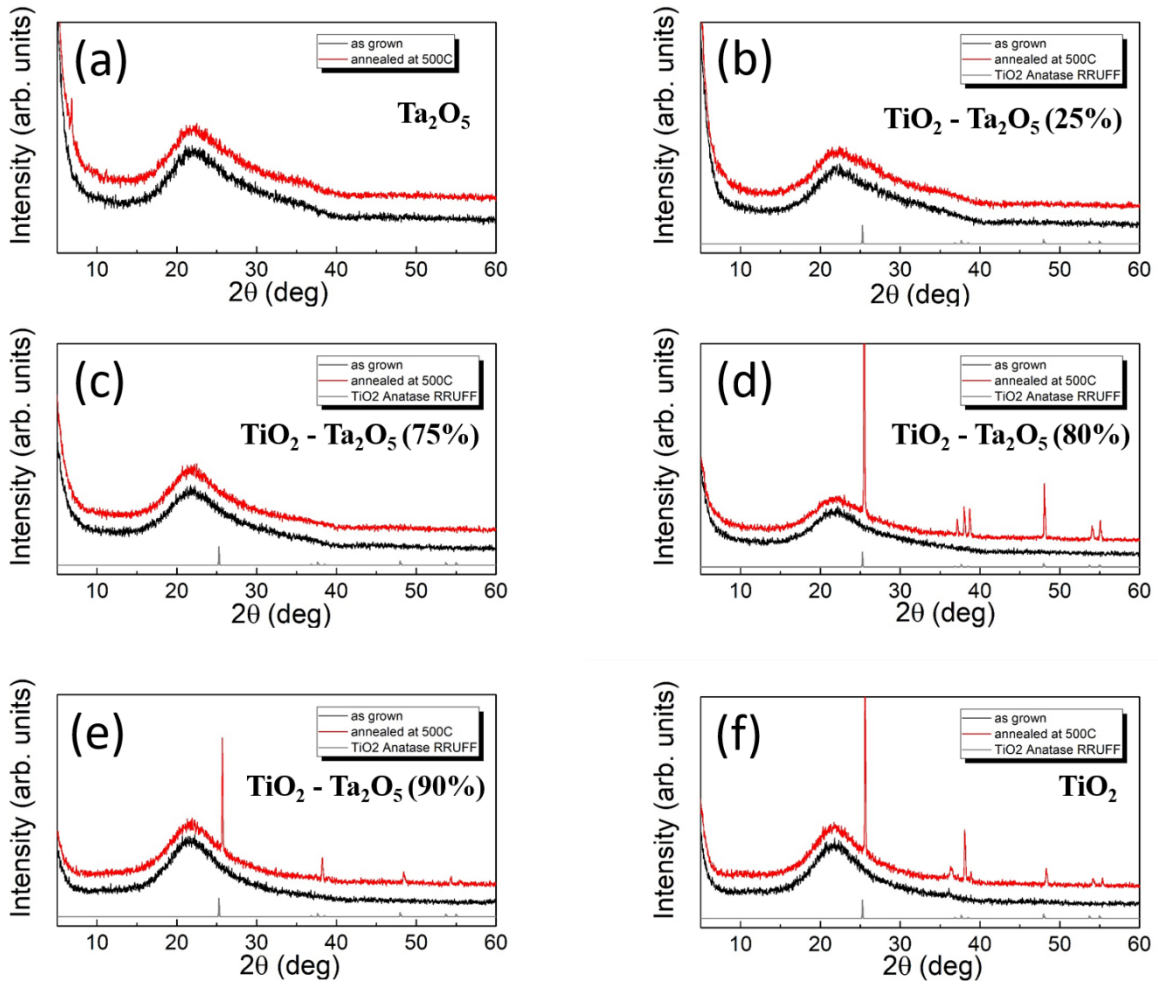


Figure 10: XRD spectra of all the samples as-grown (black) and annealed (red): (a) Ta_2O_5 , (b) $\text{TiO}_2 - \text{Ta}_2\text{O}_5$ (25%), (c) $\text{TiO}_2 - \text{Ta}_2\text{O}_5$ (75%), (d) $\text{TiO}_2 - \text{Ta}_2\text{O}_5$ (80%), (e) $\text{TiO}_2 - \text{Ta}_2\text{O}_5$ (90%), and (f) TiO_2 . The XRD measurements were performed with a time/step of 0.3 s, and a 2θ step of 0.02° . The gray spectrum in each plot corresponds to the reference TiO_2 anatase diffraction pattern [19].

6.3.2 Raman measurements

Additional structural information were obtained by performing RS. As expected and as shown in Figure 11(a-f), all the as-grown samples (black spectra) are amorphous. The bumps and modes at 492.8 cm^{-1} , 605.5 cm^{-1} , and 795.4 cm^{-1} come from the amorphous

SiO₂ substrate [31,32], as shown also in Chapter 2. The blue spectrum in each plot corresponds to the reference TiO₂ anatase Raman spectrum, as extracted from the RRUFF database [19]. No Raman modes are measured in the Raman spectra of the samples Ta₂O₅, TiO₂ - Ta₂O₅ (25%), and TiO₂ - Ta₂O₅ (75%) annealed at 500 °C, see red curves in Figure 11(a-c), confirming the XRD results (see Figure 10).

On the contrary, the Raman spectra of the TiO₂ - Ta₂O₅ (80%), TiO₂ - Ta₂O₅ (90%), and TiO₂ samples, annealed at 500 °C [red curves in Figure 11(d-f)], show the occurrence of the Raman anatase modes. In particular, these modes appear at 144 cm⁻¹ (A-Eg), 197 cm⁻¹ (B-Eg), 399 cm⁻¹ (C-B1g), and 639 cm⁻¹ (D-Eg) [26,24]. The presence of both **Eg** and **B1g** modes reveal stretching and bending vibrations of O–Ti–O bond in the anatase cell after thermal annealing.

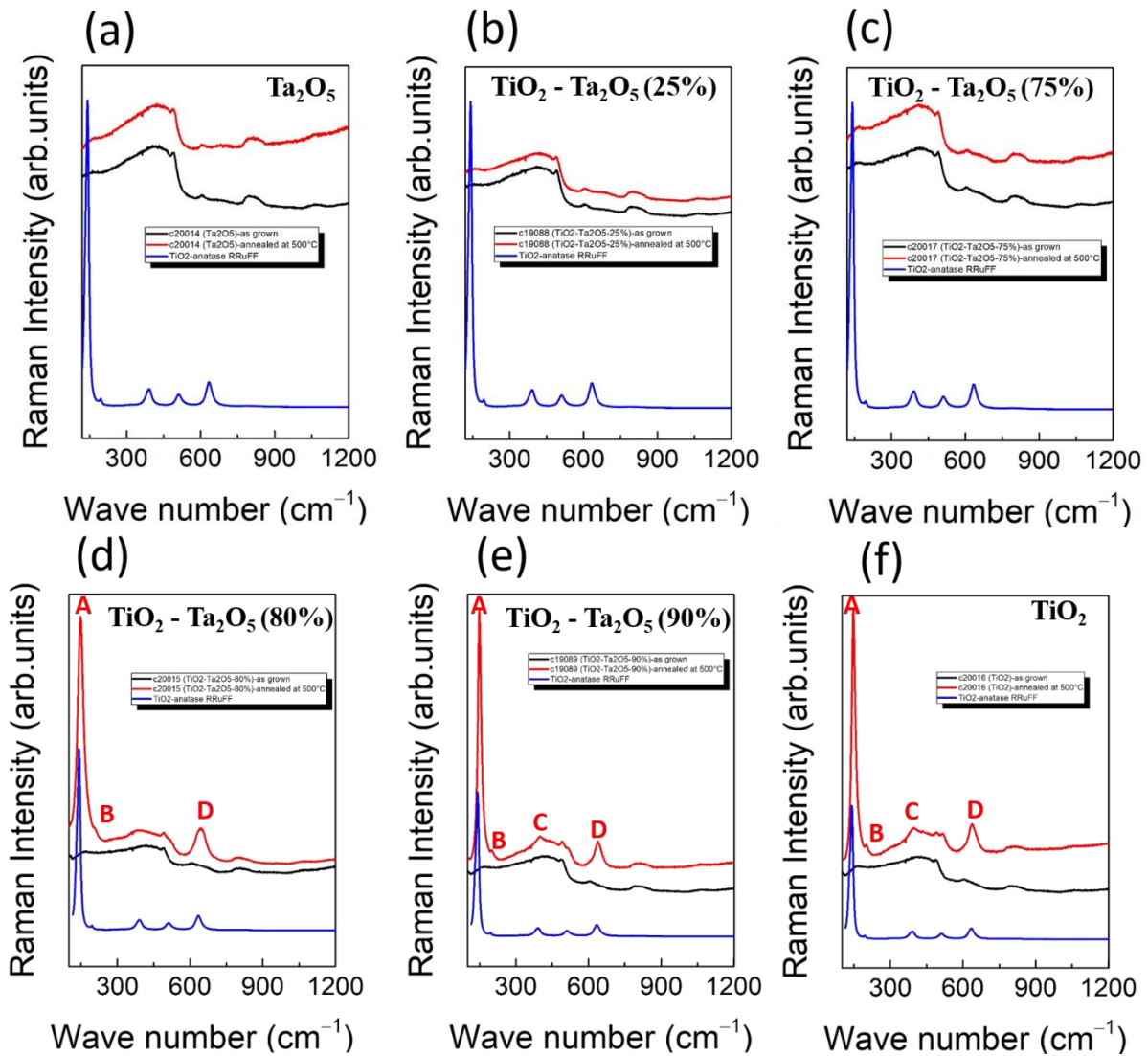
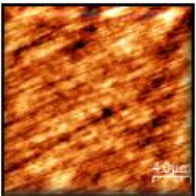
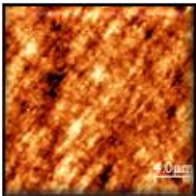
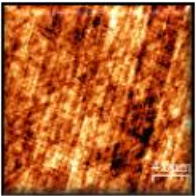
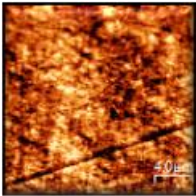
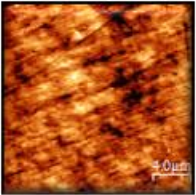
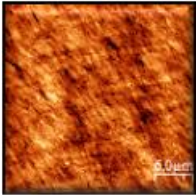
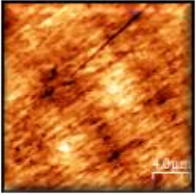
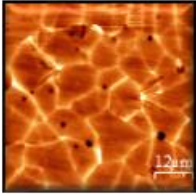
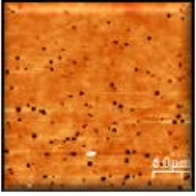
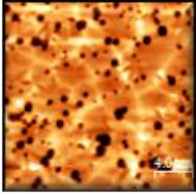
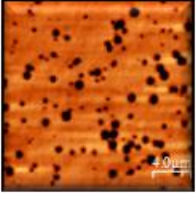
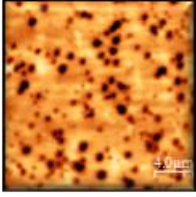


Figure 11: Raman spectra of all the samples as-grown (black) and annealed (red): (a) Ta₂O₅, (b) TiO₂ - Ta₂O₅ (25%), (c) TiO₂ - Ta₂O₅ (75%), (d) TiO₂ - Ta₂O₅ (80%), (e) TiO₂ - Ta₂O₅ (90%), (f) TiO₂. The Raman spectra were acquired with a 50× of magnification, 10 s of exposure time, 5% of laser power, and 5 accumulations. The gray spectrum in each plot corresponds to the reference TiO₂ anatase Raman spectrum, as extracted from the RRUFF database [19].

6.3.3 AFM measurements

A routinely study based on AFM measurements was then performed to compare the as-grown and annealed coating's surface. As before, AFM images have been acquired with a JPK Nanowizard III, equipped with Vortex electronics, in the standard tapping mode technique, using a Bruker SCM-PIT-V2 tip. Tables 9, 10, and 11 show the AFM topographies on a large, medium, and small scan area, respectively; a black-to-white color scale has been used to highlight the surface features.

Sample	As-grown	500°C
Ta₂O₅		
TiO₂-Ta₂O₅ (25%)		
TiO₂-Ta₂O₅ (75%)		
TiO₂-Ta₂O₅ (80%)		
TiO₂-Ta₂O₅ (90%)		
TiO₂		

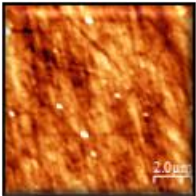
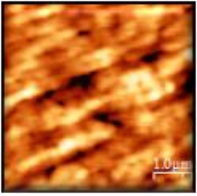
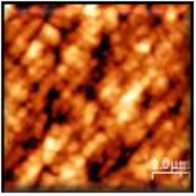
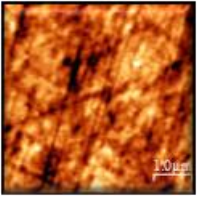
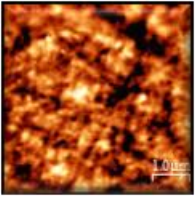
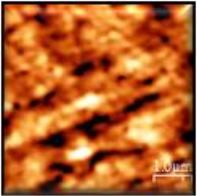
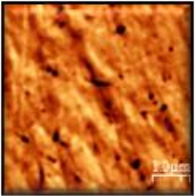
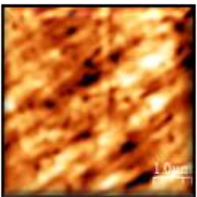
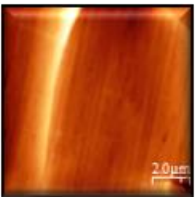
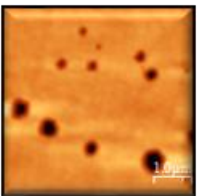
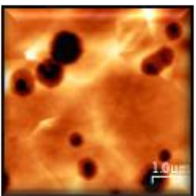
Substrate		
------------------	---	--

Table 9 Tapping-mode AFM topography on large scan areas (from a minimum of 20 μm x 20 μm, to a maximum of 60 μm x 60 μm in lateral size) of all the samples listed in Table 8, as-grown (second column) and annealed at 500 °C (third column). The last row shows the morphology of the SiO₂ substrate, obtained by imaging the back of the sample.

Sample	As-grown	500°C
Ta₂O₅		
TiO₂-Ta₂O₅ (25%)		
TiO₂-Ta₂O₅ (75%)		
TiO₂-Ta₂O₅ (80%)		
TiO₂-Ta₂O₅ (90%)		

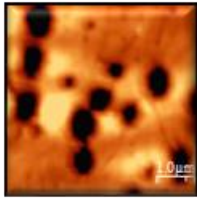
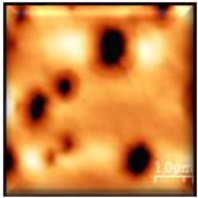
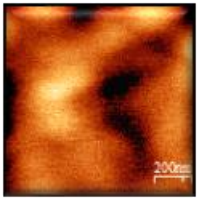
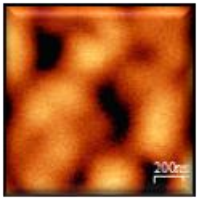
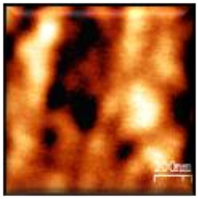
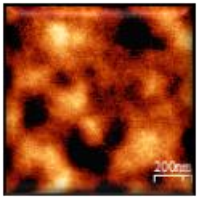
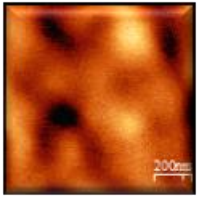
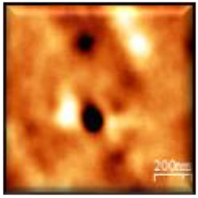
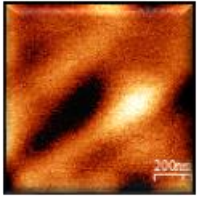
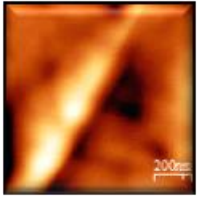
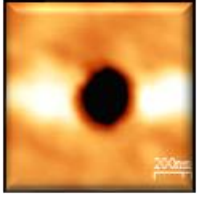
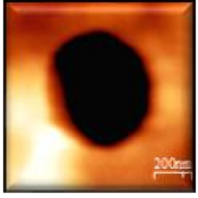

TiO₂		
------------------------	---	--

Table 10: Tapping-mode AFM topography on a medium scan area (from a minimum of 5 μm x 5 μm to a maximum of 10 μm x 10 μm in lateral size) of all the samples listed in Table 8 as-grown (second column) and annealed at 500 °C (third column).

Sample	As-grown	500°C
Ta₂O₅		
TiO₂-Ta₂O₅ (25%)		
TiO₂-Ta₂O₅ (75%)		
TiO₂-Ta₂O₅ (80%)		
TiO₂-Ta₂O₅ (90%)		



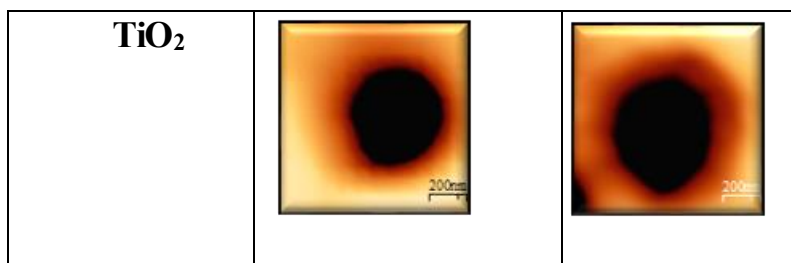


Table 11: Tapping-mode AFM topography on a small scan area, 1 μm x 1 μm in lateral size, of all the samples listed in Table 8 as-grown (second column) and annealed at 500 $^{\circ}\text{C}$ (third column).

Table 9 shows that, on a large scan area, as-grown Ta_2O_5 and $\text{TiO}_2 - \text{Ta}_2\text{O}_5$ (25%), (75%), and (80%) exhibit a material arrangement in linear structures, possibly reflecting the morphology of the SiO_2 substrate (see last row of Table 9). Indeed, similar features were never observed in the samples deposited on Si. Such a morphology is preserved in Ta_2O_5 and $\text{TiO}_2 - \text{Ta}_2\text{O}_5$ (25%) and (75%) also after the annealing at $T_a = 500$ $^{\circ}\text{C}$. In fact, as shown by XRD, these coatings remain amorphous upon the above mentioned heating treatment. On the contrary, the surface of $\text{TiO}_2 - \text{Ta}_2\text{O}_5$ (80%) evolves from a flat topography with linear structures, to the formation of plates separated by taller ridges upon annealing at $T_a = 500^{\circ}\text{C}$ (fourth row of Table 9), proving that the sample has undergone an amorphous-to-crystalline structural transition. Then, both as-grown and annealed $\text{TiO}_2 - \text{Ta}_2\text{O}_5$ (90%) and pristine TiO_2 sample's surfaces (fifth and sixth row, respectively) are characterized by deep holes, whose mean depth is (14.8 ± 3.6) nm in $\text{TiO}_2 - \text{Ta}_2\text{O}_5$ (90%) and (27.8 ± 6.7) nm in TiO_2 , accompanied by the formation of ridges upon $T_a = 500^{\circ}\text{C}$ (again proving that the samples are crystalline).

A deeper investigation has been performed by acquiring AFM morphology on medium and small scan areas, as reported in Tables 10 and 11, respectively. The latter confirmed the results of the analysis performed on large scan areas and allowed for a better visualization of small-scale features.

Finally, also in the case of samples deposited on SiO_2 , a statistical analysis of the AFM images was performed to study the variation of the RMS roughness as a function of the T_a for the different TiO_2 concentration. Figure 12 displays the behavior of the RMS roughness, calculated on a scan area of 1 μm x 1 μm , vs T_a . In agreement with the occurrence of crystallization, an increasing trend of the RMS roughness is observed in $\text{TiO}_2 - \text{Ta}_2\text{O}_5$ (80%), $\text{TiO}_2 - \text{Ta}_2\text{O}_5$ (90%), and TiO_2 (which undergo a structural transition from amorphous to crystalline upon annealing at $T_a = 500^{\circ}\text{C}$), whereas it remains almost constant and below 1 nm in Ta_2O_5 , $\text{TiO}_2 - \text{Ta}_2\text{O}_5$ (25%), and $\text{TiO}_2 - \text{Ta}_2\text{O}_5$ (75%), since the samples are amorphous.

Moreover, a TiO_2 concentration higher than 80% produces a rougher surface with bigger variation (larger error bars), due to the formation of holes.

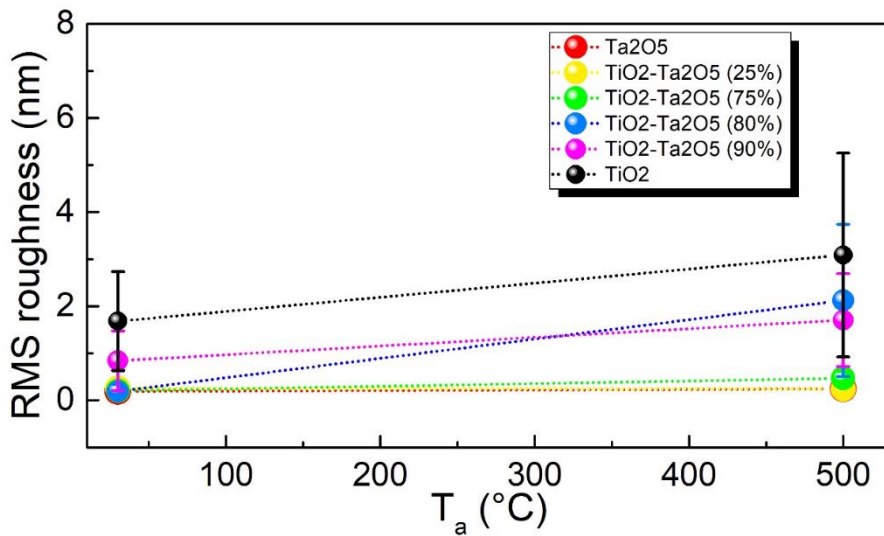


Figure 12: Average RMS roughness calculated on a small scan area, $1 \mu\text{m} \times 1 \mu\text{m}$, as a function of the T_a (as-grown and at 500°C). Different color scatters represent different samples: Ta_2O_5 (red); $\text{TiO}_2 - \text{Ta}_2\text{O}_5$ (25%) (yellow), $\text{TiO}_2 - \text{Ta}_2\text{O}_5$ (75%) (green), $\text{TiO}_2 - \text{Ta}_2\text{O}_5$ (80%) (blue), $\text{TiO}_2 - \text{Ta}_2\text{O}_5$ (90%) (magenta), and TiO_2 (black).

Summary

This chapter focused on the study of the morphological and structural properties of co-sputtered $\text{TiO}_2\text{-Ta}_2\text{O}_5$ samples with different concentrations of TiO_2 (0, 25, 75, 80, 90, 100 %) deposited at LMA on both Si and SiO_2 substrates, by using an IBS.

The first section, called *State of art of co-sputtered materials*, explained the importance of using these materials, with a proper concentration of TiO_2 (18%), combined with the thermal annealing at $T_a = 500^\circ\text{C}$, on the reduction of the absorption and mechanical losses in the coatings.

The second section, called *Co-sputtered $\text{TiO}_2\text{-Ta}_2\text{O}_5$ deposited on Si*, demonstrated that:

- 1) All as-grown co-sputtered materials are amorphous, as confirmed by both XRD and Raman measurements. The T_c , studied by XRD and Raman measurements, of the co-sputtered materials depends on the TiO_2 percentage. Indeed, Ta_2O_5 crystallizes in the range $650\text{-}700^\circ\text{C}$ as well as the compound with 25 and 50% of TiO_2 . Instead, the film with 80% of TiO_2 and the pure TiO_2 crystallize in the range of $450\text{-}500^\circ\text{C}$ and $300\text{-}350^\circ\text{C}$, respectively. Moreover, the T_c of both the TiO_2 and Ta_2O_5 counterparts in the $\text{TiO}_2\text{-Ta}_2\text{O}_5$ coatings is strongly influenced by the content of the two materials.
- 2) The Raman measurements confirmed the structural information extracted by the XRD spectra, specifically to the case of the TiO_2 . The first TiO_2 anatase modes, E_g , appears at the expected T_c and arises from the symmetrical stretching vibration of O-Ti-O bond. At higher T_a , another anatase Raman mode, B_{1g} , appears, ascribed to the symmetric bending vibration of O-Ti-O bond. Moreover, all samples annealed at 1000°C disclose an enhanced background due to a fluorescence phenomenon and possibly addressable to Na contaminations. Moreover, Raman shift as a function of T_a is studied evidencing a blue-shift at the beginning of crystallization in almost all

sample (except for $\text{TiO}_2\text{-Ta}_2\text{O}_5$ (25%)) addressable to a crystallite size in the quantum-confinement regime, and a red-shift in all sample when the crystallization is well developed, as a consequence of the buildup of tensile strain. Additional information on the crystallization are extracted from the study of the phonon lifetime.

- 3) The surface morphology for all as-grown samples, observed by AFM technique, is very flat on large, medium, and small scan area, except for the TiO_2 sample that shows holes with a mean depth of (21.9 ± 6.3) nm. Changes in the morphology are clearly visible upon annealing treatments and their evolution strongly correlates with the occurrence of crystallization and its evolution.
- 4) EDS measurements performed on the as-grown samples certify the presence of Si (coming from the substrate) and Argon (being the gas used for the ion bombardment in the deposition process), apart from the expected atoms, i.e., Ti, Ta and O., the EDS. Instead, EDS on the samples annealed at 1000°C , show the possibly presence of Na, coming from the Al_2O_3 crucible used in the thermal processes.

The third and final section, called *Co-sputtered $\text{TiO}_2\text{-Ta}_2\text{O}_5$ deposited on SiO_2* , has shown that:

- 1) Also in this case, the T_c , studied by XRD measurements, of the co-sputtered materials deposited on SiO_2 substrate depends on the TiO_2 percentage. The Ta_2O_5 , $\text{TiO}_2 - \text{Ta}_2\text{O}_5$ (25%), and $\text{TiO}_2 - \text{Ta}_2\text{O}_5$ (75%) samples have a T_c higher than 500°C . Instead, $\text{TiO}_2 - \text{Ta}_2\text{O}_5$ (80%), $\text{TiO}_2 - \text{Ta}_2\text{O}_5$ (90%), and TiO_2 samples have a T_c lower than 500°C . These results are also confirmed by the Raman measurements.
- 2) The surface morphology of all samples shows an arrangement in linear structures resembling the morphology of the SiO_2 substrate. The Ta_2O_5 , $\text{TiO}_2 - \text{Ta}_2\text{O}_5$ (25%), and $\text{TiO}_2 - \text{Ta}_2\text{O}_5$ (75%) display no changes in morphology after $T_a = 500^\circ\text{C}$. Instead, the $\text{TiO}_2 - \text{Ta}_2\text{O}_5$ (80%), $\text{TiO}_2 - \text{Ta}_2\text{O}_5$ (90%), and TiO_2 samples show the formation of plates separated by taller ridges upon $T_a = 500^\circ\text{C}$, according to the crystallization process. The RMS roughness is almost constant and below 1 nm in Ta_2O_5 , $\text{TiO}_2\text{-Ta}_2\text{O}_5$ (25%), and $\text{TiO}_2\text{-Ta}_2\text{O}_5$ (75%), since these samples remain amorphous at 500°C . Instead, it increases in the $\text{TiO}_2\text{-Ta}_2\text{O}_5$ (80%), $\text{TiO}_2\text{-Ta}_2\text{O}_5$ (90%), and TiO_2 samples after $T_a = 500^\circ\text{C}$, according to the crystallization.

Finally, from comparison of samples deposited on Si and SiO_2 substrates, one can conclude that the $\text{TiO}_2\text{-Ta}_2\text{O}_5$ samples with a TiO_2 percentage lower than 75% have crystallization temperatures higher than 500°C . Then, they show a very flat surface morphology at $T_a = 500^\circ\text{C}$, especially for the samples deposited on Si, as also confirmed by the RMS roughness. All this information can be very useful in the context of gravitational wave detectors.

References

1. Accadia, T., *et al.* Status of the Virgo project. *Classical and Quantum Gravity* **2011**, *28(11)*, 114002.
2. Acernese, *et al.* Advanced Virgo: a second-generation interferometric gravitational wave detector. *Classical and Quantum Gravity* **2014**, *32(2)*, 024001.
3. Abbott, B. P., *et al.* LIGO: the laser interferometer gravitational-wave observatory. *Reports on Progress in Physics* **2009**, *72(7)*, 076901.
4. Aasi, J., *et al.* Advanced ligo. *Classical and quantum gravity* **2015**, *32(7)*, 074001.
5. Somiya, K. Detector configuration of KAGRA—the Japanese cryogenic gravitational-wave detector. *Classical and Quantum Gravity* **2012**, *29(12)*, 124007.
6. Capote, E., *et al.* Measurements of Optical Scatter versus Annealing Temperature for Ta₂O₅ and Ti: Ta₂O₅ thin-film coatings. *Bulletin of the American Physical Society* **2020**, *65*.
7. Beauville, F., *et al.* The VIRGO large mirrors: a challenge for low loss coatings. *Classical and Quantum Gravity* **2004**, *21(5)*, S935.
8. P. R. Saulson, Thermal noise in mechanical experiments, *Physical Review D* **1990**, *42*, 2437.
9. Yu. Levin, Internal thermal noise in the LIGO test masses: a direct approach, *Physical Review D* **1998**, *57*, 659.
10. M. Granata, *et al.* Amorphous optical coatings of present gravitational-wave interferometers, *Classical and Quantum Gravity* **2020**, *37(9)*, 095004.
11. Amato, A., *et al.* High-reflection coatings for gravitational-wave detectors: State of the art and future developments. *In Journal of Physics: Conference Series* (Vol. 957, No. 1, p. 012006). IOP Publishing.
12. Harry, G. M., *et al.* Titania-doped tantala/silica coatings for gravitational-wave detection. *Classical and Quantum Gravity* **2006**, *24(2)*, 405.
13. Granata, M., *et al.* Progress in the measurement and reduction of thermal noise in optical coatings for gravitational-wave detectors. *Applied optics* **2020**, *59(5)*, A229-A235.
14. Amato, A., *et al.* Observation of a correlation between internal friction and Urbach energy in Amorphous oxides thin films. *Scientific reports* **2020**, *10(1)*, 1-9.
15. Cesarini, E., *et al.* A “gentle” nodal suspension for measurements of the acoustic attenuation in materials. *Review of Scientific Instruments* **2009**, *80(5)*, 053904.
16. Cesarini, E., *et al.* Mechanical characterization of ‘uncoated’ and ‘Ta₂O₅-single-layer-coated’ SiO₂ substrates: results from GeNS suspension, and the CoaCh project. *Classical and Quantum Gravity* **2010**, *27(8)*, 084031.
17. Fazio, M. A., *et al.* Structure and morphology of low mechanical loss TiO₂-doped Ta₂O₅. *Optical Materials Express* **2020**, *10(7)*, 1687-1703.
18. Krishnaprasanth, A., Seetha, M., Solvent free synthesis of Ta₂O₅ nanoparticles and their photocatalytic properties. *AIP advances*, **2018**, *8(5)*, 055017.
19. RRUFF, <https://rruff.info/chem=Ti,O/display=default/R070582> (accessed on 24 August 2021).
20. RRUFF, <https://rruff.info/chem=Ti,O/display=default/R120008> (accessed on 2 November 2021).

21. Lawson, D. H. *Atomic force microscopy and Raman spectroscopy study of tantalum films*. PhD Thesis, University of Glasgow, **2014**.
22. ICSD, <https://icsd.products.fiz-karlsruhe.de/> (accessed on 2 November 2021).
23. Perez, I., *et al.* Evidence for structural transition in crystalline tantalum pentoxide films grown by RF magnetron sputtering. *Journal of Alloys and Compounds* **2017**, *712*, 303-310.
24. Boda, M. A., Shah, M. A. Fabrication mechanism of compact TiO₂ nanotubes and their photo-electrochemical ability. *Materials Research Express* **2017**, *4(7)*, 075908.
25. Wei, D., *et al.* Review of fluorescence suppression techniques in Raman spectroscopy. *Applied Spectroscopy Reviews* **2015**, *50(5)*, 387-406.
26. Allen, N. S., *et al.* The effect of crystalline phase (anatase, brookite and rutile) and size on the photocatalytic activity of calcined polymorphic titanium dioxide (TiO₂). *Polymer degradation and stability* **2018**, *150*, 31-36.
27. Balaji, S. Y. D. J. R., *et al.* Phonon confinement studies in nanocrystalline anatase-TiO₂ thin films by micro Raman spectroscopy. *Journal of Raman Spectroscopy: An International Journal for Original Work in all Aspects of Raman Spectroscopy, Including Higher Order Processes, and also Brillouin and Rayleigh Scattering* **2006**, *37(12)*, 1416-1422.
28. Cuscó, R., *et al.* Temperature dependence of Raman scattering in ZnO. *Physical Review B* **2007**, *75(16)*, 165202.
29. Choudhury, B., Choudhury, A. Local structure modification and phase transformation of TiO₂ nanoparticles initiated by oxygen defects, grain size, and annealing temperature. *International Nano Letters* **2013**, *3(1)*, 1-9.
30. ALMATH, <https://almathcrucibles.com/materials/alumina/> (accessed on 7 October 2021).
31. Biswas, R. K., *et al.* Study of short range structure of amorphous Silica from PDF using Ag radiation in laboratory XRD system, RAMAN and NEXAFS. *Journal of Non-Crystalline Solids* **2018**, *488*, 1-9.
32. Vandembroucq, D., *et al.* Density hardening plasticity and mechanical ageing of silica glass under pressure: a Raman spectroscopic study. *Journal of Physics: Condensed Matter* **2008**, *20(48)*, 485221.

Conclusions

This work explores the consequences of nano-layering on the physical properties of TiO₂, specifically correlating the reduction in thickness down to few nm with the variations of structural and surface properties. In particular, TiO₂ single thin films and TiO₂ nanolayered heterostructures, formed by alternating TiO₂ with other compatible oxides, have been considered. The motivations to investigate nano-layered TiO₂ rely on the recent and growing interest on the large variety of TiO₂ electronic and optical applications, and on the possibility to tune and calibrate some of this physical properties by reducing the size (the thickness, in this case) to the nanoscale. In particular, this work is focused on the fabrication of TiO₂ nanolayers and possible post-deposition thermal treatments, to reach a full control of their final crystal phase (amorphous, crystalline and/or a mixture of different crystalline phases). Moreover, the ability to freeze the crystallization at the early stage can be sometimes also required.

Sets of both TiO₂ single layers and TiO₂-based nanolayered heterostructures, formed by pairing TiO₂ with SiO₂, Ta₂O₅, ZrO₂, or Al₂O₃ have been fabricated, by varying their thickness at the nanoscale. All samples have been deposited by IAD e-Beam. In addition, co-sputtered TiO₂- Ta₂O₅ thin film samples, fabricated by IBS at LMA, have been studied in this work.

The use of different thickness and post deposition thermal processes (at different annealing temperatures and in different environments) is employed to favor different crystallization levels and material density.

This work mainly implied the use of experimental techniques, such as XRD, RS, AFM, XRR, and EDS. Besides some routinary control of sample composition and effective thickness, the main results are related to the following points:

1) onset and evolution of crystallization:

The crystallization onset temperature has been shown to depend on i) annealing environment, ii) film thickness and iii) surface energy. In the first case, the onset of crystallization is delayed if the as-grown sample is annealed in vacuum conditions, as a consequence of oxygen vacancies formation. In light of this, the differences on the structural properties of TiO₂ have been discussed as a consequence of annealing in oxygen-rich and oxygen-poor environments. Moreover, an exponential increase of the crystallization onset temperature has been shown when reducing the TiO₂ thickness down to few nm. While exhibiting qualitatively the same trend, the absolute values of the crystallization onset temperatures have been demonstrated to be affected by the presence of interfaces, i.e., they are different when TiO₂ is interfaced with air, rather than other oxides.

2) evolution of the crystalline phases:

The evolution from the earliest anatase phase to the rutile one has been shown to be also affected by both the annealing conditions and the layer thickness. In particular, the rutile

occurs earlier when the annealing is performed in vacuum and when the film thickness is lower.

3) kinetics of crystallization:

Quantum phonon confinement effects have been identified and studied, at the earliest stage of crystallization, in the most of the investigated samples. Moreover, the observed evolution of crystallization has confirmed a gradual growth of the crystals, inside the amorphous matrix, with a growing rate that disclosed differences among different samples.

4) strain effects:

High temperature annealing (up to 1000 °C) has been demonstrated to affect the crystal lattice, with the building up of tensile strain. The latter has been often shown to affect the high-temperature morphologies, with the formation of cracks, holes, and ripples which have never been detected in the as-grown samples as well as at the earliest stage of crystallization. This topographic evolution is driven by the sintering process.

5) quality of the surfaces and interfaces:

All the as-grown materials disclosed a high-quality of surfaces and interfaces, as their typical roughness is of the nm order. The latter is extremely important for optical applications where light scattering from the surfaces and the interfaces are largely unwanted.

6) surface potential and photovoltage (i.e work function):

The surface reactivity of TiO₂ has been shown to depend on the post-deposition treatments, both as a function of temperature and environment. The results have been correlated with the formation of oxygen vacancies and interstitial Ti atoms, which affect the semiconducting properties of TiO₂, and, as a consequence, its photocatalytic activity.

The discussed results are of interest of many possible TiO₂ application fields. For instance, the optical properties of TiO₂ in co-sputtered and nanolayered-heterostructures, are deeply studied for applications requiring high precision Bragg mirrors. Among the others, the study of new generation mirrors for GWDs represents the context where the topic of this thesis originated. Indeed, the design of the TiO₂-based nanolayers, studied in this work, has been proposed for new mirror prototypes to be implemented in the new generation GWDs.

On the other hand, while the investigation of some of the electrical properties of TiO₂ after thermal annealing is a key ingredient for its photocatalytic applications, other applicative devices, such as phase change materials (PCMs) require a detailed knowledge of the TiO₂ polymorphs and their evolution.

Acknowledgements

First, I am grateful my advisor, Prof. Fabrizio Bobba, and my co-supervisor, Dr. Cinzia Di Giorgio, for their willingness and passion to impart their knowledge.

I would like to acknowledge Prof. Carmine Attanasio, as Ph.D. coordinator, and Prof. Salvatore De Pasquale, as Department Director. I am grateful to Prof. Roberta Citro for her right scientific and personal advices, and Prof. Anna Maria Cucolo for his wisdom.

I would like to thank the following people, without whom I would not have been able to complete this research: Prof. Fabrizio Bobba, Dr. Cinzia Di Giorgio, Prof. Innocenzo Pinto, Prof. Riccardo De Salvo, Dr. Veronica Granata, Dr. Joshua Neilson, Dr. Antonio Vecchione, Dr. Rosalba Fittipaldi, Prof. Vincenzo Pierro, Prof. Francesco Chiadini, Dr. Franco Dinelli, Prof. Maria Principe, and Prof. Vincenzo Fiumara.

I feel also grateful to all members of the VCR&D group for the fruitful scientific discussions. In particular, Dr. Massimo Granata that allowed me to analyze samples fabricated at Laboratoire des Matériaux Avancés (LMA) in Lyon, and Prof. Gianpietro Cagnoli of Institut Lumière Matière in Lyon that gave me his availability to carry out my period abroad in Lyon (period that unfortunately I did not spend due to Covid).

Fundamental for my research, it was the use of Raman Spectrometer and X-ray diffractometer located at Pharmacy Department (DIFARMA) and Chemistry and Biology Department (DCB), respectively, of University of Salerno. For this reason, I would like to thank Profs. Pietro Campiglia and Carlo Crescenzi, from DIFARMA, and Prof. Vincenzo Venditto and Dr. Ivano Immediata, from DCB.

Moreover, I never thought a so good working experience in the GESTIONE SILO Company. Thus, I'm thankful to Dr. Francesco Cappelli (for his knowledge, sympathy e for his great expectations about me), and all staff working in the Company.

The personal relationships allowed me to face even the most difficult situations. I should tell every important person in my life something special but a thesis would not be enough. Fortunately, they already know, but it is right to say a few words for each of them. To my great love Claudio, that has always encouraged and loved me. He always made me feel confident in my abilities during this PhD, supporting me and putting up with my stresses. To my Sicilian Family that accepted me from the beginning. To Letizia (and daughters), Lidia, Valeria, Sedi and Andrea for their friendship and patience. To my favorite Dr. Alessandro Reale that gave me more advices to face my messed up life. To my aunt Silvia who loves me as my grandmother.

To my father, my sister, my nephew, my brother in law for their special and loving support. Finally, the strong interconnection with my mother gave me strength and brave to conclude this path.

Appendix A

Phonon confinement

Phonon confinement in nanoparticles with a size smaller than 20 nm can give substantive wavenumber shifts and asymmetric line broadening of the bulk crystal Raman bands. Acoustic and optical phonons are quanta of atomic vibrations in crystalline solids that depend on the number of the atoms in the unit cell, e.g., a compound with N atoms has 3 acoustic and $3N-3$ optical phonons. In an ideal crystal of infinite size, such as a well-crystallized polycrystalline sample with micrometer-size grains, the one-phonon scattering process is due to the optical phonons close to the Brillouin zone center ($q \sim 0$) [1-4].

In this case, the vibrational wave function of confined phonon q_0 in spherical nanoparticles of diameter L , is describe by a plane wave:

$$\varphi(q_0, r) = W(r)u(q_0, r) \exp(-iq_0 \cdot r), \quad (\text{A1})$$

where

$$W(r, L) = \exp\left(\frac{-\alpha r^2}{L^2}\right) \quad (\text{A2})$$

is a Gaussian function, which is widely used as confinement function in literature [4], and α describes the decreasing behavior of the wave function at the boundary, assuming a value of $8\pi^2$ used by the Campbell and Fauchet (CF) model [5].

Equation (A1) can be rewritten as:

$$\varphi(q_0, r) = \varphi'(q_0, r)u(q_0, r), \quad (\text{A3})$$

where $u(q_0, r)$ indicates the lattice periodicity. In order to explore the effect on the Raman spectrum, $\varphi'(q_0, r)$ can expanded in Fourier series:

$$\varphi'(q_0, r) = \int C(q_0, q) \exp(iq_0 \cdot r) d^3q, \quad (\text{A4})$$

in which

$$C(q_0, q) = (2\pi)^{-3} \int \varphi'(q_0, r) \exp(-iq_0 \cdot r) d^3r \quad (\text{A5})$$

are the Fourier coefficients.

Calculating the integral explicating $\varphi'(q_0, r)$, and then $W(r)$, one obtains:

$$C(q_0, q) = \exp\left(-\frac{L^2(q-q_0)^2}{4\alpha}\right). \quad (\text{A6})$$

Considering that $q_0 = 0$ for the zone-center Raman scattering, the Fourier coefficients become:

$$|C(0, q)|^2 = \exp\left(-\frac{L^2 q^2}{16\pi^2}\right). \quad (\text{A7})$$

These coefficients are used to calculate the first-order Raman spectrum given as:

$$I(\omega) = \int \frac{|C(0, q)|^2 d^3 q}{(\omega - \omega(q))^2 + (\Gamma_0/2)^2}, \quad (\text{A8})$$

where

$$\omega(q) = \omega_0 - \Delta\omega \sin^2\left(\frac{qa}{4}\right) \quad (\text{A9})$$

is the optical phonon dispersion curve. Γ_0 is the linewidth of the zone-center optical phonon of the bulk, ω_0 is the zone-center optical phonon frequency, $\Delta\omega$ is the width of the phonon dispersion curve, and a is the lattice parameter. Moreover, the three dimensional (Eq.A8) can be reduced to a one-dimensional integration over a spherical Brillouin zone using the averaged one-dimensional dispersion curve $\omega(q)$, as written in Eq.(A9).

Eq. (A8) has been calculated through Wolfram Mathematica software. The parameters used for the TiO₂ anatase phase are: $a = 0.3785$ nm, $\Delta\omega = 20$ cm⁻¹, $\omega_0 = 144$ cm⁻¹ (for bulk value), and $\Gamma_0 = 7$ cm⁻¹. Figure A1(a) shows the behavior of $I(\omega)$ as a function of ω at fixed L . The frequency at which $I(\omega)$ approaches its maximum value, i.e., ω_{max} , can be extracted from these curves and plotted as function of the crystalline size L , see black solid line shown in Figure A1(b). The horizontal color dashed lines indicate the experimental Raman shift of the TiO₂-200 nm sample annealed at different temperatures in air. The black dotted line marks the anatase bulk mode at 144 cm⁻¹. From the intersection of the black solid curve with the dotted lines, it is possible to extract the values for the crystalline size. Then, the values 5.14, 7.46, and 11.32 nm for the samples annealed at 150, 175, and 200 °C, respectively, were estimated. At annealing temperatures higher than 300 °C, the black curve does not intersect the color dashed lines, therefore no information can be extracted on crystallite sizes in this case. Finally, Figure A1(c) shows the linear behavior of the extracted crystalline sizes as a function of the annealing temperature; only the values in the range temperatures of 150-200 °C are acceptable since the value at 250°C is beyond the limit given by the phonon confinement theory.

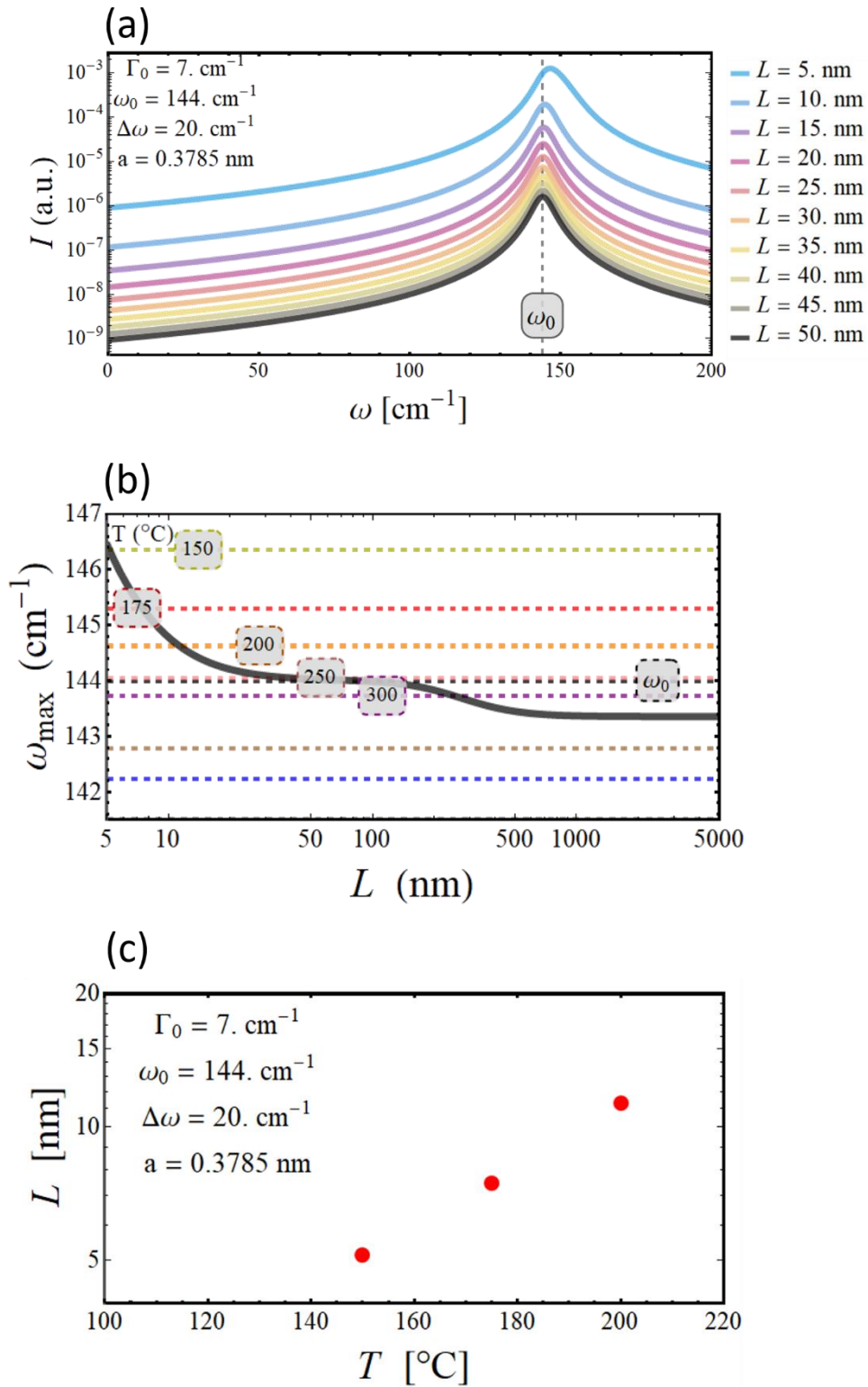


Figure A1: (a) $I(\omega)$ as a function of ω for fixed L crystalline sizes. (b) ω_{max} as function of L . (c) L as a function of the annealing temperatures.

References

1. Bersani, D. *et al.* Phonon confinement effects in the Raman scattering by TiO₂ nanocrystals. *Applied Physics Letters* **1998**, 72(1), 73-75.
2. Arora, A. K., *et al.* Phonon confinement in nanostructured materials. In *Encyclopedia of Nanoscience and Nanotechnology*. American Scientific Publishers **2004**, 8(512), 499-512.
3. Balaji, S. Y. D. J. R. *et al.* Phonon confinement studies in nanocrystalline anatase-TiO₂ thin films by micro Raman spectroscopy. *Journal of Raman Spectroscopy: An International Journal for Original Work in all Aspects of Raman Spectroscopy, Including Higher Order Processes, and also Brillouin and Rayleigh Scattering* **2006**, 37(12), 1416-1422
4. Osswald, S. *et al.* Phonon confinement effects in the Raman spectrum of nanodiamond. *Physical Review B* **2009**, 80(7), 075419.
5. Campbell, I. H., Fauchet, P. M. The effects of microcrystal size and shape on the one phonon Raman spectra of crystalline semiconductors. *Solid State Communications* **1986**, 58(10), 739-741.
6. Campbell, I. H., Fauchet, P. M. The effects of microcrystal size and shape on the one phonon Raman spectra of crystalline semiconductors. *Solid State Communications* **1986**, 58(10), 739-741.

Appendix B

Performance limits of coatings for gravitational wave detector

In Ref. [1], Pierro and co-authors formulate and design new coatings in order to minimize both coating transmittance and thermal noise by using a global optimization algorithm [Multi Objective Evolutionary Algorithm (named Borg MOEA)] without a priori assumption on both number and thickness of layers.

The main noise source in the gravitational wave detector is the thermal noise due to the high-reflectance coatings in the test-masses. In order to reduce this noise, several strategies are adopted, such as the use of new materials and optimization of coating design.

The aim of Ref. [1] is to obtain a new coating, multilayers of high and low refractive index that increase the reflectance reducing the thermal noise. An alternative coating from the standard one, which is a stack of high/low doublet with a thickness equal to a quarter wavelength at 1064 nm, is adopted. Then, design is studied without no a priori assumptions on both layer thicknesses and number minimizing both coating transmittance and thermal noise.

The multilayers structures, shown in Figure B1(a), is placed between dielectric spaces, i.e., the vacuum (left) e the substrate (right). A monochromatic plane wave is orthogonal to the coating. The transmission matrix of m-layer will be:

$$T_m = \begin{bmatrix} \cos(\varphi_m) & i (n^{(m)})^{-1} \sin(\varphi_m) \\ i n^{(m)} \sin(\varphi_m) & \cos(\varphi_m) \end{bmatrix}, \quad (\text{B1})$$

where

$$\varphi_m = \frac{2\pi}{\lambda_0} n^{(m)} d_m, \quad (\text{B2})$$

with λ_0 , d_m , $n^{(m)}$ being the free space wavelength at 1064 nm, the layer thickness and the refractive index of the m-layer, respectively. For the whole coating, the transmission matrix will be:

$$T = T_1 \cdot T_2 \cdot \dots \cdot T_{N_L}, \quad (\text{B3})$$

where N_L is the total number of layers.

About the coating thermal noise, the power spectral density is:

$$S_T(f) = \frac{2 k_B T (1-\sigma_s^2)}{\pi^4 f} \frac{1}{w Y_s} \varphi_c, \quad (\text{B4})$$

where k_B is Boltzmann's constant, T is the absolute temperature, σ_s is the Poisson ratio, Y_s is the Young's elastic modulus of the substrate, and w is the half-width of the Gaussian laser beam. The effective coating loss angle, i.e.,

$$\varphi_c = \sum_{m=1}^{N_L} \eta_m d_m, \quad (\text{B5})$$

depends on the mechanical loss angle and Young's modulus of the m -layers.

In this work, to reduce the coating loss angle φ_c , the layer thicknesses is optimized. The formulation of optimization on the thickness to minimize both transmittance (τ_c) and loss angle φ_c is:

$$\text{Minimize}_{z_1, \dots, z_{N_L}} |\overline{\varphi}_c, \tau_c|. \quad (\text{B6})$$

The result of this problem is a tradeoff curve, also known as Pareto boundary (or Pareto front), in the $|\overline{\varphi}_c, \tau_c|$ plane. Each point in the Pareto front corresponds to a z_m , with $m = 1, \dots, N_L$ of layer normalized thicknesses. The Pareto front has been investigated by using a Multi Objective Evolutionary Algorithm (MOEA) named Borg MOEA that uses an evolutionary strategy appropriate for continuous variables. For comparison, the coatings of Virgo/LIGO detector are used in the simulation. This approach is equivalent to the constrained single-objective optimization problems:

$$\begin{aligned} & \text{Minimize}_{z_1, \dots, z_{N_L} \in \Omega} \overline{\varphi}_c \\ & \text{Subject to } \tau_c \leq \tau_0, \end{aligned} \quad (\text{B7})$$

where Ω is the search space, and τ_0 is the constraint transmittance that is a few parts per million (ppm), and

$$\begin{aligned} & \text{Minimize}_{z_1, \dots, z_{N_L} \in \Omega} \tau_c \\ & \text{Subject to } \overline{\varphi}_c \leq \overline{\varphi}_0, \end{aligned} \quad (\text{B7})$$

where $\overline{\varphi}_0$ is a maximum loss angle.

The computed parameters to investigate the convergence of this algorithm are $N_L = 11, 15, 19, 39, 41, 43$ with an evolution time of $T_s = 10^5$ s. Figure B1(b) shows the Pareto curve (blue) for N_L ranging from 11 to 39 with step 4. The red points are the quarter wavelength design located on the curve described as a straight line in the log-linear of the plane $|\overline{\varphi}_c, \tau_c|$:

$$\log(\tau_c) = \log\left(\frac{4}{n_L}\right) - \frac{2n_H}{\gamma n_L + n_H} \log\left(\frac{n_H}{n_L}\right) - \overline{\varphi}_c \frac{8n_H n_L}{\gamma n_L + n_H} \log\left(\frac{n_H}{n_L}\right), \quad (\text{B8})$$

where $\gamma = \frac{n_H}{n_L}$ is the noise ratio coefficient. The horizontal dashed line, $\tau_c = 6 \text{ ppm}$ is the target transmittance required for the coatings in the gravitational wave detectors. Figures B1(c), (d), (e) show the layer thickness configuration given by the intersections between tradeoff curves with $N_L = 39, 41, 43$ and the horizontal transmittance line $\tau_c = 6 \text{ ppm}$. These configurations show a reduction of the normalized noise with the respect to the quarter wavelength reference design of about 15.5%, 15.9%, 15.9% respectively.

The height of vertical blue (yellow) bars indicate the normalized layer thicknesses z_m of high (low) refractive index material, see odd (even) m values on the bottom (top) axis. The design is consistent with the points obtained by the intersection of the Pareto boundary with the horizontal line [dashed line in Figure B1(b)] plotted at the prescribed transmittance level ($\tau_c = 6 \text{ ppm}$). Finally, Figures B1(f), (g) display results about noise reduction and effective noise ratio as a function of noise ratio coefficient, γ , showing a linear behavior for both quantities.

In conclusion, Ref. [1] describes the optimization of the design of binary (two-materials) coatings for GW detectors by using a multiobjective optimization problem, studied with global optimization algorithm (Borg MOEA), that minimize both the transmittance and the thermal noise. This study is achieve setting the refractive index and number of layers, but no priori assumptions are made on the layer thicknesses.

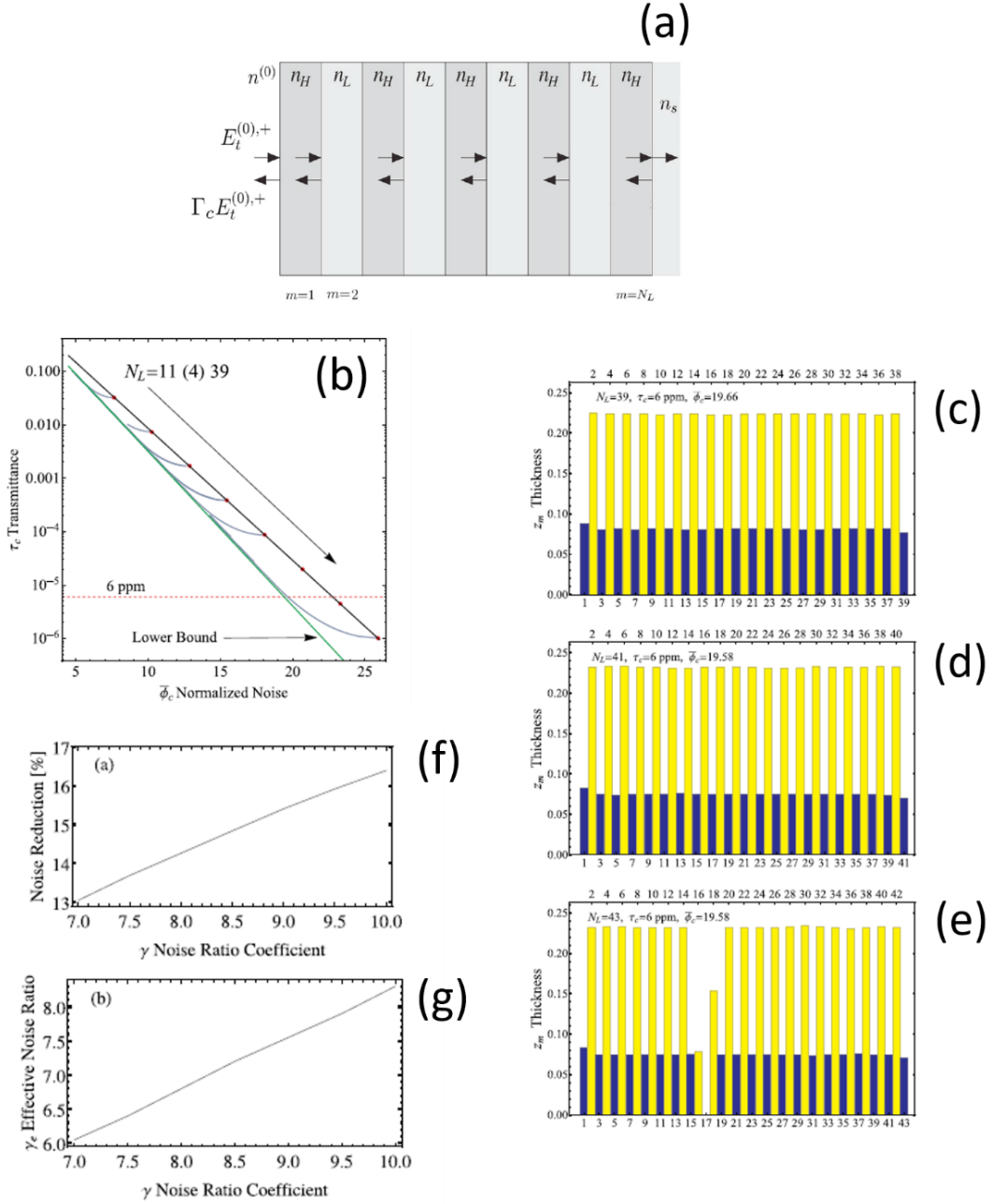


Figure B1: (a) 1. Multilayer structure made of N_L alternating high (n_H) and low (n_L) refractive indexes, deposited on a substrate of refractive index n_S in the vacuum half-space. (b) Pareto fronts for $N_L = 11$ to $N_L = 39$ in step of 4 in log-linear scale (blue curves). The normalized layer thicknesses z_m of the optimal multiobjective design for cases $N_L = 39$ (c), $N_L = 41$ (d), $N_L = 43$ (e). (f) The percent loss angle reduction and (g) the effective noise ratio coefficient as a function of γ , by fitting equation (B8) to the Pareto front. Adapted from [1].

References

1. Pierro, V. *et al.* On the performance limits of coatings for gravitational wave detectors made of alternating layers of two materials. *Optical Materials* **2019**, *96*, 109269.

Appendix C

Ternary quarter wavelength coatings for gravitational wave detector mirrors

In Ref. [1], Pierro and co-authors focus on a ternary coatings to minimize thermal noise in the gravitational wave detectors, under optical transmittance and absorbance constraints. These coatings consist of quarter-wavelength-thick layers, in which a third material, such as amorphous silicon and silicon nitride, operating at ambient and cryogenic temperatures, is added to silica (L) and titania-doped tantala (H).

In the last two decades, the research of coating materials with large dielectric contrast, low optical absorption, and low mechanical losses was undertaken to reduce thermal noise in the highly reflective dielectric-multilayer coated mirrors. Actually, the materials used are (TiO₂ doped Ta₂O₅) together with silica (SiO₂), deposited by Laboratoire des Matériaux Avancés (LMA), but other materials could be taken into account, for example amorphous silicon (aSi) and Silicon nitrides (SiNx). It was demonstrate that the use of third denser, but optically lossier, material would allow one to reduce the total number of layers and, therefore, the coating thermal noise. Nevertheless, the design constraints and requirements of the mirrors need further analysis.

The aim of Ref. [1] is to study an optimal configuration for the ternary coating design, which guarantees lowest thermal noise under optical transmittance and absorbance constraints.

By using the coating model, based on the transmission matrix formalism, and thermal noise model, one can obtain the coating loss angle for ternary coatings consisting of QWL layers made of three possible materials:

$$\varphi_c = \frac{\eta_L \lambda_0}{4Re(n_L)} (N_L + N_H \gamma_H + N_{H'} \gamma_{H'}), \quad (C1)$$

where N_L , N_H , and $N_{H'}$, are the number of layers made of the L , H , and H' materials, respectively.

Numerical experiments have been performed using a third material with different properties: i) material “ A ” with same mechanical losses as TiO₂::Ta₂O₅ and a fairly higher refractive, and larger optical losses, and ii) material “ B ” characterized by the same refractive index as TiO₂::Ta₂O₅, lower mechanical losses, and larger optical losses. The bounds in transmittance, $\tau_{ref} = 6 \text{ ppm}$, and absorbance, $\alpha_{ref} = 1 \text{ ppm}$, and different values of the extinction coefficient, $\kappa_{H'}$, (ranging from 10^{-6} to 10^{-4}) have been respected. The optimal design and parameters using the materials A and B for H' , are shown in Figure C1.

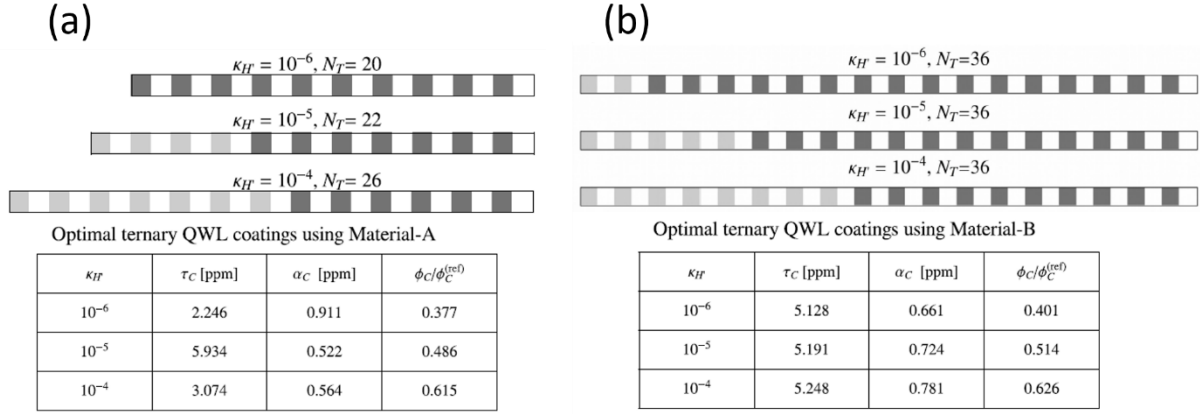


Figure C1: The optimal QWL ternary coating designs, using silica (L), $\text{TiO}_2::\text{Ta}_2\text{O}_5$ (H), and (a) A or (b) B (H') materials, assuming different values for $\kappa_{H'}$. White, light gray, and dark gray boxes represent L, H, and H' materials, respectively. Adapted from [1].

In this way, several parameters have been investigated. Indeed, it was found that the ternary QWL designs are characterized by being robust against uncertainties in the value of the extinction coefficient of the H' material. About transmittance, the spectrum of the material A is quite different from the reference spectrum compared with that of the material B. The asymmetry can derive from the two cascaded homogeneous QWL stacks. The assumptions on thickness of the ternary QWL coatings instead is more demanding. A heuristic approach is to optimize the two binary QWL stacks that form the top and bottom parts of the optimal QWL ternary coatings, assuming each of them to consist of identical non-QWL Bragg doublets.

The aSi and SiNx materials seem to satisfy the structure and properties of the optimal coatings. As shown in Figure C2(a,b), the thermal noise reduction factor is found to be almost linear in $\log_{10}(\kappa_{H'})$ for both materials.

In conclusion, Ref. [1] faces the problem of designing a ternary optical coating consisting of QWL layers, focus on the robustness, thickness, and transmittance. The choice of either aSi or SiNx, in addition to silica and $\text{TiO}_2::\text{Ta}_2\text{O}_5$ is taken into account to reduce the coating thermal noise.

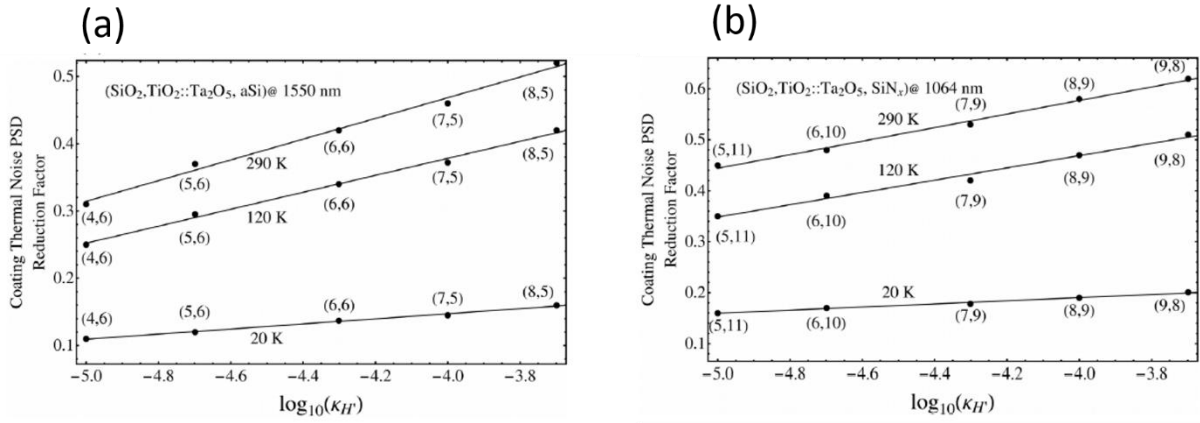


Figure C2: thermal (Brownian) noise reduction factors for optimal QWL ternary coatings vs extinction coefficient of third (H') material. $a\text{Si}$ (at 1550 nm), and SiN_x (at 1064 nm) are shown in (a) and (b) panels, respectively at three different temperatures (290, 120, and 20 K). Adapted from [1].

References

1. Pierro, V. *et al.* Ternary quarter wavelength coatings for gravitational wave detector mirrors: Design optimization via exhaustive search. *Physical Review Research* **2021**, 3(2), 023172.

Appendix D

GESTIONE SILO: company stage

During my PhD program, I spent 6 months (in presence and smart-working modality) in the Italian company Gestione SILO (Florence), to perform a stage on the use of the electron beam evaporator (OPTECH OAC-75), the thermal evaporator (MD 1100), the Spectrometer (PelkinElmer Lambda 950 UV/VIS), and the software analysis to design mirror coatings.

Gestione SILO is the Italian leader in the optics and optical devices (lenses, prisms, mirrors, flat optics, optical filters, opto-mechanical systems) as well as in the design, construction, and assembly of precision optical systems, in many sectors: aerospace industry and military, scientific instrumentation, research and biomedical sector, telecommunications. In particular, among the most used coatings, there are Anti-reflectors for UV light, Visible-Near Infrared, polarizing and non-polarizing Beam Splitter, dichroic filters, metal mirrors, dielectric mirrors. The coatings produced by Gestione SILO are tested according to the strictest international military standards.

This internship led to the acquisition of various software and hardware skills. In the following, I report in detail what has been done.

- 1) The stage on the software (Mcalc Multilayers calculation) led to design of mirror with max reflectivity, 100 % at 1064 nm, made by SiO_2 and TiO_2 materials. In light of this, under supervision of F. Cappelli, head of the production area, we design a multilayer formed by 20 alternating SiO_2 and TiO_2 layers, with a thickness of 117.022 and 182.011 nm, respectively. The substrates involved are SiO_2 and NBK7 (produced by the Ohara and Schott corporations). The simulated reflectance and transmittance curves are shown in the Figure D1. Then, if I focus on the range of interest around of 1064 nm, I can obtain a mirror prototype with 100% of reflectance and 0% of transmittance.

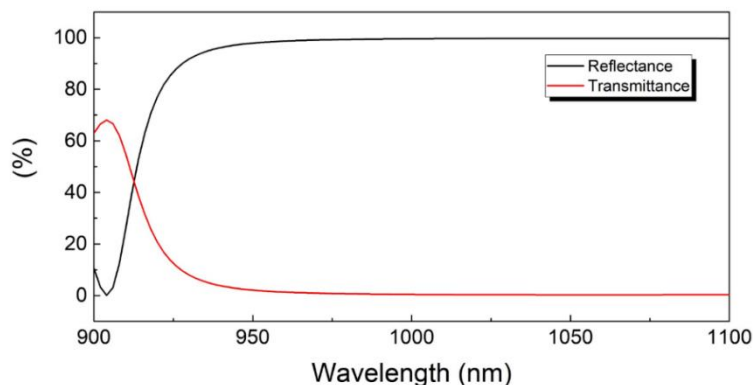


Figure D1: reflectance (black curve) and transmittance (red curve) of the multilayers $\text{SiO}_2/\text{TiO}_2$.

2) The stage on the electron beam evaporator (OPTECH OAC-75) [1], and the thermal evaporator (MD 1100) led to extend my technical background. Figure D2 (a-b) shows the outside and the electronic rack of these two systems depositions, respectively. They are both characterized by central material six crucibles and the common tools, called shades (with adjustable shapes) to guarantee uniformity in the deposition. Also, in both cases six quartz crystal sensors are used to measure the corrected film thickness during the deposition. The carousel can accommodate several substrates, depending on their size, and can be rotated during the deposition. The chamber deposition, in both cases, can reach the value of 10^{-8} *mbar* by using a pumping system formed by the root, and cryo-pumps for low and high vacuum level, respectively. Even if the company from which the coaters were acquired is the same, that in Benevento shows many technical differences, as reported in [2]. Moreover, temperatures used in all processes are set in the range of 150-250 °C. Then, these depositions not occur at room temperature, differently from the deposition performed in Benevento. In order to guarantee high quality deposition, Gestione SILO selected materials to be deposited with the electron beam and with thermal evaporations. Materials such as SiO₂, TiO₂, Y₂O₃, and ITO are deposited in the electron beam evaporator instead MgF₂, HfO₂, Cr, Ti, Ag, Al, Au are fabricated by using the thermal evaporation.

(a)



(b)



Figure D2: (a) electron-beam evaporator (b) thermal evaporator. Inside (right) and outside (left) of deposition systems. Adapted from [1].

In light of this, metal coatings are fabricated in Gestione SILO and then have been characterized in the SPnM and MUSA laboratory at University of Salerno. The metal materials, i.e., Ag and Al, with a thickness of ~ 100 nm are deposited on the SiO_2 and NBK7 substrate by using thermal evaporator and morphological and chemical properties are studied by using the Atomic Force Microscopy (AFM) and Energy Dispersive X-ray Spectrometry (EDS). AFM images have been acquired with a Nanowizard III, equipped with Vortex electronics from JPK, in the tapping mode technique, using a L-TESP-V2 tip from Bruker. The cantilever is characterized by a nominal resonance frequency and elastic constant of $f_0 \approx 190$ kHz and $k \approx 48$ N/m, respectively.

The mid panel of Figure D3(a) shows a photo of the Silver (Ag) mirror, with a thickness of 100 nm, deposited on a Silica substrate (1 cm). In order to check the film uniformity, I have investigated the center and the edge of each sample acquiring a scan area of $10 \mu\text{m} \times 10 \mu\text{m}$ (large) and $1 \mu\text{m} \times 1 \mu\text{m}$ (small). At the sample center, as well as the edge, the large scan area shows a very flat surface, instead the smallest area shows a granular structures. In fact, by enlarging the lateral size I lose the resolution of the tiniest details. This is also reported in the measure of Root-Mean-Square (RMS) roughness that is higher (smaller) than 1.5 nm on small (large) area. A black-to-white color scale has been used to highlight the surface roughness, from a minimum value of 0 nm (black) to a maximum of 13 nm (white). Instead, Figure D3(b) shows a representative EDS area of $600 \mu\text{m} \times 600 \mu\text{m}$ and EDS spectrum of the Ag sample.

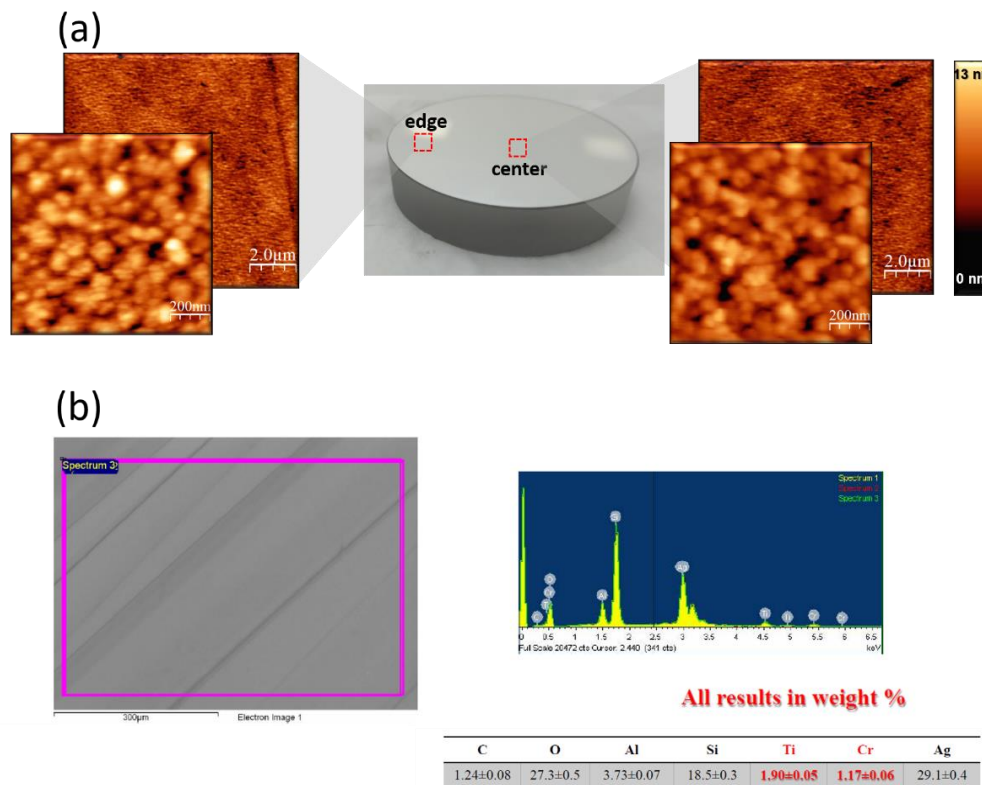


Figure D3: (a) AFM (b) EDS measurements of the Ag mirrors.

In particular, I acquired three different scan areas and three spectra for each area and the values reported in table (in the bottom) are an average on all acquired spectra. From this kind of analysis, the presence of C, O, and Si (coming from the substrate), Al (coming from the substrate and deposition chamber), and Ti and Cr (again coming from the deposition chamber) are measured.

The percentage of Ag, coming from the film, is of $(29.1 \pm 0.4) \%$. All values in the table at the bottom of the Figure D3(a) are reported in atomic weight (%).

Figure D4(a) shows representative AFM images and the photo of the Al mirror. Figure D4(b) shows the representative EDS image (600 $\mu\text{m} \times 600 \mu\text{m}$) and EDS spectrum of the Al sample. As already done for Ag mirror, I have been performed AFM and EDS measurements on Aluminum (Al) mirror with a thickness of 100 nm deposited on NBK7 substrate (0.5 cm). Also in this case, I investigate two different areas, in the center and in the edge, to check the film uniformity. Then, I acquired the scan areas of $10 \mu\text{m} \times 10 \mu\text{m}$ (large), and $1 \mu\text{m} \times 1 \mu\text{m}$ (small) and measured the RMS roughness. I observed that the surface of this sample is more rough than the Ag mirror one. In fact, the RMS roughness is higher than 1.5 nm on both scan areas. This can be due to the different materials forming the film. In fact, by EDS measurements, B, Na, Si, K, Ca, Ba, Ti coming from the substrate are measured. Instead, the presence of S can be due to the chamber contamination. Then, the percentage of Al, coming from the film, is of $(3.65 \pm 0.11) \%$.

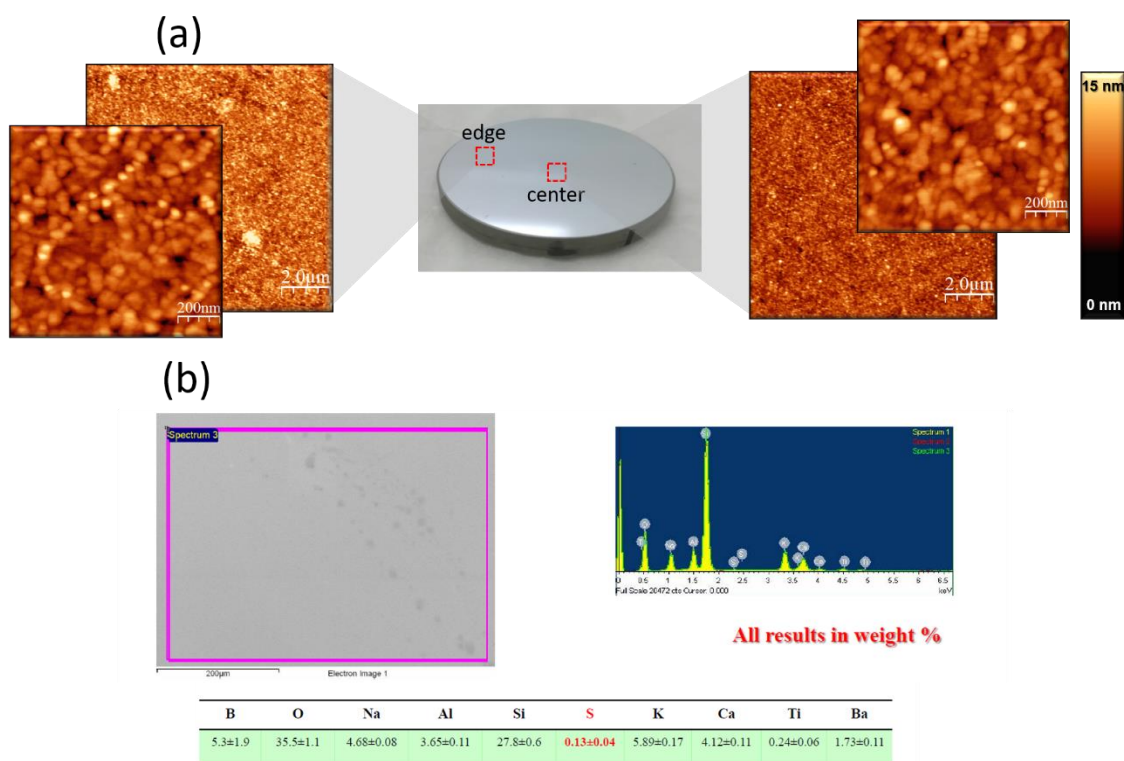


Figure D4: (a) AFM (b) EDS measurements of the Al mirrors.

In conclusion, this sample investigation is carried out to determine the possible contaminations on the sample surface (company request) and to compare metal mirrors,

deposited in Florence, with dielectric mirror, deposited in Benevento. Then, from a morphological point of view, the dielectric mirrors show better characteristics than the metal ones. Similarly, regarding chemical composition, EDS measurements performed on these metal mirrors display more contamination than the dielectric coating deposited in Benevento (see Chapter 4).

3) The stage on the Spectrometer (PelkinElmer Lambda 950 UV/VIS) led to extend my background knowledge on optimal techniques and instruments. The Lambda 950 UV/VIS is a spectrometers that operates in the near infrared region formed by double-monochromator optical system, optical component coated with silica and gratings. In Figure D5(a-c), I show a cartoon displaying the main components, a photo of the instrument used in our measurements, and a scheme of the optical setup, respectively. The optical system is formed by two lamps, deuterium (DL) and halogen (HL), that allows working on a large range of wavelength. The DL and HL lamps can be used in the UV range and in the NIR-Vis range, respectively. In light of this, a mirror M1 allows the passage of one radiation rather than another. The source change is automatic during the monochromator rotation (G1). The specific radiation coming from one of these lamps, is reflected from the M2 and M3 mirrors by using an optical filter (FW) to mirror M4. The radiation from mirror M4 is reflected in the slit of the monochromator I. The SA represent all located slits. The collimated radiation on mirror M5 is reflected to the gratings G1 (UV/Vis or NIR) producing a spectrum. The resulting radiation goes through the exit slit, and it is collimated on the mirror M6 and reflected on the rotating grating G2, synchronized to that of G1. The radiation is back reflected via mirror M6 through the exit slit to Mirror M7. Then, the radiation beam is reflected by the mirror M8 (toroid) to the chopper assembly (C), that introduces a periodic interruption of the light path. This chopper allows producing two kinds of reflected radiation: one is reflected on the mirror M9 and then on the mirror M10, to create the reference beam (R), and other is reflected on the mirror M10' to form the sample beam (S). Then, the R and S beams are reflected by mirror M11, M12, M13 and M11', M12', M13', respectively. The rotating mirror M14 selects the specific detector, i.e., a photomultiplier (PM) and a lead sulfide (PbS) detector that are used in the UV/Vis and NIR ranges, respectively [3]. For this reason, there are two single-cell holders provided with the instrument, one for the sample beam and one for the reference (transmittance) beam. After the training on Spectrometer, I have acquired the reflectance and transmittance spectra, measured in percentage (%) as function the wavelength between 280-800 nm (UV-Vis range), on the Ar and Al mirrors deposited in Gestione SILO. Figure D6(a) shows the reflectance of the Al mirror (black curve) displaying a monotonically increase from 280 to 400 nm (UV range) and a decrease up to 60% from 400 to 800 nm (Vis range). The maximum value of ~80% is reaches at ~450 nm. Different situation is shown for the Ag mirror (red curve). The reflectance is 20% at 280 nm and after decreases up to 320 nm (10%). From 320 to 380 nm (UV range), the reflectance increase up to 70%, then there is a plateau up to 400 nm. The reflectance increases again from 400 to 450 nm measuring a value from 70 to 90%. In the range of 450-800 nm (Vis range), a weak monotonically increase is observed and the reflectance assume a value of 95% at 800 nm. If I compare, the reflectance in

the Vis range (400-800 nm) for both mirrors, the best performance is reached from the Ag mirror, due to probably to lower surface contaminations, as shown in the EDS measurements. Transmittance for both mirrors is shown in the Figure D6(b). In both cases, in the Vis range (400-800 nm) no radiation is transmitted by these mirror. Then, these results are comparable with those reported in literature [4].

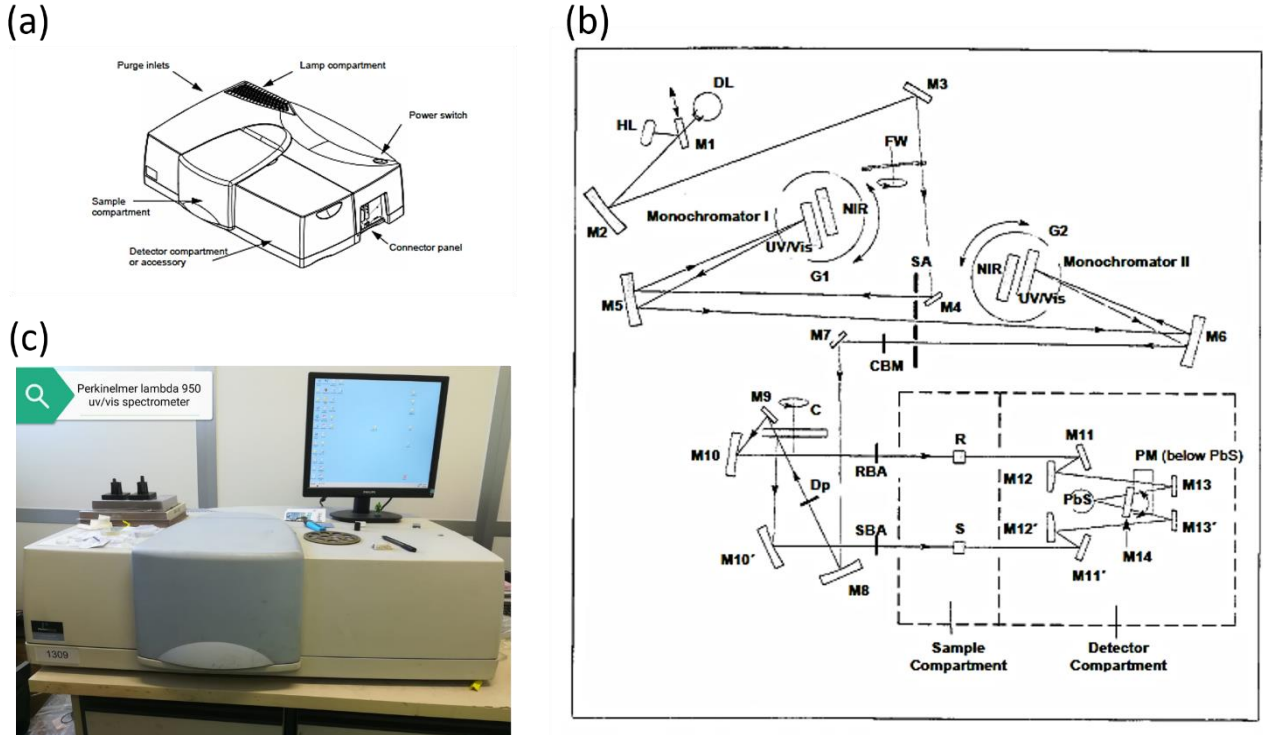


Figure D5: (a) Cartoon, (b) photo, (c) and a schematic of optical system of this instrument. Adapted from [3].

In any optical or spectroscopic measurement, the sample (including surface, volume, internal interfaces) is irradiated with light under a given angle of incidence ϕ . After the interaction, the light can be transmitted (T), reflected (R), scattered (S) or absorbed (A). All light components are defined respect to the incoming light, and in presence of absorption and scatter, the energy law can be written as:

$$T + R + A + S = 1. \tag{D1}$$

These four quantities depend on both the material and geometry sample, the experimental conditions, and the light wavelength. Moreover, they are dependent but can be measured independently from each other. In our case, through the Spectrometer (PerkinElmer Lambda 950 UV/VIS) T and R can be accurately measured. In this way, I can extract also the value of the optical loss via [5]:

$$L \equiv S + A = 1 - R - T. \quad (\text{D2})$$

In general, the transmittance $T(\lambda)$ and the reflectance $R(\lambda)$ for a thin film, are correlated by the equation:

$$T(\lambda) = (1 - R(\lambda))^2 e^{-\alpha(\lambda)d}, \quad (\text{D3})$$

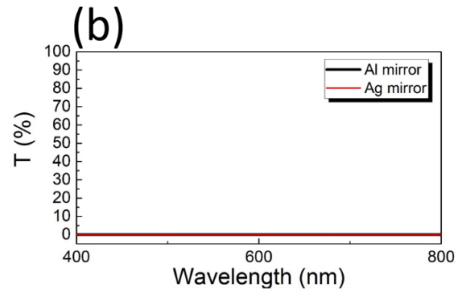
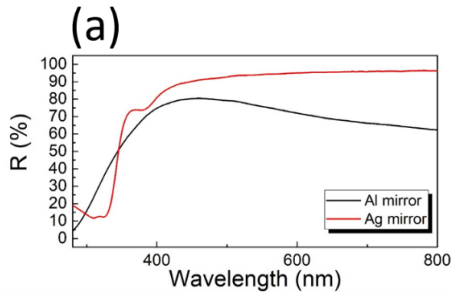
where $\alpha(\lambda)$ and d are the absorption coefficient and the films thickness, respectively. Equation (D3) is of course only valid close to the optical band gap of the material under the condition $e^{\alpha d} \gg R^2$ [6,7].

Then, usually when I performed the spectroscopic measurements, I can consider also scattered and absorbed light. The next measurements have been performed on the samples deposited in Benevento by IAD. First, I acquired the transmittance and reflectance spectra of the Silicon and Silica substrate, see Figure D6(c-d). In the case of the Silicon substrate, I observed constant value of 0% transmittance (black curve) in the range 280-900 nm and an increase from 900 to 1200 nm, in which the transmittance reaches the 60% at 1200 m. The reflectance behavior (red curve) show a different behavior, in which all reflectance values stay below the 35% from 280 to 1200 nm. The step observed in the reflectance could be due to instrumental issues.

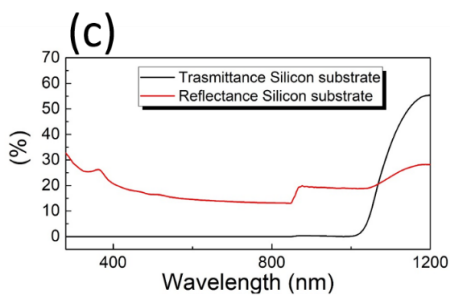
On the contrary, different situation is observed for the Silica substrate. The transmittance (red curve) and reflectance (black curve) show in all range of wavelength a constant value of 95 and 0%, respectively.

The transmittance and reflectance of amorphous TiO_2 thin film, with a thickness of 200 nm, is shown in Figure D6(e-f). The transmittance behavior is the same as that of Silicon, but the reflectance is characterized by constructive and destructive interference of light due to multiple reflections between the interfaces of TiO_2/Si and TiO_2/air . In fact, the red curve shows four maxima (crests) at 362 (47%), 464 (38%), 850 (31%), and 1176 (38%) nm, and four minima (valley) at 366 (15%), 400 (3%), 602 (1.75%), and 1048 (36%) nm, respectively. Then, I observe that this material is characterized by high reflectance at 362 nm (UV region), that corresponds to a gap of 3.42 eV, very close to that the TiO_2 (~3.2 eV).

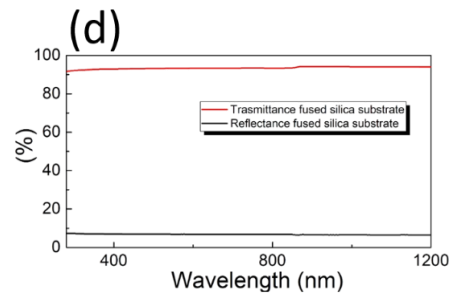
Metal mirrors



Si substrate



SiO₂ Substrate



TiO₂ 200 nm as grown on Si

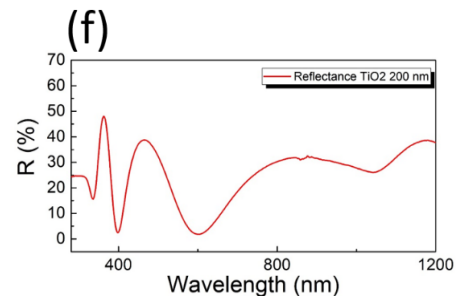
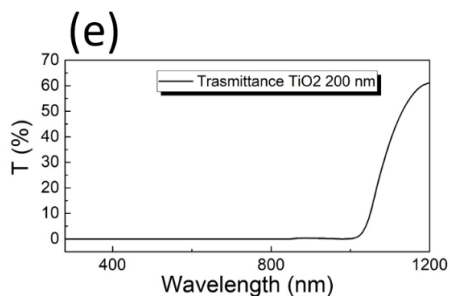


Figure D6: Reflectance (a) and transmittance (b) of Al, and Ag mirror. Reflectance and transmittance of Silicon substrate (c), Reflectance and transmittance of Silica (SiO₂) substrate (d). Transmittance (e) and reflectance (f) of thin film TiO₂ 200 nm on fused Si substrate.

In Figure D7(a,b) transmittance and reflectance of amorphous SiO₂/TiO₂ multilayers, deposited on fused Silica by using the IAD, are shown. In the Table D1, I summarize the number of layers and the thickness of the each SiO₂ and TiO₂ layers (for more deposition details, see Chapter 2).

Number of layers	Samples
11	127.4 nm (6x 69 Å SiO ₂ , 5x 172 Å TiO ₂)
19	127.5 nm (10x 42 Å SiO ₂ , 9x 95 Å TiO ₂)
45	127.2 nm (23x 18 Å SiO ₂ , 22x 39 Å TiO ₂)
76	124.5 nm (38x 13 Å SiO ₂ , 38x 20 Å TiO ₂)
85	126.9 nm (43x 9 Å SiO ₂ , 42x 21 Å TiO ₂)

Table D1: Sample list for the transmittance and reflectance measurements.

In this case, transmittance and reflectance of all multilayers show constructive and destructive interferences of light due to multiple reflections between the interfaces of fused SiO₂/SiO₂, TiO₂/ SiO₂, and SiO₂/air. This can be due to the silica substrate that exhibits a transmittance of 100% and the decrease in peaks/valleys may be due to the reduction of the thickness of the total film (128 instead of 200 nm). Indeed, the number of peaks and valleys depend on the thickness, as shown in Ref. [8]. The values of these maxima and minima in the transmittance and reflectance spectra are listed in Table D2.

All transmittance curves in Figure D(7) behave similarly. In fact, they show two maxima and one minimum, except to 11-layer sample for which the low-wavelengths peak is still not well formed. Moreover, the transmittance of all samples sharply rise at wavelengths higher than 280 nm, while all curves converge at the same value at high wavelengths (T~78% at 1200 nm). Then, increasing the number of layers, i.e., reducing the single layer thickness, I observe: i) a shift towards high wavelengths and an increase of transmittance of the first maximum, and ii) only a shift for the second maximum with a constant value of transmittance.

Sample	Transmittance		Reflectance	
	Maximum	Minimum	Maximum	Minimum
11-layer	94% at 530 nm		34% at 378 nm 22% at 293 nm	13% at 332 nm 7% at 527 nm
19-layer	64.0 % at 362 nm 94% at 530 nm	63.9 % at 372 nm	33% at 382 nm 20% at 283 nm	11% at 335 nm 6.5 % at 536 nm
45-layer	75% at 359 nm 93% at 558 nm	68% at 412 nm	30% at 400 nm 22% at 308 nm	9.6% at 345 nm 7 % at 570 nm
76-layer	79% at 361 nm 93% at 582 nm	67% at 410 nm	28% at 416 nm 23% at 315 nm	9.2% at 350 nm 7.2 % at 596 nm
85-layer	92% at 400 nm 93% at 700 nm	69% at 500 nm	33% at 351 nm 30% at 496 nm	18% at 322 nm 7.5 % at 400 nm 7.3% at 720 nm

Table D2: Sample list for the transmittance and reflectance measurements.

Also in the case of the reflectance, multilayers samples show an alternate of maxima and minima values, reported in Table D2. All curves of samples, except for 85-layer sample, are characterized by two maxima and two minima. I observe that the peak at ~ 400 nm shifts towards higher wavelengths and reduces by increasing the number of layers. Correspondingly, the minimum at ~ 550 nm, shifts and slightly increases. A different situation is observed for the 85-layer sample in which a shift towards high wavelengths is more pronounced, and a more pronounced maximum emerges at ~ 350 nm. Moreover, all reflectance curves converge to the value $\sim 24\%$ at high wavelengths (1200 nm).

As shown for the TiO_2 single layers, considering Equation (D1), I can conclude that the incident light is also absorbed and scattered, but if the scattering sites are smaller than the wavelength, the scattered light can be negligible and I can extract directly from transmittance and reflectance information about absorbance. In Figure D7(c), I show the absorbance as a function of wavelength. In the approximation of a transparent substrate, I observe that the absorbance decreases monotonically from 80 to 0% at 280 and 400 nm, respectively, for all samples. From 400 nm, the absorbance contribute is null, for all sample, i.e, I have only the component of light transmitted and reflected.

Finally, I conclude that the multilayers total thickness, the thickness of each single SiO_2 and TiO_2 layers [9], and the content of SiO_2 [10] affect both the reflectance and the transmittance. It's quite evident that by increasing the number of layers (i.e., reducing the thickness of single layers) promote interference fringes in the spectrum, as shown in the Reflectance of 85-layer sample [11], and a shift toward high wavelengths. I observe also that, in order to increase optical properties of the multilayers different thermal treatments can be also carried out [13].

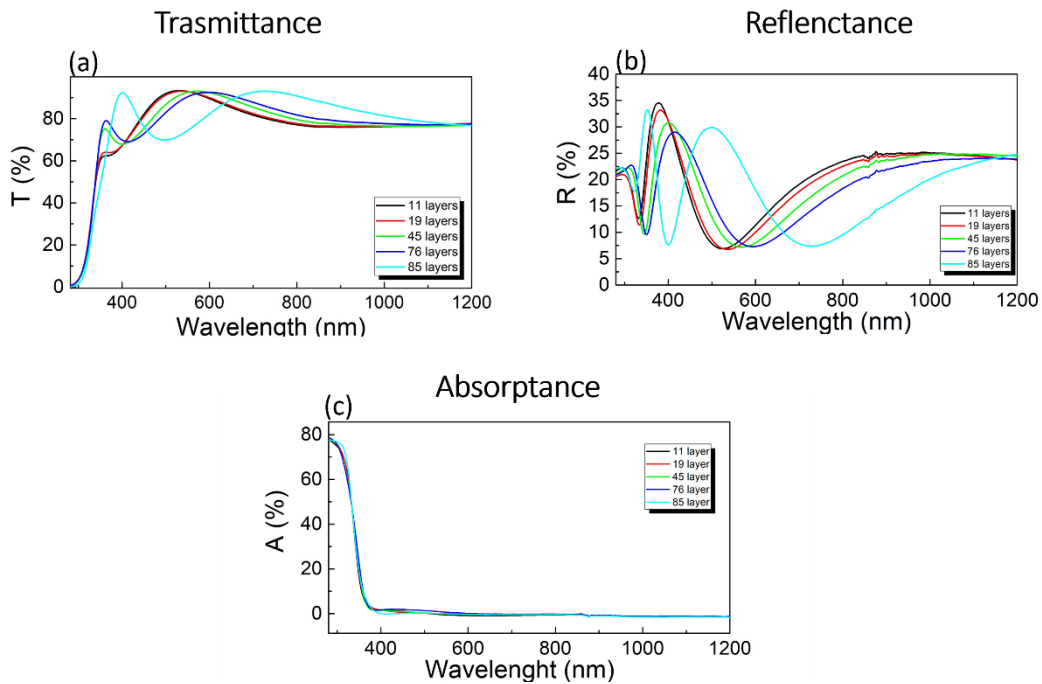


Figure D7: Transmittance (a), reflectance (b), and (c) absorbance of multilayers $\text{SiO}_2/\text{TiO}_2$ deposited on fused Silica substrate.

References

1. GESTIONE SILO, Available online: <https://www.gestionesilo.it/> (accessed on 31 July 2021).
2. Neisohn, J. *et al.* Pushing the precision of e-beam evaporation for nanolayered coatings, *in preparation*.
3. PerkinElmer, Available online: <https://cmdis.rpi.edu/sites/default/files/UVis-PerkinElmer-Lambda950-HardwareGuide.pdf> (accessed on 31 July 2021).
4. Li, L. The advances and characteristics of high-power diode laser materials processing. *Optics and lasers in engineering* **2000**, *34*(4-6), 231-253.
5. Stenzel, O. *Optical coatings: Material Aspects in theory and Practice*. Springer. **2014**.
6. Horprathum, M., *et al.* Oxygen partial pressure dependence of the properties of TiO₂ thin films deposited by DC reactive magnetron sputtering. *Procedia Engineering* **2012**, *32*, 676-682.
7. Martin, N., *et al.* Microstructure modification of amorphous titanium oxide thin films during annealing treatment. *Thin solid films* **1997**, *300*(1-2), 113-121.
8. Dewasi, A., Mitra, A. Effect of variation of thickness of TiO₂ on the photovoltaic performance of n-TiO₂/p-Si heterostructure. *Journal of Materials Science: Materials in Electronics* **2017**, *28*(23), 18075-18084.
9. Sta, I., *et al.* Structural and optical properties of TiO₂ thin films prepared by spin coating. *Journal of sol-gel science and technology* **2014**, *72*(2), 421-427.
10. Li, D., *et al.* Broadband antireflection TiO₂-SiO₂ stack coatings with refractive-index-graded structure and their applications to Cu (In, Ga) Se₂ solar cells. *Solar energy materials and solar cells* **2014**, *130*, 505-512.
11. De Jesus, M. A. M. L., *et al.* A systematic study of multifunctional x TiO₂/(100-x) SiO₂ thin films prepared by sol-gel process. *Journal of Sol-Gel Science and Technology* **2019**, *89*(2), 380-391.
12. Feng, I. W., *et al.* SiO₂/TiO₂ distributed Bragg reflector near 1.5 μ m fabricated by e-beam evaporation. *Journal of Vacuum Science & Technology A: Vacuum, Surfaces, and Films* **2013**, *31*(6), 061514.

Appendix E

Thermal shock effect in electron beam evaporation: Hardware and software upgrades.

In Ref. [1], Neilson J. and co-authors, used an electron beam evaporator to fabricate coatings for gravitational wave detector. Achieving this goal proved to be quite challenging due to the thermal shock suffered by the quartz crystal monitor. For this reason, combination of hardware and software upgrades with new coating techniques are useful to reduce the thermal shock effect, and coatings with angstrom-level of precision have been obtained.

The sensitivity of the gravitational wave detector, like LIGO and Virgo interferometers, are affected by several noise sources, but, in the range in which the gravitational waves are expected (10-100 Hz), the predominant noise source is the thermal one. This is produced by the Brownian motion of the position of test masses mirror, dielectric mirror formed by a number of half-wavelength-thick doublet alternating low (SiO_2) and high (TiO_2 -doped Ta_2O_5) refractive index. In recently years, a strategy to reduce the thermal noise is to replace the high losses material (TiO_2 -doped Ta_2O_5) with nanolayers. Then, the nanolayering can provide a uniform surface, so as to reduce the Brownian noise and inhibit the crystallization, since crystallites act a light scatter.

An Optotech OAC-75RF coater, with plasma assisted electron gun, was chosen for its commercial availability and capacity to rapidly produce coatings. During three years of activities, this commercial coater for the optics industry was modified to deposited atomic layers. Early samples production gave back highly granular coatings, due to the poor quality substrates and software issues, so that root-mean-square (RMS) roughness higher than 1 nm results [1]. But the main issues of the nanolayering process were the software and hardware limitations on the deposition of the thin films. The first problem was about the software that operates on Quartz crystal monitors (QCMs), i.e., crystals that monitors the thickness exposed to the deposition flow. During the deposition process, their resonant frequency decrease by increasing the mass. At the end of the deposition, the software closes the shutter when the thickness is measured by the QCM, introducing however two problems depending on evaporated materials: i) QCM is continuously exposed to the evaporation source; ii) QCM thermal shock. When the shutter first opens, the quartz temperature is suddenly changed by the hot material flow, measuring a negative deposition rate. At the end of the process, due to cooling, a higher deposition rate is estimated. Therefore, the quartz thermalization is a quite long but very important procedure that allows to the software a correct reading of the film thickness. However, for the nanolayering process, this time is too short and the QCM is not thermalized. For this reason, several approaches were adopted, such as set of an automatic thickness offset function obliging the shutter to close before the measurement of the nominal thickness, or other criteria depending on the thickness. Then, Macrotech Company proposed a software and hardware upgrades on long time term. In light of this, and waiting these

improvements, it has proceeded to reduce the thermal shock causes also by the heat radiated by the material in the crucibles. Two kinds of material required two different strategies. Materials like Titania and Tantalum (Fully melted materials) request the use of a smaller crucible to minimize heating on the QCM and target substrate. On the contrary, Silica (sublimating material), need larger crucibles, but for this material there is no way to reduce the thermal shock. Moreover, the change of QCM for every new deposition introduces advantages such as more reliability, less use of substrate and consumables. Then, the software corrections have been implemented: the new measurements considered only the QCM frequency when the shutter is first opened (not affected by the thermal shock) or when the shutter closes (QCM is still hot). Different ideas have been proposed for the Hardware upgrades (second shutter, static mask and rotating substrate shutter, replaced six-crystal QCD head with two-crystal head) of QCM thermalization, but these proposals were incompatible with the second gun, which was actually installed, see Figure E1(a). Anyway, these upgrades (software and hardware) have improved the coatings quality. Figure E1(b) shows three different prototypes deposited in three different situations: i) left sample is deposited without a second e-gun, ii) central sample is deposited with a second e-gun, iii) right sample is deposited by using a recipe of $\text{TiO}_2/\text{SiO}_2$ with 76 layers considering a second e-gun. The color of central and right samples, despite the different coating recipe, are the same indicating that the nominal thicknesses are correct (before these upgrades, same recipes showed different colors). The morphological and structural properties of right sample in Figure E1(b) are studied intensively by using different techniques such as Atomic Force microscopy (AFM), Scanning transmission electron microscopy (STEM), X-ray reflectivity (XRR), X-Ray diffractometry (XRD), and Raman spectroscopy (RS). The main results are:

- 1) XRD and RS measurements confirm that the as grown samples are amorphous [Figure E1(c)]. The only reflection and modes are relative to the Si substrate;
- 2) XRR measurements show average layer thicknesses very close to the nominal ones. The measured value for the TiO_2 is 1.4 nm (nominal 1.3 nm) and for SiO_2 is 2.2 nm (nominal 2 nm), see Figure E1(d).
- 3) AFM measurements show a very flat surface. In fact the RMS roughness is 0.1-0.2 nm [Figure E1(e)];
- 4) STEM measurements show well-defined nanolayers [Figure E1(f)].

Then, more precise coatings are obtained even if the thickness is still affected by the chamber geometry. For this reason, to achieve the uniformity, shades (with different shapes) can be introduced inside the coater.

In conclusion, the QCM thermal shock problem in the coating nanolayered production is revealed when an electron beam evaporator is used. Then, it was possible to mitigate the thermal shock producing very high-precision coatings.

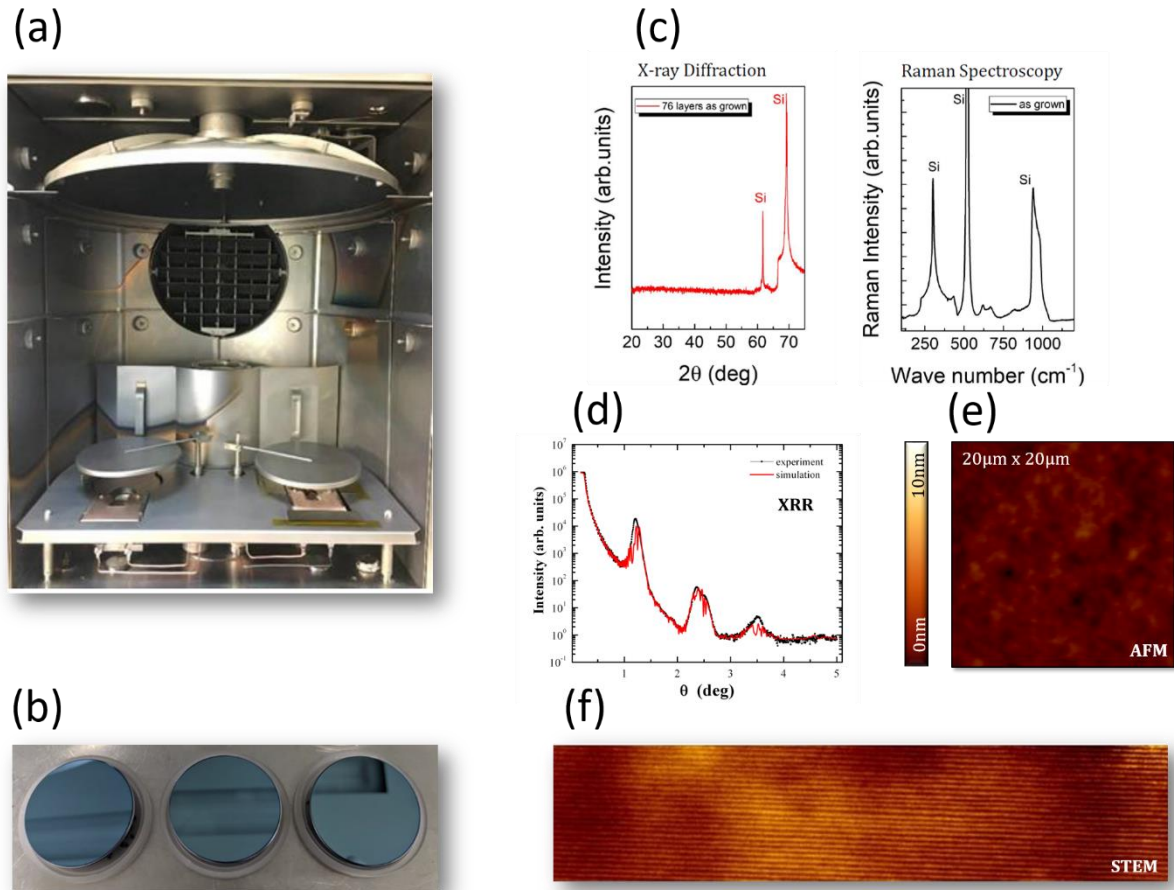


Figure E1: (a) OptoTech OAC-75-RF coater with dual e-gun configuration. (b) Optically equivalent coatings on 2" Si substrates. (c) XRD and RS, (d) XRR, (e) AFM, (f) STEM measurements performed on the 76-layer $\text{TiO}_2/\text{SiO}_2$ sample. Adapted from [1].

References

1. Neisln, J. *et al.* Pushing the precision of e-beam evaporation for nanolayered coatings, *in preparation*.

Appendix F

Period abroad

During my PhD program, I spent one week in 2018 at University of Lancaster (UK) under the supervision of Prof. Oleg V. Kolosov, to perform measurements by using Scanning Thermal Microscopy (S_{Th}M) on the nanolayer-samples. This was the first experimental evidence of the nanolayer structures deposited at University of Sannio in collaboration with University of Salerno.

First, I learned how to operate the S_{Th}M. This kind of microscopy allows to measure the thermal transport on the nanoscale and to use a thermal sensor with a sharp thermally conductive tip [1-3]. Originally, S_{Th}M probes used a 5 μm thick of Platinum (Pt) that worked as a heater and a resistive thermal sensor with a micrometer lateral resolution [1]. Modern probes are fabricated by using silicon, silicon oxide, silicon nitride materials [4], or carbon nanotubes or nanostructures incorporating a graphene [3]. The aim of the improvement was to enhance thermal contact between sensor and samples since these materials have extreme thermal conductivity, ranging from hundreds to thousands of W m⁻¹ K⁻¹. In Figures F1(a) and (b), I show a doped Si (DS) and SiO₂/Si₃N₄ silicon nitride cantilever with Palladium (Pd) thermal sensing element S_{Th}M probes, respectively, characterized by thermal conductivity of 130 and 1 W m⁻¹ K⁻¹.

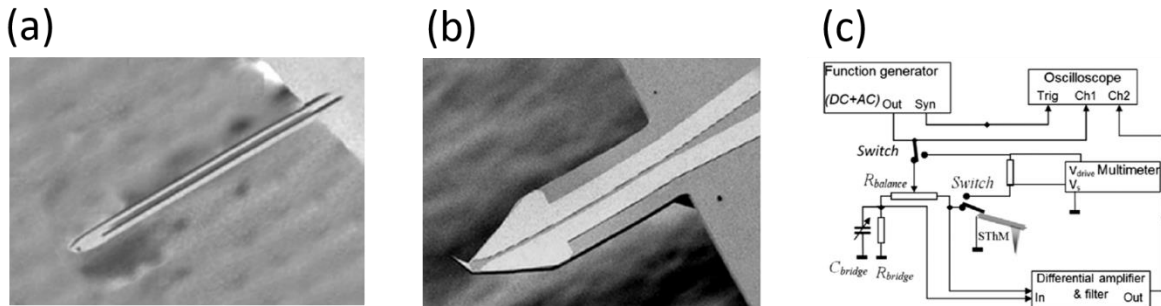


Figure F1: (a) doped Si (DS) and (b) SiO₂/Si₃N₄ silicon nitride cantilever with Pd thermal sensing element S_{Th}M probes. (c) S_{Th}M electronics. Adapted from [3].

During the scanning, the feedback loop maintains constant tip-surface force and the temperature of the probe, which reaches 100 °C above ambient temperature, can be monitored by measuring its resistance in a balanced Wheatstone bridge in AC-DC configuration [1,3]. In light of this, Figure F1(c) shows the schematic diagram of AC and DC measurement S_{Th}M electronics. Briefly, an AC current flows in the tip and it is heated by Joule effect. When tip approaches the sample surface, the tip temperature decreases due to thermal transport through the sample. This is due to radiation, convection, and conduction phenomena through the sample, which are correlated to the thermal conductivity of the sample [5].

In order to perform the thermal measurements on the nanolayers, I used a SPM by Bruker MultiMode Nanoscope III controller, and a SThM probe holder by Anasys Instruments. The resistive SThM probes has a 0.3 N/m of spring constant and a tip radius < 100 nm.

In order to perform SThM measurements and reveal nanostructures, the sample has to first cut. The preparation occurs by using a novel cross-sectioning method, beam-exit Arion cross-sectional polishing (BEXP) [6,7], in which the Ar-ion is not normal to the sample surface, mounted close to a masking plate, but impinges with a shallow angle and exits the surface far from the masking plate (see Figure F2(a)). This technique gives back a very flat surface with roughness of nanometer-scale value, and it is able to reveal the morphology of the subsurface nanostructures. The instrument used is a Leica EM TIC020 triple ion beam cutter, with a wide milling-region sector of 100°, and with an adjustable voltage during the process.

The combination of vertical and lateral movements, and the BEXP geometry allows high resolution and to reduce the tip-size effect on measurements. In Figure F3(b) is shown an example of the measurement process.

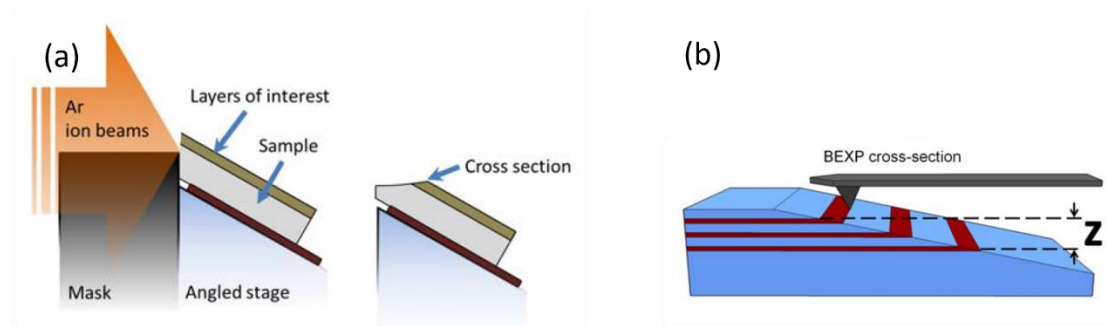


Figure F2: (a) Beam-exit Ar-ion cross-sectional polishing. (b) Vertical movement of the cantilever on the cut sample. Adapted from [6].

The investigated sample is a multilayer of ZrO_2/TiO_2 formed by 8 layers deposited by ion-plasma deposition on glass substrate at University of Sannio. The total thickness of the film is ~200 nm, with a layer thickness of 25.6 nm.

The SThM experiments allowed determining several information about the multilayers. First, during the scanning I can acquired different measurement channels: topography, friction, and thermal conductivity. In Figure F3(a), I show the morphology, on a scan area of $1 \mu m \times 1 \mu m$, of the top surface of the sample. Here, I investigated the area far from the cut, displaying a granular texture due to also the high roughness of the substrate that is higher than 1 nm. Indeed, I measure a RMS roughness of sample of 2.5 nm. Figure F2(b) shows the morphology of the cross section, on a scan area of $5 \mu m \times 5 \mu m$, in which the cut is barely visible in the middle, and I can identify the sample surface, on the left, and the glass substrate, on the right. In Figure F3(c), a 3D view of the morphology

displayed in Figure F2(b) shows the cross-sectioned area that has been cut with an angle of about 11° . A slight change in the cut-angle can be recognized when going from the sample to the substrate.

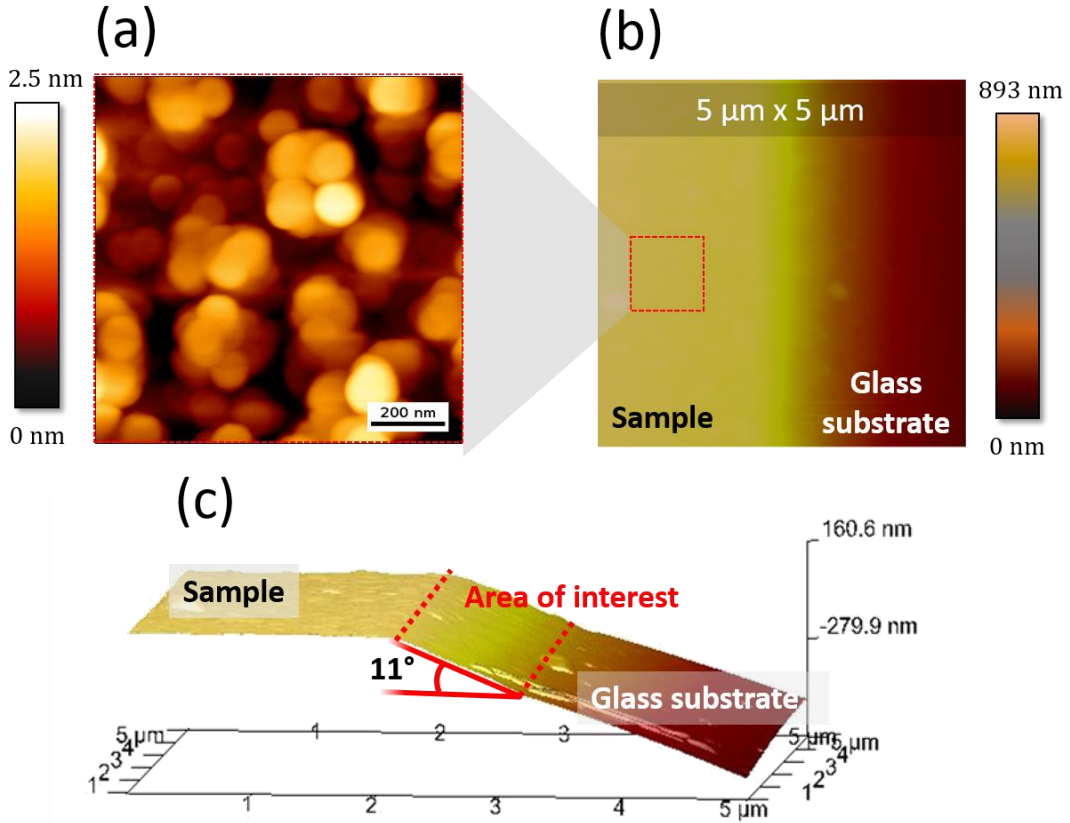


Figure F3: (a) Top surface on a scan area of $1 \mu\text{m} \times 1 \mu\text{m}$, (b) 2D view and (c) 3D view on a scan area of $5 \mu\text{m} \times 5 \mu\text{m}$ of the 8-layer sample.

Moreover, during the scanning, the cantilever of the AFM probe in contact, can be bend vertically due to the interaction between the sample-tip, and can be twisted due to the friction. This cantilever torsion is called “lateral deflection” and depends on the frictional coefficient of the material, the topography of the surface, the direction of the cantilever movement, the scanning speed, and the cantilever’s lateral spring constant. The microscopy connected to the cantilever torsion is known as Lateral Force Microscopy (LFM). By using this technique, it is possible to study the tribology, i.e., the science and engineering of interacting surfaces in relative motion at the nanoscale [8]. In Figure F4(a), the lateral deflection map, $5 \mu\text{m} \times 5 \mu\text{m}$ in lateral size, across the cross-sectioned area is showed. The color scale indicates the area with more (blue) or less (black) friction. In the yellow rectangle, the appearance of 8 layers is clearly recognized, as expected. Here, the glass substrate, as well as the TiO_2 , shows a higher value of friction than ZrO_2 material. Indeed, the friction coefficient value find in the literature for thin films, is 0.3-0.4 for the glass substrate (and the TiO_2), and 0.08-0.16 for the ZrO_2 [9]. In light of this, I have indicated with white and yellow numbers the TiO_2 and ZrO_2 , respectively.

From this measurement, I am able to measure the total thickness of the sample and the periodicity of the layers. In Figure F4(a), I traced a line profile on the multilayers, corresponding to the plot with several peaks (periodicity) showed in Figure F4(b). From simple geometric considerations, I can calculate:

- 1) Total thickness: $h_t = L \sin\theta \approx 190 \text{ nm}$,
where L is the length of profile line across the section, and $\theta = 11^\circ$ is the angle cut;
- 2) Thickness of $\text{TiO}_2/\text{ZrO}_2$ doublet: $h_d = L_d \sin\theta = (50 \pm 10) \text{ nm}$
where L_d [L' , L'' , L''' in Figure F4(b)] is the periodicity of each peak, and $\theta = 11^\circ$ is the angle cut.

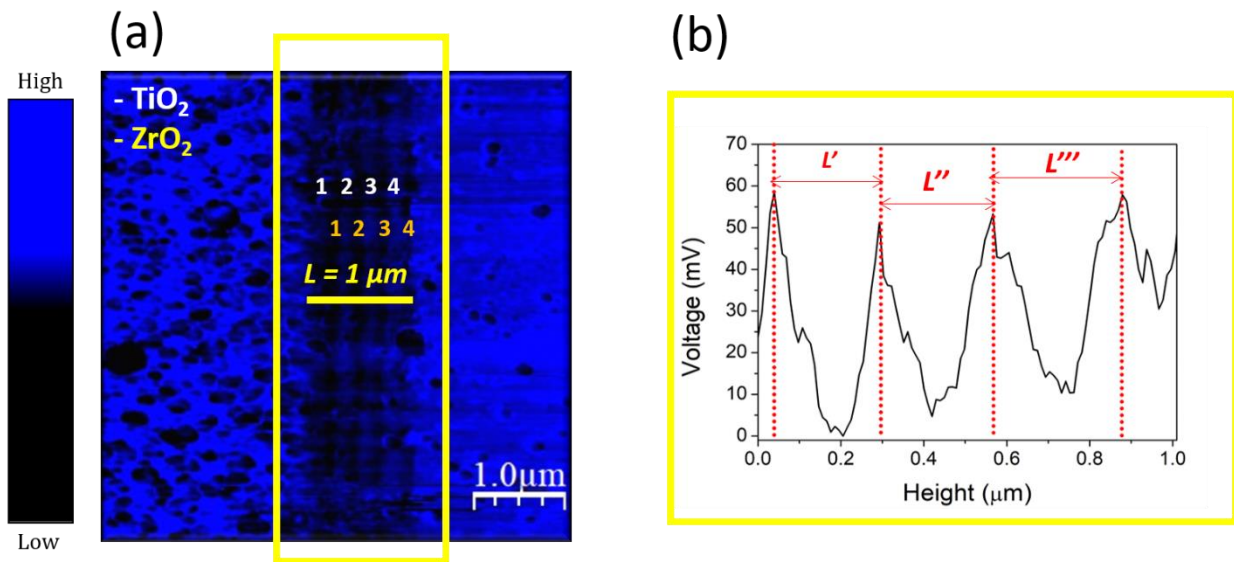


Figure F4: (a) Friction map (LFM), and (b) profile line of the 8-layer sample.

Figure F5(a) shows the map of the thermal conductivity along the cross-section of the 8-layer sample. As mentioned before, the SThM can map the heat locally transferred from the probe to the sample. This heat is related to the thermal conductivity of the material. The black-to-white color scale indicates the area with higher (black) and lower (white) thermal conductivity value, and in this case, the contrast is less evident because ZrO_2 and TiO_2 materials show similar values of thermal conductivity, i.e., 5.5 W/mK and 8 W/mK , respectively [10].

Finally, I have performed the measurement of Ultrasonic Force Microscopy (UFM) on this sample. This derived-AFM technique detects ultrasonic vibration in the range frequencies from MHz to GHz using an AFM cantilever with a resonant frequency below 100 kHz. This kind of analysis gives information about the elastic properties of the sample, e.g., the Young's modulus [11]. Figure F5(b) shows the UFM map in the cross-sectioned region (yellow rectangle). Here, I can clearly recognize alternating of red

(higher stiffness) and blue (low stiffness) layers of TiO_2 and ZrO_2 . The Young's modulus reported in the literature are 244 and 171 GPa for TiO_2 and ZrO_2 [10], showing that the TiO_2 is stiffer than ZrO_2 , in agreement with our experiments. In light of this, I have indicated with blue and yellow numbers the TiO_2 and ZrO_2 , respectively.

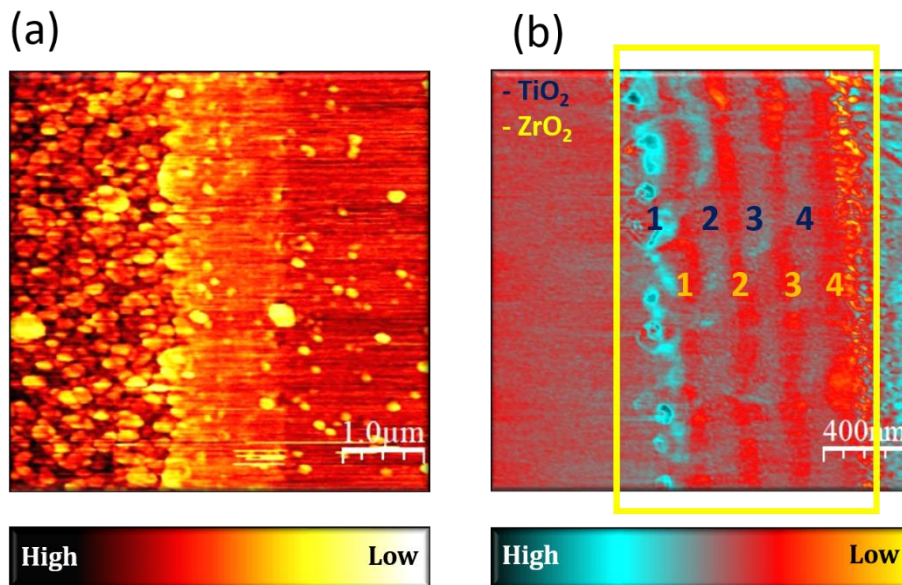


Figure F5: (a) Thermal conductivity (SThM), and (b) Ultrasonic Force Microscopy (UFM) maps of 8-layer sample.

References

1. Majumdar, A. Scanning thermal microscopy. *Annual review of materials science* **1999**, *29(1)*, 505-585.
2. Pollock, H. M., Hammiche, A. Micro-thermal analysis: techniques and applications. *Journal of Physics D: Applied Physics* **2001**, *34(9)*, R23.
3. Tovee, P., *et al.* Nanoscale spatial resolution probes for scanning thermal microscopy of solid state materials. *Journal of Applied Physics* **2012**, *112(11)*, 114317.
4. Leinhos, T., *et al.* Micromachined fabrication of Si cantilevers with Schottky diodes integrated in the tip. *Applied Physics A: Materials Science & Processing* **1998**, *66(7)*.
5. Poon, S. W., *et al.* Probing thermal transport and layering in disk media using scanning thermal microscopy, **2017**.
6. Kolosov, O. V., *et al.* Material sensitive scanning probe microscopy of subsurface semiconductor nanostructures via beam exit Ar ion polishing. *Nanotechnology* **2011**, *22(18)*, 185702.
7. Robson, A. J., *et al.* High-accuracy analysis of nanoscale semiconductor layers using beam-exit ar-ion polishing and scanning probe microscopy. *ACS applied materials & interfaces* **2013**, *5(8)*, 3241-3245.
8. Ruan, J. A., Bhushan, B. Atomic-scale friction measurements using friction force microscopy: part I—general principles and new measurement techniques, **1994**.
9. MEMSNET. Available online: <https://www.memsnet.org/material> (accessed on 15 Spetember 2021).
10. Shackelford, J. F., Alexander, W. *CRC materials science and engineering handbook*. CRC press, **2000**.
11. Kolosov, O., Yamanaka, K. Nonlinear detection of ultrasonic vibrations in an atomic force microscope. *Japanese journal of applied physics* **1993**, *32(8A)*, L1095.

List of publications

1. V. Pierro, et al. (O.Durante), On the performance limits of coatings for gravitational wave detectors made of alternating layers of two materials, *Optical Materials* 96 (2019): 109269.
2. Strambini, *et al.* (O.Durante), A Josephson phase battery, *Nature Nanotechnology* 15.8 (2020): 656-660.
3. C. Guarcello, *et al.* (O.Durante), rf-SQUID measurements of anomalous Josephson effect, *Physical Review Research* 2.2 (2020): 023165.
4. Pierro, V., *et al.* (O.Durante), Ternary quarter wavelength coatings for gravitational wave detector mirrors: Design optimization via exhaustive search. *Physical Review Research* 3.2 (2021): 023172.
5. O.Durante *et al.*, Emergence and Evolution of Crystallization in TiO₂ Thin Films: A Structural and Morphological Study. *Nanomaterials* 11.6 (2021): 1409

Publications within LIGO-Virgo-Kagra (LVK) collaboration

1. B.P. Abbott *et al.* (O.Durante), All-sky search for long-duration gravitational-wave transients in the second Advanced LIGO observing run, *Physical Review D* 99 (2019) no.10, 104033.
2. Abbott, B. P., *et al.* (O.Durante), Search for Subsolar Mass Ultracompact Binaries in Advanced LIGO's Second Observing Run, *Physical review letters* 123.16 (2019): 161102.
3. Abbott, Benjamin P., *et al.* (O.Durante), Search for gravitational-wave signals associated with gamma-ray bursts during the second observing run of Advanced LIGO and Advanced Virgo, *The Astrophysical Journal* 886.1 (2019): 75.
4. Acernese, F., *et al.* (O.Durante), Increasing the astrophysical reach of the advanced Virgo detector via the application of squeezed vacuum states of light, *Physical Review Letters* 123.23 (2019): 231108.

5. B.P. Abbott *et al.* (O.Durante), All-sky search for short gravitational-wave bursts in the second Advanced LIGO and Advanced Virgo run, *Physical Review D* 100.2 (2019): 024017.
6. B.P. Abbott *et al.* (O.Durante), Search for Eccentric Binary Black Hole Mergers with Advanced LIGO and Advanced Virgo during Their First and Second Observing Runs, *The Astrophysical Journal* 883.2 (2019): 149.
7. B.P. Abbott *et al.* (O.Durante), Search for intermediate mass black hole binaries in the first and second observing runs of the Advanced LIGO and Virgo network, *Physical Review D* 100.6 (2019): 064064.
8. Hamburg, R., *et al.* (O.Durante), A joint fermi-gbm and ligo/virgo analysis of compact binary mergers from the first and second gravitational-wave observing runs, *The Astrophysical Journal* 893.2 (2020): 100.
9. Abbott, B. P., *et al.* (O.Durante), GW190425: Observation of a compact binary coalescence with total mass $\sim 3.4 M_{\odot}$, *The Astrophysical Journal Letters* 892.1 (2020): L3.
10. Abbott, R., *et al.* (O.Durante), GW190814: Gravitational waves from the coalescence of a 23 solar mass black hole with a 2.6 solar mass compact object, *The Astrophysical Journal Letters* 896.2 (2020): L44.
11. Abbott, B. P., *et al.* (O.Durante), Model comparison from LIGO–Virgo data on GW170817’s binary components and consequences for the merger remnant, *Classical and Quantum Gravity* 37.4 (2020): 045006.
12. Acernese, F. *et al.* (O.Durante), The advanced Virgo longitudinal control system for the O2 observing run, *Astroparticle Physics* 116 (2020): 102386.
13. Abbott, B. P., *et al.* (O.Durante), Optically targeted search for gravitational waves emitted by core-collapse supernovae during the first and second observing runs of advanced LIGO and advanced Virgo, *Physical Review D* 101.8 (2020): 084002.
14. Abbott, R., *et al.* (O.Durante), Gravitational-wave constraints on the equatorial ellipticity of millisecond pulsars. *The Astrophysical journal letters* 902.1 (2020): L21.
15. Acernese, *et al.* (O.Durante), Quantum back action on kg-scale mirrors: Observation of radiation pressure noise in the Advanced Virgo detector. *Physical review letters* 125.13 (2020): 131101.

16. Abbott, R., *et al.* (O.Durante), GW190521: A binary black hole merger with a total mass of $150 M_{\odot}$. *Physical review letters* 125.10 (2020): 101102.
17. Abbott, R., *et al.* (O.Durante), Properties and astrophysical implications of the $150 M_{\odot}$ binary black hole merger GW190521. *The Astrophysical Journal Letters* 900.1 (2020): L13.
18. Abbott, R., *et al.* (O.Durante), GW190412: Observation of a binary-black-hole coalescence with asymmetric masses. *Physical Review D* 102.4 (2020): 043015.
19. Abbott, R., *et al.* (O.Durante), Open data from the first and second observing runs of Advanced LIGO and Advanced Virgo. *SoftwareX* 13 (2021): 100658.
20. Abbott, R., *et al.* (O.Durante), All-sky search in early O3 LIGO data for continuous gravitational-wave signals from unknown neutron stars in binary systems, *Physical Review D* 103.6 (2021): 064017
21. Abbott, B.P., *et al.* (O.Durante), A Gravitational-wave Measurement of the Hubble Constant following the Second Observing Run of Advanced LIGO and Virgo, *The Astrophysical Journal* 909.2 (2021): 218.
22. Calloni E., *et al.* (O.Durante), High-bandwidth beam balance for vacuum-weight experiment and Newtonian noise subtraction, *The European Physical Journal Plus* 136.3 (2021): 1-14.
23. Abbott, R., *et al.* (O.Durante), Population properties of compact objects from the second LIGO–Virgo Gravitational-Wave Transient Catalog. *The Astrophysical Journal Letters* 913.1 (2021): L7.
24. Abbott, R., *et al.* (O.Durante), Constraints on cosmic strings using data from the third Advanced LIGO–Virgo observing run. *Physical review letters* 126.24 (2021): 241102.
25. Abbott, R., *et al.* (O.Durante), Tests of general relativity with binary black holes from the second LIGO–Virgo gravitational-wave transient catalog. *Physical Review D* 103.12 (2021): 122002.
26. Abbott, R., *et al.* (O.Durante), Diving below the spin-down limit: Constraints on gravitational waves from the energetic young pulsar PSR J0537-6910. *The Astrophysical Journal Letters* 913.2 (2021): L27.

27. Abbott, R., *et al.* (O.Durante), Gwtc-2: Compact binary coalescences observed by ligo and virgo during the first half of the third observing run. *Physical Review X* 11.2 (2021): 021053.
28. Abbott, R., *et al.* (O.Durante), Observation of gravitational waves from two neutron star–black hole coalescences. *The Astrophysical Journal Letters* 915.1 (2021): L5.
29. Abbott, R., *et al.* (O.Durante), Search for Gravitational Waves Associated with Gamma-Ray Bursts Detected by Fermi and Swift during the LIGO-Virgo Run O3a. *Astrophysical Journal* 915.2 (2021): 86.
30. Abbott, R., *et al.* (O.Durante), Upper limits on the isotropic gravitational-wave background from Advanced LIGO and Advanced Virgo’s third observing run. *Physical Review D* 104.2 (2021): 022004.
31. Abbott, R., *et al.* (O.Durante), All-sky search for continuous gravitational waves from isolated neutron stars in the early O3 LIGO data. *Physical Review D* 104.8 (2021): 082004.